Forschungszentrum Karlsruhe
in der Helmholtz-Gemeinschaft

Wissenschaftliche Berichte
FZKA 7197

Development of Calculation Methods to Analyze Radiation Damage, Nuclide Production and Energy Deposition in ADS Materials and Nuclear Data Evaluation

C.H.M. Broeders, A.Yu. Konobeyev

Institut für Reaktorsicherheit
Programm Nukleare Sicherheitsforschung

August 2006

Forschungszentrum Karlsruhe

in der Helmholtz-Gemeinschaft

Wissenschaftliche Berichte

FZKA 7197

Development of calculation methods to analyze radiation damage, nuclide production and energy deposition in ADS materials and nuclear data evaluation

C.H.M. Broeders, A.Yu. Konobeyev

Institut für Reaktorsicherheit
Programm Nukleare Sicherheitsforschung

Forschungszentrum Karlsruhe GmbH, Karlsruhe

2006

Forschungszentrum Karlsruhe GmbH
Postfach 3640, 76021 Karlsruhe

Mitglied der Hermann von Helmholtz-Gemeinschaft
Deutscher Forschungszentren (HGF)

ISSN 0947-8620

urn:nbn:de:0005-071975

Abstract

A method of the evaluation of the defect production rate in metals irradiated with neutrons in various power units has been proposed. The method is based on the calculation of the radiation damage rate using nuclear models and the NRT model and the use of corrections obtained from the analysis of available experimental data and from the molecular dynamics simulation.

A method combining the method of the molecular dynamics and the binary collision approximation model was proposed for the calculation of the number of defects in irradiated materials. The method was used for the displacement cross-section calculation for tantalum and tungsten irradiated with protons at energies from several keV up to 1 GeV and with neutrons at energies from 10^{-5} eV to 1 GeV.

A new approach has been proposed for the calculation of the non-equilibrium fragment yields in nuclear reactions at intermediate and high energies. It was used for the evaluation of the non-equilibrium component of the ^{4}He and ^{3}He production cross-section. The helium production cross-section has been obtained for iron, ^{181}Ta and tungsten at proton energies from several MeV to 25 GeV and for ^{181}Ta and tungsten at neutron energies up to 1 GeV.

A new model for the simulation of interactions of intermediate and high energy particles with nuclei was discussed. The non-equilibrium particle emission is simulated by the intranuclear cascade model using the Monte Carlo method. The deterministic evaporation model is used for the description of the equilibrium de-excitation. The model was used for the analysis of radionuclide yields in proton induced reactions at energies from 0.8 to 2.6 GeV. The results of calculations show the advantage of the model proposed in accuracy of predictions comparing with other popular intranuclear cascade evaporation models.

A new approach was proposed for the calculation of non-equilibrium deuteron energy distributions in nuclear reactions induced by nucleons of intermediate energies. The calculated deuteron energy distributions are in a good agreement with the measured data for nuclei from ^{12}C to ^{209}Bi.

The energy deposition has been calculated for the targets from lithium to uranium irradiated with intermediate energy protons using the models from the MCNPX code package and the CASCADE/INPE code.

Entwicklung von Berechnungsmethoden für die Analyse von Strahlenschäden, Nuklidproduktion und Energiefreisetzung in Materialien für ADS und für Kerndatenauswertungen.

Zusammenfassung

Es wurde eine Methode vorgeschlagen für die Auswertung der Produktionsraten für Strahlenschäden in Metallen durch Neutronenbestrahlung in verschiedenen Reaktorsystemen. Die Methode basiert auf der Berechnung der Strahlenschädigungsraten mit nuklearen Modellen und der NRT Methode und einer nachfolgenden Korrektur auf der Basis von Auswertungen von experimentellen Daten und Simulationen der molekularen Dynamik.

Eine Kombination der Methode der Simulation der molekularen Dynamik und der „Binary Collision Approximation“ wurde vorgeschlagen für die Berechnung der Anzahl der Schädigungen in bestrahlten Materialien. Diese Methode wurde benutzt für die Berechnung von Displacement Querschnitten für Tantal und Wolfram nach Bestrahlung mit Protonen im Energiebereich von einigen KeV bis 1 GeV und mit Neutronen im Bereich 10-5 eV bis 1 GeV.

Ein neuer Ansatz wurde vorgeschlagen für die Berechnung der Ausbeuten der Fragmente der Nicht-Gleichgewichtsprozesse bei intermediären und hohen Energien. Dieser wurde angewandt für die Auswertung der Nicht-Gleichgewicht Komponenten von 4He und 3He Produktionsquerschnitten. He Produktionsquerschnitte wurden bestimmt für Eisen, 181Ta und Wolfram für Protonen Energien von mehreren MeV bis 25 GeV und für 181Ta und Wolfram für Neutronenenergien bis 1 GeV.

Weiter wurde ein neues Modell diskutiert für die Simulation der Wechselwirkung von Teilchen mit intermediären und hohen Energien mit Atomkernen. Die Nicht-Gleichgewicht Teilchenemission wird nach der Monte Carlo Methode simuliert, während das deterministische Verdampfungsmodell benutzt wird für die Gleichgewichts Entregung. Dieses Modell wurde angewandt für die Analyse von Ausbeuten von Radionukliden nach durch Protonen induzierten Reaktionen bei Energien von 0.8 bis 2.6 GeV. Die Ergebnisse der Untersuchungen zeigen die Vorteile des vorgeschlagenen Modells bei den Vorhersagen, im Vergleich mit anderen häufig angewandten intranuklearen Kaskade Verdampfungsmodellen.

Ein neuer Ansatz wurde vorgeschlagen für die Berechnung von Nicht-Gleichgewicht Energieverteilungen von Deuteronen bei nuklearen Reaktionen ausgelöst durch Nukleonen mit mittleren Energien. Die berechneten Energieverteilungen von Deuteronen sind in guter Übereinstimmung mit gemessenen Daten für eine Reihe von Nukliden von 12C bis 209Bi.

Schließlich wurden für Materialien von Lithium bis Uran Energiefreisetzungen nach Bestrahlung mit Protonen mit intermediären Energien berechnet unter Benutzung der Modelle in den Codes MCNPX und CASCADE/INPE.

CONTENTS

1. Defect production efficiency in metals and evaluation of radiation damage rate in various units using results of molecular dynamics simulation

A method of the defect production rate evaluation in metals irradiated with neutrons in various power units is proposed. The method is based on the calculation of the radiation damage rate using the NRT model [1] and obtained values of the defect production efficiency using results of the molecular dynamics simulation.

The NRT model [1] is frequently used for the calculation of the damage accumulation in irradiated materials. The relative simplicity of the approach provides its use in the popular codes as NJOY [2], MCNPX [3], LAHET [4], SPECTER [5] and others. The available experimental data and more rigorous calculations show the substantial difference with the predictions of the NRT model that makes its use for the reliable calculation of radiation damage rather questionable. However, the previous analysis of the experimental damage rates shown the deviations from the NRT calculation has been performed using the out-of-dated versions of neutron data libraries like as ENDF/B-IV, ENDF/B-V and JENDL-1, which are not in use for applications now. Different authors have used the different sets of Frenkel pair resistivity values and effective threshold energies for the data analysis that complicates the interpretation of the results obtained and the analysis of different irradiation experiments.

The defect production efficiency in metals irradiated with neutrons of different sources were analyzed in the present work. The available data for Frenkel pair resistivity were compiled and analyzed (Section 1.2). The evaluated and recommended values are presented along with the systematics of Frenkel pair resistivity. The available experimental data for damage production rates were collected and examined (Section 1.3). The damage energy cross-sections were calculated with the data from ENDF/B-VI (Release 8), JENDL-3.3, JEFF-3.0, BROND-2.2 and CENDL-2.2 for realistic neutron spectra. The average efficiency of the defect production was calculated for different type of the irradiation.

The MARLOWE code [6] was applied for the calculations of the number of defects in irradiated materials. The results were compared with the simulations performed by the method of the molecular dynamics. The theoretical values of the defect production efficiency were applied to the neutron damage calculations for various types of nuclear power facilities, as the thermal reactor, the fast breeder reactor, the fusion reactor and others (Section 1.4).

1.1 Efficiency of the defect production in materials

The efficiency of defect production in irradiated materials is defined as follows

$$\eta = \frac{N_D}{N_{NRT}}, \qquad (1)$$

where N_D is the number of stable displacements at the end of collision cascade, N_{NRT} is the number of defects calculated by the NRT model [1].

In the theoretical simulations based on the method of molecular dynamics (MD) and the binary collision approximation model (BCA) the N_D value in Eq.(1) is considered equal to the total number of single interstitial atom-vacancy pairs including the amount in a clustered fraction remaining after the recombination in collision cascade is complete.

The number of defects (Frenkel pair) predicted by the NRT formula [1] is equal to

$$N_{NRT} = \frac{0.8}{2E_d} T_{dam}, \qquad (2)$$

where E_d is the effective threshold displacement energy, T_{dam} is the "damage energy" equal to the energy transferred to lattice atoms reduced by the losses for electronic stopping of atoms in displacement cascade.

The effective threshold displacement energy E_d in Eq.(2) which is called also as the "averaged threshold energy" [7,8] is derived from electron irradiation experiments. The compilation of E_d values is presented in Section 1.3. According to other definition [9,10] the value of the effective displacement energy is defined from a condition $\eta = 1$ which relates to a number of defects N_D defined from the experiments for neutron irradiation of materials. This effective threshold energy is referred as $E_d(\eta=1)$ in the present work to separate it from the commonly used effective threshold displacement energy E_d.

The average defect production efficiency, $\langle\eta\rangle$ is derived from the experimentally observed resistivity damage rate with the help of the following relation

$$\left(\frac{d\Delta\rho}{d\Phi}\right)\Bigg|_{\Delta\rho=0} = \langle\eta\rangle \rho_{FP} \frac{0.8\langle\sigma T_d\rangle}{2E_d}, \tag{3}$$

where $\left(d\Delta\rho / d\Phi\right)\big|_{\Delta\rho=0}$ is the initial resistivity-damage rate equal to the ratio of resistivity change $\Delta\rho$ per irradiation fluence Φ extrapolated to zero dose value, ρ_{FP} is the specific Frenkel pair resistivity, $\langle\sigma T_d\rangle$ is the damage energy cross-section averaged for the particle spectrum basing on the NRT model.

The spectrum averaged damage energy cross-section is calculated as follows

$$\langle\sigma T_d\rangle = \sum_{i=1} \iint \varphi(E) \frac{d\sigma_i(E,T)}{dT} T_{dam}(T)\, dT\, dE \Bigg/ \int \varphi(E)\, dE \quad , \tag{4}$$

where $d\sigma_i/dT$ is the spectrum of recoils produced in irradiation of material with primary particle, $\varphi(E)$ is the particle spectrum, T_{dam} is the damage energy calculated according to Ref.[1], the summation is for all channels of the primary particle interaction with material.

The use of Eq.(3) supposes that the resistivity per Frenkel pair does not depend from the degree of defect clusterization in matter and that the resistivity of a cluster is equal to the sum of resistivity of isolated defects. For small clusters it is considered usually as a good approximation [11-14].

According to Eq.(3) the value of defect production efficiency $\langle\eta\rangle$ derived from experimental data depends from the value of Frenkel pair resistivity ρ_{FP} and the effective threshold energy E_d adopted for the analysis and from the quality of the $\langle\sigma T_d\rangle$ data. It is the main reason of the considerable scattering of the $\langle\eta\rangle$ values obtained by different authors for the same metals.

1.2 Resistivity per Frenkel defect and effective threshold displacement energy

1.2.1 Data compilation and evaluation

Data for the specific Frenkel pair resistivity ρ_{FP} were taken from the papers [9,10,15-68,102-126] relating to the measurements performed after 1962. The reference for the early measurements for copper, silver and gold can be found in Refs.[34,41].

Data for Frenkel pair resistivity were subdivided in several groups by the method of their derivation: the data obtained by the X-ray diffraction method, the data extracted from the electron irradiation of single crystals at low temperature, the ρ_{FP} values obtained from the experiments with polycrystals, the data evaluated by the analysis of various experiments and the data obtained with the help of systematics. If the detailed information about the method of data derivation is absent, the data are referred as “adopted” by the authors of a certain work.

The collected values of ρ_{FP} are shown in Table 1. The data are presented for the metals with face-centered cubic lattice (*fcc*) at first, than for the body-centered cubic metals (*bcc*), for the metals with hexagonal lattice (*hcp*) and for other metals.

The evaluation of Frenkel pair resistivity for each element from Table 1 was performed by the statistical analysis taking into account the relative accuracy of the method of data derivation and the experimental errors. If only systematics data are available for a certain metal the recommended value of ρ_{FP} is not given. The evaluated values of Frenkel pair resistivity are shown in Table 1 (sixth column).

The adopted values of ρ_{FP} are slightly different from ones obtained in Ref.[102]. Mainly, it results from the different principles of the evaluation in Ref.[102] and in the present work. As a rule, the ρ_{FP} value for a certain element recommended in Ref.[102] corresponds to a single reliable measurement. In the present work the results of the different most reliable measurements were analyzed statistically.

The effective threshold displacement energies E_d taken from literature are shown in Table 1. If the same E_d value was used by different authors only the single reference is given. Also, the adopted E_d values used in the present work for damage production efficiency calculations are shown in Table 1 (ninth column).

It should be noted that the exact absolute values of threshold energy E_d is of secondary importance in the case the experimental dose rates are known. They are used only for the comparison of defect production efficiency in different experiments.

1.2.2 Systematics of Frenkel pair resistivity

The evaluated and adopted values of Frenkel pair resistivity (Table 1) were used to constrain the systematics of ρ_{FP} by the method proposed by Jung [18]. The systematics combines the Frenkel pair resistivity, the resistivity at the melting point and the bulk modulus of the material. The general form of the systematics is as follows [18]

$$\rho_{FP} = \rho(T_{melt})\left(\alpha_1 + \alpha_2 (B\Omega)^{\alpha_3}\right), \qquad (5)$$

where $\rho(T_{melt})$ is the resistivity at the melting temperature, B is the bulk modulus, Ω is the atomic volume, α_i are the parameters to be obtained by the fitting procedure.

The experimental values of the resistivity at the melting point $\rho(T_{melt})$ were taken from Ref.[69]. If absent, the $\rho(T_{melt})$ values were taken from Ref.[18] or evaluated with the help of the following approximate formula [70]

$$\rho(T_{melt}) = \rho(T_0)\,\frac{T_{melt}}{T_0}\,\frac{F(\theta/T_{melt})}{F(\theta/T_0)}\,, \qquad (6)$$

where $\rho(T_0)$ is the resistivity at the temperature T_0 , θ is the Debye temperature and F is the universal function.

The values of F(x) function are tabulated in Ref.[70] and can be approximated with a good accuracy at $x \le 6$ by the following formula

$$F(x) = 2.884\times10^5\,(55.5 + x^{1.98})^{-3.13} \qquad (7)$$

Data for the resistivity $\rho(T_0)$ were taken from Ref.[69] at T_0 = 293-300 K, the Debye temperature and the bulk modulus are from Ref.[71]. The atomic volume Ω was calculated as the inverse of the atomic concentration.

The fitting of Eq.(5) to the adopted values of ρ_{FP} from Table 1 gives the following systematics of Frenkel pair resistivity

$$\rho_{FP} = \rho(T_{melt})\left(12.08 + 52.36\,(B\Omega)^{-2.603}\right), \qquad (8)$$

where the product $B\Omega$ is taken in the units 10^{-18} Nm.

Below, the systematics Eq.(8) is used for the ρ_{FP} value evaluation if the experimental data are absent.

Frenkel pair resistivity predicted by the systematics Eq.(8) is shown for various metals in Table 2 and Fig.1.

Table 1

The Frenkel pair resistivity ρ_{FP} and the effective threshold displacement energy E_d taken from literature and the values of ρ_{FP} and E_d evaluated and adopted for the analysis of the defect production efficiency. Methods of the data derivation: “Exp D” is X-ray diffraction method, “Exp T” is the threshold energy determination for electron irradiation of single crystals at low temperature, “Exp T(p)” is for the electron irradiation of polycrystals, “Evl E” is the evaluation performed basing on the analysis of different experiments, “Evl S” is the estimation made with the help of the systematics, “Adp” is the data adopted by the authors of cited works.

Metal	Lattice	ρ_{FP} [μΩ m]	Type	Ref	Adopted ρ_{FP} [μΩ m]	E_d [eV]	Ref	Adopted E_d [eV]
13 Al	fcc	3.9 ± 0.6	Exp D	[15]	3.7	27.	[22]	27.
		4.2 ± 0.8	Exp D	[16]		45.	[23]	
		3.2 ± 0.6	Exp D	[17]		66.	[9]	
		3.4	Exp T(p)	[33]				
		1.4...4.4	Exp T(p)	[102,103]				
		1.32	Exp T(p)	[104]				
		1.35	Exp T(p)	[102,105]				
		4.0	Evl E	[22,102]				
		4.0 ± 0.6	Evl E	[10,18]				
		4.2 ± 0.5	Evl E	[19]				
		6.8	Adp	[20]				
		4.3	Evl S	[18]				
28 Ni	fcc	7.1 ± 0.8	Exp D	[24]	7.1	33.	[22]	33.
		3.2	Exp T(p)	[33]		40.	[25]	
		6.7 ± 0.4	Evl E	[19]		69.	[9]	
		6.0	Adp	[38]				
		6.4	Adp	[20]				
		11.2	Evl S	[18]				
29 Cu	fcc	1.7 ± 0.3	Exp T	[26]	2.2	25.	[29]	30.
		2.0 ± 0.4	Exp D	[27]		29.	[22]	
		2.2 ± 0.5	Exp D	[106]		30.	[14]	
		$2.75^{+0.6}_{-0.2}$	Exp T	[28]		43.± 4	[9]	
		2.5 ± 0.3	Exp D	[102]				
		1.3	Exp T(p)	[33]				
		1.15...2.06	Exp T(p)	[102,103]				
		1.9 ± 0.2	Evl E	[19]				
		2.2	Evl E	[31]				
		3.0	Evl E	[34]				
		2.5	Adp	[20]				
		2.2	Evl S	[18]				

Table 1 continued

Metal	Lattice	ρ_{FP} [$\mu\Omega$ m]	Type	Ref	Adopted ρ_{FP} [$\mu\Omega$ m]	E_d [eV]	Ref	Adopted E_d [eV]
46 Pd	**fcc**	**9.0 ± 1.0**	**Exp T(p)**	**[32]**	**9.0**	**34.**	**[32]**	**41.**
		10.5	**Adp**	**[9]**		**41.**	**[22]**	
		9.2 ± 0.5	**Evl S**	**[19]**		**46.**	**[9]**	
		9.0	**Evl S**	**[18]**				
47 Ag	**fcc**	**1.4**	**Exp T(p)**	**[33]**	**2.1**	**39.**	**[22]**	**39.**
		2.5	**Adp**	**[20]**		**44.**	**[9]**	
		2.1 ± 0.4	**Evl S**	**[19]**		**60.**	**[30]**	
		2.1	**Evl S**	**[10]**				
		1.8	**Evl S**	**[18]**				
77 Ir	**fcc**	**6.7 ± 0.5**	**Exp T(p)**	**[122]**	**6.7**			
78 Pt	**fcc**	**9.5 ± 0.3**	**Exp T**	**[26]**	**9.5**	**43.**	**[25]**	**44.**
		7.5	**Exp T(p)**	**[35]**		**44.**	**[22]**	
		6.0	**Exp T(p)**	**[40]**		**44.±5**	**[9]**	
		9.5 ± 0.5	**Evl E**	**[19]**				
		7.0	**Adp**	**[31]**				
		9.5	**Evl S**	**[18]**				
79 Au	**fcc**	**1.2**	**Exp T**	**[36]**	**2.6**	**30.**	**[30]**	**43.**
		3.2 ± 0.3	**Exp D**	**[37]**		**35.**	**[29]**	
		0.89	**Exp T(p)**	**[39]**		**43.**	**[22]**	
		5.1 ± 0.3	**Evl S**	**[19]**		**44.**	**[9]**	
		2.3	**Evl S**	**[18]**				
		2.5	**Adp**	**[20]**				
82 Pb	**fcc**	**> 1**	**Exp T(p)**	**[107]**	¾	**19.**	**[7]**	**25.**
		16.4	**Evl S**	**[18]**		**25.**	**[30]**	
		20.0	**Adp**	**[22,102]**				
90 Th	**fcc**	**15.**	**Exp T(p)**	**[102]**	**19.**			
		19.	**Evl E**	**[22,102]**				
		18.6	**Evl S**	**[18]**				
23 V	**bcc**	$6^{+1.52}_{-0.84}$	**Exp T(p)**	**[108]**	**21.**	**40.**	**[30]**	**57.**
		22.0 ± 7.0	**Evl S**	**[19]**		**57.**	**[43]**	
		18.0	**Adp**	**[38]**		**92.**	**[9]**	
		23.	**Adp**	**[9]**				
		40.	**Evl S**	**[50]**				
		21.6	**Evl S**	**[18]**				
		22.	**Evl S**	**[10]**				
		16.	**Evl S**	**[42]**				

Table 1 continued

Metal	Lattice	ρ_{FP} [μΩ m]	Type	Ref	Adopted ρ_{FP} [μΩ m]	E_d [eV]	Ref	Adopted E_d [eV]
24 Cr	**bcc**	**37 + 2. - 12.**	**Exp T**	**[109]**	**37.**	**40.**	**[30]**	**40.**
		40.	**Exp T(p)**	**[109,110]**				
		27.1	**Evl S**	**[18]**				
		30.0	**Evl S**	**[49]**				
26 Fe	**bcc**	**30. ± 5.0**	**Exp T**	**[44]**	**24.6**	**24.**	**[45]**	**40.**
		20.	**Exp D**	**[46]**		**25.**	**[29]**	
		12.5	**Exp T(p)**	**[33]**		**40.**	**[30]**	
		15.	**Adp**	**[22,47]**		**44.**	**[22]**	
		17. ± 6.	**Evl S**	**[19]**				
		25.2	**Evl S**	**[18]**				
		19.	**Adp**	**[49]**				
41 Nb	**bcc**	**14.0 ± 3.0**	**Exp D**	**[48]**	**14.**	**40.**	**[30]**	**78.**
		14.0 ± 3.0	**Evl E**	**[19]**		**78.**	**[22]**	
		16.0	**Evl S**	**[10]**		**98.**	**[9]**	
		15.4	**Evl S**	**[18]**				
		27.0	**Evl S**	**[49]**				
		18.0	**Adp**	**[9]**				
		10.0	**Adp**	**[42]**				
42 Mo	**bcc**	**13. ± 2.0**	**Exp T**	**[51]**	**13.4**	**33.**	**[54]**	**65.**
		15. ± 4.0	**Exp D**	**[52]**		**60.**	**[30]**	
		4.5	**Exp T(p)**	**[33]**		**60-70**	**[22]**	
		15. ± 4.	**Evl E**	**[19]**		**70.**	**[43]**	
		15. ± 5.	**Evl E**	**[18]**		**77.**	**[47]**	
		14. ± 3.	**Evl E**	**[53]**		**82.**	**[9]**	
		13.2	**Evl S**	**[18]**				
		14.	**Evl S**	**[10]**				
		10.	**Evl S**	**[21,50,111]**				
73 Ta	**bcc**	**17. ± 3.**	**Exp T**	**[55]**	**16.5**	**85.**	**[43]**	**90.**
		16. ± 3.	**Exp T**	**[56]**		**80-90**	**[22]**	
		16. ± 3.	**Evl E**	**[19]**		**88.**	**[9]**	
		17.8	**Evl S**	**[18]**		**90.**	**[30]**	
74 W	**bcc**	**7.5…16**	**Exp T**	**[102,112]**	**27.**	**84.**	**[57,65]**	**90.**
		28.	**Exp T(p)**	**[102,113]**		**90.**	**[30]**	
		27. ± 6.	**Evl S**	**[19]**		**100.**	**[43]**	
		18.	**Evl S**	**[10]**				
		18.3	**Evl S**	**[18]**				
		13.	**Evl S**	**[49]**				
		14.	**Adp**	**[57]**				

Table 1 continued

Metal	Lattice	ρ_{FP} [μΩ m]	Type	Ref	Adopted ρ_{FP} [μΩ m]	E_d [eV]	Ref	Adopted E_d [eV]
63 Eu	**bcc**	³ **100.**	**Exp T(p)**	**[121]**	¾			
12 Mg	**hcp**	**9.0**	**Exp D**	**[66]**	**9.**	**20.**	**[22]**	**20.**
		³ **0.8**	**Exp T(p)**	**[102,114]**		**25.**	**[30]**	
		4.5	**Exp T(p)**	**[58]**				
		4.0	**Evl E**	**[22,102]**				
		21.5	**Evl S**	**[18]**				
		4.0	**Adp**	**[22,52]**				
21 Sc	**hcp**	**50.0**	**Exp T(p)**	**[124]**	**50.0**			
22 Ti	**hcp**	**18.0**	**Exp T(p)**	**[59]**	**24.9**	**30.**	**[22]**	**30.**
		42.0	**Exp T(p)**	**[33]**		**40.**	**[30]**	
		32.3	**Evl S**	**[18]**				
		22.0	**Evl S**	**[43]**				
		10.0	**Adp**	**[22,43]**				
27 Co	**hcp**	**30.+ 20** **- 10**	**Exp T**	**[61]**	**15.5**	**36.**	**[22]**	**36.**
		15. ± 5.	**Exp T**	**[60]**		**40.**	**[30]**	
		16. ± 5.	**Exp D**	**[66]**				
		14. ± 4.	**Evl E**	**[19]**				
		18.4	**Evl S**	**[18]**				
		20.0	**Evl S**	**[50]**				
		10.0	**Evl S**	**[21]**				
30 Zn	**hcp**	**15. ± 5.**	**Exp T**	**[60]**	**17.9**	**29.**	**[22]**	**29.**
		15. ± 5.	**Exp D**	**[52]**				
		15.3	**Exp D**	**[62]**				
		20. ± 3.	**Exp T**	**[61]**				
		4.2 ± 0.5	**Exp T(p)**	**[116]**				
		15.1	**Evl S**	**[18]**				
		5.	**Adp**	**[115]**				
		10.	**Adp**	**[22,52]**				
39 Y	**hcp**	**50 ± 20**	**Exp T(p)**	**[125]**	**50.**			
40 Zr	**hcp**	**35. ± 8.**	**Exp D**	**[66]**	**37.5**	**40.**	**[22]**	**40.**
		40.	**Exp(p)**	**[67]**				
		35. ± 8.	**Evl E**	**[19]**				
		30.1	**Evl S**	**[18]**				
		40.	**Adp**	**[22,43]**				

Table 1 continued

Metal	Lattice	ρ_{FP} [μΩ m]	Type	Ref	Adopted ρ_{FP} [μΩ m]	E_d [eV]	Ref	Adopted E_d [eV]
48 Cd	hcp	5. ± 1. 10. 19. ± 8. 10.9 10.	Exp T Exp D Evl S Evl S Adp	[61] [66] [19] [18] [52]	14.5	30.	[22]	30.
59 Pr a)	hcp	135. ± 35.	Exp T(p)	[123]	135.			
60 Nd a)	hcp	135. ± 35.	Exp T(p)	[123]	135.			
64 Gd	hcp	160. ± 30.	Exp T(p)	[118]	160.			
65 Tb	hcp	155. ± 30.	Exp T(p)	[118]	155.			
66 Dy	hcp	145. ± 30.	Exp T(p)	[118]	145.			
67 Ho	hcp	145. ± 30.	Exp T(p)	[118]	145.			
68 Er	hcp	180. ± 35.	Exp T(p)	[118]	180.			
69 Tm	hcp	140. ± 30.	Exp T(p)	[118]	140.			
70 Yb	hcp	75. ± 25.	Exp T(p)	[125]	75.			
71 Lu	hcp	75. ± 15. 145.± 30. 81.0	Exp T(p) Exp T(p) Evl S	[117] [118] [18]	145.			
75 Re	hcp	20. 22. 20.	Exp T(p) Evl S Adp	[119] [18] [22,63]	20.	60.	[22]	60.
31 Ga	bco b)	5.4 ± 0.5	Exp T(p)	[64]	5.4	12.	[64]	12.
92 U	bco	22.	Exp T	[126]	22.			
49 In	bct c)	2.6	Exp T(p)	[107]	2.6			
50 βSn	bct	1.1 ± 0.2 4. ± 2.	Exp T(p) Evl S	[68] [19]	1.13	22.	[68]	22.
62 Sm	rho d)	140 ± 30	Exp T(p)	[125]	140.			

Table 1 continued

Metal	Lattice	ρ_{FP} [μΩ m]	Type	Ref	Adopted ρ_{FP} [μΩ m]	E_d [eV]	Ref	Adopted E_d [eV]
83 Bi	rho	7500 ± 2000	Exp T(p)	[120]	¾			
SS$^{e)}$		25.	Adp	[10]	25.			40.

$^{a)}$ “double hcp” lattice
$^{b)}$ base-centered orthorhombic lattice
$^{c)}$ body-centered tetragonal lattice
$^{d)}$ rhombohedral lattice
$^{e)}$ stainless steel, the composition is not shown [10]

Table 2

The resistivity at the melting point $\rho(T_{melt})$, the BΩ value, the Frenkel pair resistivity ρ_{FP}(sys) predicted by Eq.(8) and the adopted ρ_{FP} values used to constrain the systematics.

Metal	$\rho(T_{melt})$ [μΩ m]	BΩ [10^{-18} Nm]	ρ_{FP}(sys) [μΩ m]	ρ_{FP}(adopted) [μΩ m]
Aluminum	0.108	1.197	4.8	3.7
Antimony	1.190	1.158	56.9	
Arsenic	1.210	0.856	109.6	
Barium	2.760	0.669	444.8	
Beryllium	0.537	0.812	54.8	
Bismuth	2.151	1.115	110.8	
Cadmium	0.170	1.009	10.7	15.0
Cesium	0.212	0.235	483.9	
Calcium	0.145	0.657	24.4	
Cerium	2.796	0.833	269.3	
Chromium	1.520	2.280	27.7	28.6
Cobalt	1.000	2.105	19.6	15.5
Copper	0.093	1.621	2.5	2.1
Dysprosium	5.737	1.212	251.4	
Erbium	5.033	1.259	205.5	
Gadolinium	7.329	1.266	296.2	
Gallium	0.142	1.116	7.3	5.4
Gold	0.136	2.934	2.1	2.6
Holmium	5.309	1.236	224.3	

Table 2 continued

Metal	$\rho(T_{melt})$ [μΩ m]	BΩ [10^{-18} Nm]	ρ_{FP}(sys) [μΩ m]	ρ_{FP}(adopted) [μΩ m]
Indium	0.118	1.073	6.6	
Iridium	0.504	5.053	6.5	
Iron	1.310	1.984	27.4	24.6
Lanthanum	2.552	0.908	202.6	
Lead	0.490	1.304	18.8	
Lithium	0.156	0.250	303.4	
Lutetium	2.060	1.213	90.1	
Magnesium	0.170	0.823	16.8	13.0
Manganese	8.252	0.731	1076.4	
Mercury	0.751	0.939	55.4	
Molybdenum	0.820	4.254	10.9	13.4
Neodymium	2.896	1.118	148.4	
Nickel	0.590	2.038	12.0	7.1
Niobium	0.930	3.064	13.9	14.0
Osmium	1.109	5.873	14.0	
Palladium	0.480	2.658	7.8	9.0
Platinum	0.590	4.203	7.9	9.5
Potassium	0.092	0.241	196.7	
Praseodymium	2.751	1.057	157.9	
Rhenium	1.370	5.603	17.4	
Rhodium	0.385	3.727	5.3	
Rubidium	0.142	0.287	193.3	
Ruthenium	0.744	4.377	9.8	
Samarium	4.025	0.976	273.1	
Silver	0.082	1.722	2.0	2.1
Sodium	0.069	0.268	112.1	
Strontium	0.656	0.649	113.8	
Tantalum	1.090	3.620	15.2	16.5
Thallium	0.296	1.028	18.0	
Thorium	0.890	1.794	20.9	
Thulium	6.048	1.195	272.2	
Tin	0.177	3.005	2.7	1.13
Titanium	1.600	1.850	36.2	24.9
Tungsten	1.140	5.099	14.6	27.0
Uranium	1.224	2.049	24.7	
Vanadium	1.200	2.298	21.7	23.2
Ytterbium	0.740	0.549	193.5	
Zinc	0.170	0.909	13.5	17.9
Zirconium	1.540	1.944	32.9	37.5

1.3 Average efficiency of defect production derived from experimental damage rates for materials irradiated at low temperature (4-5 K)

The experimental damage resistivity rates were taken from Refs.[7,12,31,38,43,47,63, 65,72-75]. The data are shown in Table 3 for various metals and types of irradiation.

If the detail information about the neutron irradiation spectrum was available, the averaged damage energy cross-section $\langle \sigma T_d \rangle$ was calculated and checked in the present work.

The NJOY code system [2] has been applied for the damage energy cross-section calculation. The calculations were performed with the data taken from ENDF/B (different versions), JENDL-3.3 and JEFF-3.0 for the temperature of materials at 4-5 K. The additional calculations show that the influence of the temperature on the averaged $\langle \sigma T_d \rangle$ values is rather weak.

Below the values of the averaged damage energy cross-sections used for the analysis of the damage production efficiency in Section 1.3.2 are discussed for the different types of irradiation.

1.3.1 Averaged damage energy cross-sections

Data are discussed for various neutron sources listed below.

1.3.1.1 CP-5 (VT53), ANL

The $\langle \sigma T_d \rangle$ data shown in Table 3 are taken mainly from Ref.[47]. Probably, the most uncertainty is for platinum, where the evaluated data are absent in ENDF/B and JENDL. The value 32.4 b·keV for platinum shown in Table 3 is the approximate value from Ref.[47]. The authors of Ref.[65] have used 29.6 b·keV for CP-5 (VT53) spectrum at the neutron energies E > 0.1 MeV.

Table 3

Low temperature damage-resistivity rate $\left(d\Delta\rho/d\Phi\right)\Big|_{\Delta\rho=0}$, the averaged damage energy cross-section $\langle\sigma T_d\rangle$, the defect production efficiency and the effective threshold displacement energy $E_d(\eta=1)$.

Metal	Source	$\left(d\Delta\rho/d\Phi\right)\Big\|_{\Delta\rho=0}$ [$10^{-31}\ \Omega\cdot m^3$]	$\langle\sigma T_d\rangle$ [b·keV]	Reference	Efficiency	$E_d(\eta=1)$ [eV]
fcc metals						
Al	CP-5 (VT53),ANL	1.49	76.2	[47]	0.357	75.7
Al	FISS FRAGM	57.6	2492.	[47,72]$^{a)}$	0.422	64.0
Al	LTIF,ORNL	2.19	98.55	[43,38,65]	0.405	66.6
Al	RTNS,LLL	4.18	156.9	[65]	0.486	55.6
Al	LHTL,JPR-3	2.20	81.0	[63]	0.495	54.5
Al	TTB(1),FRM	2.57	87.6	[7]	0.535	50.4
Ni	CP-5 (VT53),ANL	1.14	59.0	[47]	0.225	147.0
Ni	FISS FRAGM	48.0	3400.	[47,72]$^{a)}$	0.164	201.2
Ni	LTIF,ORNL	1.71	85.4	[43,38]	0.233	141.8
Ni	LHTL,JPR-3	2.3	83.2	[63]	0.321	102.7
Ni	TTB(2),FRM	1.86	76.05	[7,31]	0.284	116.1
Cu	CP-5 (VT53),ANL	0.424	56.3	[47]	0.257	116.8
Cu	FISS FRAGM	30.0	3295.	[47,72]$^{a)}$	0.310	96.7
Cu	HEAVY IONS			[47,12]	0.333	90.1
Cu	Be(40 MeV-d,n)	2.11	233.4	[47,65]	0.308	97.3
Cu	LTIF,ORNL	0.723	81.7	[43,38,65]	0.302	99.4
Cu	RTNS,LLL	2.48	288.5	[65]	0.293	102.4
Cu	LHTL,JPR-3	0.70	81.6	[63]	0.292	102.6
Cu	TTB(1),FRM	0.71	68.9	[7]	0.351	85.4
Pd	LTIF,ORNL	1.90	73.	[43,38]	0.296	138.3
Pd	TTB(2),FRM	1.78	59.41	[7,31]	0.341	120.2
Ag	CP-5 (VT53),ANL	0.295	47.3	[47]	0.290	134.7
Ag	FISS FRAGM	13.8	4004.	[47,72]$^{a)}$	0.160	243.7
Ag	HEAVY IONS			[47,12]	0.400	97.5
Ag	LTIF,ORNL	0.666	72.	[43]	0.429	90.8
Ag	LHTL,JPR-3	0.70	71.7	[63]	0.453	86.0
Ag	TTB(1),FRM	0.70	76.4	[7]	0.425	91.7
Pt	CP-5 (VT53),ANL	0.818	32.4	[47]	0.292	150.5
Pt	Be(40 MeV-d,n)	4.72	175.	[47,65]	0.312	140.9
Pt	LTIF,ORNL	1.59	48.4	[43,65]	0.380	115.7
Pt	LHTL,JPR-3	1.7	48.8	[63]	0.403	109.1
Pt	TTB(1),FRM	1.56	40.55	[7]	0.445	98.8
Au	LHTL,JPR-3	0.5	50.2	[63]	0.412	104.4
Au	TTB(2),FRM	0.61	55.78	[7,31]	0.452	95.1
Pb	TTB(2),FRM	1.3	46.68	[7,73]	0.101$^{b)}$	247.0

Table 3 continued

Metal	Source	$\left(d\Delta\rho / d\Phi\right)\Big\|_{\Delta\rho=0}$ [10^{-31} Ω·m^3]	$\langle \sigma T_d \rangle$ [b·keV]	Reference	Efficiency	$E_d(\eta=1)$ [eV]
			bcc metals			
K	TTB(2),FRM	1.56	71.68	[7,75]	0.065$^{c)}$	619.4
V$^{d)}$	LTIF,ORNL	7.17	98.05	[43,38,65]	0.496	114.9
V	RTNS,LLL	18.01	257.1	[65]	0.475	119.9
V	LPTR (FNIF-10)	6.56	79.2	[65]	0.562	101.4
V	Be(30 MeV-d,n)	14.03	200.	[65]	0.476	119.7
V	LHTL,JPR-3	8.0	98.5	[63]	0.551	103.4
V	TTB(2),FRM	7.3	90.78	[7,73]	0.546	104.5
Fe	CP-5 (VT53),ANL	3.33	50.7	[47]	0.267	149.8
Fe	LHTL,JPR-3	6.5	84.6	[63]	0.312	128.1
Fe	TTB(1),FRM	6.39	70.9	[7]	0.366	109.2
Nb	CP-5 (VT53),ANL	2.19	55.7	[47]	0.548	142.4
Nb$^{d)}$	LTIF,ORNL	3.43	80.25	[43,38,65]	0.595	131.0
Nb	Be(30 MeV-d,n)	7.38	197.	[65]	0.522	149.5
Nb	Be(40 MeV-d,n)	10.1	223.9	[47,65]	0.628	124.1
Nb	LPTR (FNIF-10)	3.47	60.3	[65]	0.802	97.3
Nb	RTNS,LLL	11.44	283.3	[65]	0.562	138.7
Nb	LHTL,JPR-3	6.5	80.2	[63]	1.129	69.1
Nb	TTB(2),FRM	2.7	68.8	[7,73]	0.547	142.7
Mo	CP-5 (VT53),ANL	1.86	61.2	[47]	0.369	176.4
Mo$^{d)}$	LTIF,ORNL	3.38	84.55	[43,38,65]	0.485	134.1
Mo	Be(30 MeV-d,n)	6.10	192.	[65]	0.385	168.7
Mo	LPTR (FNIF-10)	3.00	69.5	[65]	0.523	124.2
Mo	RTNS,LLL	9.47	253.5	[65]	0.453	143.5
Mo	LHTL,JPR-3	3.2	69.6	[63]	0.558	116.6
Mo	TTB(1),FRM	3.34	76.3	[7]	0.531	122.4
Ta	LTIF,ORNL	2.52	54.7	[43]	0.628	143.3
Ta	LHTL,JPR-3	3.2	55.7	[63]	0.783	114.9
Ta	TTB(1),FRM	2.51	44.3	[7]	0.773	116.5
W$^{e)}$	LTIF,ORNL	4.2	52.2	[43]	0.670	134.2
W	RTNS,LLL	11.55	195.1	[65]	0.493	182.4
W	LHTL,JPR-3	3.9	51.3	[63]	0.634	142.1
W	TTB(1),FRM	3.3	42.8	[7]	0.643	140.1
			hcp metals			
Mg	LTIF,ORNL	7.0	92.7	[43]	0.420	47.7
Mg	LHTL,JPR-3	6.5	75.2	[63]	0.480	41.6

Table 3 continued

Metal	Source	$\left(d\Delta\rho / d\Phi\right)\vert_{\Delta\rho=0}$ [10^{-31} $\Omega\cdot m^3$]	$\langle\sigma T_d\rangle$ [b·keV]	Reference	Efficiency	$E_d(\eta=1)$ [eV]
Ti	LTIF,ORNL	22.4	97.6	[43]	0.691	43.4
Ti	LHTL,JPR-3	35.0	94.9	[63]	1.111	27.0
Ti	TTB(1),FRM	21.6	80.8	[7]	0.805	37.3
Co	CP-5 (VT53),ANL	2.42	56.0	[47]	0.251	143.5
Co	LHTL,JPR-3	4.9	85.0	[63]	0.335	107.6
Co	TTB(1),FRM	3.27	86.6	[7]	0.219	164.2
Zn	LHTL,JPR-3	8.0	87.9	[63]	0.369	78.7
Zr	LTIF,ORNL	24.0	74.8	[43]	0.856	46.8
Zr	LHTL,JPR-3	23.0	84.6	[63]	0.725	55.2
Zr	TTB(1),FRM	16.5	75.0	[7]	0.587	68.2
Cd	LHTL,JPR-3	5.8	67.1	[63]	0.447	67.1
Gd	LHTL,JPR-3	13.0	52.51	[63]	0.155[f]	258.5
Re	LHTL,JPR-3	6.0	51.61	[63]	0.872	68.8
			other metals			
Ga	LHTL,JPR-3	13.0	79.57	[63]	0.908	13.2
Sn	TTB(2),FRM	1.12	69.07	[7,74]	0.789	27.9
SS	LTIF,ORNL	6.37	86.73	[38]	0.294	136.2

[a] The $\langle\sigma T_d\rangle$ value is calculated formally using the data from Table 6 and 4 of Ref.[47]

[b] Pb: ρ_{FP} = 17.2 μΩm, Eq(8); E_d = 25 eV

[c] K: ρ_{FP} = 33.7 μΩm, Eq(8), E_d = 40 eV

[d] Material is doped with 300 ppm Zr.

[e] High level of impurities and cold-worked conditions for the measurement for tungsten were noted in Ref.[43]. The possible error for damage rate was estimated as 20-50 % [43].

[f] Gd: Ed = 40 eV

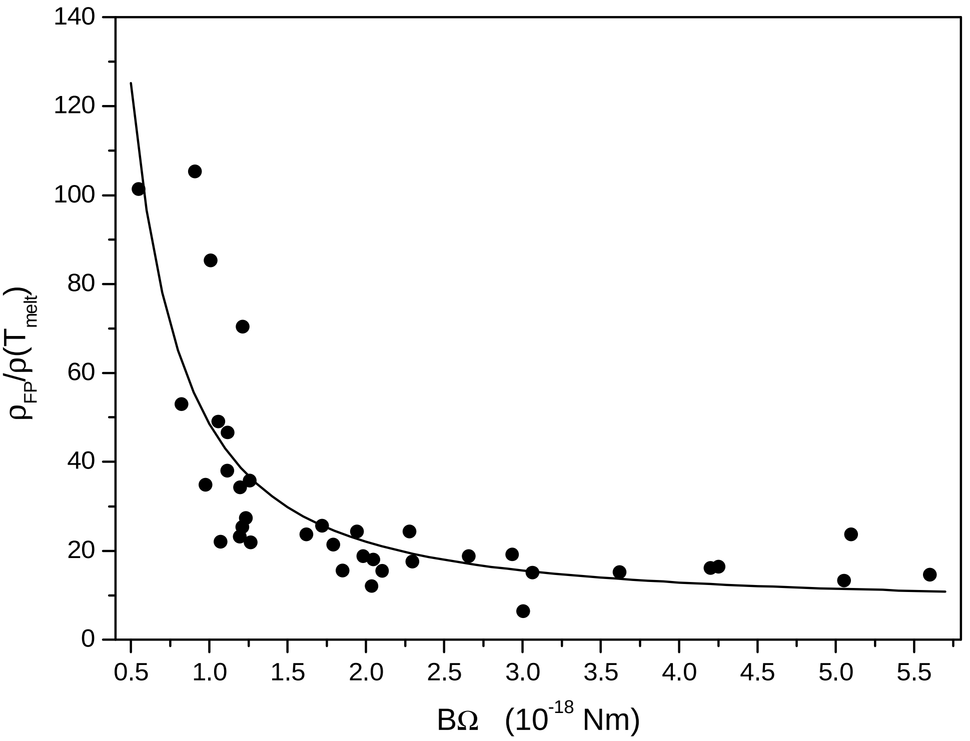

Fig.1 The ratio of the Frenkel pair resistivity to the resistivity at the melting point versus BΩ for various metals (black circle) and the systematics prediction (line).

1.3.1.2 LTIF, ORNL

Data for Al, Cu, Pt, V, Nb and Mo were obtained by the averaging-out the $\langle\sigma T_d\rangle$ values from Ref.[43] and Ref.[65]. For other metals the origin of the data is shown in Table 3.

The $\langle\sigma T_d\rangle$ value for the stainless steel (15 Cr/15 Ni/70 Fe) has been calculated approximately. The averaged damage energy cross-section was calculated with the data from ENDF/B-VI (Release 8) for various elements from Ref.[43] for the fission neutron spectrum. The mean ratio of $\langle\sigma T_d\rangle$ values obtained in Ref.[43] for LTIF spectrum to the $\langle\sigma T_d\rangle$ values calculated for the fission spectrum was found equal to 1.147. This ratio was used for the evaluation of the $\langle\sigma T_d\rangle$ value for stainless steel irradiated with neutrons with the LTIF spectrum basing on the calculations performed for Cr, Fe and Ni for the fission neutron spectrum.

1.3.1.3 RTNS, LLL

The values of $\langle \sigma T_d \rangle$ shown in Table 3 were obtained using the ENDF/B-VI (8) data at the neutron energy equal to 14.8 MeV. These data are compared with the damage energy cross-section from JENDL-3.3 and the $\langle \sigma T_d \rangle$ values from Ref.[65] in Table 4.

The mean deviation[1] of the $\langle \sigma T_d \rangle$ values from JENDL-3.3 and ENDF/B-VI(8) is equal to 4.7 %, for the values from Ref.[65] and ENDF/B-VI(8) - 5.2 %.

1.3.1.4 Be(d,n)

For the Be(d,n) reaction induced by the 40-MeV deuterons the $\langle \sigma T_d \rangle$ values were calculated with the neutron spectrum from Ref.[47] and the ENDF/B-VI(8) data which are available at energies covering the spectrum of the Be(d,n) reaction.

Table 4

The damage energy cross-section (b·keV) calculated with the help of the NJOY code and data from ENDF/B-VI (Release 8) and JENDL-3.3 at 14.8 MeV and the cross-sections from Ref.[65] for RTNS spectrum.

Element	ENDF/B-VI (8)	JENDL-3.3	Ref.[65]
Al	156.9	165.2	178.
Cu	288.5	288.5	288.
V	257.1	272.7	267.
Nb	283.3	260.8	263.
Mo	253.5	274.6	263.
W	195.1	196.5	201.

---

[1] Defined as $(100/N)\Sigma\,|\text{value}(1)-\text{value}(2)|/\text{value}(2)$

The $\langle\sigma T_d\rangle$ value for platinum was calculated approximately. Data for 38 nuclides from ^{27}Al to ^{209}Bi from ENDF/B-VI (8) which are suitable to perform the calculations[2] were used to obtain the contribution of the energy range below 20 MeV in the total averaged damage energy cross-section. Fig.2A shows the relative value of this contribution equal to $\langle\sigma T_d\rangle$(E < 20 MeV)/$\langle\sigma T_d\rangle$(total) and the approximation curve. The value of $\langle\sigma T_d\rangle$(E < 20 MeV) for platinum has been calculated with the data from JEFF-3.0 (ENDL-78). Basing on the simple approximation for the obtained ratio $\langle\sigma T_d\rangle$(E < 20 MeV)/$\langle\sigma T_d\rangle$(total), the total $\langle\sigma T_d\rangle$value for platinum has been estimated (Fig.2B). This value equal to 175 b·keV is shown in Table 3. It should be noted that the authors of Ref.[65] have used the $\langle\sigma T_d\rangle$ value equal to 182 b·keV and the authors of Ref.[47] – 198 b·keV.

The $\langle\sigma T_d\rangle$ values for 30-MeV deuteron irradiation of V, Nb and Mo were taken from Ref.[65].

1.3.1.5 LHTL, JPR-3

The radiation damage rates for materials irradiated in the LHTL facility have been measured in Ref.[63]. The $\langle\sigma T_d\rangle$ cross-sections have been calculated by the authors Ref.[63] for the fission neutron spectrum with the ENDF/B-IV and JENDL-1 data.

Unfortunately, the detail description of irradiation neutron spectrum is absent in Ref.[63]. The calculation performed in the present work with the ENDF/B-IV data for different types of fission neutron spectrum does not reproduce the $\langle\sigma T_d\rangle$ values from Ref.[63] precisely. The difference in the $\langle\sigma T_d\rangle$ values may result as from the shapes of fission neutron spectra as from the methods of the $\langle\sigma T_d\rangle$ calculation.

---

[2] Data for Pd and Sb isotopes and ^{165}Ho are available up to 30 MeV, other data are up to 150 MeV

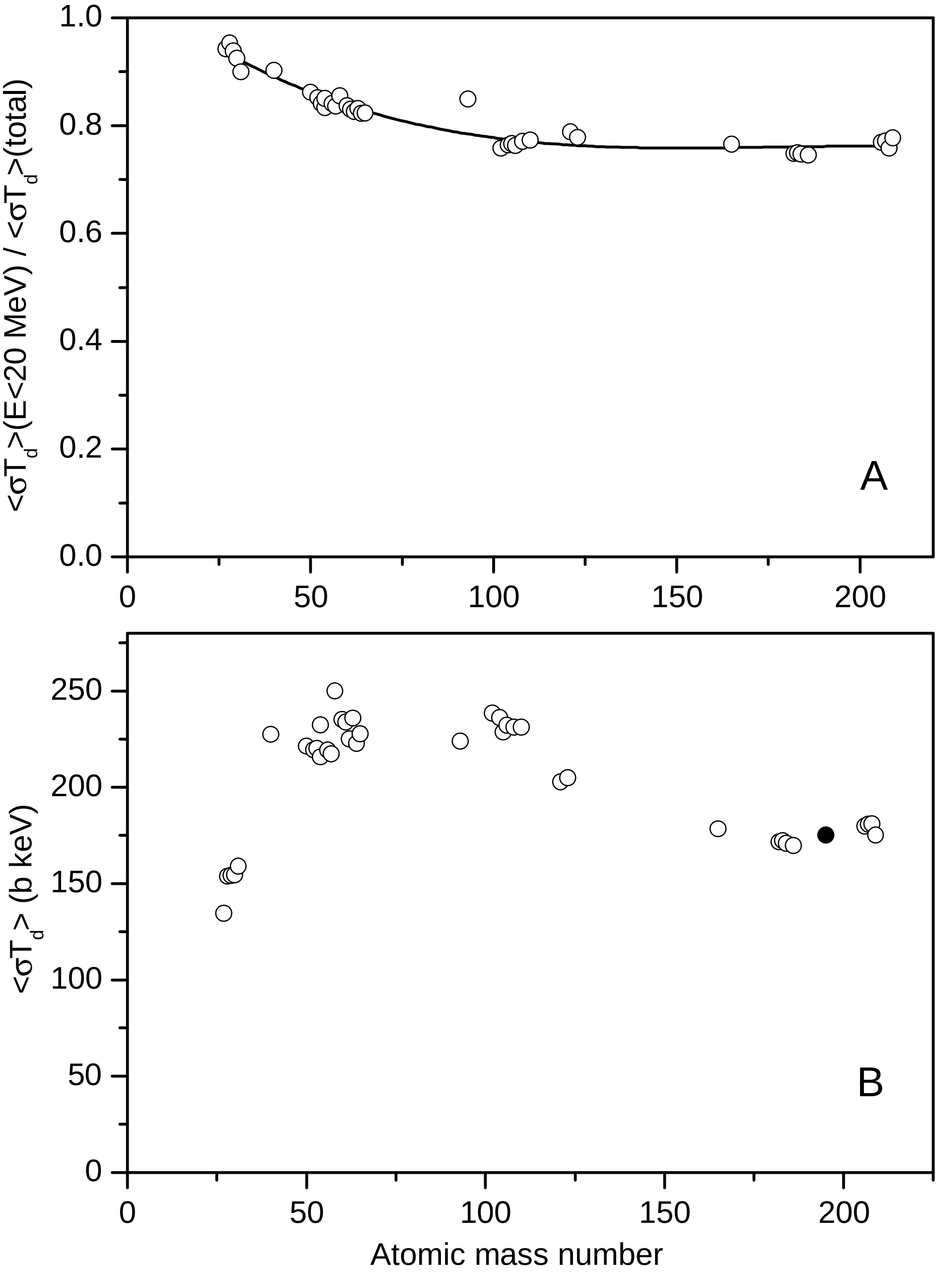

Fig.2 A: The relative contribution of the energies below 20 MeV in the total averaged damage energy cross-section for the Be(d,n) spectrum calculated with the data from ENDF/B-VI(8) (circle) and the approximation curve. B: The total averaged damage energy cross-sections for Be(d,n) spectrum calculated for different nuclides (open circle) and the value evaluated for platinum (black circle).

Fig.3 shows the $\langle\sigma T_d\rangle$ values from Ref.[63] and the cross-sections calculated in the present work for elements with atomic number from 11 to 83 and nuclear data from ENDF/B-VI(8) and from JENDL-3.3. The calculations are performed for the Maxwellian fission neutron spectrum with θ = 1.318 MeV which provide the best description of the $\langle\sigma T_d\rangle$ values from Ref.[63] integrally. The noticeable difference in the $\langle\sigma T_d\rangle$ values obtained in Ref.[63] and in the present work is for the light elements (Al, Mg) and for Mo. The mean averaged deviation[3] of the $\langle\sigma T_d\rangle$ values from Ref.[63] and the cross-sections obtained here with the data from ENDF/B-VI(8) is equal to 6.6 %, with the data from ENDF/B-IV – 7.6 %. At the same time the deviation of the $\langle\sigma T_d\rangle$ values obtained in the present work using the ENDF/B-IV data and the ENDF/B-VI(8) data is equal to 3.2 % for metals investigated in Ref.[63]. The most difference in ENDF/B-IV and ENDF/B-VI(8) based $\langle\sigma T_d\rangle$ calculations is for cadmium (22 %).

The observed difference in the $\langle\sigma T_d\rangle$ values calculated here and in Ref.[63] must be allowed to obtain the approximate values of averaged damage cross-section for a certain metals not evaluated in Ref.[63] due to the lack of neutron data or other reasons.

For platinum the $\langle\sigma T_d\rangle$ value shown in Table 3 has been obtained using the data from JEFF-3.0 and Maxwellian spectrum with θ = 1.318 MeV. The use of the fission spectrum with θ = 1.375 MeV gives the $\langle\sigma T_d\rangle$ value equal to 50.3 b·keV and the use of the combined fission spectrum[4] from Ref.[76] – 42.7 b·keV.

The averaged damage energy cross-section for molybdenum was obtained by the averaging-out of the $\langle\sigma T_d\rangle$ values data from Ref.[63] obtained with the data from different data libraries.

---

[3] Footnote (1)

[4] The spectrum defined as $\varphi(E)= E \exp(-E/kT)/kT$ at E = 0 to 4 kT; $\varphi(E)= C_1/E$ at E=4 kT to 67 keV; $\varphi(E)= C_2 \cdot \exp(-E/a_1) \sinh((E \cdot a_2)^{0.5})$ at E > 67 keV, where kT = 0.253 eV, $a_1 = 9.65 \cdot 10^5$, $a_2 = 2.29 \cdot 10^{-6}$, C_1 and C_2 defined to make spectrum continuous

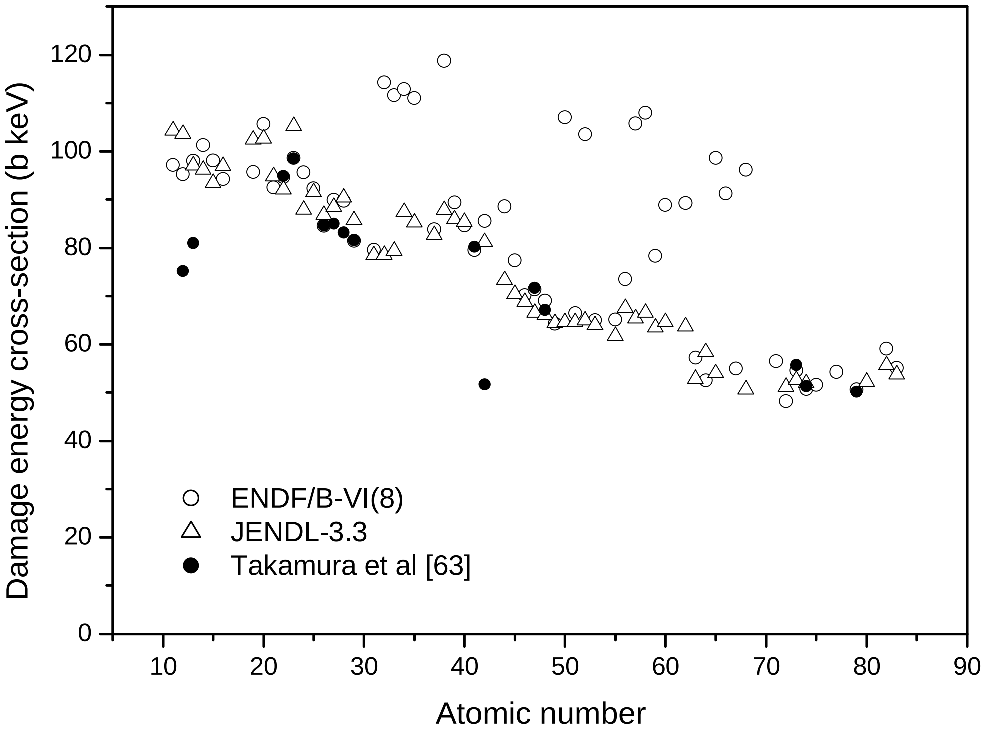

Fig.3 The averaged damage energy cross-section for natural mixtures of isotopes with atomic number from 11 to 83 calculated with the help of the NJOY code for fission neutron spectrum using the data from ENDF/B-VI(8) (open circle) and JENDL-3.3 (triangle) and the values calculated in Ref.[63] with the data taken from ENDF/B-IV (black circle).

For zinc the averaged $\langle\sigma T_d\rangle$ value was evaluated using the data from CENDL-2.1 (90.6 b·keV) and JEFF-3.0 (BROND-2.2) (85.2 b·keV). The $\langle\sigma T_d\rangle$ value for zirconium was obtained using ENDF/B-VI(8) and the same fission neutron spectrum with θ = 1.318 MeV.

For gadolinium the average damage energy cross-section was obtained with the help of the data taken from different origins. Table 3 shows the $\langle\sigma T_d\rangle$ value equal to 52.51 b·keV calculated with the ENDF/B-VI(8) data. The use of the data from JENDL-3.3 gives 58.37 b·keV, JEFF-3.0 – 76.72 b·keV and BROND-2.2 – 59.54 b·keV for the Maxwellian spectrum with θ equal to 1.318 MeV. It should be noted that the $\langle \sigma T_d \rangle$ value for gadolinium is rather sensitive to the shape of the neutron spectrum at low energies. Mainly, it originates from the anomalous high radiative capture cross-section for ^{155}Gd and ^{157}Gd isotopes at energies below 10 eV. The calculation with the fission spectrum[4] from Ref.[76] gives the $\langle \sigma T_d \rangle$ values, which are highly different from the ones mentioned above: ENDF/B-VI(8) – 283.4 b·keV, JENDL-3.3 – 288.7 b·keV, JEFF-3.0 – 255.2 b·keV, BROND-2.2 – 289.5 b·keV (weighted sum for individual isotopes). In all cases the effective threshold displacement energy was taken equal to 40 eV for gadolinium.

Table 3 shows the $\langle \sigma T_d \rangle$ value for rhenium obtained with the help of the data from ENDF/B-VI(8). This value is close to $\langle \sigma T_d \rangle$ calculated with the data from BROND-2.2 which is equal to 48.09 b·keV.

For gallium the calculation with the data from ENDF/B-VI(8) gives 79.57 b·keV (Table 3) and with the data from JENDL-3.3 – 78.48 b·keV.

1.3.1.6 TTB, FRM

Data for the TTB neutron spectrum (Fig.6,7) are subdivided on two groups in Table 3. The first group (TTB(1)) contains the $\left(d\Delta\rho / d\Phi\right)\big|_{\Delta\rho=0}$ rates and the $\langle \sigma T_d \rangle$ values obtained in Ref.[7] for the measured neutron spectrum. The second group (TTB(2)) includes data for $\left(d\Delta\rho / d\Phi\right)\big|_{\Delta\rho=0}$ obtained in Refs.[31,73-75] for modified TTB spectrum and corrected as described in Ref.[7].

In the present work the $\langle \sigma T_d \rangle$ values were calculated for the TTB spectrum measured in Ref.[7] and tabulated in Ref.[77]. Table 5 shows the average damage energy cross-sections calculated with the help of the SPECTER code in Ref.[77] and with the help of the NJOY code with the data from ENDF/B-V, ENDF/B-VI(8) and JENDL-3.3 for a number of metals examined in Ref.[7]. The calculations by the SPECTER code [77] are based mainly on the ENDF/B-V data.

Table 5

The averaged damage energy cross-section (b·keV) for TTB neutron spectrum [7] calculated with the help of the SPECTER code [77] and the NJOY code with the data from ENDF/B-V, ENDF/B-VI(8) and JENDL-3.3. The calculations are performed with the same effective threshold displacement energies E_d.

Metal	SPECTER [77]	NJOY		
		ENDF/B-V	ENDF/B-VI(8)	JENDL-3.3
Al	26.39	26.98	26.94	27.02
K	21.56	22.99	23.01	24.26
Ti	24.22	24.71	24.65	24.86
V	27.45	27.55	27.25	28.61
Fe	21.36	21.48	21.44	21.95
Co	26.03	26.29	26.99	26.16
Ni	22.87	23.74	23.95	24.08
Cu	20.76	20.59	21.33	22.28
Zr	22.64	22.43	22.41	22.11
Nb	20.80	21.00	20.77	18.78
Mo	23.11	23.04	22.35	21.17
Ag	24.16	25.35	25.35	18.33
Ta	13.86	13.72	13.72	13.66
W	13.00	12.89	12.97	13.52
Au	16.76	18.67	16.09	–
Pb	14.54	14.54	14.37	13.64

There is a good agreement in $\langle \sigma T_d \rangle$ values obtained by the different tools and data libraries. The mean deviation of the averaged cross-sections obtained with the help of the SPECTER code and the NJOY code with the data from ENDF/B-V is equal to 2.2 %, for the NJOY calculation with the data from ENDF/B-V and ENDF/B-VI(8) – 1.9 %, for the NJOY calculation with the data from JENDL-3.3 and ENDF/B-VI(8) – 5.0 %.

The values of $\langle \sigma T_d \rangle$ calculated by the SPECTER code were used in Ref.[7] for the analysis of the defect production efficiency. The measured $\left(d\Delta\rho / d\Phi \right)\Big|_{\Delta\rho=0}$ values were scaled in Ref.[7] according to the neutron flux contribution above 0.1 MeV. The corresponding change was done for the averaged damage energy cross-sections, which explains the main difference in the $\langle \sigma T_d \rangle$ values shown in Table 3 and Table 5.

The $\langle \sigma T_d \rangle$ values shown in Table 3 for palladium (59.41 b·keV) and lead (46.68 b·keV) were obtained with the neutron data from ENDF/B-VI(8). The corresponding values calculated with the data from JENDL-3.3 are 59.82 b·keV and 44.28 b·keV. For tin the averaged value equal to 69.07 b·keV obtained with the help of ENDF/B-VI(8) (85.75 b·keV) and JENDL-3.3 (52.39 b·keV) is shown.

The calculation of the $\langle \sigma T_d \rangle$ value for platinum has been performed with the data from JEFF-3.0 (ENDL-78).

1.3.2 Defect production efficiency

The calculated values of defect production efficiency $\langle \eta \rangle$ and the effective threshold displacement energy $E_d(\eta=1)$ are shown in Table 3 for each measured value of the resistivity damage rate. The η values and $E_d(\eta=1)$ values obtained for a same metal from the analysis of different experiments are rather in a good agreement. The exception is for titanium, nickel, niobium and silver, where there is a noticeable scattering of the data. For niobium and titanium the highest value of $\langle \eta \rangle$ (~1.1) observed for the LHTL neutron irradiation [63] is not in an agreement with the other measurements. The same is for the lowest $\langle\eta\rangle$ value for nickel and silver (~0.16) obtained from the data of Refs.[47,72].

For each metal from Table 3 the mean value of the defect production efficiency $\overline{\langle\eta\rangle}$ and threshold energy $\overline{E_d(\eta=1)}$ has been calculated. The obtained mean values along with the statistical errors are shown in Table 6. It should be noted that the mean values of the efficiency and the threshold energy have the physical sense in case of the relative insensitivity of $\langle\eta\rangle$ and $E_d(\eta=1)$ from the shape of the neutron irradiation spectrum (Section 1.4).

Table 6 shows that the maximal value of defect production efficiency is observed for rhenium ($\langle\eta\rangle=1$) and gallium (0.91) and the minimal $\langle\eta\rangle$ values is obtained for lead (0.093), potassium (0.011) and gadolinium (0.084). Unfortunately, at present, the uncertainty of the obtained $\langle\eta\rangle$ values can not be evaluated precisely, because there is only single measurement of damage rate for each of these metals. The low values of $\langle\eta\rangle$ for Pb, K and Gd results mainly from the high values of Frenkel pair resistivity ρ_{FP} for these metals. For these metals the experimental information about ρ_{FP} is absent and the Frenkel pair resistivity has been estimated according to the systematics (Table 2). For gadolinium the high ρ_{FP} value is in the general agreement with other systematics of Frenkel pair resistivity from Ref.[50]. According to Ref.[50] the ρ_{FP} value is about 200 to 300 $\rho(0^0C)$, which gives ρ_{FP}~$230\rho(0^0C)$ for gadolinium. For lead and potassium the agreement is worse and the ρ_{FP} value is about $105\cdot\rho(0^0C)$ for Pb and ~ $3000\cdot\rho(0^0C)$ for K. The ρ_{FP} value for Pb is in a qualitative agreement with the empirical rule $\rho_{FP} = 154\cdot\rho(0^0C)$ from Ref.[19].

Table 6 shows the good agreement between the efficiency values for iron, nickel and stainless steel.

The mean efficiency value $\overline{\langle\eta\rangle}$ for *fcc* metals is equal to 0.34 ± 0.10, for *bcc* metals 0.53 ± 0.19 and for *hcp* metals 0.54 ± 0.31. For all metals the $\overline{\langle\eta\rangle}$ value is equal to 0.46 ± 0.21.

Table 6

The mean values of the defect production efficiency and effective threshold energy obtained from the experimental damage resistivity rates at the temperatures T=4–5 K.

Metal	$\overline{\langle\eta\rangle}$	$\overline{E_d(\eta=1)}$ [eV]
fcc		
Al	0.45 ± 0.07	61 ± 9
Ni	0.25 ± 0.06	142 ± 38
Cu	0.31 ± 0.03	99 ± 9
Pd	0.32 ± 0.03	129 ± 13
Ag	0.36 ± 0.11	124 ± 61
Pt	0.37 ± 0.06	123 ± 22
Au	0.43 ± 0.03	100 ± 7
Pb	0.10	247
bcc		
K	0.065	619
V	0.52 ± 0.04	111 ± 9
Fe	0.32 ± 0.05	129 ± 20
Nb	0.67 ± 0.21	124 ± 28
Mo	0.47 ± 0.07	141 ± 23
Ta	0.73 ± 0.09	125 ± 16
W	0.61 ± 0.08	150 ± 22
hcp		
Mg	0.45 ± 0.04	45 ± 4
Ti	0.87 ± 0.22	36 ± 8
Co	0.27 ± 0.06	138 ± 29
Zn	0.37	79
Zr	0.72 ± 0.13	57 ± 11
Cd	0.45	67
Gd	0.15	259
Re	0.87	69
others		
Ga	0.91	13
Sn	0.79	28
Stainless steel	0.29	136

1.4 *Calculation of defect production efficiency*

1.4.1 The general dependence of defect production efficiency from the primary ion energy

The defect production efficiency in metals has been calculated by the method of molecular dynamics by many authors [8,14,57,78-94].

One should note the definite agreement between the results of the most of MD simulations. The typical dependence of η from the primary knock-on atom (PKA) energy obtained from the MD calculations [8,14,86,88] is shown in Fig.4 for a number of metals. It is supposed that the E_{MD} energy [8,14,86,88] is equal approximately to T_{dam} in Eq.(2).

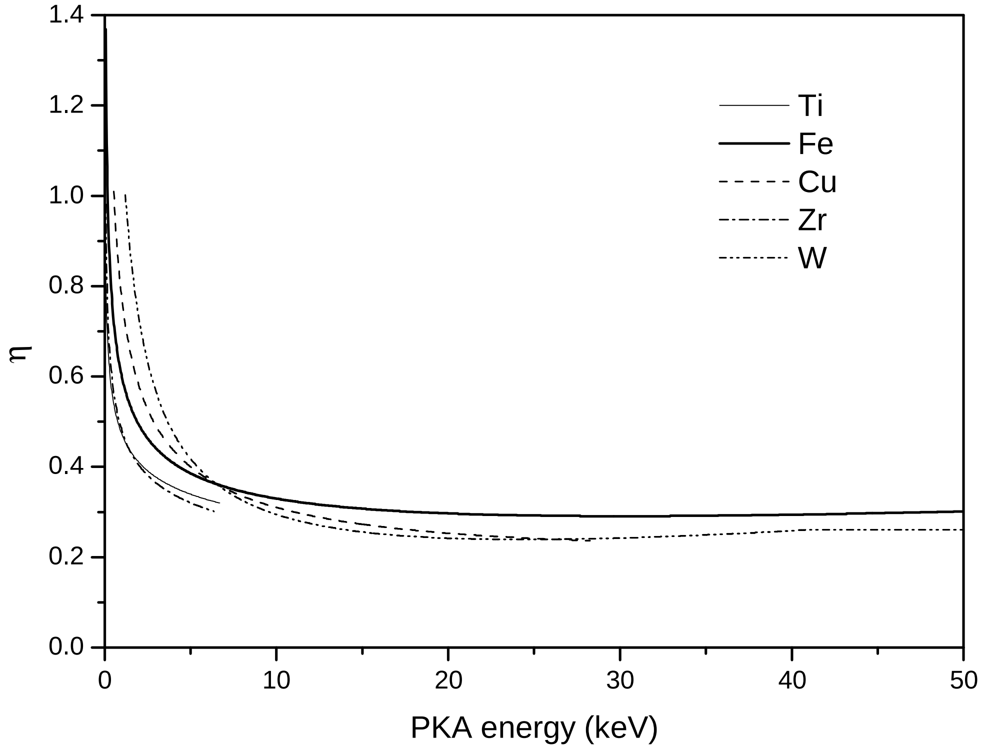

Fig.4 The defect production efficiency obtained by the MD method for Ti [8], Fe [86,88], Cu [14], Zr [8] and W [14] plotted against the PKA energy. The E_d value is equal to 30 eV for Ti and Cu, 40 eV for Fe and 90 eV for W.

In the present work the MARLOWE code [6] based on the BCA approach [95-97] was applied for the calculation of the number of defects in irradiated materials. The parameters of the model [6] are chosen to get the agreement with the results of the defect production calculations by the MD method at the ion energies above 10 keV. The interatomic potential from Ref.[98] has been applied for iron, as in the MD simulation in Ref.[89]. For tungsten the interatomic potential from Ref.[99] has been used.

Fig.5 shows the efficiency of defect production calculated by the MARLOWE code for iron and tungsten and the results of the MD calculations [14,86,88]. There is a substantial difference between the η values calculated by the BCA approach and the MD method at the energies below 10 keV. The binary collision approximation can not reproduce the realistic dependence of η from the primary ion energies. In particular, it does not describe a few-body effects in a thermal spike phase, which plays a fundamental role in the defect production at the energies above 250 eV.

1.4.2 The average efficiency of defect production in metals irradiated by neutrons with realistic spectra

The energy dependent η values calculated by the MD method in Refs.[8,14,86,88] were used for the calculation of the average defect production efficiency ⟨η⟩ in metals irradiated by neutrons of different energies.

The following functions were used for the efficiency calculation

titanium [8]:

$$\eta = 6.02\ E_{MD}^{0.786} / N_{NRT}, \qquad E_{MD} \le 5\ \text{keV}, \qquad (9)$$

iron [86,88]:

$$\eta = 0.5608 E_{MD}^{-0.3029} + 3.227\times10^{-3}\, E_{MD}, \qquad E_{MD} \le 40\ \text{keV}, \qquad (10)$$

copper [14]:

$$\eta = 0.7066 E_{MD}^{-0.437} + 2.28\times10^{-3}\, E_{MD}, \qquad E_{MD} \le 20\ \text{keV}, \qquad (11)$$

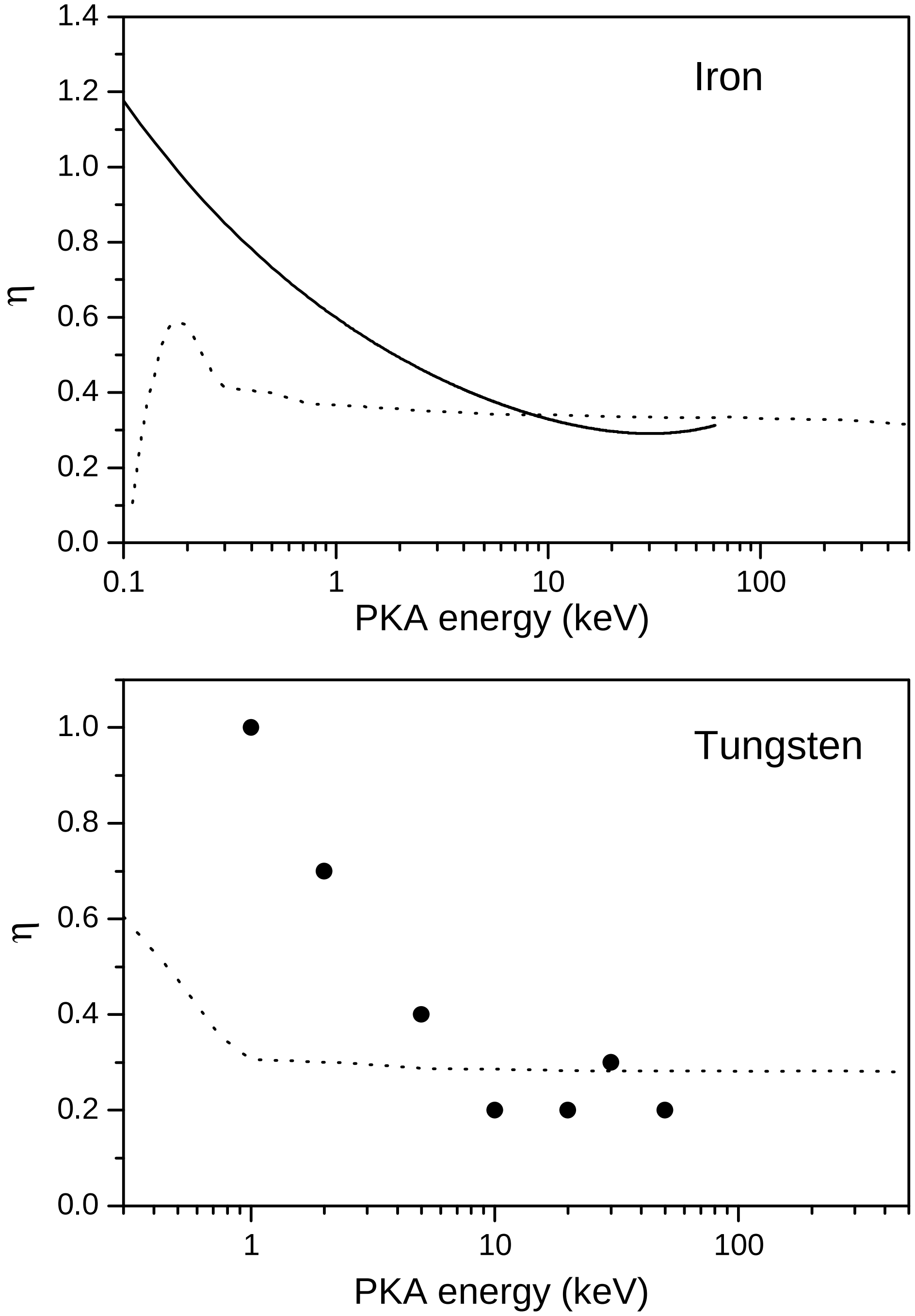

Fig.5 The defect production efficiency calculated with the help of the MARLOWE code (dotted line) and obtained by the MD simulation for Fe [86,86] (solid line) and W [14] (black circle).

zirconium [8]:

$$\eta = 4.58\ E_{MD}^{0.740} / N_{NRT}\,, \qquad E_{MD} \le 5\text{ keV}, \tag{12}$$

tungsten [14]:

$$\eta = 1.0184\,E_{MD}^{-0.667} + 5.06\times10^{-3}\,E_{MD}\,, \qquad E_{MD} \le 30\text{ keV}, \tag{13}$$

where E_{MD} is the initial energy in the MD simulation taken in keV, $E_{MD} \approx T_{dam}$. It is supposed that the E_d value is equal to 30 eV for Cu and 90 eV for W.

The functions $\eta(E_{MD})$ shown above correspond to the different temperatures adopted for the MD simulations. For titanium and zirconium the temperature is equal to 100 K [8], for copper and tungsten - 10 K [14], for iron the $\eta(E_{MD})$ function relates to the temperature range from 100 to 900 K [86,88].

The energy dependent efficiencies, Eq.(9)-(13) were introduced in the NJOY code [2] as a multiplication factors for the calculations based on the NRT model. At the energies above the limits shown in Eq.(9)-(13) the constant efficiency values were assumed for the calculations. This approximation discussed in Refs.[14,86,88] is based on the idea of the subcascade formation at the high PKA energies. It is in agreement with the BCA calculations (Fig.5).

The calculation of defect production efficiency $\langle\eta\rangle$ has been performed for neutron irradiation spectra from the following sources

- TRIGA reactor (core)
- PWR reactor (core)
- Tight Lattice Light Water Reactor (TLLWR) (core)
- SNR-2 fast breeder reactor (core)
- TTB, FRM reactor [7]
- fission spectrum (Maxwellian, θ = 1.35 MeV)
- HCPB fusion reactor (first wall) [100]
- 14.8 MeV neutrons
- neutron spectrum from the Be(d,n) reaction induced by 40 MeV-deuterons [47]

The neutron spectra described above and normalized on the unity flux are plotted in Fig.6. The detail view of the spectra in the energy range above 1 keV is given in Fig.7.

Table 7 shows the averaged efficiency ⟨η⟩ calculated for titanium, iron, copper, zirconium and tungsten irradiated with neutrons of different sources. The data from ENDF/B-VI(8) were used for the calculations.

Table 7

The averaged defect production efficiency ⟨η⟩ calculated for different neutron spectra.

Source	Ti	Fe	Cu	Zr	W
TRIGA	0.34	0.33	0.29	0.31	0.34
PWR	0.33	0.32	0.27	0.31	0.35
TLLWR	0.34	0.32	0.28	0.31	0.37
SNR-2	0.36	0.34	0.33	0.33	0.47
TTB, FRM	0.34	0.33	0.28	0.31	0.35
Fission	0.32	0.31	0.25	0.30	0.31
Fusion reactor, first wall	0.33	0.32	0.26	0.31	0.31
14.8 MeV neutrons	0.32	0.31	0.24	0.30	0.27
Be(d,n), 40 MeV deuterons	–	0.31	0.24	–	0.27

The comparison of the data from Table 7 shows that the average value of the efficiency for titanium, iron, copper and zirconium is rather independent from the shape of the nuclear spectrum. It gives an opportunity to predict realistic ⟨σT_d⟩ values for these metals basing on the mean values of ⟨η⟩ shown above and on the simple NRT calculations.

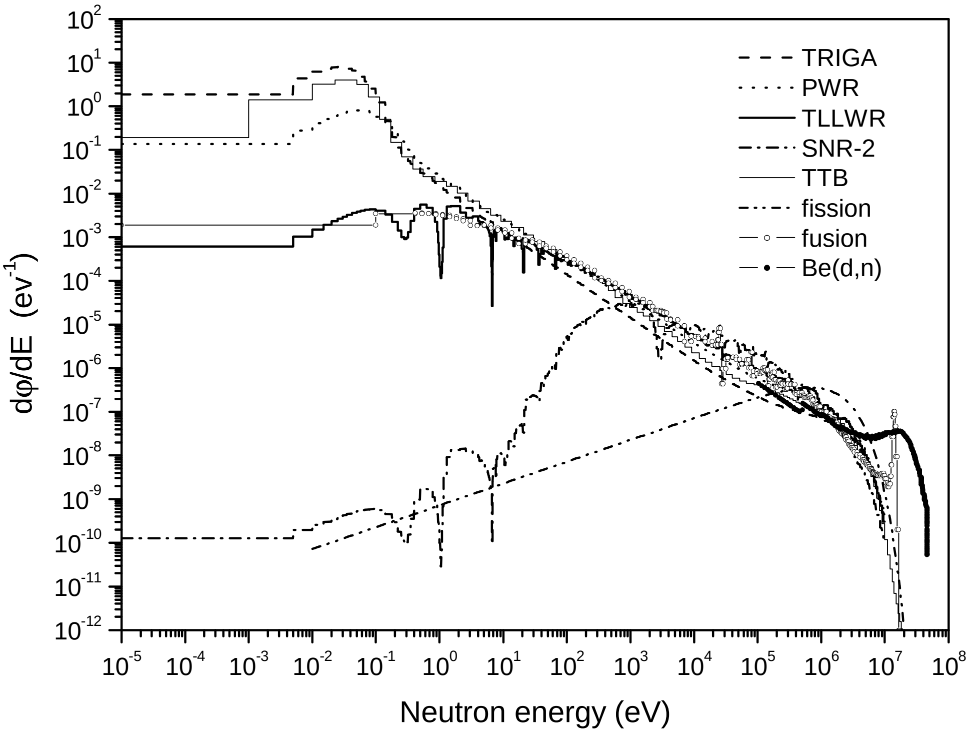

Fig.6 Neutron spectra for various nuclear facilities

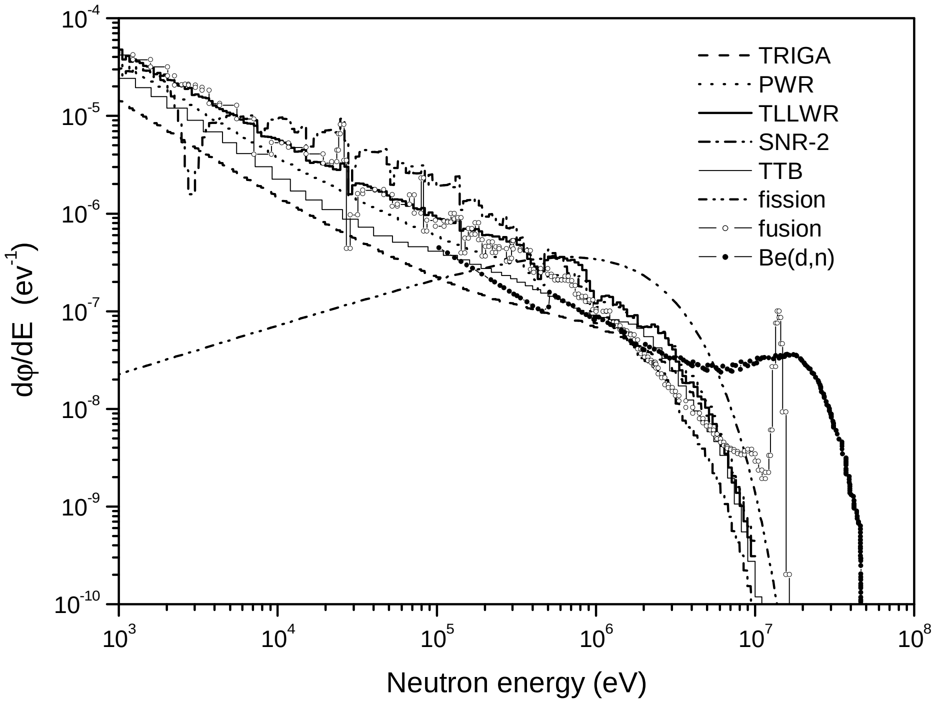

Fig.7 Neutron spectra for various nuclear facilities at the energies above 1 keV.

The value of defect production efficiency for tungsten is more sensitive to the type of the neutron irradiation spectrum. The maximal difference in the $\langle\eta\rangle$ value is for the Be(d,n) spectrum and 14.8 MeV neutrons (0.27) and the SNR-2 spectrum (0.47).

With an increase of the contribution of high energy neutrons in the total flux the average efficiency value $\langle\eta\rangle$ decreases coming close to the asymptotic $\eta(T)$ value (Fig.4). For this reason the lowest $\langle\eta\rangle$ values shown in Table 7 relates to the fission spectrum and the Be(d,n) spectrum. The highest $\langle\eta\rangle$ value is observed for the SNR-2 spectrum which has the lowest contribution of the energy range above 1 MeV in the total flux.

1.4.3 Comparison of the average defect production efficiency calculated with the help of the theoretical models and derived from the experimental dose rates

Comparison of the efficiency values $\langle\eta\rangle$ obtained with the help of the MD calculations (Table 7) with the efficiency derived from experimental damage rates (Table 3,6) shows the good agreement for iron. The mean value $\overline{\langle\eta\rangle}$ obtained from Table 7 data (0.32 ± 0.1) is actually equal to the mean efficiency value derived from the experimental data (Table 6). It can be considered as an indication of the weak temperature dependence of the defect production efficiency for iron discussed in Ref.[89].

There is a good agreement in $\overline{\langle\eta\rangle}$ values for copper, $\overline{\langle\eta\rangle}$ (theory, Table 7) = 0.27 ± 0.03 and $\overline{\langle\eta\rangle}$ (experiment, Table 6) = 0.32 ± 0.03.

For titanium, zirconium and tungsten the experimental $\overline{\langle\eta\rangle}$ values are about twice more than the theoretical efficiency values. It can be explained by the temperature dependence of the efficiency for titanium and zirconium. The same reduction of the η value was observed for copper at the temperatures from 0 to 100 K in Ref.[101]. On the other hand there is a strong dependence of the measured initial dose rate from the purity of zirconium and titanium [7], which complicates the interpretation of the difference between the theoretical and experimental efficiency values for these metals.

For tungsten the difference between the experimental and theoretical $\langle\eta\rangle$ values has the other origin. The comparison of the calculated and measured resistivity change for tungsten irradiated with high energy protons [14] shows the similar discrepancy between experimental data and the values obtained with the help of the efficiency η calculated by the MD method (Eq.(13), Fig.4). The authors [14] have ascribed the discrepancy between experimental and theoretical resistivity change to the incorrect energy deposition calculation by the LAHET code.

In case of the neutron irradiation the nuclear data from ENDF/B-VI(8) used for the recoil calculations for tungsten seem to be rather reliable. The use of other data libraries gives the similar $\langle\sigma T_d\rangle$ values (Table 5). For this reason the observed discrepancy in the theoretical and experimental $\langle\eta\rangle$ values for tungsten should be related to the problems of the measurement of the initial damage rate in Refs.[7,43,63,65] or to the MD calculations in Refs.[14,57]. The further study is needed to understand the observed difference in the $\langle\eta\rangle$ values.

1.5 Summary about defect production efficiency. Method of the radiation damage rate evaluation basing on results of the MD simulation

The available data for Frenkel pair resistivity ρ_{FP} were compiled and analyzed. The evaluated and recommended ρ_{FP} values were obtained for 22 metals and stainless steel (Table 1). The systematics of Frenkel pair resistivity has been constrained (Eq.(8), Table 2). The experimental data for damage resistivity rate in metals were compiled and analyzed. The latest versions of nuclear data libraries ENDF/B-VI (Release 8), JENDL-3.3, JEFF-3.0, BROND-2.2 and CENDL-2.1 were used for the averaged damage energy cross-section calculation. The average defect production efficiency in metals $\langle\eta\rangle$ has been calculated for various neutron irradiation spectra (Table 3,6).

The energy dependence of the defect production efficiency $\eta(E)$ has been calculated with the help of the BCA model and the MARLOWE code. The comparison with the result of the MD simulation shows the significant difference in the $\eta(E)$ values at the energies below 10 keV (Fig.5).

The energy dependent efficiency values obtained by the MD method were used for the calculation of the average efficiency values $\langle\eta\rangle$ for the neutron spectra of the thermal reactor, the fast breeder reactor, the fusion facility and the Be(d,n) reaction. The comparison of the obtained $\langle\eta\rangle$ values with the efficiency values derived from experimental damage rates shows the good agreement for iron and copper. For titanium, zirconium and tungsten the theoretical $\langle\eta\rangle$ values are about twice less than the experimental ones. In the case of titanium and zirconium the discrepancy in $\langle\eta\rangle$ values can be explained by the temperature dependence of the defect production efficiency. For tungsten the difference between the theoretical and experimental efficiency values may originate from the lack of the measurement routine as from the problems of the MD simulation.

Obtained results can be used for simple and reliable evaluation of the number of defects generated in metals under the neutron irradiation in different power units. The method of the evaluation includes

- calculation of the number of defects in metals irradiated with neutrons using the NRT model
- correction of the result obtained using the average value of the defect production efficiency calculated in various units by the MD method (Table 7). For titanium, iron and zirconium the efficiency $\overline{\langle\eta\rangle}$ does not depend upon the shape of the neutron spectrum. The average efficiency value for titanium is equal to 0.34, for iron to 0.32 and for zirconium to 0.31. The weak dependence of the defect

production efficiency upon the shape of the neutron spectrum is observed for tungsten and copper (Table 7). For these metals one should take it into account and, at least, to define to what neutron spectrum from Table 7 the investigated neutron spectrum is close.

2. Displacement cross-sections for tantalum and tungsten irradiated with nucleons at energies up to 1 GeV. Combined BCA-MD method for the calculation of the number of defects in irradiated materials

A method combining the method of the molecular dynamics and the binary collision approximation model was proposed. The method was used for the displacement cross-section calculation for tantalum and tungsten irradiated with nucleons of the intermediate energy.

The calculation of the displacement cross-sections for tantalum and tungsten is important for the evaluation of the radiation durability of these materials for use as solid target in the various concepts of the sub-critical accelerator driven systems. The determination of reliable neutron and proton displacement cross-sections for tantalum and tungsten has got special interest in the TRADE project [127]. The evaluation of the displacement cross-sections for these elements encounters certain difficulties. The measurements of the defect production rate for tantalum and tungsten [7,43,63,65,128] show noticeable differences with the NRT model [1] predictions. At the same time the calculations basing on the method of the molecular dynamics (MD) are not in a good agreement with the experimental data for high energy proton irradiation [14].

The different approaches used for the displacement cross-section calculation are compared and analyzed for the primary nucleon energy range up to 1 GeV. The displacement cross-section for the elastic channel is calculated using various modern optical potentials and ENDF/B-VI data. The MCNPX code [3] is used to obtain the displacement cross-sections for the nonelastic proton-nucleus interactions. The number of defects produced by the primary knock on atoms (PKA) in material is calculated with the help of the NRT model and the binary collision approximation model (BCA) using the results obtained by the MD method.

2.1 *Proton irradiation*

2.1.1 Calculations using the NRT model

This Section concerns the calculation of displacement cross-sections based on the NRT model [1]. The displacement cross-section is calculated by the formula

$$\sigma_d(E_p)=\sum_i \int_{E_d}^{T_i^{max}} \frac{d\sigma(E_p,Z_T,A_T,Z_i,A_i)}{dT_i}\nu(T_i,Z_T,A_T,Z_i,A_i)\,dT_i \quad , \qquad (14)$$

where E_p is the incident proton energy; $d\sigma/dT_i$ is the cross-section of energy transfer to recoil atom; Z_i and A_i are the atomic number and the mass number of the recoil atom, correspondingly; Z_T and A_T are the same for the target material; $\nu(T_i)$ is the number of Frenkel pairs produced by PKA with the kinetic energy T_i; T_i^{max} is the maximal energy of the PKA spectrum; E_d is effective threshold displacement energy; the summing is for all recoil atoms produced in the irradiation.

The number of defects produced by the PKA in material $\nu(T)$ is calculated according to NRT approach with the value of “k” parameters defined according to Robinson [96], (see also Eq.(2))

$$T_{dam}(T)=\frac{T}{1+k\left(3.4008\,\varepsilon^{1/6}+0.40244\,\varepsilon^{3/4}+\varepsilon\right)}, \qquad (16)$$

$$k=\frac{32}{3\pi}\left(\frac{m_e}{M_T}\right)^{1/2}\frac{(A_i+A_T)^{3/2}Z_i^{2/3}Z_T^{1/2}}{A_i^{3/2}(Z_i^{2/3}+Z_T^{2/3})^{3/4}}, \qquad (17)$$

$$\varepsilon = \left[A_T T/(A_i + A_T)\right]\left[a/(Z_i Z_T e^2)\right], \tag{18}$$

$$a = a_0 (9\pi^2/128)^{1/3}\left(Z_i^{2/3} + Z_T^{2/3}\right)^{-1/2}, \tag{19}$$

where η is the defect production efficiency; m_e is the mass of an electron; M_T is the mass of the target atom; a_0 is the Bohr radius; "e" is the electron charge; the kinetic energy T is taken in keV.

2.1.1.1 Elastic proton scattering

The displacement cross-section for the proton elastic scattering is calculated as follows

$$\sigma_{d,el} = \int_{E_d}^{T_{max}} \frac{d\sigma(Z_T, A_T)}{dT} \nu(T(Z_T, A_T))\, dT \ , \tag{20}$$

Generally, the spectrum of PKA produced by the proton elastic scattering includes the contributions from the screened Coulomb scattering in material, from the nuclear scattering and their interference.

For the initial proton energy below 5 MeV the nuclear scattering does not make a real contribution in the $d\sigma/dT$ spectrum for tantalum and tungsten, and the recoil spectrum is formed mainly by the screened Coulomb scattering. With the increase of the primary proton energy the screening effect disappears and at the energies above several mega-electron volts the displacement cross-section $\sigma_{d,el}$ can be calculated with a high accuracy by the Rutherford formula for the recoil spectrum: $d\sigma/dT=\alpha\cdot dT/T^2$, where α is a constant. For tantalum and tungsten isotopes the ratio of the elastic displacement cross-section calculated for the screened Coulomb field to the cross-section obtained by the Rutherford formula is equal to 0.943 for the primary proton energy equal to 1 MeV, 0.975 for the proton energy 5 MeV and 0.983 for the 10 MeV-protons. In the present work the displacement cross-section for screened Coulomb scattering was calculated with the help of the approach from Refs.[129,130].

With the increase of the primary proton energy the contribution of the nuclear scattering in the recoil spectrum $d\sigma/dT$ increases simultaneously. The contribution becomes appreciable for the $\sigma_{d,el}$ calculation at the energies above 10 MeV, where the screening effect is small. It allows applying the nuclear optical model for the elastic displacement cross-section calculations for the initial proton energies considered.

Fig.8 shows the ratio of the elastic displacement cross-section calculated taking into account the Coulomb scattering, the nuclear scattering and their interference to the cross-section obtained for the recoil spectrum corresponding to the pure Coulomb scattering for ^{181}Ta and ^{184}W. The angular distribution for proton elastic scattering on ^{181}Ta was calculated with the help of the optical model using the optical potential from Ref.[131]. For ^{184}W the angular distributions were taken from ENDF/B-VI Proton Sublibrary (Release 7). One can see that the nuclear scattering has an essential influence on the calculated $\sigma_{d,el}$ value at the proton energies above 10 MeV.

The use of different modern optical potentials demonstrates similar description of the experimental proton angular distribution and gives similar values of the elastic displacement cross-section. Fig.9 shows the proton angular distributions for ^{181}Ta calculated using the global optical potentials from Refs.[131-134] at different primary proton energies. The experimental data are from Refs.[135-137]. The good agreement is observed between the calculations and the measured data at the relatively small scattering angles for the initial proton energy 146 MeV and 340 MeV. For the 55 MeV-protons the agreement is worse and the different calculations give the similar result. Fig.10 shows the $\sigma_{d,el}$ values for ^{184}W calculated with the help of the global optical potential from Ref.[132] at proton energies from 80 to 180 MeV, from Ref.[134] at 50 – 400 MeV and from Ref.[131] at the energies below 200 MeV. Fig.10 shows also the displacement cross-sections calculated using the evaluated proton elastic angular distributions from ENDF/B-VI at the energies up to 150 MeV.

There is a good agreement between the $\sigma_{d,el}$ values obtained with the help of different optical potentials and the ENDF/B-VI data.

For the comparison with the results of the optical model calculation the displacement cross-section was calculated with the help of the MCNPX code [3]. The PKA spectrum for elastic scattering has been evaluated from the standard output file “histp” by the HTAPE3X code [138]. The calculated $\sigma_{d,el}$ values are shown in Fig.10. One can see a certain difference between the results obtained using the ENDF/B-VI data, the optical model and the elastic scattering model incorporated in the MCNPX code. The reason of the discrepancy is not well clear. Most likely that the use of the “proton elastic cross-section” in the MCNPX calculations ([138], page 53) is based on a certain simplification in the description of the Coulomb scattering in the code. It could result in the discrepancy with an accurate optical model calculation.

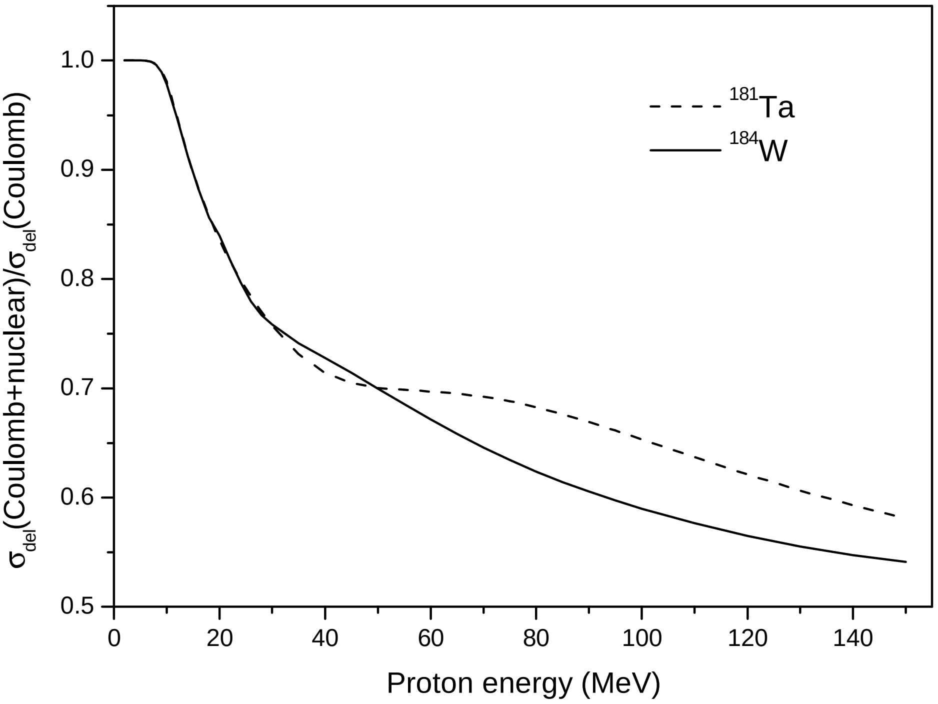

Fig.8 The ratio of the elastic displacement cross-section calculated taking into account the Coulomb scattering, the nuclear scattering and their interference to the displacement cross-section obtained for the pure Coulomb scattering for ^{181}Ta and ^{184}W

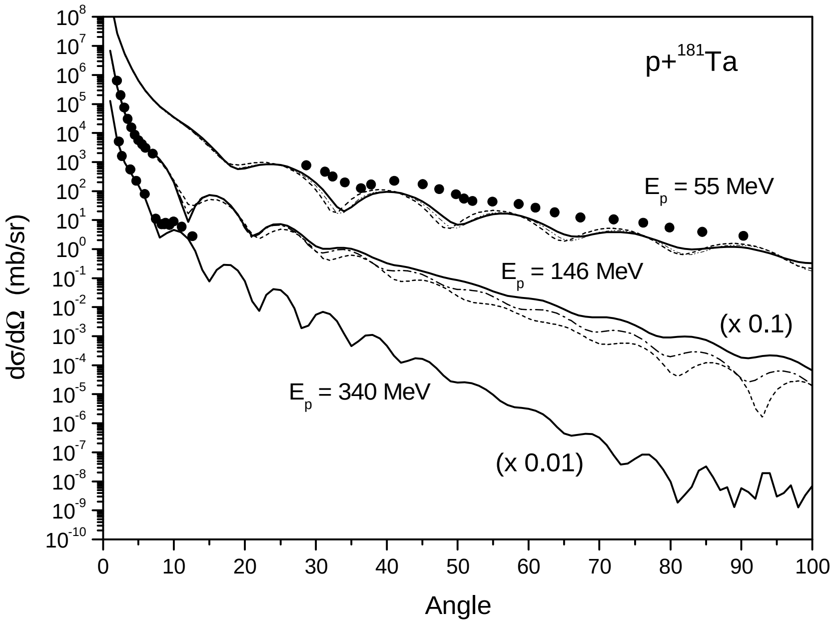

Fig.9 The proton elastic angular distributions for ^{181}Ta calculated with the help of the optical potential from Ref.[132] (dash-dotted line), Ref.[133] (dash- double dotted line), Ref.[134] (solid line) and Ref.[131] (dashed line). The experimental data (cycles) are from Ref.[135] (55 MeV-protons), Ref.[136] (146 MeV) and Ref.[137] (340 MeV).

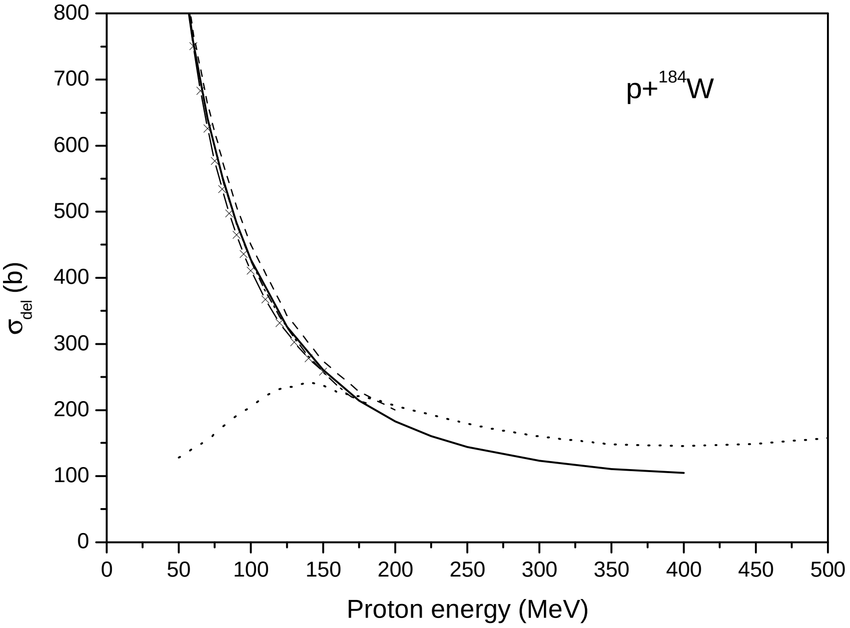

Fig.10 The displacement cross-section for the proton elastic scattering calculated for ^{184}W using the optical potential from Ref.[132] (dash-dotted line), Ref.[134] (solid line), Ref.[131] (dashed line), the ENDF/B-VI data (solid cross line) and the MCNPX code [3] (dotted line).

2.1.1.2 Nonelastic proton interactions

The displacement cross-section for proton nonelastic interactions with target material $\sigma_{d,non}$ has been calculated with the help of the different models incorporated in the MCNPX code.

Fig.11 shows the displacement cross-section $\sigma_{d,non}$ calculated with the help of the MCNPX code and the $\sigma_{d,non}$ values obtained using the recoil spectra from ENDF/B-VI for ^{184}W. The following intranuclear cascade evaporation models were used for the calculations [3]: Bertini/Dresner, ISABEL/Dresner, CEM2k, INCL4/ABLA with the default model parameters from Ref.[3]. The nonelastic displacement cross-section was calculated at the energies from 50 MeV up to 1 GeV.

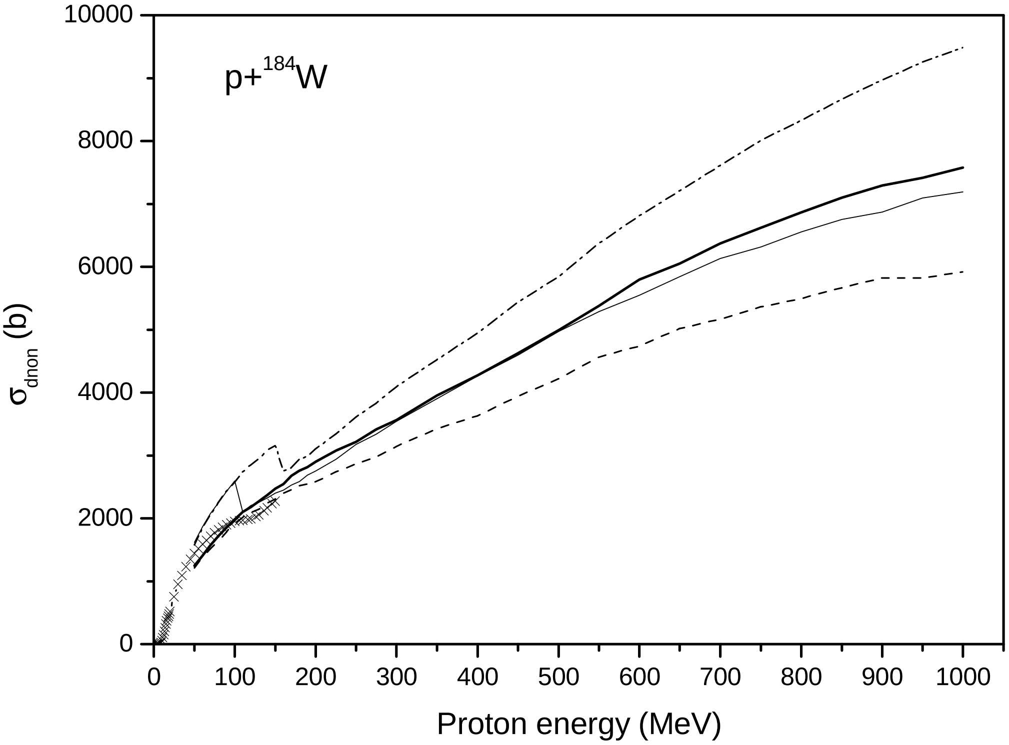

Fig.11 The displacement cross-section for the proton nonelastic interactions with ^{184}W calculated using the ENDF/B-VI data (solid cross line) and the different nuclear models incorporated in the MCNPX code: Bertini/Dresner (solid thick line), ISABEL/Dresner (dashed line), CEM2k (dash-dotted line) and INCL4/ABLA (solid thin line).

There is a satisfactory agreement between the cross-sections obtained using the data from ENDF/B-VI below 150 MeV and the $\sigma_{d,non}$ values calculated with the help of the Bertini/Dresner and ISABEL/Dresner models. The $\sigma_{d,non}$ cross-sections calculated by the INCL4/ABLA and CEM2k have a jumps near 100 MeV and 150 MeV. Good agreement is observed for the Bertini/Dresner and INCL4/ABLA calculations at the energies from 100 MeV up to 1 GeV. The cross-sections calculated by the CEM2k model and by the ISABEL/Dresner model are noticeably different from the $\sigma_{d,non}$ values obtained with the help of the Bertini/Dresner and ICNCL4/ABLA models.

The observed difference in the calculated $\sigma_{d,non}$ values results from the different description of the particle emission spectra by the nuclear models considered. An example of such calculations is shown in Fig.12 for the double differential cross-sections in ^{181}Ta(p,p’) reaction. The experimental points are from Ref.[139].

Fig.13 shows the integral recoil spectrum calculated with the help of the considered nuclear models for ^{184}W irradiated by 1 GeV-protons. The integral spectrum is the sum of the individual spectra for all nuclides produced in the nonelastic proton interactions with ^{184}W. The observed difference in the recoil spectra results in the scattering of the $\sigma_{d,non}$ values predicted by the different nuclear models. The most influence is due to the shape of the first peak in the $d\sigma/dT$ distribution (Fig.13), which corresponds to the (p,xnyp) reactions. The fission peak does not play an important role due to the small contribution of the fission in the nonelastic proton cross-section (~ 0.9 % for 1 GeV), and in the nonelastic displacement cross-section (~ 3.7 %). The recoil spectra for ^{181}Ta and ^{184}W.calculated by the Bertini/Dresner model and the INCL4/ABLA model are compared in Fig.14

The observed uncertainty in the $\sigma_{d,non}$ values calculated using the different modern nuclear models (Fig.11) can not be overcome at present time. It should be considered as an error of the nonelastic displacement cross-section value obtained theoretically. This error is about 20-25 %.

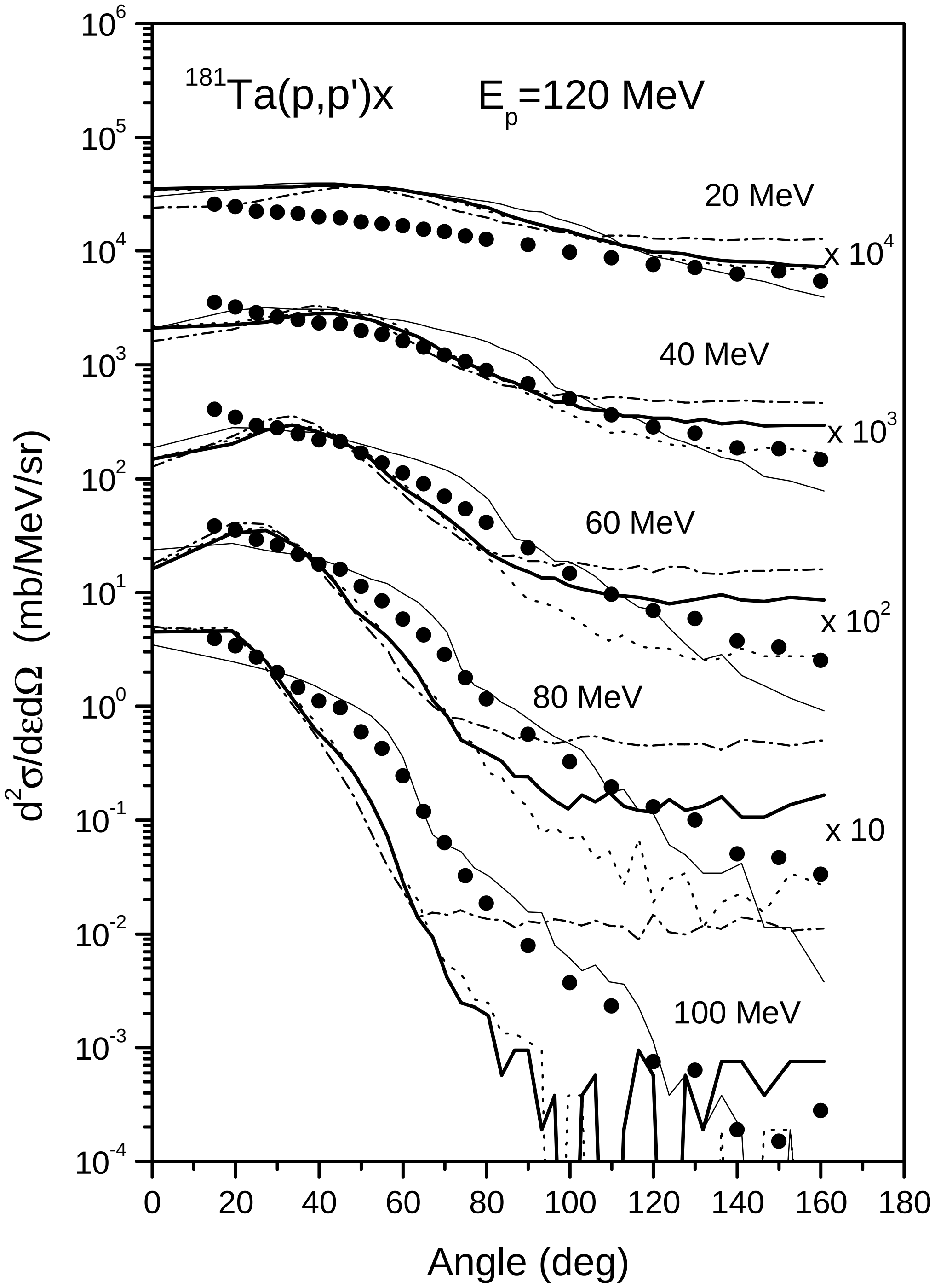

Fig.12 The angular distributions for ^{181}Ta(p,p') reaction at 120 MeV primary proton energy and various proton emission energies calculated with the help of the different nuclear models incorporated in the MCNPX code and measured in Ref.[139]. See also captions for Fig.11.

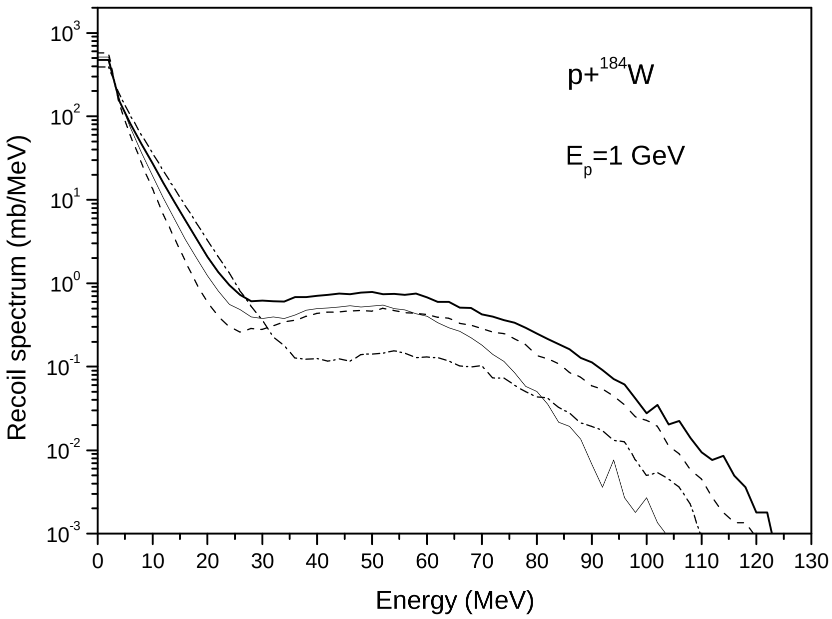

Fig.13 The integral recoil spectrum for nonelastic 1 GeV-proton interactions with ^{184}W calculated with the help of the different nuclear models incorporated in the MCNPX code. See also captions for Fig.11.

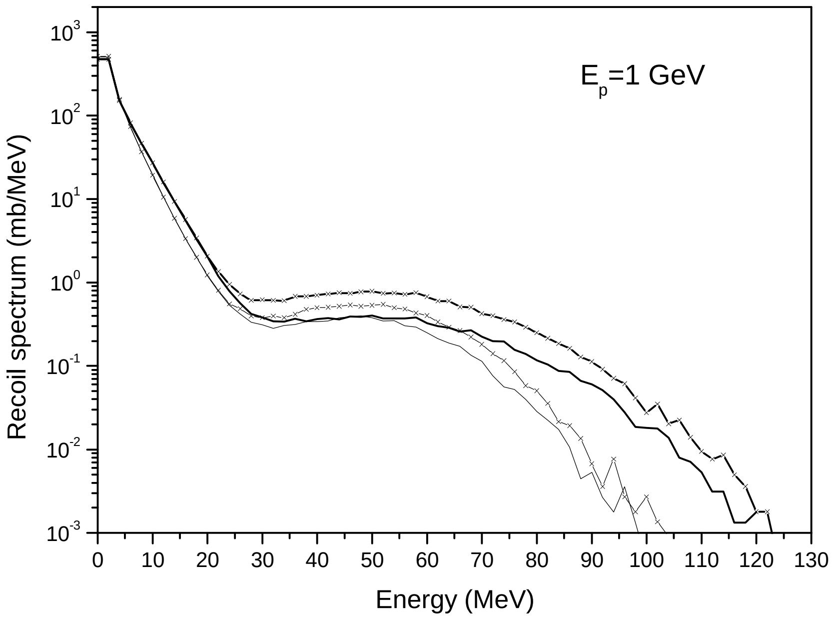

Fig.14 The integral recoil spectrum for nonelastic 1 GeV-proton interactions calculated with the help of the Bertini/Dresner model for ^{181}Ta (solid thick line) and ^{184}W (crossed solid thick line), and with the help of the INCL4/ABLA model for ^{181}Ta (solid thin line) and for ^{184}W (crossed solid thin line).

2.1.1.3 Evaluation of the total displacement cross-section

The total value of the displacement cross-section was calculated as a sum of the proton elastic displacement cross-section $\sigma_{d,el}$ and the displacement cross-section for the proton nonelastic interactions $\sigma_{d,non}$.

The displacement cross-section for the proton elastic scattering has been calculated with the help of the optical model using the optical potentials from Refs.[131,134] at the initial proton energies above 5 MeV. Below 5 MeV the $\sigma_{d,el}$ values were calculated using the differential scattering cross-section from Ref.[129,130].

The nonelastic displacement cross-section has been calculated with the help of the Bertini/Dresner model and the MCNPX code. The recoil spectra from ENDF/B-VI were used to calculate the $\sigma_{d,non}$ values for tungsten isotopes with the mass number 182, 183, 184 and 186 at the energies below 150 MeV.

The evaluated total displacement cross-section is shown in Table 8 and in Fig.17 for ^{181}Ta and natural mixture of tungsten isotopes.

2.1.2 Calculations using the BCA and MD models to obtain the number of defects produced in irradiated material

2.1.2.1 Tungsten

The number of defects produced by tungsten self-ion irradiation has been calculated by the MD method in Ref.[14,57]. The calculations have been performed at the energies below 100 keV.

According to Ref.[14] the efficiency of the defect production η is equal to unity at 1 keV and decreases with the energy growing up to ~ 30 keV up to the value about 0.26.

Table 8

The total proton displacement cross-section evaluated for ^{181}Ta and ^{nat}W irradiated with protons at energies up to 1 GeV. The number of defects has been calculated by the NRT model. Effective threshold energy is equal to 90 eV.

Proton energy (MeV)	Displacement cross-section (b)	
	^{181}Ta	^{nat}W
4.0×10^{-3}	0.0	0.0
4.1×10^{-3}	0.0	1.87
4.2×10^{-3}	2.30×10^{4}	7.27×10^{3}
4.3×10^{-3}	4.93×10^{4}	3.18×10^{4}
4.4×10^{-3}	7.37×10^{4}	5.69×10^{4}
4.5×10^{-3}	9.66×10^{4}	8.03×10^{4}
4.6×10^{-3}	1.18×10^{5}	1.02×10^{5}
4.7×10^{-3}	1.38×10^{5}	1.23×10^{5}
4.8×10^{-3}	1.56×10^{5}	1.42×10^{5}
5.0×10^{-3}	1.90×10^{5}	1.77×10^{5}
5.3×10^{-3}	2.33×10^{5}	2.21×10^{5}
5.6×10^{-3}	2.69×10^{5}	2.58×10^{5}
6.0×10^{-3}	3.07×10^{5}	2.97×10^{5}
8.0×10^{-3}	4.02×10^{5}	3.97×10^{5}
1.0×10^{-2}	4.30×10^{5}	4.27×10^{5}
1.2×10^{-2}	4.41×10^{5}	4.38×10^{5}
1.4×10^{-2}	4.42×10^{5}	4.40×10^{5}
1.6×10^{-2}	4.38×10^{5}	4.37×10^{5}
1.8×10^{-2}	4.32×10^{5}	4.31×10^{5}
2.0×10^{-2}	4.24×10^{5}	4.23×10^{5}

Table 8 continued

3.0×10^{-2}	3.79×10^{5}	3.80×10^{5}
5.0×10^{-2}	3.07×10^{5}	3.08×10^{5}
7.0×10^{-2}	2.58×10^{5}	2.59×10^{5}
0.10	2.10×10^{5}	2.11×10^{5}
0.15	1.63×10^{5}	1.64×10^{5}
0.20	1.34×10^{5}	1.35×10^{5}
0.30	1.00×10^{5}	1.01×10^{5}
0.40	8.10×10^{4}	8.17×10^{4}
0.50	6.84×10^{4}	6.89×10^{4}
0.70	5.26×10^{4}	5.31×10^{4}
1.0	3.95×10^{4}	3.99×10^{4}
1.5	2.84×10^{4}	2.86×10^{4}
2.0	2.23×10^{4}	2.25×10^{4}
3.0	1.58×10^{4}	1.60×10^{4}
4.0	1.24×10^{4}	1.25×10^{4}
5.0	1.02×10^{4}	1.03×10^{4}
7.0	7.66×10^{3}	7.74×10^{3}
10.0	5.53×10^{3}	5.59×10^{3}
15.0	3.84×10^{3}	3.87×10^{3}
20.0	3.05×10^{3}	3.08×10^{3}
30.0	2.53×10^{3}	2.55×10^{3}
40.0	2.41×10^{3}	2.41×10^{3}
50.0	2.37×10^{3}	2.37×10^{3}

Table 8 continued

60.0	2.34×10^3	2.34×10^3
70.0	2.35×10^3	2.34×10^3
80.0	2.36×10^3	2.35×10^3
90.0	2.37×10^3	2.36×10^3
100.0	2.38×10^3	2.36×10^3
110.0	2.37×10^3	2.34×10^3
120.0	2.35×10^3	2.33×10^3
130.0	2.39×10^3	2.36×10^3
140.0	2.48×10^3	2.45×10^3
150.0	2.57×10^3	2.54×10^3
175.0	2.86×10^3	2.89×10^3
200.0	3.00×10^3	3.05×10^3
250.0	3.33×10^3	3.38×10^3
300.0	3.64×10^3	3.71×10^3
350.0	3.94×10^3	4.02×10^3
400.0	4.28×10^3	4.37×10^3
450.0	4.63×10^3	4.74×10^3
500.0	5.01×10^3	5.15×10^3
550.0	5.37×10^3	5.52×10^3
600.0	5.68×10^3	5.86×10^3
650.0	5.97×10^3	6.16×10^3
700.0	6.25×10^3	6.45×10^3
750.0	6.49×10^3	6.72×10^3

Table 8 continued

800.0	6.72×10^3	6.96×10^3
850.0	6.93×10^3	7.19×10^3
900.0	7.12×10^3	7.38×10^3
950.0	7.33×10^3	7.57×10^3
1000.0	7.46×10^3	7.73×10^3

The interaction of 1 GeV-protons with tungsten produces the recoil atoms with the kinetic energy considerably exceeding the maximal energy in the MD simulation [14,57].

To obtain the number of defects produced in material under the high energy proton irradiation the calculations were performed in the present work with the help of the BCA model basing on the results of the MD simulation from Ref.[14].

For an energetic ion moving in the material the simulation of the atomic collision was performed with the help of the binary collision approximation model up to a certain “critical” energy of the ion. Below this energy the BCA calculation was stopped and the number of defects has been calculated according to the result of the MD simulation [14] (Eq.(21a)). The value of the “critical” energy was taken equal to 31 keV, which corresponds to the defect production efficiency η equal to 0.26. Such procedure was performed for all PKAs produced in the atomic collision cascade. The BCA calculations were carried out with the help of the IOTA code [140].

Fig.15 shows the defect production efficiency η calculated by the discussed combined BCA-MD method for the self-irradiation of iron. Fig.16 shows the results obtained for the irradiation of tungsten with As- and W-ions. The efficiency value is shown in Fig.16 as a function of the damage energy T_{dam} in the energy range which corresponds to the primary kinetic energy of As- and W-ions up to 1 GeV.

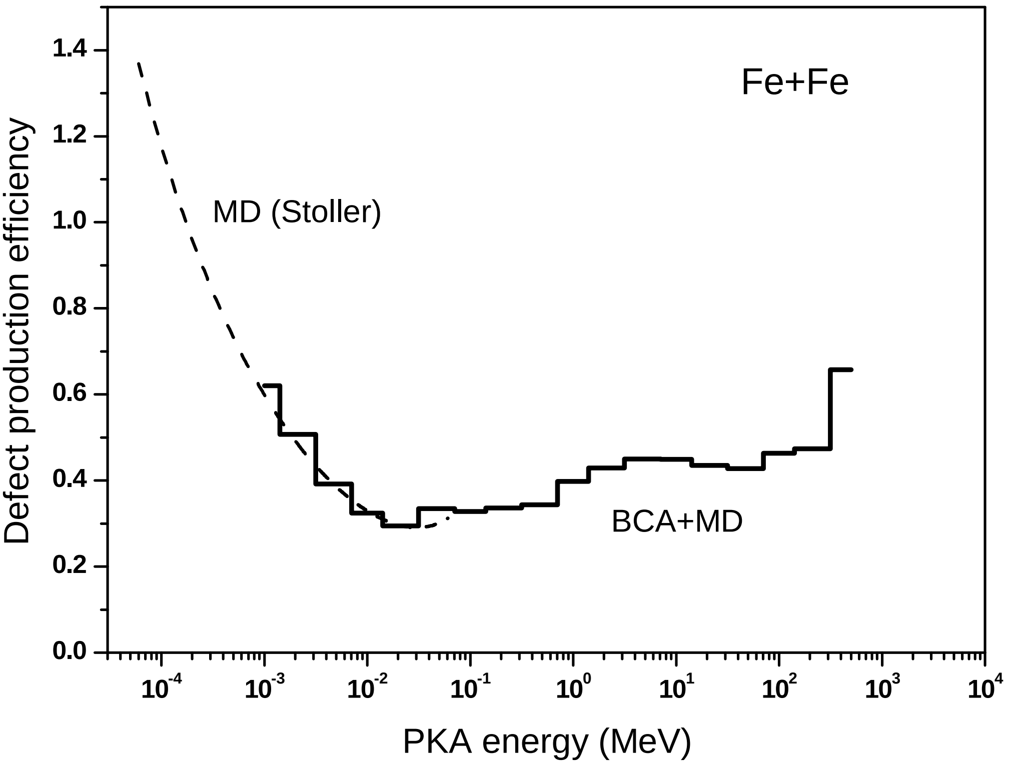

Fig.15 The efficiency of the defect production for Fe+Fe irradiation obtained with the help of the combined BCA-MD method (histogram). The result obtained by Stoller [83,86,88,89,92] at low PKA energies is shown (dashed line).

The defect production efficiency calculated for the W+W irradiation (Fig.16) can be approximated by the following functions

1 keV ≤ $T_{dam} \leq$ 31.02 keV [14]:

$$\eta = 1.0184 T_{dam}^{-0.667} + 5.06 \times 10^{-3}\, T_{dam}\,, \tag{21a}$$

31.02 keV < $T_{dam} \leq$ 72.08 keV:

$$\eta = 0.26, \tag{21b}$$

72.08 keV < $T_{dam} \leq 10^4$ keV:

$$\eta = 5.71 \times 10^{-3} \ln^2(T_{dam}) - 3.87 \times 10^{-2} \ln(T_{dam}) \times 10 + 0.32 \tag{21c}$$

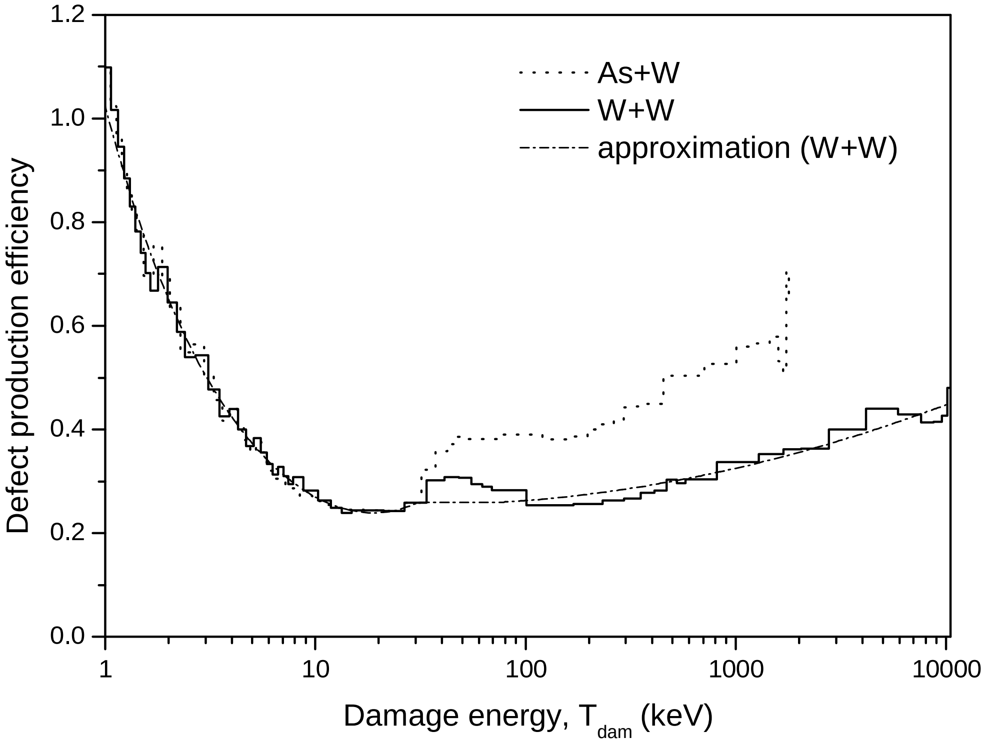

Fig.16 The efficiency of the defect production in tungsten irradiated with As- and W-ions obtained with the help of the combined BCA-MD method. The approximating curve is shown for W+W irradiation (Eq.(21)).

It is supposed that the defect production efficiency has the constant value at the energy below 1 keV and is equal to η(1 keV)=1.023.

The combined BCA-MD calculations together with nuclear model calculations were carried out for the irradiation of tungsten with protons at the energies up to 1 GeV. The number of defects was calculated as described above.

The recoil characteristics were calculated with the help of the MCNPX code using the Bertini/Dresner model. For each recoil atom with the atomic number Z > 2 produced in the pW interaction the simulation of the defect production has been made with the help of the BCA model and the results of the MD simulation as described above. Table 9 shows the results obtained for the proton irradiation of ^{184}W. Also

Table 9 shows the nonelastic displacement cross-section calculated using the NRT model and the $\sigma_{d,non}$ values obtained using the constant approximation of the efficiency η above 31 keV.

Table 9

The nonelastic displacement cross-section for p+^{184}W interaction calculated with the help of the combined BCA-MD approach (column 2), with the constant approximation of the defect production efficiency value above 31 keV (column 3) and with the help of the NRT model (column 4).

Proton energy (MeV)	Displacement cross-section (b)		
	BCA-MD	MD, above 31 keV η = const	NRT
100.	469.	517.	1987.
150.	673.	643.	2474.
200.	855.	754.	2901.
300.	1141.	925.	3560.
400.	1468.	1111.	4275.
600.	2166.	1507.	5797.
800.	2728.	1784.	6864.
1000.	3183.	1971.	7582.

In the last case the $\eta(T)$ value has been calculated using Eq.(21a) obtained in Ref.[14]. At the energy above 31 keV the constant η value equal to 0.26 has been used for the calculations as adopted in the analysis [14] of the high energy proton irradiation of tungsten. One can see a certain difference between the “constant approach” and the result of the combined BCA-MD calculations. The most difference is about 60 % at the proton energy equal to 1 GeV.

Recoil spectra for the elastic proton scattering were calculated as described in Section 2.1.1.1.

Fig.17,18 show the total displacement cross-section σ_d for tungsten calculated using the BCA and MD models. Also, Fig.17 shows the σ_d values derived from the experimental resistivity damage rates in Ref.[10] and recovered using the Frenkel pair resistivity equal to 27 μΩm for tungsten (Table 1). The figure shows the data from Ref.[10] lie between the results obtained with the help of the BCA, MD models and by the NRT approach at the proton energy above 0.2 MeV. The discrepancy between σ_d derived from the experiments [10] and the BCA-MD calculations is not clear yet. It can be related to the problem of the initial damage rate measurements and σ_d derivation for tungsten or to the problems of the MD simulation in Ref.[14]. The same discrepancy was observed in Ref.[14] for the experimental resistivity change in the high energy proton irradiation of tungsten and the results obtained with the help of the MD model.

Table 10 shows the ratio of the displacement cross-section obtained by the BCA and MD models to the σ_d cross-section calculated with the help of the NRT model (Table 8).

2.1.2.2 Tantalum

There is no detailed information about the energy dependence of the defect production efficiency η for tantalum.

The comparison of the averaged efficiency values derived from the neutron irradiation experiments shows that the $<\eta>$ values for tantalum and tungsten are fairly close (Tables 3,6). Moreover, both metals have a bcc lattice, the same effective threshold displacement energy and similar nuclear properties. This justifies to use the main results obtained for tungsten in present work (Section 2.1.2.1) for the approximate data evaluation for tantalum.

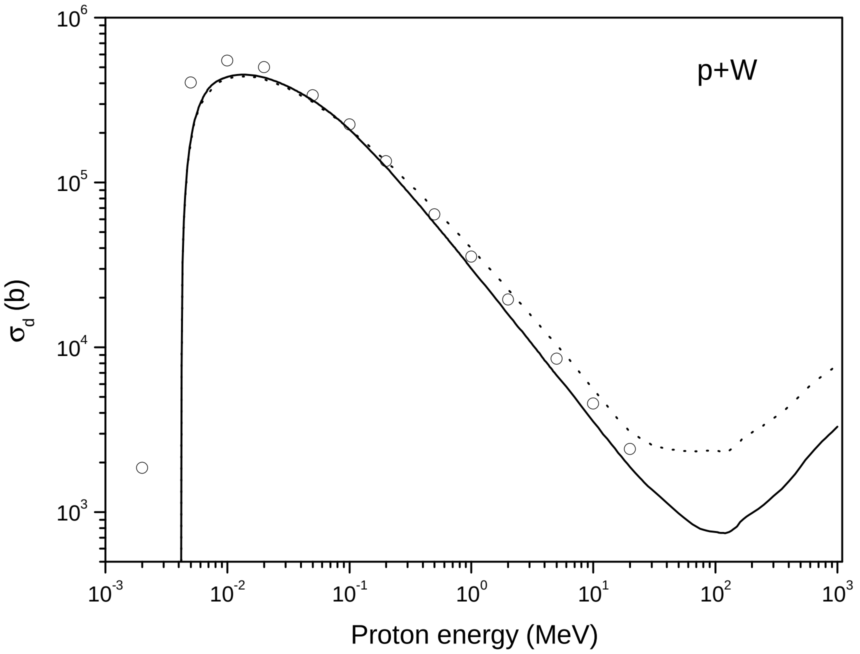

Fig.17 The total displacement cross-section for tungsten irradiated with protons calculated with the help of the BCA and MD models (solid line), calculated by the NRT model (dashed line) and derived from experimental data in Ref.[10] (cycles).

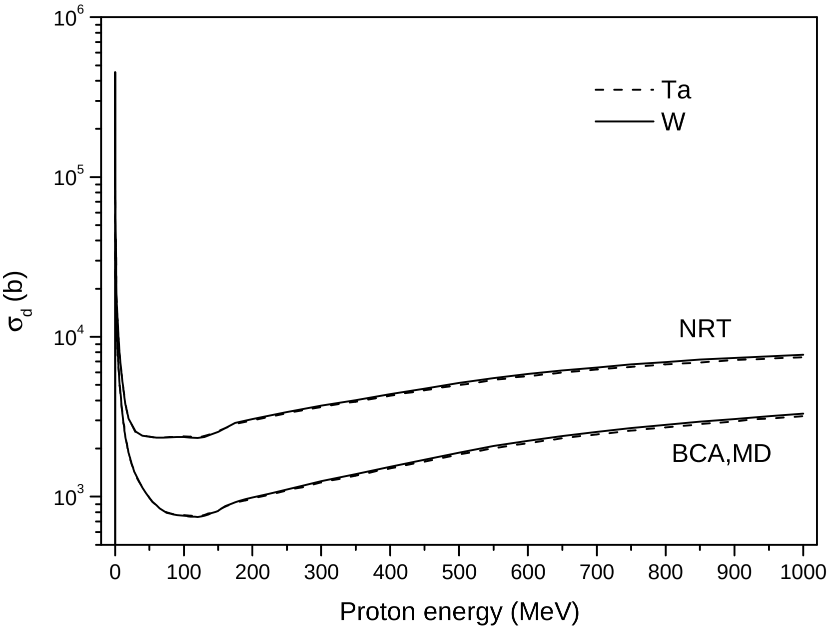

Fig.18 The total displacement cross-section for tantalum and tungsten irradiated with protons obtained with the help of the NRT model and the BCA,MD models. See explanations in the text.

Table 10

The ratio of the displacement cross-section obtained with the help of the BCA and MD models to the cross-sections calculated with the help of the NRT model for the proton irradiation of tungsten.

Proton energy (MeV)	σ_d(BCA-MD)/σ_d(NRT)
4.1×10-3	1.023
5.5×10-2	1.023
9.7×10-2	0.993
0.13	0.965
0.16	0.942
0.20	0.917
0.25	0.892
0.31	0.869
0.39	0.844
0.49	0.821
0.63	0.796
0.81	0.773
1.0	0.755
1.3	0.735
1.7	0.716
2.4	0.695
3.5	0.675
5.0	0.658
8.0	0.639
10.0	0.634
18.0	0.621

Table 10 continued

20.0	0.611
22.0	0.599
24.0	0.585
26.0	0.571
28.0	0.556
30.0	0.540
35.0	0.507
40.0	0.472
45.0	0.442
50.0	0.414
55.0	0.395
60.0	0.378
65.0	0.363
70.0	0.350
75.0	0.339
80.0	0.333
95.0	0.323
100.0	0.322
275.0	0.332
300.0	0.336
350.0	0.344
400.0	0.352
450.0	0.360
500.0	0.367

Table 10 continued

550.0	0.375
600.0	0.382
700.0	0.393
800.0	0.405
900.0	0.416
1000.0	0.427

The ratio of the displacement cross-section calculated using the BCA, MD models to the σ_d value obtained by the NRT approach shown in Table 10 for tungsten is the average defect production efficiency $<\eta>$ related to a certain initial proton energy. With some reservation these $<\eta>$ values can be used obtaining the approximate displacement cross-section for tantalum basing on the σ_d values presented in Table 8. These evaluated values are presented in Fig.18.

One should note that the uncertainty in the σ_d values obtained using different nuclear models (Section 2.1.1.2) is probably more than the expected difference between realistic displacement cross-sections for tantalum and tungsten. This conclusion results from the similar $<\eta>$ values for tantalum and tungsten obtained from the analysis of measured resistivity damage rates in various neutron irradiation experiments ($<\eta>$(Ta) = 0.73 ± 0.09, $<\eta>$(W) = 0.61 ± 0.08). It can not diminish the importance of the further investigations for tantalum.

2.2 Neutron irradiation

2.2.1 Nuclear models and tools used for the recoil spectra calculation

The recoil spectrum for neutron elastic scattering, $(d\sigma/dT)_{el}$ is completely defined by the angular distribution of scattered neutrons. In the present work the nuclear optical model [141] used for the calculation of $(d\sigma/dT)_{el}$. The comparison of the results obtained with the help of different optical potentials is discussed below in Section 2.2.4.1.

The evaluation of the recoil spectrum for reactions implies the calculation of the energy and angular distributions of the secondary particles and the residual nucleus basing on the relativistic conservation laws. In the present work, the nonelastic component of the recoil spectrum, $(d\sigma/dT)_{non}$ is calculated with the help of the various nuclear models incorporated in the MCNPX code package [142]: the Bertini, ISABEL, CEM2k and INCL4 models. They are combined with the pre-equilibrium exciton model and with the evaporation model.

Historically, the development of the Bertini model [143,144] was linked with the widely used NMTC [145] code and the HETC [146] code operation. The ISABEL model [147,148] is the further development of the approach of Chen, Fraenkel, Friedlander et al. [149] which was put in the basis of the VEGAS code. The popular CEM model has being created and improved during last three decades [150-156]. The INCL4 model was developed in Refs.[157,158].

The common feature of the Bertini, ISABEL and CEM2k models is the approximation of the real nuclear density distribution by concentric zones with constant density. The ISABEL model presents the division of the nucleus in sixteen zones, CEM2k implies seven zones and the Bertini model presents three-zone division. In INCL4 the nuclear density is approximated by the Woods-Saxon function. The main difference between all models consists in the approaches used for the intranuclear interaction simulation, determination of the point of particle interaction, selection of collision partners for the moving nucleons and pions and the parameterization of ***n-n*** and *π-**n*** cross-sections.

The description of the multistage pre-equilibrium exciton model used in the combination with the Bertini model and the ISABEL model is given in Refs.[159,160] The exciton model incorporated in CEM2k is described in Refs.[161,162].

The equilibrium particle emission is simulated by the simple Dresner model [163] and by the advanced ABLA model [164] in the calculations carrying out using the Bertini, ISABEL and INCL4 models. The CEM2k has its own separate evaporation algorithm described in Refs.[161,162].

In the calculations discussed below the intranuclear cascade model, except the INCL4 model, was always used together with the pre-equilibrium and evaporation models. An indication on the cascade model “Bertini” and “ISABEL” implies also the application of the pre-compound exciton algorithm describing the de-excitation of residual nuclei formed after the fast particle emission. “CEM2k” always means the use of intranuclear cascade, pre-equilibrium exciton and evaporation models.

A special case is presented when the use of the intranuclear cascade model and pre-equilibrium model is chosen randomly. A selection of pure pre-equilibrium calculation is made by Monte Carlo according to the formula [138]: min(25 MeV/E, 1.0), where E is the projectile energy. If the random choice is for the intranuclear cascade calculation the pre-equilibrium model is applied only at the end of the cascade particle emission. In the MCNPX code the procedure is used only for the Bertini intranuclear cascade model. This approach is noted as “MBP” (Mixed Bertini Pre-equilibrium model) in the present work.

The calculations with the help of the nuclear models from MCNPX were performed with a set of default parameters described in Refs.[138,142].

2.2.2 Comparison of calculations with available experimental data

The experimental data for recoil atom spectra are absent for both tantalum and tungsten. For this reason the comparison of the calculations and experimental data was performed for other values, which accuracy of the description is significant for the accuracy of the dσ/dT calculation.

Figs.19,20 show the neutron total cross-section for natural tantalum and tungsten, calculated with the help of the MCNPX code and the measured data [165-171]. It should be noted that the computation of the total cross-section in MCNPX is based on the approximation of results of the optical model calculation [138] and does not depend on the type of the intranuclear cascade model selected for the calculation. There is a good agreement between the MCNPX cross-sections and the available experimental data at the energies above 20 MeV. A small systematic difference between the calculated and measured cross-section is observed at the energies below 450 MeV. Figs.21,22 show the neutron emission spectra for ^{181}Ta and ^{184}W irradiated with 20-MeV and 26-MeV neutrons. The calculations were performed with the help of the different combinations of the intranuclear cascade model and evaporation model: Bertini/Dresner, Bertini/ABLA, ISABEL/Dresner, MBP/ABLA and with the CEM2k model. The measured data are from Refs.[172,173]. Generally, the agreement between the calculations and the experiment is rather good. It is not surprising taking into account that the calculations by the high energy intranuclear models are added with the pre-compound exciton model algorithm. For the hard part of the spectra the best agreement is between the experimental data and the Bertini and Mixed Bertini Pre-equilibrium model (MBP). The low energy part is reproduced better by the use of the ABLA approach.

The double differential cross-section is another nuclear reaction characteristic which prediction has direct sense for the accuracy of the recoil spectra calculation. Such cross-sections of neutrons emitted from the reaction on ^{181}Ta and ^{184}W induced by 20-MeV and 26-MeV neutrons are shown in Figs.23,24. The data for the outgoing neutron energy equal to 2.8 and 4.8 MeV (Fig.23) correspond to the evaporation part of the ^{181}Ta(n,n’) spectrum and the data for other emission energies (Fig.23,24) relate to the non-equilibrium part of the neutron spectrum for ^{181}Ta and ^{184}W.

The comparison of the data plotted in Fig.23,24 shows that the best description of the experimental data is presented by the MBP/ABLA approach. The CEM2k model is also successful for the prediction of the pre-equilibrium part of the spectra at the neutron emission energy above 4.8 MeV.

The experimental information about the energy and angular distribution of the secondary particles emitted in neutron induced reaction on tantalum and tungsten above 20 MeV is limited by the data set discussed above. In this case the data for proton induced reactions can be used for the verification of the methods of the calculation. The comparison is performed for the double differential cross-sections of neutrons and protons emitted from the p+Ta reaction at the primary proton energy around 600 MeV.

Calculated and measured [174,175] distributions of neutrons and protons are plotted in Figs.25,26. The comparison shows that none of the models gives the detailed description of the experimental data. The neutron double-differential cross-section calculated with the help of the intranuclear cascade models is found to be lower than the measured data at various emission angles (Fig.25). The MBP and Bertini models present the best result for the 150^0-angle neutron emission. The proton distribution (Fig.26) calculated by the INCL4 model is in the good agreement with the experimental data at the angles $60\text{-}150^0$. For small proton angle (30^0) the result obtained by INCL4 is the worst comparing with other codes.

The comparison performed for the neutron and proton angular distributions gives the definite freedom in choosing the model of calculation to obtain the neutron displacement cross-sections around 600 MeV, because none of the models shows an excellent agreement with the experimental data [174,175].

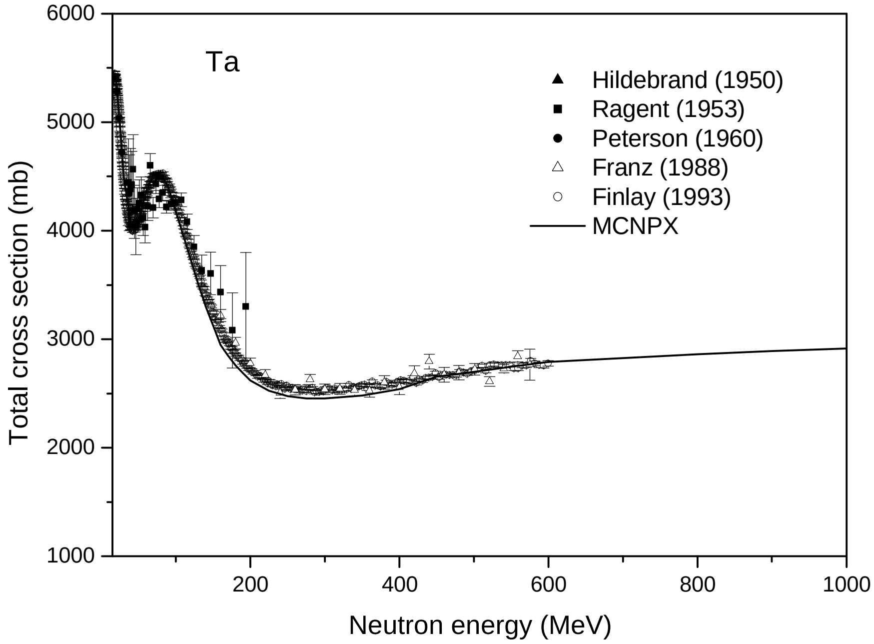

Fig.19 The neutron total cross-section for natural tantalum calculated with the help of the MCNPX code and measured in Refs.[165-169].

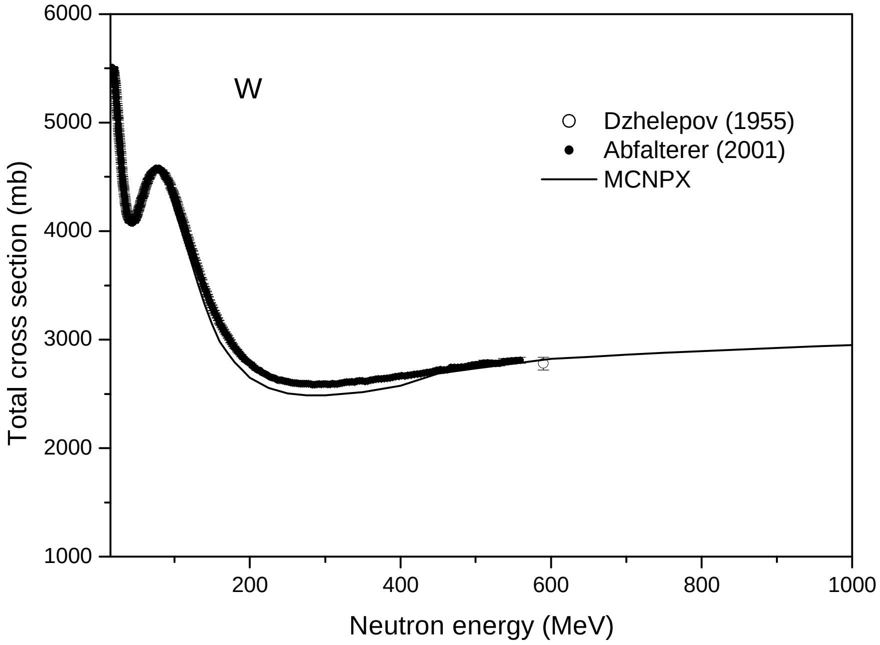

Fig.20 The neutron total cross-section for natural tungsten calculated with the help of the MCNPX code and measured in Refs.[170,171].

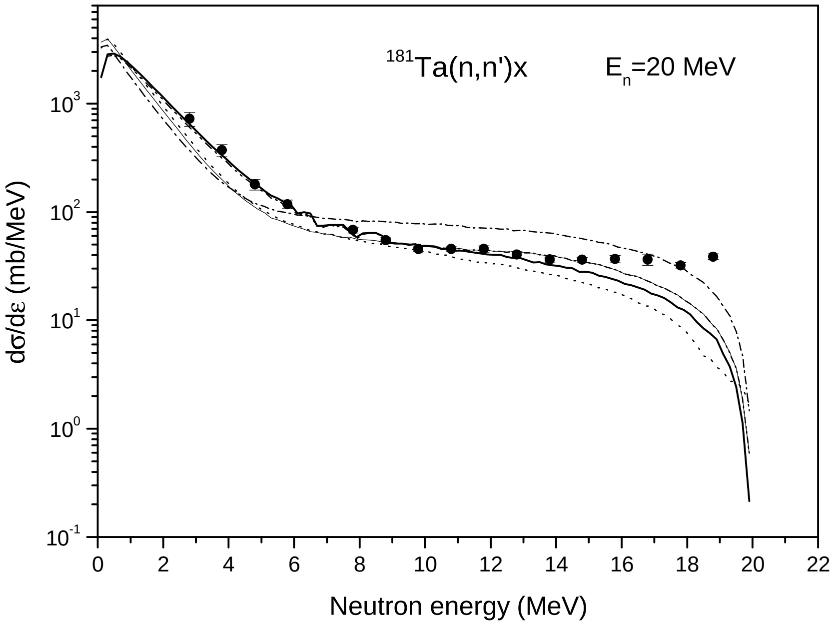

Fig.21 The neutron emission spectra for ^{181}Ta irradiated with 20-MeV neutrons calculated with the help of the different nuclear models incorporated in the MCNPX code: Bertini/Dresner (thin solid line), CEM2k (dot line), ISABEL/Dresner (dash-dot line), Bertini/ABLA (dash-dot-dot line) and MBP/ABLA (thick solid line). The measured data are from Ref.[172] (black circle).

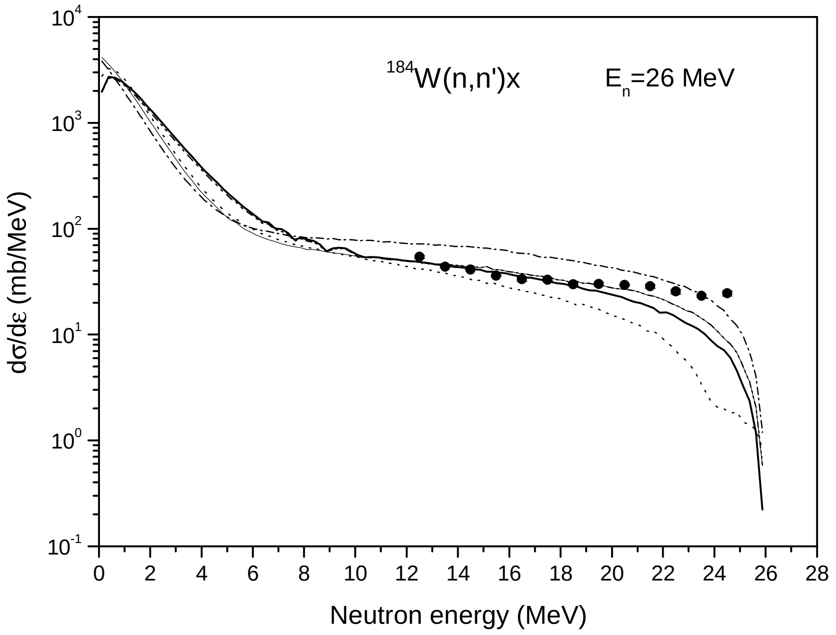

Fig.22 The neutron emission spectra for ^{184}W irradiated with 26-MeV neutrons calculated with the help of the different nuclear models incorporated in the MCNPX code. The measured data are from Ref.[173] (black circle). See also captions for Fig.21.

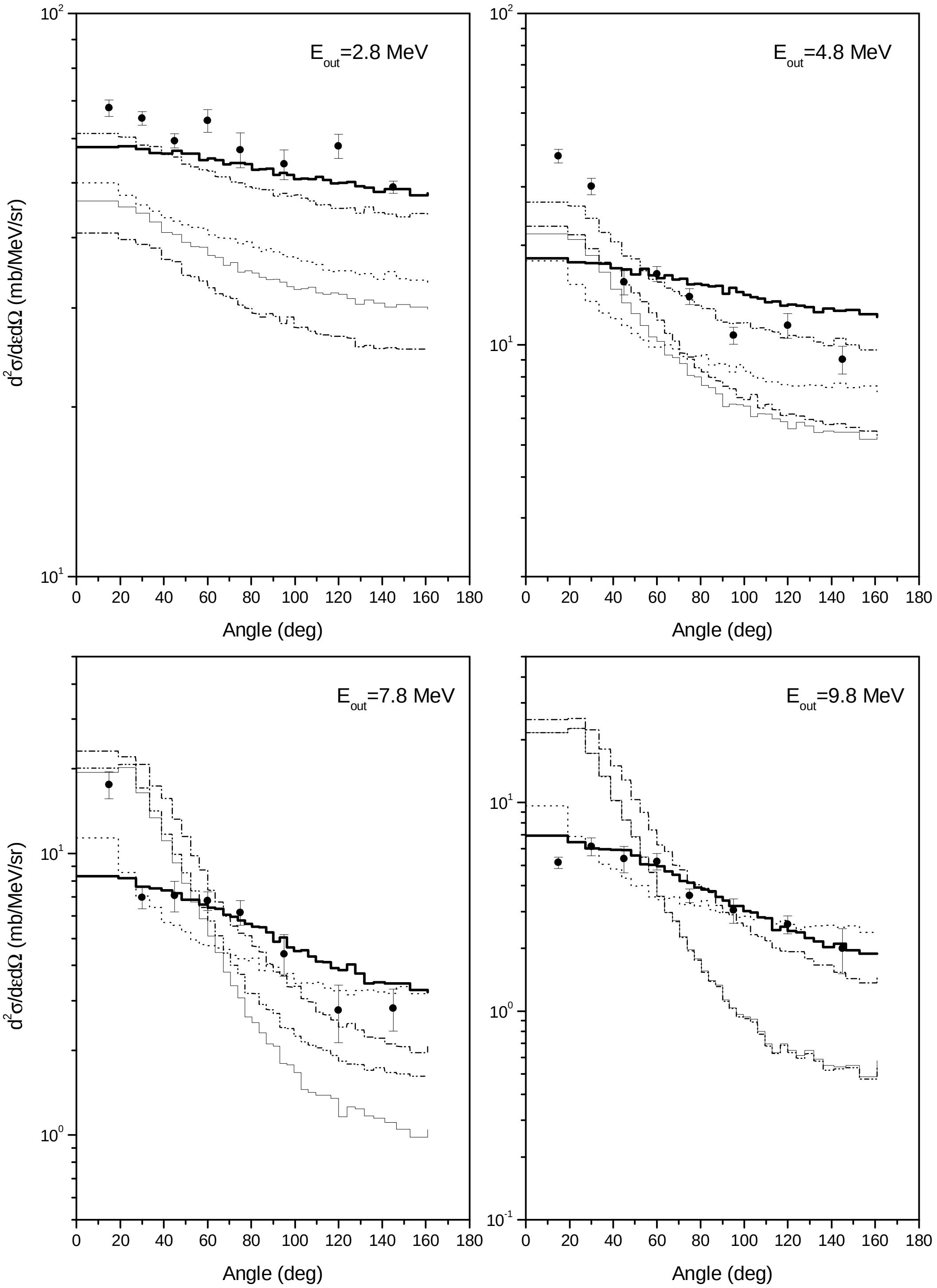

Fig.23A The double differential cross-section of neutrons emitted with the energies 2.8, 4.8, 7.8 and 9.8 MeV from the reaction on ^{181}Ta induced by 20-MeV neutrons calculated with the help of the different nuclear models incorporated in the MCNPX code. The measured data are from Ref.[172] (black circle). See also captions for Fig.21.

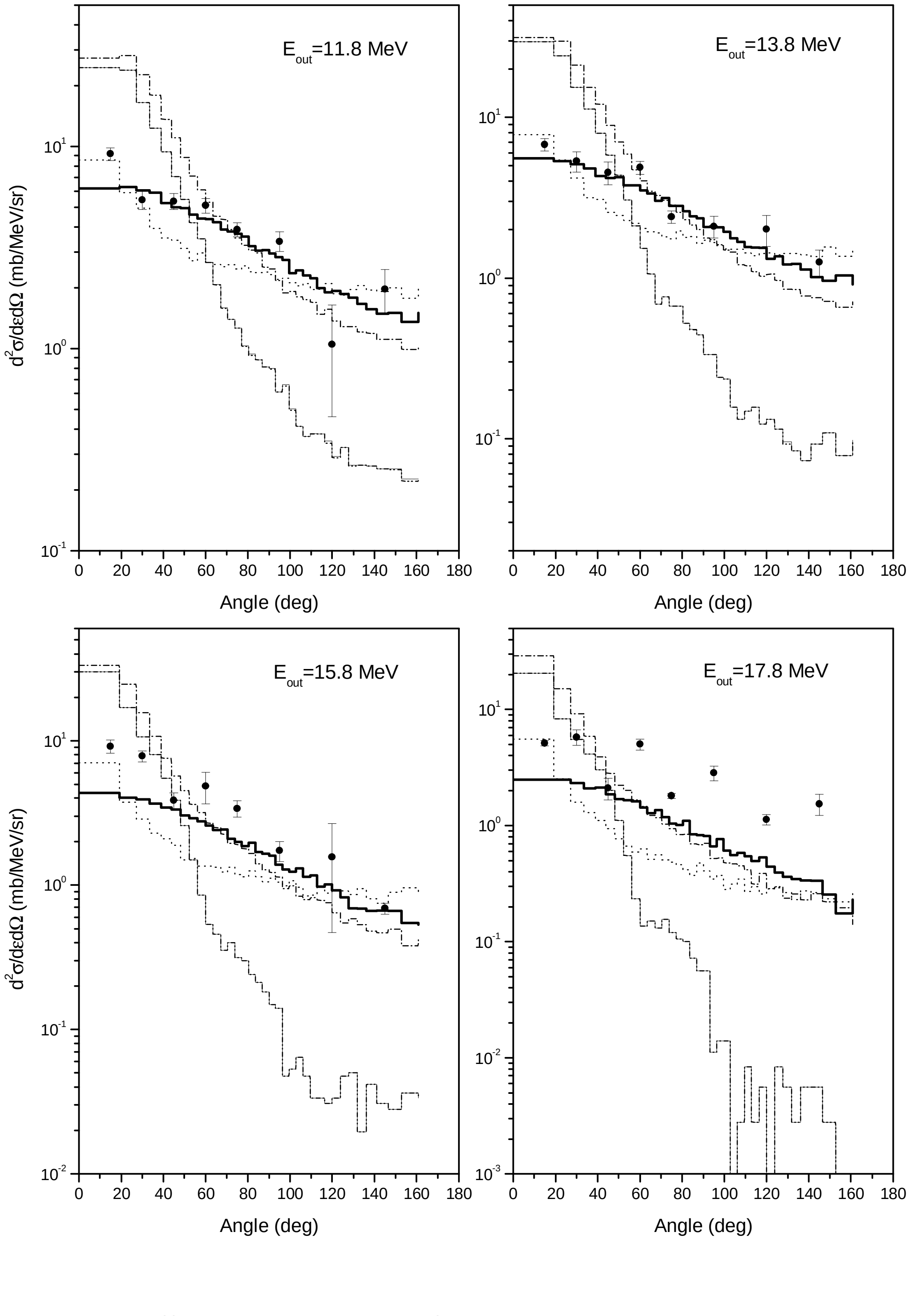

Fig.23B The double differential cross-section of neutrons emitted with the energies 11.8, 13.8, 15.8 and 17.8 MeV from the reaction on ^{181}Ta induced by 20-MeV neutrons calculated with the help of the different nuclear models incorporated in the MCNPX code. The results of the Bertini/Dresner and Bertini/ABLA calculations almost coincide. The measured data are from Ref.[172] (black circle). See also captions for Fig.21.

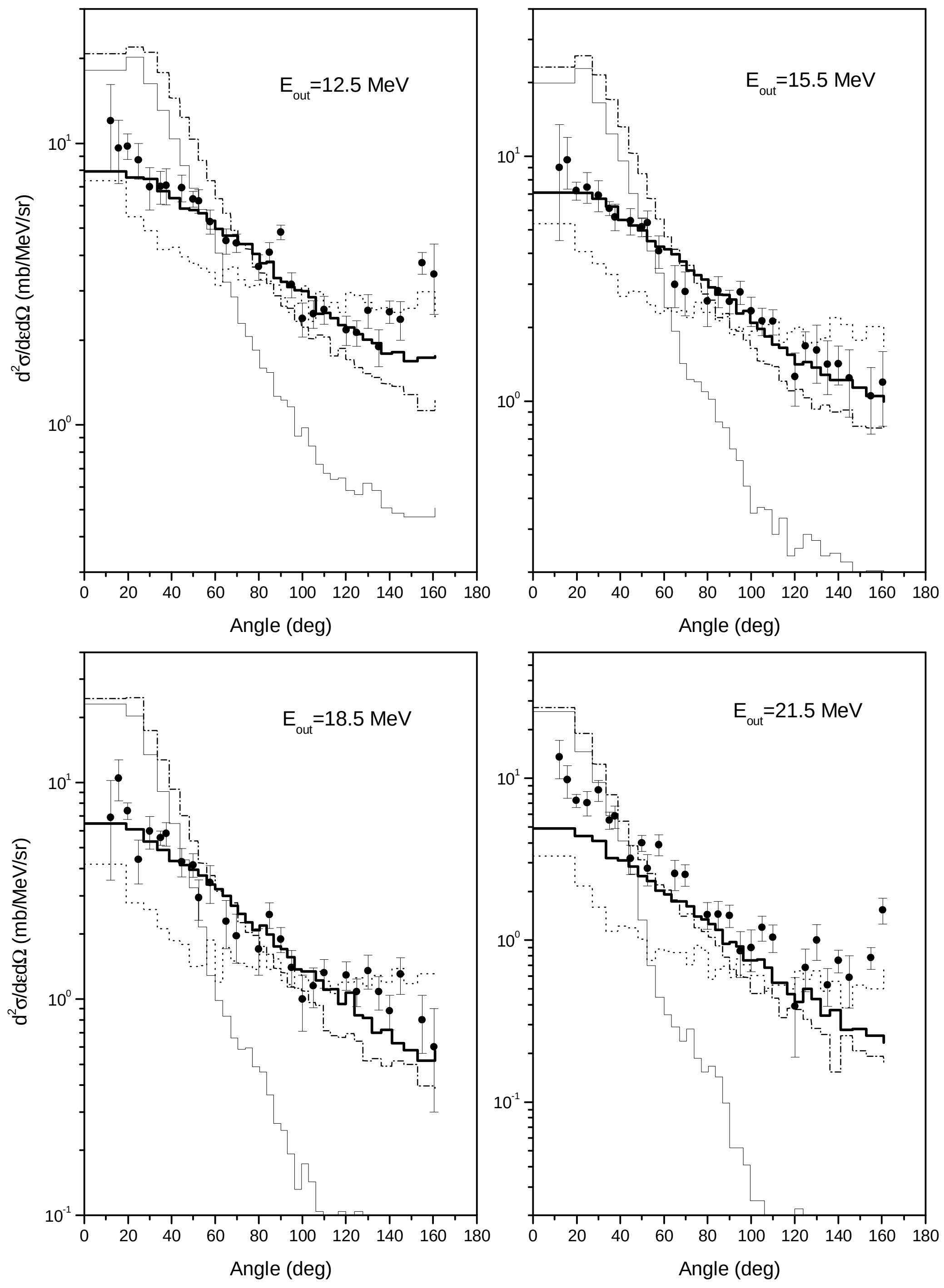

Fig.24 The double differential cross-section of neutrons emitted with the energies 12.5, 15.5, 18.5 and 21.5 MeV from the reaction on ^{184}W induced by 26-MeV neutrons calculated with the help of the different nuclear models incorporated in the MCNPX code. The results of the Bertini/Dresner and Bertini/ABLA calculations almost coincide. The measured data are from Ref.[173] (black circle). See also captions for Fig.21.

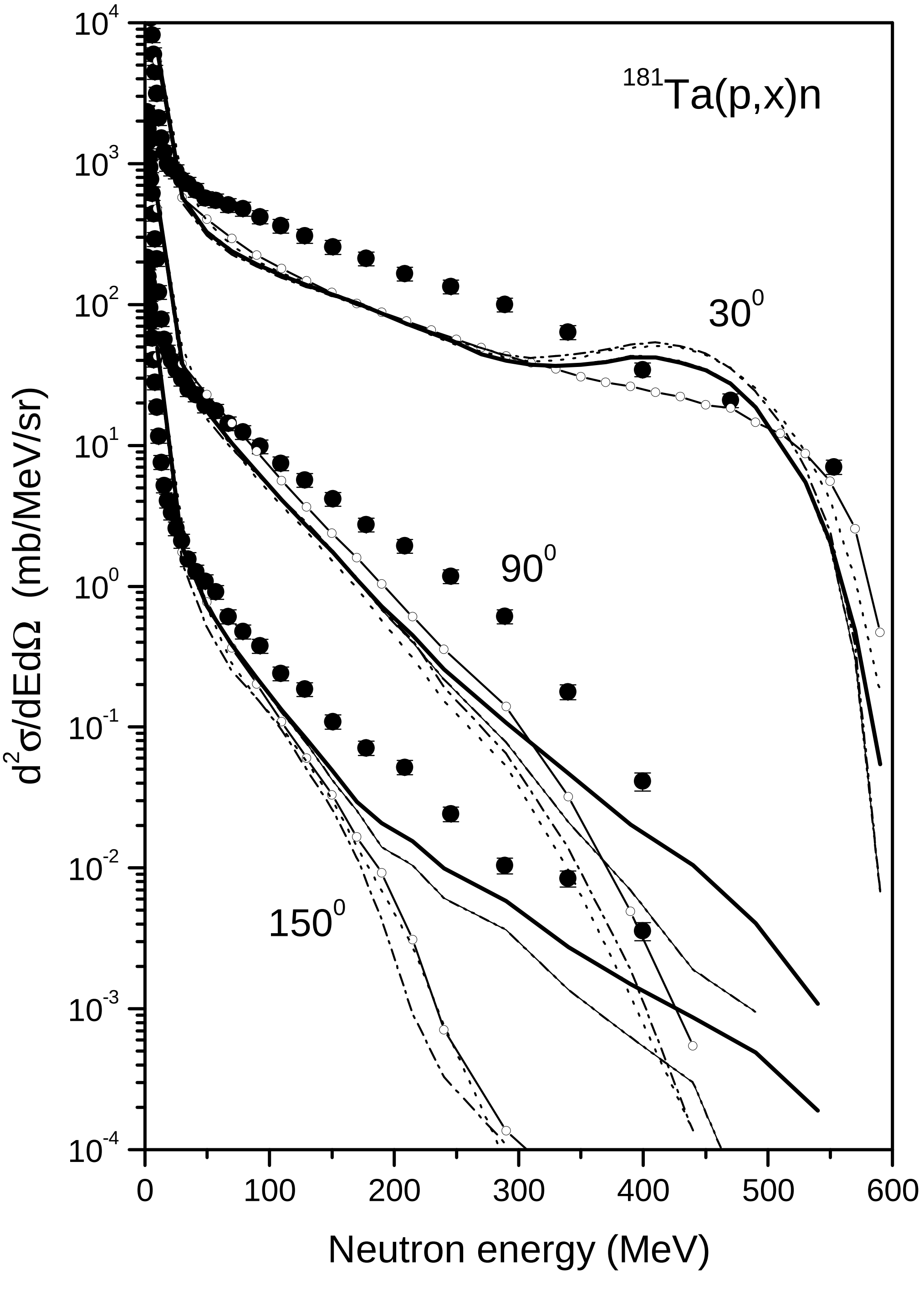

Fig.25 The double differential cross-section of neutrons emitted from the reaction on ^{181}Ta induced by 590-MeV protons calculated with the help of the different nuclear models incorporated in the MCNPX code: Bertini/Dresner (thin solid line), CEM2k (dot line), ISABEL/Dresner (dash-dot line), Bertini/ABLA (dash-dot-dot line), INCL4/ABLA (open circle-solid line) and MBP/ABLA (thick solid line). The results of the Bertini/Dresner and Bertini/ABLA calculations almost coincide. The measured data are from Ref.[174] (black circle).

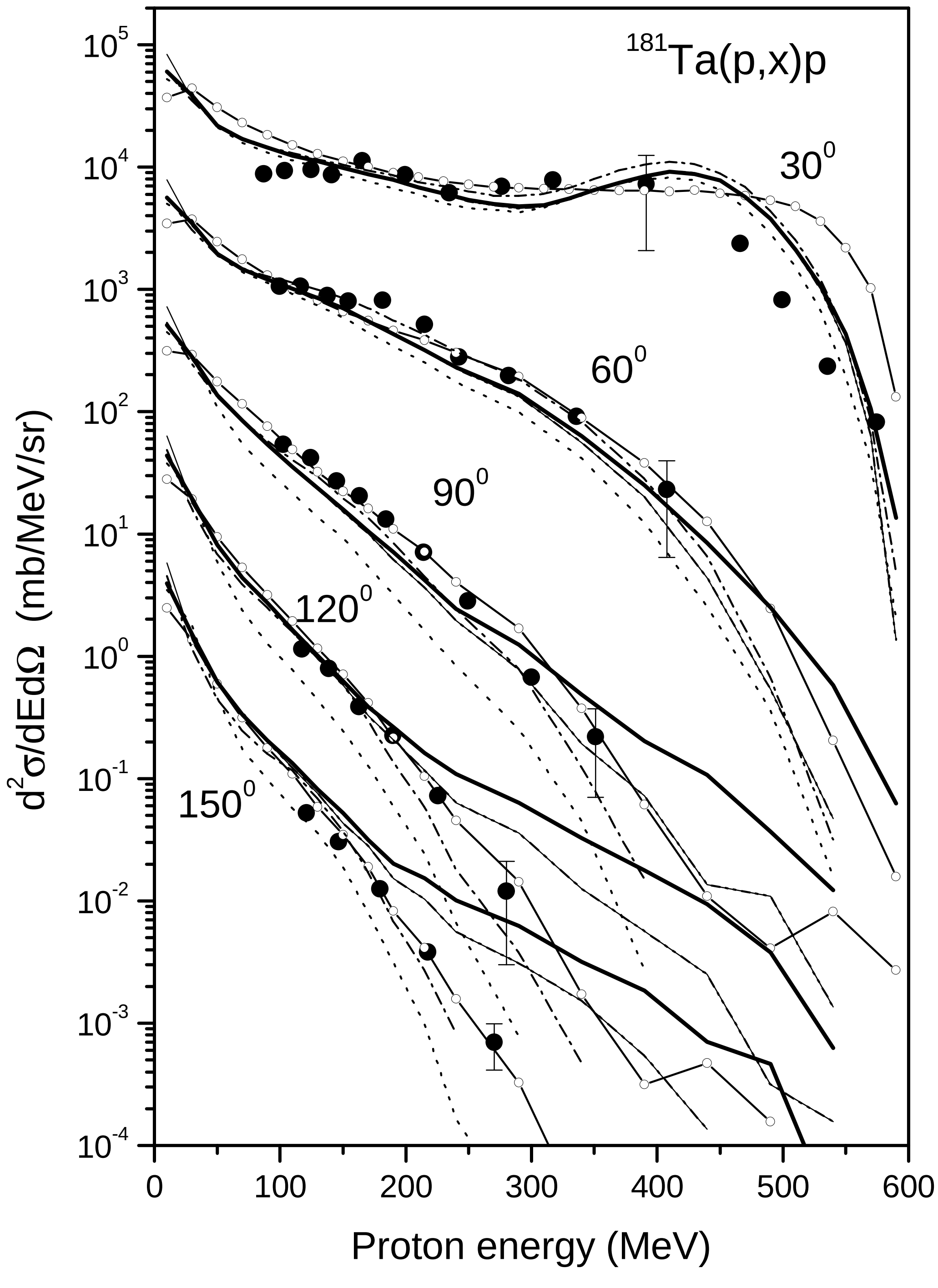

Fig.26 The double differential cross-section of protons emitted from the reaction on ^{181}Ta induced by 600-MeV protons calculated with the help of the different nuclear models incorporated in the MCNPX code. The measured data are from Ref.[175] (black circle). See also captions for Fig.25.

2.2.3 Comparison of calculations with ENDF/B-VI data

For tungsten isotopes the comparison of the calculations with the ENDF/B-VI (Release 8) data above 20 MeV can be performed directly for the recoil atom spectra. Figs.27,28 show the integral recoil spectra for ^{184}W irradiated with 26-MeV and 150-MeV neutrons. The spectra were taken from ENDF/B-VI (8) by summing of the individual spectra for all nuclides produced in the nonelastic neutron interactions with ^{184}W and calculated with the help the different approaches in the present work.

The result of the calculation for 26-MeV neutron induced reaction (Fig.27) is in a general agreement with ENDF/B-VI. The best agreement is observed between the ENDF/B-VI data and the $(d\sigma/dT)_{non}$ spectrum calculated with the help of the CEM2k model and the MBP model combined with the ABLA approach.

In the analysis, the recoil spectrum can not be simply divided on the “evaporation” and “pre-equilibrium” parts as in the case of the spectrum of particle emission. The wide plateau in $(d\sigma/dT)_{non}$ above 0.6 MeV (Fig.27) is rather due to the α-particle emission contribution in the recoil spectrum [176] than it results from the nucleon pre-compound emission. Also the low energy part of the spectrum ($T < 0.1$ MeV) is formed by the contributions of particles emitted on the pre-compound and equilibrium reaction stage. Here the results obtained with the help of the Dresner and ABLA evaporation models are close (Fig.27), although the use of these models results in different values of the particle evaporation spectrum (Figs.21,22).

Fig.28 shows the considerable discrepancy between the ENDF/B-VI (8) data and the recoil spectrum calculated for 150-MeV neutron induced reaction. At the same time the $(d\sigma/dT)_{non}$ values obtained with the help of the different models are in a good agreement.

It seems to be rather impossible to give an exhaustive explanation of the discrepancy between the ENDF/B-VI data and the recoil spectrum calculated with the help of the intranuclear cascade - pre-equilibrium exciton - evaporation models

(Fig.28). Nevertheless a number of reasons can be mentioned helping to elucidate the problem. The data evaluation for ENDF/B-VI at the energies above 20 MeV has been performed with the help of the GNASH code [177]. The code is based on the pre-equilibrium exciton model [177-181] and the statistical Hauser-Feshbach model. The multiple pre-compound particle emission is taken into account according to Ref.[181]. The emission of the second pre-equilibrium particle is described approximately [181] and the escape of third and other fast particles is not considered. At the same time the detailed description of the multiple pre-equilibrium emission is significant to get the agreement between calculated spectra and the experimental data at the intermediate energies [182]. In addition, the recoil atom spectra have been prepared for ENDF/B-VI using an approximate procedure [183] separated from the main GNASH calculation.

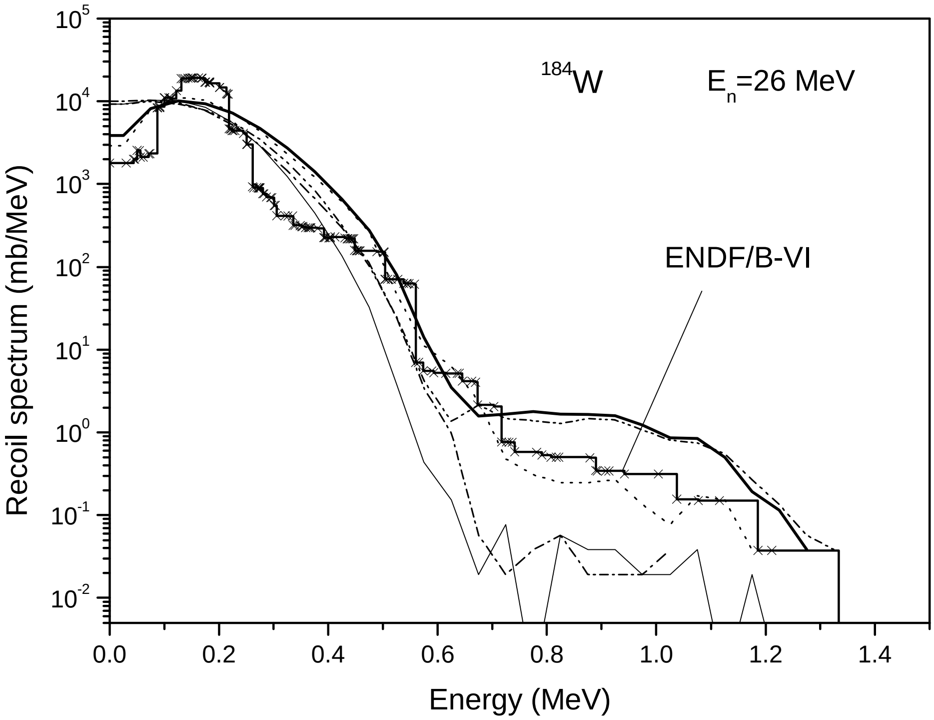

Fig.27 The integral recoil atom spectrum for the reaction on ^{184}W induced by 26-MeV neutrons derived from the ENDF/B-VI data (cross-solid line) and calculated with the help of the different nuclear models from MCNPX. See also captions for Fig.25.

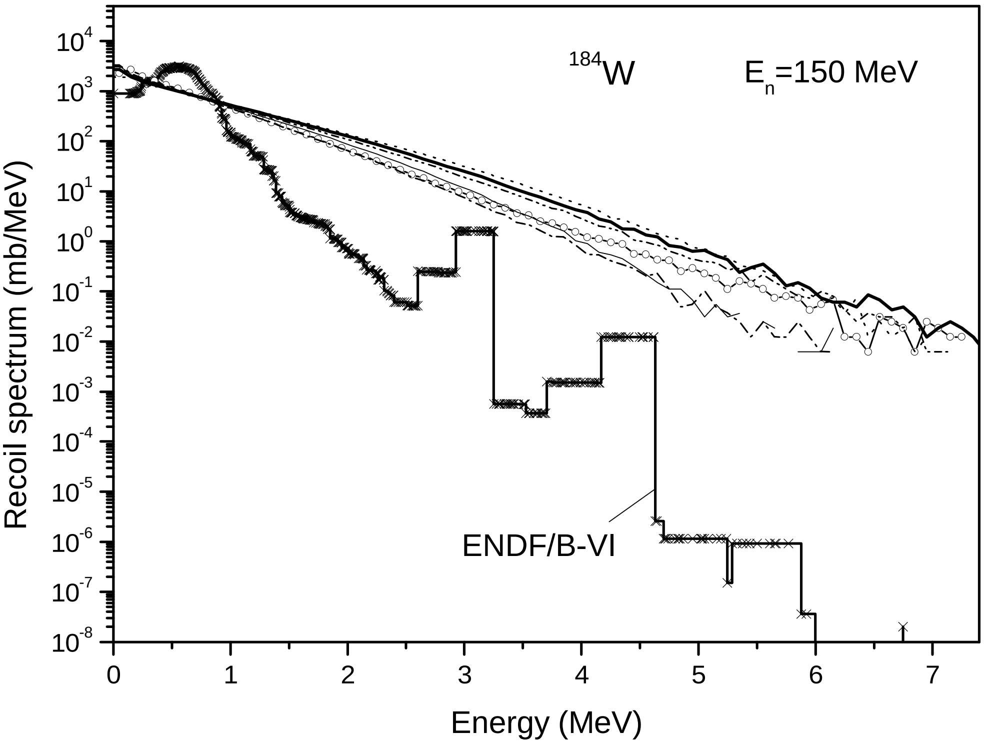

Fig.28 The integral recoil atom spectrum for the reaction on ^{184}W induced by 150-MeV neutrons derived from the ENDF/B-VI data and calculated with the help of the different nuclear models from MCNPX. See also captions for Figs.25,27.

The necessity to use the approximations discussed above in the ENDF/B-VI data preparation was not a consequence of the limitation of theoretical models, and it resulted from the GNASH code algorithm based on the common integration of particle emission rates. These approximations are completely substituted for the accurate calculations in the codes using the Monte Carlo method.

The initial energy about 150 MeV was justified in many works for the application of quasi-classical intranuclear cascade model especially combined with the pre-equilibrium model [184]. It is an indication that probably at the energies around 150 MeV the preference should be given to the calculation of $(d\sigma/dT)_{non}$ with the help of the models incorporated in the MCNPX code rather than to the evaluated data from ENDF/B-VI.

2.2.4 Calculation of displacement cross-section using the NRT model

2.2.4.1 Elastic neutron scattering

The elastic displacement cross-section $\sigma_{d,el}$ has been calculated with the help of the nuclear optical model, using the neutron angular distributions from ENDF/B-VI (8) and with the help of the MCNPX code. The comparison of the $\sigma_{d,el}$ values obtained is discussed below after a short comment about the codes used for the calculation.

The Raynal code [141] has been used for the spherical optical model calculation. The relativistic corrections were taken into account. The ENDF/B-VI (8) data were transformed to the displacement cross-sections by the NJOY code [2]. The angular elastic distributions were calculated by MCNPX basing on the interpolation of the tabulated data [138]. The standard output file “histp” was used to obtain the $\sigma_{d,el}$ values.

Figs.29-31 show the elastic displacement cross-section calculated with the help of the optical model and the optical potentials from Refs.[131,133,134,185], the $\sigma_{d,el}$ values obtained from the ENDF/B-VI data and the cross-sections calculated using the MCNPX code. The detailed view of the cross-sections $\sigma_{d,el}$ at the energies up to 150 MeV is shown in Figs.29,30 for ^{181}Ta and ^{184}W. The values obtained at the energies up to 1 GeV are shown in Fig.31 by the example of ^{181}Ta.

The comparison of the data plotted in Figs.29-31 shows a discrepancy between the elastic displacement cross-sections calculated using different sets of the optical model parameters and the ENDF/B-VI (8) data. Partly, the agreement is observed for the $\sigma_{d,el}$ values calculated with the help of the Koning, Delaroche potential [131] and the Walter, Guss potential [133] at the energies below 50 MeV (Figs.29,30). These values are close to the ENDF/B-VI data for ^{181}Ta at 20 MeV (Fig.29). Also, the cross-section calculated using the Koning, Delaroche optical potential [131] is close to the $\sigma_{d,el}$ value obtained with the help of the Madland potential [134] at 140-200 MeV. The ENDF/B-VI data for ^{184}W are in the agreement with the calculations performed using the Becchetti, Greenlees optical model parameters [185] at the energies 20 -40 MeV.

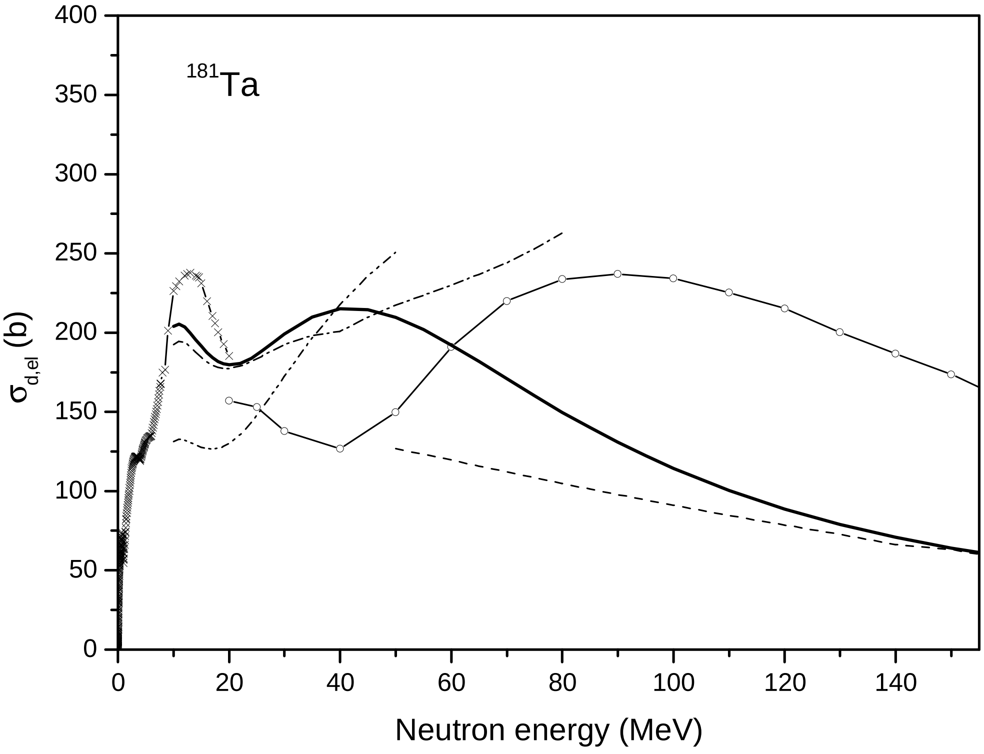

Fig.29 The elastic displacement cross-section for ^{181}Ta calculated at the energies below 150 MeV using the ENDF/B-VI data (cross-solid line), using the MCNPX code (open circle-solid line) and with the help of the optical model with optical potentials of Becchetti, Greenlees (dash-dot-dot line), Walter, Guss (dash-dot line), Madland (dash line) and Koning, Delaroche (solid line).

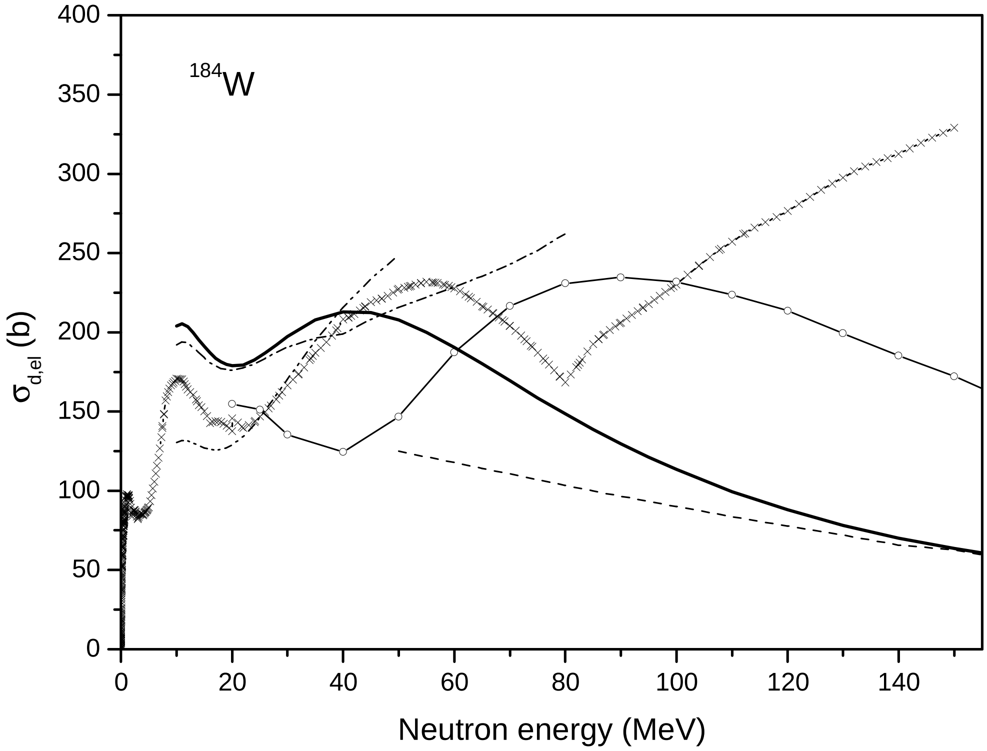

Fig.30 The elastic displacement cross-section for ^{184}W calculated at the energies below 150 MeV using the ENDF/B-VI data, using the MCNPX code and with the help of the optical model and different optical potentials. See also captions for Fig.29.

The observed discrepancy between the $\sigma_{d,el}$ values obtained with the help of the different sets of the optical model parameters fairly complicates the evaluation of the elastic displacement cross-section.

In the present work the preference is given to the calculations of $\sigma_{d,el}$ basing on the newest optical potential of Koning and Delaroche [131] and the Madland potential [134]. Above 50 MeV a relative uncertainty of the evaluated elastic displacement cross-section does not make a strong impact on the total displacement cross-section value, because the possible contribution of $\sigma_{d,el}$ in the total displacement cross-section does not exceed 10-13 %.

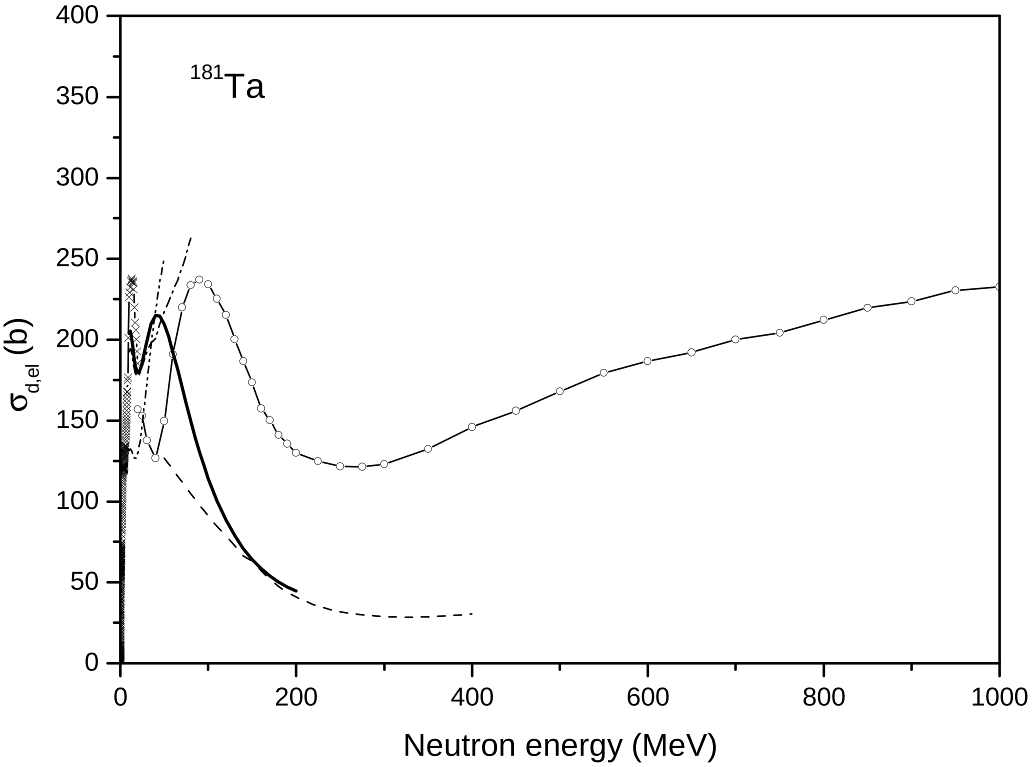

Fig.31 The elastic displacement cross-section for ^{181}Ta calculated at the energies below 1 GeV using the ENDF/B-VI data, using the MCNPX code and with the help of the optical model and different optical potentials. See also captions for Fig.29.

2.2.4.2 Nonelastic neutron interactions

The displacement cross-section related to the neutron nonelastic interaction with nucleus, $\sigma_{d,non}$ has been calculated with the help of the different models incorporated in the MCNPX code. The ENDF/B-VI (8) data were treated by the NJOY code.

Figs.32,33 show the $\sigma_{d,non}$ values calculated for ^{181}Ta and ^{184}W at the energies up to 150 MeV. The displacement cross-section obtained in the whole energy range up to 1 GeV is shown in Fig.34 for ^{181}Ta.

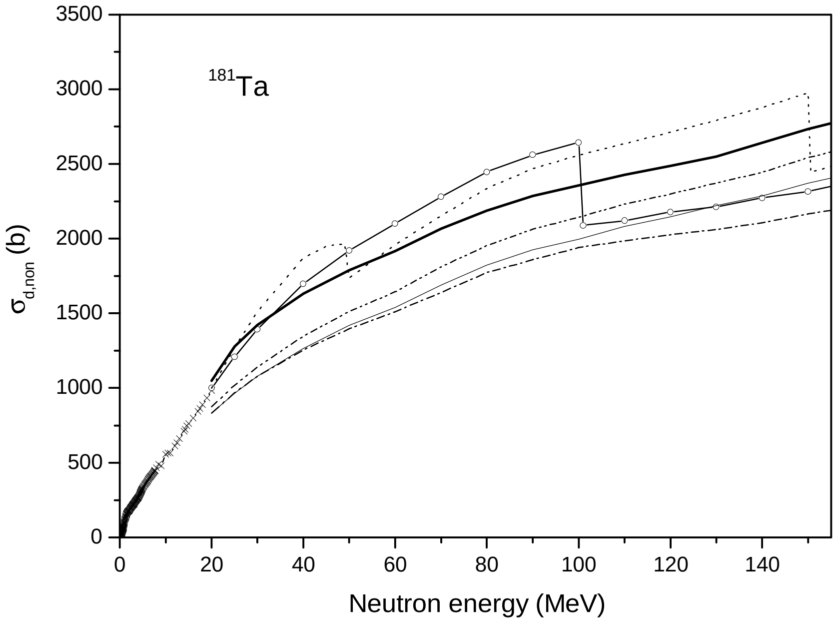

Fig.32 The displacement cross-section for neutron nonelastic interactions with ^{181}Ta at the energies below 150 MeV calculated using the ENDF/B-VI data (cross) and the different nuclear models from the MCNPX code: Bertini/Dresner (thin solid line), CEM2k (dot line), ISABEL/Dresner (dash-dot line), Bertini/ABLA (dash-dot-dot line), INCL4/ABLA (open circle-solid line) and MBP/ABLA (thick solid line).

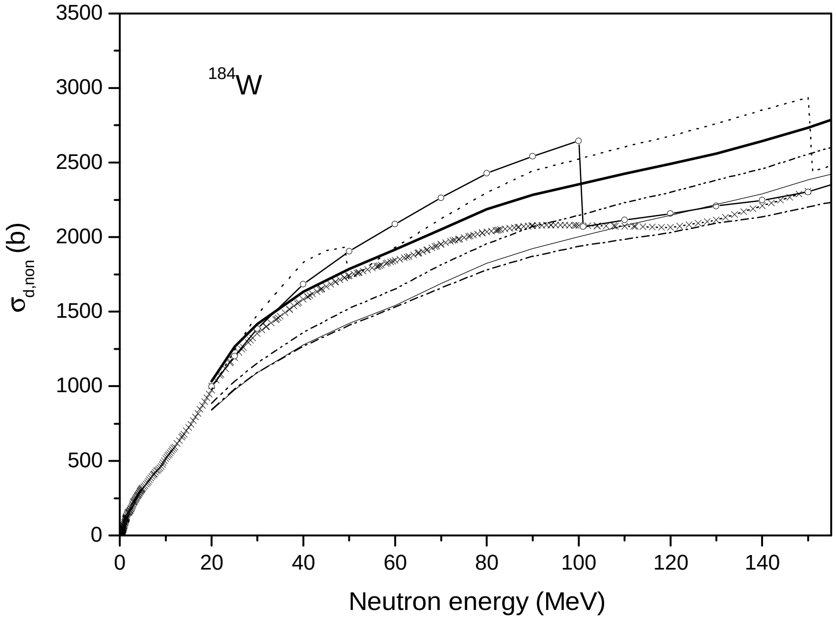

Fig.33 The displacement cross-section for neutron nonelastic interactions with ^{184}W at the energies below 150 MeV calculated using the ENDF/B-VI data and the different nuclear models from the MCNPX code. See also captions for Fig.32.

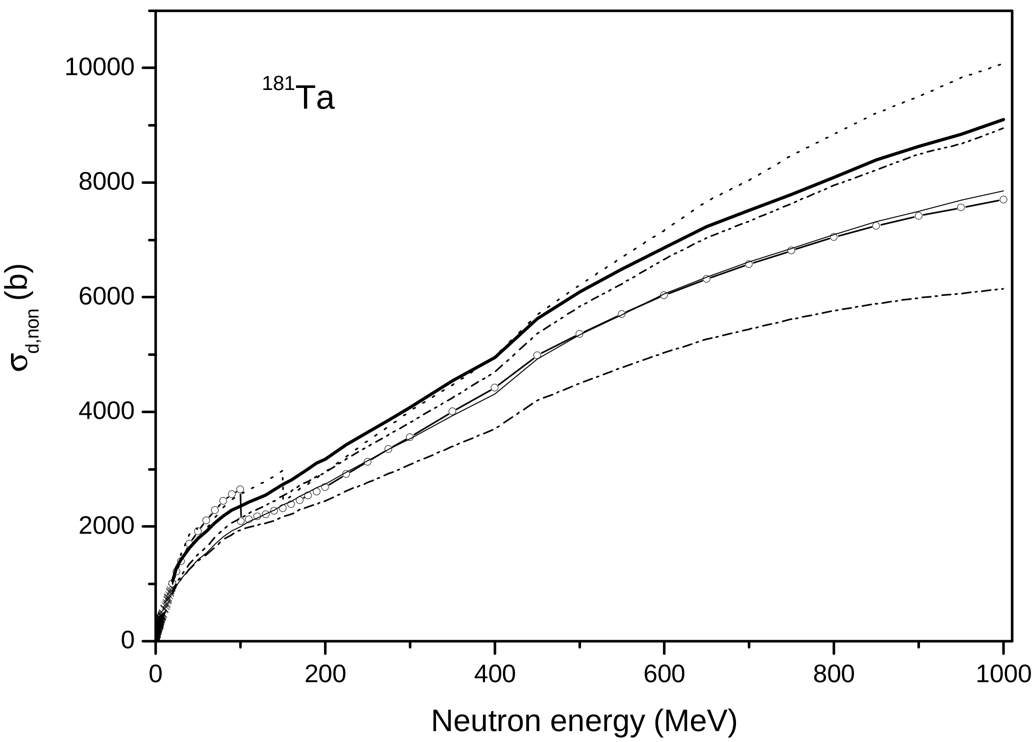

Fig.34 The displacement cross-section for neutron nonelastic interactions with ^{181}Ta at the energies below 1 GeV calculated using the ENDF/B-VI data and the different nuclear models from the MCNPX code. See also captions for Fig.32.

The curve calculated using the INCL4/ABLA model has an unphysical breaks at the neutron energy 100 MeV. The break at 100 MeV has its origin in the intranuclear cascade INCL4 code, because calculations with INCL4/Dresner give the same break at the same energy.

A good agreement is observed between the ENDF/B-VI data and the displacement cross-sections calculated using the MBP/ABLA model for ^{181}Ta at the energy 20 MeV. The same agreement is observed for tungsten at the energies up to 70 MeV.

In general, the difference between the $\sigma_{d,non}$ values obtained with the help of the different models is significant (Fig.34). The ISABEL/Dresner model gives the smallest values of the displacement cross-section comparing with other approaches. The largest values of $\sigma_{d,non}$ correspond to the results obtained by the MBP/ABLA model at the energies from 150 to 450 MeV and to the CEM2k calculations at the energies above 450 MeV.

The $\sigma_{d,non}$ value calculated with the use of the ABLA evaporation model is always larger than the value obtained by the Dresner model. The example is shown in Figs.32-34 for the Bertini/ABLA and Bertini/Dresner calculations. The same difference is observed also for the INCL4 and ISABEL models combined with the ABLA and Dresner models.

It is interesting that the value of the displacement cross-section calculated with the help of the oldest Bertini and Dresner models almost coincides with results obtained by the combination of the newest INCL4 and ABLA models at energies above 100 MeV (Fig.34).

As for a proton irradiation (Section 2.1)observed uncertainty in the neutron $\sigma_{d,non}$ values calculated using different nuclear models (Figs.32-34) can not be overcome at present time. It should be considered as an error of the neutron nonelastic displacement cross-section value obtained theoretically. This error is up to 25 %.

2.2.4.3 Total displacement cross-section for neutron irradiation

The total value of the displacement cross-section σ_d was calculated as a sum of the displacement cross-section for elastic neutron scattering $\sigma_{d,el}$ and the displacement cross-section for the neutron nonelastic interactions $\sigma_{d,non}$.

The $\sigma_{d,el}$ cross-section has been calculated with the help of the optical model with Koning, Delaroche potential [131] at the energies 20-200 MeV. Above 200 MeV the elastic displacement cross-section has been obtained with the help of the Madland potential [134] and by the calculation with the MCNPX code.

The MBP/ABLA model showing the relative success in the description of the experimental data (Section 2.2.2) and the good agreement with ENDF/B-VI (8) has been used to get the $\sigma_{d,non}$ values at the energies from 20 to 80 MeV. At the high energies the nonelastic displacement cross-section has been calculated with the help of the Bertini/Dresner model. The use of this model is consistent with the proton displacement cross-section evaluation for tantalum and tungsten (Section 2.1.1.3) and results in the $\sigma_{d,non}$ values close to ones obtained by the INCL4/ABLA approach.

The cross-sections obtained were adjusted to the ENDF/B-VI (Release 8) data for ^{181}Ta and tungsten isotopes at 20 MeV.

The evaluated total displacement cross-sections σ_d are shown in Table 11 and in Fig.35 at the energies above 20 MeV. Below 20 MeV the σ_d values can be easily obtained from the ENDF/B-VI data with the help of the NJOY code.

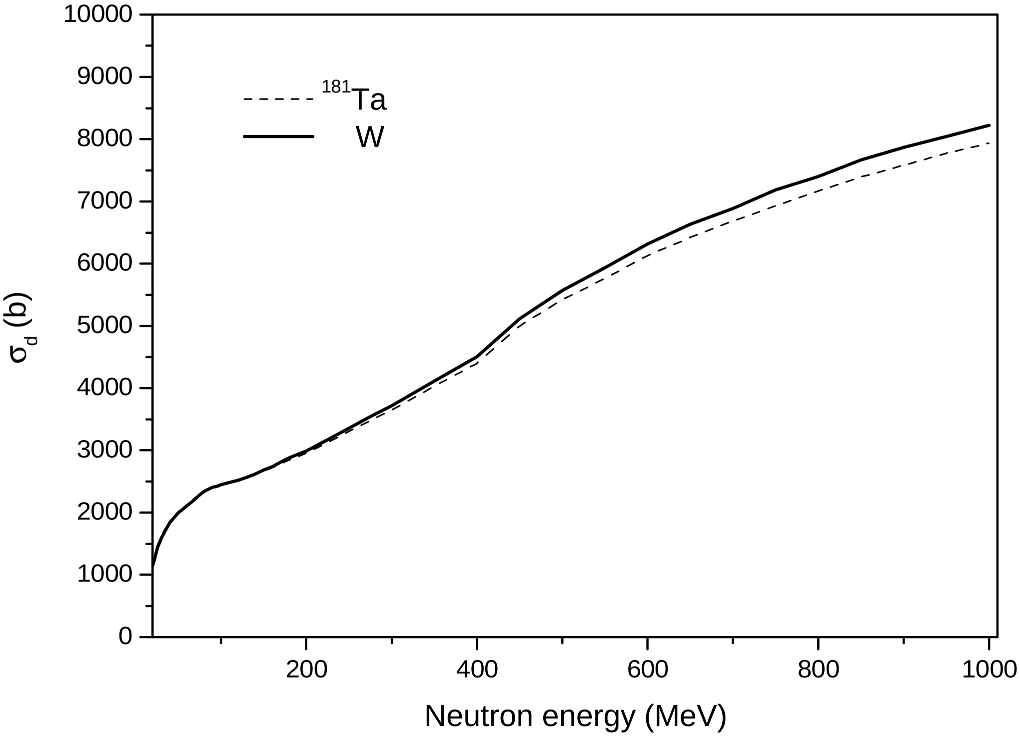

Fig.35 The total displacement cross-sections evaluated for ^{181}Ta (dash line) and natural tungsten (solid line) at the energies above 20 MeV.

Table 11

The total neutron displacement cross-section evaluated for ^{181}Ta and ^{nat}W at the energies up to 1 GeV. The number of defects has been calculated by the NRT model. The effective threshold displacement energy is equal to 90 eV.

Neutron Energy (MeV)	^{181}Ta	^{nat}W
20.	1167.	1147.
22.	1280.	1245.
24.	1398.	1353.
26.	1490.	1442.
28.	1556.	1512.
30.	1622.	1583.
35.	1736.	1712.
40.	1846.	1842.
45.	1924.	1923.
50.	1998.	1995.
55.	2056.	2051.
60.	2111.	2106.
65.	2175.	2164.
70.	2238.	2221.
75.	2287.	2279.
80.	2337.	2337.
85.	2370.	2369.
90.	2404.	2402.
95.	2420.	2422.
100.	2437.	2442.
110.	2490.	2486.
120.	2523.	2522.
130.	2569.	2567.
140.	2608.	2613.
150.	2673.	2684.
160.	2717.	2738.

Table 11 continued

170.	2788.	2813.
180.	2840.	2875.
190.	2903.	2938.
200.	2951.	2986.
225.	3130.	3169.
250.	3305.	3352.
275.	3480.	3544.
300.	3649.	3718.
350.	4027.	4109.
400.	4396.	4503.
450.	5001.	5116.
500.	5421.	5566.
550.	5762.	5934.
600.	6127.	6313.
650.	6418.	6633.
700.	6688.	6882.
750.	6922.	7181.
800.	7164.	7395.
850.	7394.	7665.
900.	7580.	7867.
950.	7771.	8040.
1000.	7937.	8221.

2.2.5 Calculation of neutron displacement cross-section using “BCA” and “MD” models

Detailed information about the number of defects produced under the irradiation, which is necessary for the displacement cross-section calculation at the energies up to 1 GeV, is available for tungsten only.

The calculation of the number of Frenkel pairs in tungsten using the BCA and MD models was discussed above (Section 2.1.2.1).

The displacement cross-sections obtained are shown in Fig.36 at the primary neutron energies from 5 keV up to 1 GeV. For the comparison the displacement cross-section calculated using the NRT model is also shown.

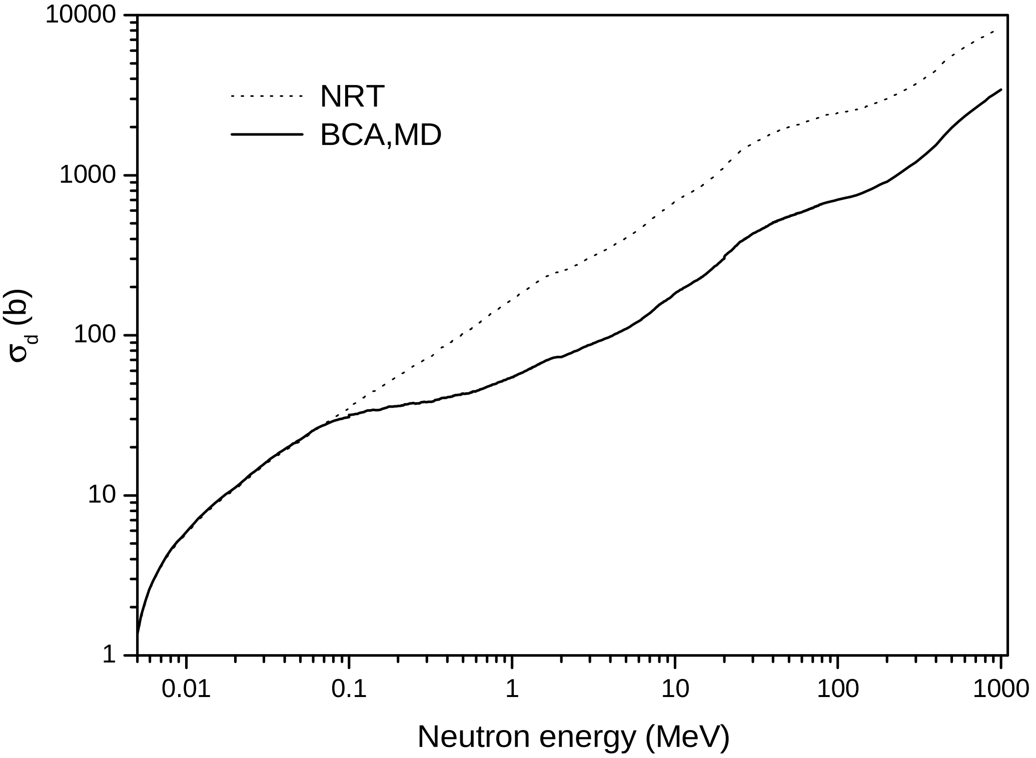

Fig.36 The total displacement cross-section for natural tungsten irradiated with neutrons calculated with the help of the NRT model (dash line) and the BCA and MD models (solid line) at the energies from 5 keV to 1 GeV.

The ratio of the displacement cross-section calculated for natural tungsten with the help of the BCA and MD models to the cross-section obtained by the NRT model can be approximated by the following functions

E ≤ 0.0657 MeV:

$$\sigma_d^{\mathrm{BCA,MD}}/\sigma_d^{\mathrm{NRT}} = 1.0 \qquad (22a)$$

$0.0657 < E \leq 0.9$ MeV:

$$\sigma_d^{\mathrm{BCA,MD}}/\sigma_d^{\mathrm{NRT}} = -3.706 \cdot E^{0.13175} + 0.4825 \cdot E + 3.559 \qquad (22b)$$

$0.9 < E \leq 1000$ MeV:

$$\sigma_d^{\mathrm{BCA,MD}}/\sigma_d^{\mathrm{NRT}} = 3.279 \cdot 10^{-4} \cdot \ln^4(E) - 4.052 \cdot 10^{-3} \cdot \ln^3(E) + 2.291 \cdot 10^{-2} \cdot \ln^2(E) - $$
$$- 5.969 \cdot 10^{-2} \cdot \ln(E) + 0.3245, \qquad (22c)$$

where E is the initial neutron energy in MeV.

Formula, Eq.(22) can be used to recover the realistic values of the displacement cross-section for natural tungsten using the cross-section obtained with the help of the NRT model σ_d^{NRT}. The σ_d^{NRT} values are shown in Table 11 at the energies above 20 MeV. Below 20 MeV the σ_d^{NRT} cross-section is prepared with the help of the NJOY code using the ENDF/B-VI data.

For tantalum the reliable information about the energy dependence of the number of Frenkel pairs produced under the irradiation is absent. Evidently, tantalum and tungsten have fairly similar averaged efficiency values derived from the experimental damage resistivity rates for neutron irradiation (Tables 3,6). Both metals have a bcc lattice, the same effective threshold displacement energy and similar nuclear properties. Nevertheless, it not seems to be a rigorous justification of the use Eq.(22) obtained for tungsten to get the realistic displacement cross-section for tantalum. For tantalum Eq.(22) can be used for a crude approximate evaluation of displacement cross-section only.

2.3 Summary about the computation of displacement cross-sections for tantalum and tungsten and the combined BCA-MD method for the calculation of the number of defects in irradiated materials

A method has been proposed for the calculation of the number of defects in materials irradiated with intermediate and high energy particles. It includes the use of the MD method for the simulation at low ion energies (5 – 50 keV) and the application of the BCA model at higher ion energies. The method was implemented in the IOTA code. The efficiency of defect generation in materials calculated in the present work at high energies shows the substantial difference with the “constant efficiency” approach used by other authors, e.g. in Refs.[14,86].

The displacement cross-section has been obtained for tantalum and tungsten irradiated with protons at energies from several keV up to 1 GeV and with neutrons at energies from 10^{-5} eV to 1 GeV.

The displacement cross-section for proton and neutron elastic scattering has been calculated using the data from ENDF/B-VI and by the optical model with the help of the ECIS96 code. The good agreement was found for the proton $\sigma_{d,el}$ values obtained using various modern optical potentials. For neutrons the agreement is observed for $\sigma_{d,el}$ calculated using the Koning, Delaroche optical potential [131] and the Walter, Guss potential [133] at the energies below 50 MeV. The neutron elastic displacement cross-section obtained by the Koning, Delaroche potential is close to the $\sigma_{d,el}$ value calculated using the Madland optical potential [134] at 140-200 MeV.

The displacement cross-section for the nucleon nonelastic interactions $\sigma_{d,non}$ has been calculated using the MCNPX code package. The total displacement cross-section has been evaluated for tantalum and tungsten at nucleon incident energies up to 1 GeV.

3. ^{4}He production cross-section for heavy nuclei irradiated with neutrons and protons at the energies up to 1 GeV

Popular nuclear models and approaches used for the description of the α-particle emission in the nucleon induced reactions at the intermediate energies were analyzed. The α-particle emission spectra, the non-equilibrium α-particle yields and the total α-production cross-sections were calculated with the help of the GNASH code, the modified ALICE code, the DISCA code and the different codes from the MCNPX package. The results of the calculation were compared with available experimental data, systematics values and data from ENDF/B-VI and JENDL-HE. Data from FENDL/A-2, JENDL-3.3, CENDL-2 and JEFF-3/A were also used for the comparison with calculations and measured data for neutron induced reactions below 20 MeV. The discrepancies between the calculations and the experimental data have been analyzed. The ^{4}He-particle production cross-section has been evaluated for ^{181}Ta, ^{nat}W and ^{197}Au at the energies of the incident neutrons and protons from several MeV to 1 GeV.

3.1 Brief description of models and codes used for ^{4}He production cross-section calculation

3.1.1 Pre-compound model combined with evaporation model

3.1.1.1 The GNASH code

The GNASH code implements the pre-equilibrium exciton model and the statistical Hauser-Feshbach model [186]. The basic description of the code and the models used is given in Ref. [177].

The pre-equilibrium nucleon emission is described by the following expression resulting from an analytical solution of master equations of the exciton model

$$\frac{d\sigma}{d\varepsilon_x}=\sigma_{non}(E_p)\frac{(2S_x+1)\mu_x\,\varepsilon_x\,\sigma_x^{inv}(\varepsilon_x)}{\pi^2\mathbf{h}^3}\sum_{n=n_0}R_x(n)\frac{\omega(p-1,h,U)}{\omega(p,h,E)}\frac{1}{\lambda_n^{+}+\lambda_n^{-}+\gamma_n}D(n)\,,\quad(23)$$

where σ_{non} is the cross-section of nonelastic interaction of the primary particle with a nucleus at the kinetic energy E_p; S_x and μ_x are spin and reduced mass of the outgoing nucleon of x-type; ε_x is the kinetic energy of the nucleon; σ_x^{inv} is the inverse reaction cross-section for x-particle; ω(p,h,E) is the density of exciton states with “p” particles and “h” holes (p+h=n) at the excitation energy E calculated according to Williams [188]; U is the final excitation energy, $U=E-Q_x-\varepsilon_x$ and Q_x is the separation energy for nucleon; λ_n^{+} and λ_n^{-} are transition rates from the n-exciton state to the states with n+2 and n-2 excitons, correspondingly; γ_n is the nucleon emission rate; $R_x(n)$ is the factor describing the difference between the number of neutrons and protons in the n-exciton state; D(n) is the factor, which takes into account the “depletion” of the n-exciton state due to the nucleon emission; n_0 is the initial exciton number. The transition rates λ_n^{+} and λ_n^{-} are calculated as follows

$$\lambda_n^{+/-}=(2\pi/\mathbf{h})<|M|^2>\omega^{+/-}(n,E)\,,\quad(24)$$

where $<|M|^2>$is the averaged squared matrix element for two-body interaction parameterized as the set of functions of E/n in Ref. [188]; $\omega^{+/-}$ is the density of states available for transitions from “n” to “n+2” and “n-2” exciton states calculated according to Refs. [177,189].

The multiple pre-equilibrium emission (two pre-compound nucleons escape) is described according to Ref.[181]. The improvement of the approach [181] is discussed in Ref.[182].

The pre-equilibrium α-particle emission spectrum for nucleon induced reaction is calculated as a sum of components corresponding to the mechanism of pick-up and knock-out

$$\frac{d\sigma}{d\varepsilon_\alpha} = \frac{d\sigma^{\text{pick-up}}}{d\varepsilon_\alpha} + \frac{d\sigma^{\text{knock-out}}}{d\varepsilon_\alpha} \quad , \tag{25}$$

and the components are evaluated according to the phenomenological Kalbach approach [189]

$$\frac{d\sigma^{\text{pick-up}}}{d\varepsilon_\alpha} = \\ (2S_\alpha + 1) A_\alpha \, \varepsilon_\alpha \, \sigma_\alpha^{\text{inv}}(\varepsilon_\alpha) \, \omega_f^{\text{pick-up}}(U) \; f(N, Z, \Delta_\nu, \Delta_\pi) \; (780/A)^3 \; E_p^{-6} \; 2.8 \times 10^{-3}, \tag{26}$$

where S_α and A_α are spin and mass number of the α-particle emitted; A, Z, N are atomic mass number, atomic number and number of neutrons for a target nuclide, respectively; the energy units are MeV; $\omega_f^{\text{pick-up}}$ is the final state density for pick-up process and “f” is the function defined below

$$\omega_f^{\text{pick-up}} = \frac{6}{\Delta_\nu \, \Delta_\pi} \sum_{i=1}^{3} \omega(0, i, U), \tag{27}$$

$$f(N, Z, \Delta_\nu, \Delta_\pi) = (2Z/A)^{6\Delta_\pi} \, (2N/A)^{(1-\Delta_\pi)\Delta_\nu(\Delta_\nu+1)/2} \quad , \tag{28}$$

where Δ_ν and Δ_π are number of neutrons and protons transferred in the pick-up process. The knock-out component of spectrum is calculated as follows

$$\frac{d\sigma^{\text{knock-out}}}{d\varepsilon_\alpha} = \sigma_{\text{non}}(E_p) \times \\ \left(\frac{A+1}{A\,E}\right)^3 (2S_\alpha + 1) A_\alpha \, \varepsilon_\alpha \, \sigma_\alpha^{\text{inv}}(\varepsilon_\alpha) \, \omega_f^{\text{knock-out}}(U) \, f(N, Z, \Delta_\nu, \Delta_\pi) \; A^{-3} \, Z \; 0.06, \tag{29}$$

where the units are mb for the cross-sections and MeV for the energy, $\omega_f^{\text{knock-out}}$ is the final state density for the knock-out process

$$\omega_f^{\text{knock-out}} = g_x\, g_\alpha \left(U - \frac{1}{2g_x} - \frac{1}{2g_\alpha} \right), \qquad (30)$$

here g_x is the single particle density for neutrons and protons depending from projectile, g_n=N/13, g_p=N/13; the level density for α-particle g_α is equal to A/52.

The pre-equilibrium emission of α-particles following the nucleon emission, i.e. the multiple pre-compound α-emission is not considered in the GNASH code.

Equilibrium particle emission is described with the help of the Hauser-Feshbach model. The combination of the exciton model formulated without the consideration of angular momentum, Eq.(23) and the angular dependent statistical model is discussed in Refs.[177,180].

In the present work two different approaches were used for the nuclear level density calculation in equilibrium states. The calculation was done with the help of the Fermi gas model with the nuclear level density parameter depending from the excitation energy [190] and the generalized superfluid model [191].

In the approach of Ignatyuk and coauthors [190] the nuclear level density is described by expressions basing on the Fermi gas model. The nuclear level density parameter is calculated as follows

$$a(U) = \tilde{a}\,\left(1 + \varphi(U)\,\delta W / U\right), \qquad (31)$$

where U is the energy of the excitation corrected for the odd-even difference in the nuclear level density; ã is the asymptotic value of the nuclear level density parameter; δW is the shell correction to the mass formula equal to the difference between experimental mass defect and one calculated from the liquid drop model; φ(U) is the dimensionless function equal to

$$\varphi(U) = 1 - \exp(-\gamma\, U), \qquad (32)$$

with γ = 0.054 MeV^{-1}. The asymptotic value ã is defined by the equation

$$\tilde{a} / A = \alpha + \beta\, A, \qquad (33)$$

where α and β are parameters defined in Ref.[177] α = 0.1375 and $\beta = -8.36\times10^{-5}$, which values are different from ones obtained in the original work [190]. This model is used for the calculation of the nuclear level density at high excitation energy. At low energy of excitation the constant temperature approach [177] is applied for the calculations.

Other model used for the nuclear level density calculation is the generalized superfluid model with the parameters fitted to the cumulative number of low-lying levels and observed neutron resonance densities [191]. The expression for nuclear level density is written as follows

$$\rho(U,J,\pi)=\rho_{qp}(U',J,\pi)\,K_{vib}(U')\,K_{rot}(U')\,, \qquad (34)$$

where $\rho_{qp}(U',J,\pi)$ is the density of quasi-particle nuclear excitation [191], $K_{vib}(U')$ and $K_{rot}(U')$ are the vibrational and rotational enhancement factors at the effective energy of excitation U' calculated according to Refs. [191,192].

The nuclear level density parameters are calculated according to the expression [191,193]

$$a(U)=\begin{cases}\tilde{a}\left(1+\delta W\varphi(U'-E_{cond})/(U'-E_{cond}\right), & U'>U_{cr}\\ a(U_{cr}), & U'\le U_{cr}\,,\end{cases} \qquad (35)$$

where the effective energy of excitation U', the critical energy of the phase transition U_{cr} and the condensation energy E_{cond} are calculated according to Refs.[191,193]. The function $\varphi(U)$ is defined by Eq.(32) with the γ value equal to $0.4/A^{1/3}$ MeV^{-1}. The asymptotic value of the nuclear level density parameter is equal to

$$\tilde{a}/A=\alpha+\beta A^{-1/3}, \qquad (36)$$

where α and β are coefficients obtained in Ref.[194] from the fitting of Eq.(36) to the RIPL-1 data [195], α = 0.118 and $\beta = -0.172$.

The calculation of the nuclear level density with the help of the Fermi gas model [190] was carried out by the GNASH built-in routines. The constant temperature and

Fermi gas expressions for the level density were matched approximately, which corresponds to the input parameter IBSF controlling the level density option equal to 2. The generalized superfluid model [191,193] is used in modified version of the GNASH code [182,194,196].

The neutron and proton optical potential from Ref. [131] was used for the calculation of the reaction cross-section and transmission coefficients. The transmission coefficients for α-particles were obtained with the help of the optical potential from Ref.[197]. The calculations were carried out by the ECIS96 code [141].

3.1.1.2 The ALICE/ASH code

The code is based on the geometry dependent hybrid pre-compound decay model [198,199] (GDH) and the evaporation Weisskopf-Ewing model [200]. The ALICE/ASH code is an advanced version of the original M.Blann code [201]. Partly, the modification is described in Refs.[202,203]. It concerns the implementation in the code the models describing the pre-compound composite particle emission [204-206] and fast γ-emission [207], different approaches for the nuclear level density calculation [202,203,208] and the model for the fission fragment yield calculation [209,194].

The code under different names [202,203] was successfully used for the preparation of activation data libraries at intermediate energies MENDL [210,208, 211], IEAF [212-214] and WIND [213,215-217]. The neutron, charged particle, photon and recoil spectra applied for the composition of nuclear data files, the transport and heat deposition calculations [176,213,218] have been obtained with the help of the code. ALICE/ASH has been used for the description of the heavy cluster pre-compound emission [219] and for the calculation of fission fragment distributions for actinides irradiated with nucleons at intermediate energies [182,194,196].

In the GDH model the pre-equilibrium spectrum of nucleons is calculated as follows [199]

$$\frac{d\sigma}{d\varepsilon_x} = \pi \mathbf{D}^2 \sum_{l=0}^{\infty} (2l+1) T_l \sum_{n=n_0} R_x(n) \frac{\omega(p-1,h,U)}{\omega(p,h,E)} \frac{\lambda_x^e}{\lambda_x^e + \lambda_x^+} g\, D(n), \qquad (37)$$

where $\mathbf{D}$ is the reduced de Broglie wavelength of the incident particle; T_l is the transmission coefficient for l-th partial wave; $R_x(N)$ is the number of nucleons of x-type in the n-exciton state calculated according to Ref.[199]; g is the single particle level density equal to A/14; λ_x^e is the emission rate of nucleon calculated with the following formula

$$\lambda_x^e = \frac{(2S_x + 1)\, \mu_x\, \varepsilon_x\, \sigma_x^{inv}(\varepsilon_x)}{\pi^2\, \mathbf{h}^3\, g_x}, \qquad (38)$$

where the single particle density g_x is equal to Z/14 for protons and N/14 for neutrons. The intranuclear transition rate λ_x^+ is defined as follows

$$\lambda_x^+ = V \sigma_0(\varepsilon_x)\, \rho_l, \qquad (39)$$

where V is the velocity of nucleon inside the nucleus; σ_0 is the nucleon-nucleon scattering cross-section corrected for the Pauli principle; ρ_l is the average nuclear density at the distance from $l\mathbf{D}$ to $(l+1)\mathbf{D}$.

For the initial nuclear state with three excitons the density of the excited states $\omega(p,h,E)$ is calculated by the model [220] considering the final depth of the nuclear potential well. The multiple pre-compound emission is described by the approximate approach [199]. As in the GNASH code, only two fast particles escape is considered. The correction made for the high energy tails of (p,x)n and (n,x)p reaction spectra calculated by the GDH model is discussed in Ref.[213].

The pre-equilibrium α-particle emission spectrum is calculated as a sum of components corresponding to the mechanism of pick-up and knock-out, Eq.(25). The models used here are rather different from ones implemented in the GNASH code.

The contribution of the pick-up mechanism is calculated with the help of the coalescence pick-up model [221,222] combined with the hybrid exciton model [204]

$$\frac{d\sigma^{pick-up}}{d\varepsilon_\alpha} = \sigma_{non}(E_p) \sum_{n=n_0} \sum_{k+m=4} F_{k,m}(\varepsilon_\alpha) \frac{\omega(p-k,h,U)}{\omega(p,h,E)} \frac{\lambda^e_\alpha(\varepsilon_\alpha)}{\lambda^e_\alpha(\varepsilon_\alpha)+\lambda^+_x(\varepsilon_\alpha)} g_\alpha D(n), \quad (40)$$

where $F_{k,m}(\varepsilon_\alpha)$ is the alpha formation factor [221] equal to the probability that the of α-particle is composed of “k” particles above Fermi level and “m” particles below; the residual excitation energy U is equal to E – Q_α–ε_α; λ^e_α is the emission rate of α-particle; λ^+_α is the intranuclear transition rate corresponding to the absorption of α-particle in a nucleus; g_α is the density of single states for α-particle. The emission rate of α-particle is calculated with the following formula

$$\lambda^e_\alpha = \frac{(2S_\alpha+1)\mu_\alpha\,\varepsilon_\alpha\,\sigma^{inv}_\alpha(\varepsilon_\alpha)}{\pi^2\,\mathbf{h}^3\,g_\alpha}, \quad (41)$$

and the inverse reaction cross-section for α-particle $\sigma^{inv}_\alpha(\varepsilon_\alpha)$ is calculated by the optical model with the parameters described in Ref. [23]. The absorption rate of α-particle is defined as follows

$$\lambda^+_\alpha = 2W^{opt}_\alpha/\mathbf{h}, \quad (42)$$

where W^{opt}_α is the imaginary part of the optical potential for α-particle.

The knock-out contribution to the α-particle spectrum is calculated with the following expression [205]

$$\frac{d\sigma^{knock-out}}{d\varepsilon_\alpha} = \sigma_{non}(E_p) \sum_{n=n_0} \varphi_\alpha \frac{g}{g_\alpha p} \frac{\omega(p-1,h,U)}{\omega(p,h,E)} \frac{\lambda^e_\alpha(\varepsilon_\alpha)}{\lambda^e_\alpha(\varepsilon_\alpha)+\lambda^+_x(\varepsilon_\alpha)} g_\alpha D(n), \quad (43)$$

where the factor $g/(g_\alpha p)$ justifies the substitution of the level density $\omega(\pi,\tilde{\pi},\nu,\tilde{\nu},\alpha,\tilde{\alpha},E)$ for the three-component system (neutron, proton, α-particle) [223,205] by the one-component state density $\omega(p,h,E)$ in Eq.(43); φ_α is the probability of interaction of the incident particle with “pre-formed” α-cluster resulting in its excitation in the nucleus [223].

The pre-compound α-emission after the pre-compound escape of neutrons and protons (multiple pre-equilibrium emission) is taken into account [205]. The formula for the calculation of the pre-compound emission spectrum of α-particle formed due to the nucleon pick-up process and escaped after the pre-equilibrium nucleon emission is written as follows

$$\frac{d\sigma}{d\varepsilon_\alpha} = \pi \mathbf{D}^2 \sum_{l=0}^{\infty} (2l+1) T_l \sum_{x=\pi,\nu}^{2} \int_{E_x^{min}}^{E_x^{max}} \sum_{n=n_0} R_x(n) \frac{\omega(p-1,h,E-Q_x-\varepsilon_x)}{\omega(p,h,E)} \frac{\lambda_x^e(\varepsilon_x)}{\lambda_x^e(\varepsilon_x)+\lambda_x^+(\varepsilon_x)} \, g \, D(n)$$
$$\times \sum_{n'=p+h-1} \sum_{k+m=4} F_{k,m}(\varepsilon_\alpha) \frac{\omega(p'-k,h',E-Q_x-\varepsilon_x-Q'_\alpha-\varepsilon_\alpha)}{\omega(p',h',E-Q_x-\varepsilon_x)} \frac{\lambda_\alpha^e(\varepsilon_\alpha)}{\lambda_\alpha^e(\varepsilon_\alpha)+\lambda_x^+(\varepsilon_\alpha)} \, g_\alpha \, D(n') \, d\varepsilon_x \tag{44}$$

where “x” refers to proton and neutron; Q'_α is the separation energy for α-particle in the nucleus formed after the emission of nucleon of x-type; E_x^{min} and E_x^{max} define the energy range, where the emission of the x-particle occurs. The analogous formula is written for α-particle knock-out process following the fast nucleon emission [205]. The successive emission of three and more pre-equilibrium particles is not considered.

The following parameters of the models were used for the calculations: $\sum_{k+m=4} F_{k,m} = 0.3$ and φ_α =0.012. The imaginary part of the optical potential for α-particle was calculated as follows W_α^{opt} = $(\varepsilon_\alpha/\varepsilon_0)$W’ at $\varepsilon_\alpha \le \varepsilon_0$, W_α^{opt} = W’ at $\varepsilon_0 < \varepsilon_\alpha <$ 72 MeV, and W_α^{opt} = W’·exp(0.06ε_α – 4.32) at $\varepsilon_\alpha \ge$ 72 MeV, where W’ = βW_0 and ε_0=0.228A, β=0.25. The value of W_0 was taken from Refs.[224,225], W_0=10 +0.345(A–2Z) MeV. The values of the parameters listed above are from Refs.[202, 203] except the W_α^{opt} value calculation at the energy ε_α above 72 MeV. The adopted value of the single state density for α-particle is equal to A/13 (see discussion in Ref. [203]).

Principally the same models used in the GNASH calculations were applied to the nuclear level density calculation. In a difference with Section 3.1.1.1, the asymptotic value of the level density parameter in the Fermi gas model [10] was defined with α and β coefficients obtained in the original work [190] $\alpha = 0.154$ and $\beta = -6.3\times10^{-5}$. The model [190] was used at the high excitation energy of nuclei. At low excitation energy the “constant temperature” approach [201] was applied. In calculations using the superfluid model the systematics values of parameters [193,203,208] were used rather than the individual parameter values [191]. The asymptotic value of nuclear level density parameter was calculated as follows [193, 203,208] $\tilde{a}/A = 0.073 + 0.115\, A^{-1/3}$.

3.1.2 Intranuclear cascade evaporation model describing cascade a-cluster emission

3.1.2.1 The DISCA-C code

DISCA-C is the first code, which implements the intranuclear cascade evaporation model describing the interaction of particles with pre-formed clusters and their emission in nuclear reactions induced by projectiles of intermediate energy [162]. The code was used for the calculation of energy and angular distributions of α-particles, the (p,xnypzα) reaction cross-sections and other applications. The brief description of the model is given in Refs. [151,226].

In the model the nucleus is broken up into ten concentric zones with uniform density. The radius of the outermost zone is estimated by the condition that the nucleon density in this region being 0.01 of that in the nucleus center. The nuclear density for medium and heavy nuclei ($A > 16$) is estimated by Woods-Saxon function. The momentum distribution for nucleons for each zone is defined according to Fermi gas model. It is supposed that besides of nucleons the nucleus consists of “pre-formed” clusters tritons, ^{3}He nuclei and α-particles. The deuteron clusters are not considered. Maximum kinetic energy of clusters, i.e. the Fermi energy, and their potentials are defined by following relations

$$T^F_{\alpha,i} = 4T^F_{n,i}, \quad T^F_{t,i} = T^F_{h,i} = 3T^F_{n,i}, \tag{45}$$

$$U_{\alpha,i} = T^F_{n,i} + Q_\alpha, \quad U_{ti} = T^F_{t,i} + Q_t, \quad U_{h,i} = T^F_{h,i} + Q_h, \tag{46}$$

where $T^F_{n,i}$ is the Fermi energy for nucleon in i-th nuclear zone; $T^F_{t,i}$, $T^F_{h,i}$ and $T^F_{\alpha,i}$, are the Fermi energy for tritons, ^{3}He and α-particles, respectively; Q_z is the separation energy calculated from the experimental nuclide masses, z=t, ^{3}He and α; $U_{z,i}$ is the nuclear potential for each type of particles. According to Ref.[227] the momentum distributions for tritons, ^{3}He and α-particles are taken as

$$N_t(\mathbf{p}_t)\,d\mathbf{p}_t = N_h(\mathbf{p}_h)\,d\mathbf{p}_h \propto p^6\,dp\,d\Omega \tag{47}$$

and

$$N_\alpha(\mathbf{p}_\alpha)\,d\mathbf{p}_\alpha \propto p^8\,dp\,d\Omega \tag{48}$$

The definition of the point of the intranuclear interaction and partner characteristics is discussed in detail in Ref.[226].

For a nucleon “x” moving inside the nucleus with the kinetic energy T, the probability of the interaction with nuclear matter is calculated as follows

$$Q_i = \rho_i\left(\varphi_n\sigma^{xn}(T) + \varphi_p\sigma^{xp}(T) + \varphi_\alpha\sigma^{x\alpha}(T) + \sigma^x_{p-u}(T)\right), \tag{49}$$

where ρ_i is the nucleon density in the i-th zone; σ^{xn} and σ^{xp} are cross-sections for the interactions with intranuclear neutron and proton, correspondingly; $\sigma^{x\alpha}$ is the cross-section for interaction with pre-formed α-cluster; σ^x_{p-u} is the cross-section for the pick-up process combining the nucleon of x-type and pre-formed triton or ^{3}He cluster to form an α-particle; φ_n, φ_p and φ_α are relative numbers of neutrons, protons and α-clusters in the nucleus. A value of φ_α adopted in the present work is equal to 0.05. Values φ_n and φ_p are calculated from the total number of nucleons and the φ_α value.

For excited α-particles, the elastic scattering and break-up processes in the interactions with intranuclear nucleons are considered. The approximations from Refs.[149,226] are used for calculating the nucleon- nucleon and nucleon- α-particle interaction cross-sections. The energy dependence of the pick-up cross-section $\sigma^x_{p-u}(T)$ is defined according to the form-factor $F_{1,3}$ calculated in Ref.[221], which corresponds to the formation of the α-particle from three nucleons with energy below the Fermi energy and one nucleon with energy above the Fermi energy. The cross-section is equal to

$$\sigma^x_{p-u}(T) = \varsigma\left(-1{,}011\times10^{-6}\varepsilon^3 + 1{,}748\times10^{-4}\varepsilon^2 - 1{,}128\times10^{-2}\varepsilon + 0{,}275742\right)/(R\,\rho_i)\,, \quad (50)$$

where $\varepsilon = T - T^F_{n,i}$ ($\varepsilon < 67$); $R = 1.25\ A^{1/3}$; ζ is the fitting parameter equal to 14 in the present work. The angular distribution for nucleon-nucleon and nucleon- α-particle scattering is calculated with the help of the formulas from Refs.[151,226,228].

The reflection and refraction of particle momenta on the nuclear zone boundaries is considered. The Pauli principle is taken into account as for nucleon-nucleon, as for nucleon-α- collisions. In an addition, the restriction on the orbital momenta of nucleons after the interaction [184] is considered. According to Ref.[229] the orbital momenta *l* of nucleons colliding within the square potential well should not exceed the product of asymptotic nucleon momentum and the nucleus radius: $l \le p_a R$, where p_a is the linear momentum the nucleon would have outside the nucleus, R is the nucleus radius. This restriction on *l* results from the fact that the nucleus has no states below the centrifugal barrier [229]. For a multi-zone nuclear density model, the restriction on the orbital momenta of nucleons colliding in the i-th zone has the form

$$l_i \le p_{i+1} R_i, \quad (51)$$

where l_i is the orbital momentum of the nucleon with momentum p_i in the i-th zone; p_{i+1} is the momentum the nucleon would have in the i+1-th zone (the zones are numbered beginning from the nucleus center); R_i is the radius of the i-th zone in which the two nucleons collide.

The restriction on the orbital momenta, superimposed by Eq.(51), reduces the total number of intranuclear interactions, which results to an increase in the emission of high energy particles from the nucleus [184,229]. The calculations show [184] that use of Eq.(51) along with the Pauli principle and with the consideration of reflection/refraction effects on nuclear zone boundaries improves substantially the agreement with experimental data at low and intermediate energies of primary particles.

The majority of computer codes based on the intranuclear cascade evaporation model, e.g. the codes included in the MCNPX package [142], disregard condition Eq.(51). To some extent the effect can be compensated by the neglect the refraction and reflection of the particle momentum at the boundary of nuclear zones (default MCNPX option). However, such neglect is not physically well-founded [229].

The equilibrium particle emission is described by the Weisskopf-Ewing model [200]. The nuclear level density is calculated according to the Fermi gas model

$$\rho(U) = (1/12)\pi^{1/2}a^{-1/4}U^{-5/4}\exp(2\sqrt{aU}) \tag{52}$$

at the high excitation energy U and by the “constant temperature” model at low energy of excitation. The value of the nuclear level density parameter is taken equal to A/9. The inverse reaction cross-sections are calculated according to phenomenological formulas from Ref.[230] approximating the results of optical model calculations. Evaporation is considered for neutrons, protons, deuterons, tritons, ^{3}He nuclei and α-particles.

3.1.2.2 The DISCA-S code

DISCA-S is the simplified version of the DISCA code. The simulation of processes involving α-clusters is not performed. The model used for the description of nucleon-nucleon interactions is discussed in Refs. [151,184,231]. The code was successfully used for the calculation of activation and transmutation cross-sections [232,233], atomic displacement cross-sections [234], complex particle production cross-sections [235,236], energy and angular distributions of nucleons [184,231].

The yield of composite particles emitted during the cascade stage of reaction is described by the nuclear bond breakdown approach [237]. According to Ref.[237] the fragment "x" formation cross-section is equal to

$$\sigma_x^{casc}(E_p)=\sigma_{non}(E_p)\ N_0\ (A/A_x)\ (N_{casc}/A)^{m_0\varepsilon}\ , \tag{53}$$

where $\sigma_{non}(E_p)$ is the nonelastic cross-section for the interaction of the primary particle with kinetic energy E_p and a nucleus; A_x is mass number of the fragment; A is the mass number of target nucleus; N_{casc} is the average number of nucleons emitted from nucleus on the cascade stage of the reaction; $\varepsilon = Q_x+V_x$, where Q_x is the separation energy for the fragment in the nucleus; V_x is the Coulomb potential for the fragment; N_0 and m_0 are parameters. The values of parameters obtained in Ref. [235] for the α-particle emission are used in the present work, $N_0 = 0.12$ and $m_0 = 0.06$. The Coulomb potential V_x is calculated as 0.21Z+2.5 MeV, where Z is atomic number of the target nucleus.

The nuclear density distribution is calculated as in the DISCA-C code. The Pauli principle and the restriction on the orbital momenta, Eq.(51) are checked for each intranuclear interaction. The refraction and reflection of nucleon momentum are considered at the nuclear zone boundaries.

The nuclear level density for equilibrium states is calculated with the approximate formula $\rho(U) = C\exp(2\sqrt{aU})$, where a=A/9. The inverse reaction cross-section for neutrons is calculated according to Ref.[238]. The “sharp cut-off” formulas from Ref.[201] are used for the calculation of the inverse reaction cross-sections for charged particles.

3.1.3 Intranuclear cascade model combined with pre-equilibrium exciton model and evaporation model

The section makes an outline of nuclear models used in the MCNPX code package [142] for the description of particle interactions with nuclei. Four intranuclear cascade models are implemented in MCNPX: Bertini [143,144], ISABEL [147-149], CEM2k [150-156,239] and INCL4 [157,158]. Except INCL4, the models are combined with the pre-equilibrium exciton model and with the evaporation model. Namely first three models (Bertini, ISABEL and CEM2k) describe fast complex particles emission with the help of the exciton model. The approach [240] proposed for the light cluster emission description by authors of the INCL4 model is not implemented in MCNPX yet. It is not discussed here, although the INCL4 model combined with the evaporation model is used for the comparison with the experimental data in Section 3.2.3.

3.1.3.1 The Bertini and ISABEL modules of MCNPX

The brief overview of the models is given in Ref.[241]. As typical intranuclear cascade models, Bertini and ISABEL underestimate the angular distribution of secondary nucleons at high emission angles. The necessity to solve this problem by the consideration of the nucleon and pre-formed cluster interactions was mentioned thirty years ago [242]. It is not done yet. To improve the agreement between calculations and experimental data the pre-equilibrium exciton model algorithm [138,159] has been added to intranuclear cascade models. The basic expressions for the calculation of pre-equilibrium particle emission spectra have been obtained from the analytical solution of master equations describing the evolution of excited nucleus. The pre-equilibrium emission rate for the α-particle leaving the exciton state (p,h) with the excitation energy E is calculated as follows [159]

$$W_\alpha(\varepsilon_\alpha, p, h, E) = \frac{(2S_\alpha + 1)\mu_\alpha \varepsilon_\alpha \sigma_\alpha(\varepsilon_\alpha)}{\pi^2 \mathbf{h}^3} \frac{\omega(p-4, h, E - Q_\alpha - \varepsilon_\alpha)}{\omega(p, h, E)} F_\alpha \qquad (54)$$

where the factor F_α defines the probability of the α-particle formation.

Eq.(54) relates to the first pre-equilibrium model for complex particle emission formulated by Kalbach-Cline [243]. The model has been analyzed and criticized in Ref.[244]. From the formal point of view, the consideration of the final nuclear state corresponding to the α-emission as with the n–4 excitons and the use of the energy independent α-formation probability factor result in too low emission rates for α-particles comparing with experimental data [244].

The equilibrium particle emission is described by the Dresner approach [163] and by the advanced ABLA model [164]. They are used in a various combination with the Bertini and ISABEL intranuclear cascade models. Dresner and ABLA implement different models for the nuclear level density calculation. Both models are based on the simplified approaches for the calculation of particle emission widths and inverse reaction cross-sections. Simplifications are made to get analytical expressions for the widths avoiding the integration of emission rates during the simulation of the particle evaporation cascade. Their justifications can be made from the thorough comparison of results of the calculation with experimental data.

In the calculations discussed below intranuclear cascade models are always used together with the pre-equilibrium and evaporation models. An indication on the cascade model “Bertini” and “ISABEL” implies also the application of the pre-compound exciton algorithm describing the de-excitation of residual nuclei formed after the fast particle emission.

The present calculations are based on the default set of input parameters of the models, which are described in Refs.[142,245].

3.1.3.2 The CEM2k module of MCNPX

The Cascade Exciton Model (CEM) implemented in the MCNPX was a first model [152] combining the intranuclear cascade evaporation model and the pre-equilibrium exciton model. Later such combination was applied for many codes [162].

The nuclear density distribution is approximated in CEM by the step function with seven nuclear regions of the uniform density. The refraction and reflection effects for nucleon momentum are not considered as in calculations with the Bertini and ISABEL models using the default set of the input MCNPX parameters. New approximation for elementary cross-sections is used for the intranuclear event simulation. Many refinements and improvements of the model including the description of momentum-energy conservation on the cascade stage of reaction and new systematics for the level density parameters are discussed in Ref.[156].

The pre-equilibrium exciton model employed after the simulation of the cascade stage of reaction is described in Refs.[152,162]. The pre-equilibrium emission rate for α-particles is calculated according to the “coalescence” model proposed by Ribanský, Obložinský [244]

$$
\begin{aligned}
W_\alpha(\varepsilon_\alpha, p, h, E) = {} & \frac{(2S_\alpha + 1)\mu_\alpha \varepsilon_\alpha \sigma_\alpha(\varepsilon_\alpha)}{\pi^2 \hbar^3} \gamma_\alpha \frac{\omega(4, 0, \varepsilon_\alpha + Q_\alpha)}{g_\alpha} \\
& \times \frac{\omega(p-4, h, E - Q_\alpha - \varepsilon_\alpha)}{\omega(p, h, E)} R_\alpha
\end{aligned}
\qquad (55)
$$

where γ_α is the formation probability for the α-particle; R_α is the factor providing the correct combination of protons and neutrons to form outgoing α-particle [244]. The values of γ_α and R_α are evaluated theoretically. The approach [244] is analyzed in Ref. [221].

3.1.4 Systematics

Systematics is a useful tool for the evaluation of nuclear reaction cross-sections in case experimental data are absent and theoretical calculations are not reliable. A set of systematics is used in the present work for the evaluation of α-particle production cross-section for proton and neutron induced reactions.

3.1.4.1 Proton induced reactions

The α-particle production cross-section is evaluated at the primary proton energies equal to 18, 62, 90, 160 and 600 MeV as follows

E_p= 18 MeV, $Z \geq 60$ $\sigma_\alpha = \pi r_0^2 (A^{1/3} + 1)^2 A^{-5.42} (-4991\cdot P+2252)^3$, (56)

E_p= 62 MeV, $Z \geq 6$ $\sigma_\alpha = 183.05 \exp(-7.578\cdot R)$ mb, (57)

E_p= 90 MeV, $Z \geq 13$ $\sigma_\alpha = 245.85 \exp(-4.9572\cdot R)$ mb, (58)

E_p= 160 MeV, $Z \geq 12$ $\sigma_\alpha = 226.7 \exp(-0.01047\cdot Z)$ mb, (59)

E_p= 600 MeV, $Z \geq 26$ $\sigma_\alpha = 537\cdot Z^{-0.102}$ mb, (60)

where Z and A are the atomic number and the atomic mass number of target nucleus; r_0=1.3 fm; $P = (A-2\cdot Z+0.5)/A$; $R= (A-2Z)/A$. Eq.(56) refers to the (p,α) cross-section rather than to the α-particle production cross-section. Eq.(59) and Eq.(60) were obtained for natural mixtures of isotopes.

Eq.(56) was obtained using the (p,α) cross-section for five nuclei from ^{150}Nd to ^{176}Yb measured at 18 MeV and for ^{197}Au measured at 18.4 MeV in Ref.[246]. The cross-section for ^{197}Au at 18 MeV was estimated basing on the excitation function for the (p,α) reaction calculated by GNASH and fitted to the measured cross-section at

18.4 MeV. Eq.(57) and Eq.(58) have been obtained in Ref.[194] with the help of experimental data from Ref.[247] for eight nuclei from ^{12}C to ^{209}Bi at 62 MeV, and from Ref.[248] for four nuclei from ^{27}Al to ^{209}Bi at 90 MeV. The systematics at 160 MeV, Eq.(59) was produced using the measured cross-sections for Mg, Al and Si from Ref.[249], for Fe from Refs.[250,251], for Ni from the compilation Ref.[151], for Ag, Au and Bi from Ref.[252] and for Th from Refs.[253,254]. Data from Ref.[255], which seem incomplete, were not included in the analysis. The necessary interpolation and extrapolation of data from Refs.[249,151] for Mg, Al, Si and Ni were done to get the cross-section values at the proton energy 160 MeV. The α-particle production cross-sections measured in Refs.[256,257] for Fe, Ni, Ag, Pb and Bi were used to derive Eq.(60). The cross-section for Cu at 600 MeV equal to 575 mb [151] essentially different with other measurements [256,257] was not included in the analysis.

One should note that Eqs.(56)-(60) have been obtained using a few numbers of experimental points. These formulas can be used only for a crude estimation of α-particle production cross-section.

3.1.4.2 Neutron induced reactions

A theoretical formula for the evaluation of the (n,α) reaction cross-section has been derived in Refs.[258,259] using basic expressions for the particle emission spectrum of the pre-equilibrium exciton and evaporation models. The parameters of the formula were obtained from the fitting to the (n,α) reaction cross-sections measured for 120 nuclei with $A \geq 39$ at the neutron energy of 14.5 MeV [258]. The formula is

E_n= 14.5 MeV,

$18 \leq Z \leq 50$

$$\sigma(n,\alpha) = \pi r_0^2 (A^{1/3} + 1)^2 \exp(-209.11 \cdot S^2 + 8.4723 \cdot P - 0.19253 \cdot Z/A^{1/3} - 0.96249), \quad (61a)$$

$Z > 50$

$$\sigma(n,\alpha) = \pi r_0^2 (A^{1/3} + 1)^2 (-1.6462 \cdot P + 0.39951)^3, \qquad (61b)$$

where Z and A are the atomic number and the atomic mass number of target nucleus; r_0=1.3 fm; $P = (A-2\cdot Z+0.5)/A$, $S= (A-2Z+1)/A$.

At the neutron energy of 20 MeV the parameter values of the systematics for the (n,α) reaction cross-section have been obtained using the results of theoretical calculations [259]

E_n= 20 MeV,

$18 \leq Z \leq 50$

$$\sigma(n,\alpha) = \pi r_0^2 (A^{1/3} + 1)^2 \exp(-37.317\cdot S^2 - 7.2027\cdot P - 0.22669\cdot Z/A^{1/3} - 2.027)\,, \qquad (62a)$$

$Z > 50$

$$\sigma(n,\alpha) = \pi r_0^2 (A^{1/3} + 1)^2 (-0.86267\cdot P + 0.26976)^3 \qquad (62b)$$

Eq.(61) and Eq.(62) are used in the present work for the (n,α) reaction cross-section evaluation.

3.1.5 *Nonelastic interaction cross-sections*

To exclude the difference in the calculated α-particle production cross-sections caused by the use of different reaction cross-sections (σ_{non}) the calculations with the help of the GNASH, ALICE/ASH, DISCA and MCNPX codes were performed with the same nonelastic reaction cross-section for a certain nucleus under investigation. The adopted σ_{non} values were taken from ENDF/B-VI, calculated with the help of the optical model with the potential from Ref.[131] or obtained from the MCNPX calculations.

3.2 Comparison of calculations with experimental data

The available experimental data for ^{197}Au give detail information about the total and differential cross-sections for the α-particle production. These data are used for the comparison with results of the calculation.

3.2.1 Energy distribution of a-particles emitted

The experimental energy distribution of emitted α-particles is an information, which is suitable for comprehensive test of nuclear models describing the complex particle emission.

Fig.37 shows the α-particle emission spectra for p+^{197}Au reaction measured in Refs.[260,261] and calculated with the help of the GNASH code and by the ALICE/ASH code at the primary proton energy 72.3 and 200 MeV. Experimental double differential cross-sections for the α-particle emission for the reaction induced by the 200 MeV protons [261] were angle integrated to get the energy distribution. The calculation of the α-particle emission spectra was done with the help of different models for the nuclear level density calculation [190,191,193].

Rather good agreement is observed between the pre-equilibrium α-spectrum calculated with the help of the ALICE/ASH code and experimental data. The GNASH code underestimates the α-particle emission spectrum at the energies after the evaporation peak and strongly overestimates the spectrum at high emission energies. The use of different models for nuclear level density calculation results in a considerable difference in the description of the evaporation spectrum. The calculation using GNASH and ALICE/ASH using the superfluid nuclear model overestimates the equilibrium part of the spectrum comparing with experimental data. Most probably, it is caused by the lack of nuclear level density parameters derived from experimental data and by the use of global systematics to get the parameter values for many residual nuclei. The use of the Fermi gas model [190] results in too much low values of the evaporation spectrum (upper Fig.37) calculated by the ALICE/ASH code.

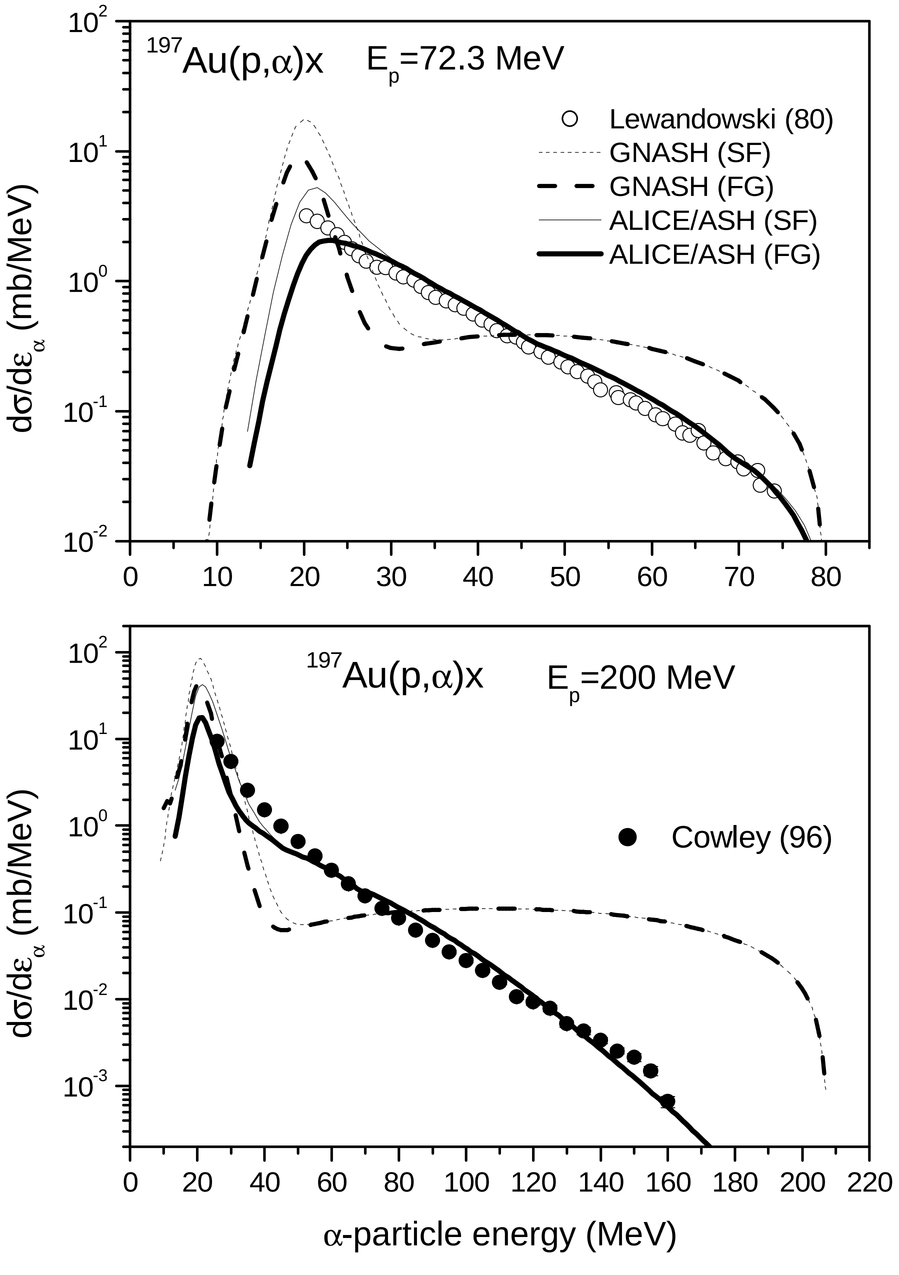

Fig.37 The α-particle emission spectra for p+^{197}Au reaction induced by protons with the energy 72.3 and 200 MeV calculated with the help of the GNASH code and the ALICE/ASH code using different models for the description of the nuclear level density: the Fermi gas model [190] (FG) and the generalized superfluid model (SF). The measured data are from Refs.[260,261].

A reasonable description of the measured evaporation peak in the α-particle spectrum and the experimental total α-particle yield (see below) for the p+^{197}Au reaction is obtained using the simple model for nuclear level density calculation based on the use of Eq.(52) with the nuclear level density parameter equal to A/13. The example of such calculation of α-particle emission spectra performed with the help of the ALICE/ASH code is shown in Fig.38 for proton induced reactions at primary energies from 28.8 to 200 MeV. The use of this approach can not be considered as a consistent solution of the problem of the agreement of calculations and experimental data. It is used only for evaluation purposes.

Fig.39 shows α-particle emission spectra from the p+^{197}Au reaction obtained by the simulation of nucleon and pre-formed nuclear clusters interactions with the help of the intranuclear cascade evaporation model implemented in the DISCA-C code. The contribution of the equilibrium α-emission is shown. It is seen that the main mechanism of the α-particle production at the ejectile energy above 30 MeV is the non-equilibrium emission. In whole, there is a satisfactory agreement between the result of calculations performed by the DISCA-C code and experimental spectra.

The α-particle spectra calculated with the help of different codes from the MCNPX package [142] are shown in Fig.40. The calculation was done with the help of the Bertini model and the ISABEL model combined with the Multistage Pre-equilibrium Model (MPM) [159] and with the Dresner and ABLA evaporation models. Also, the CEM2k model implemented the intranuclear cascade, pre-equilibrium and evaporation model was used for the α-emission spectrum calculation. The agreement between calculations and experimental data [260,261] is quite poor. The α-particle spectrum calculated by the CEM2k model is the most close to experimental data. The Bertini and ISABEL models in different combinations with the Dresner and ABLA evaporation models describe only the evaporation range of the α-particle emission spectra. The application of the MPM pre-equilibrium exciton model

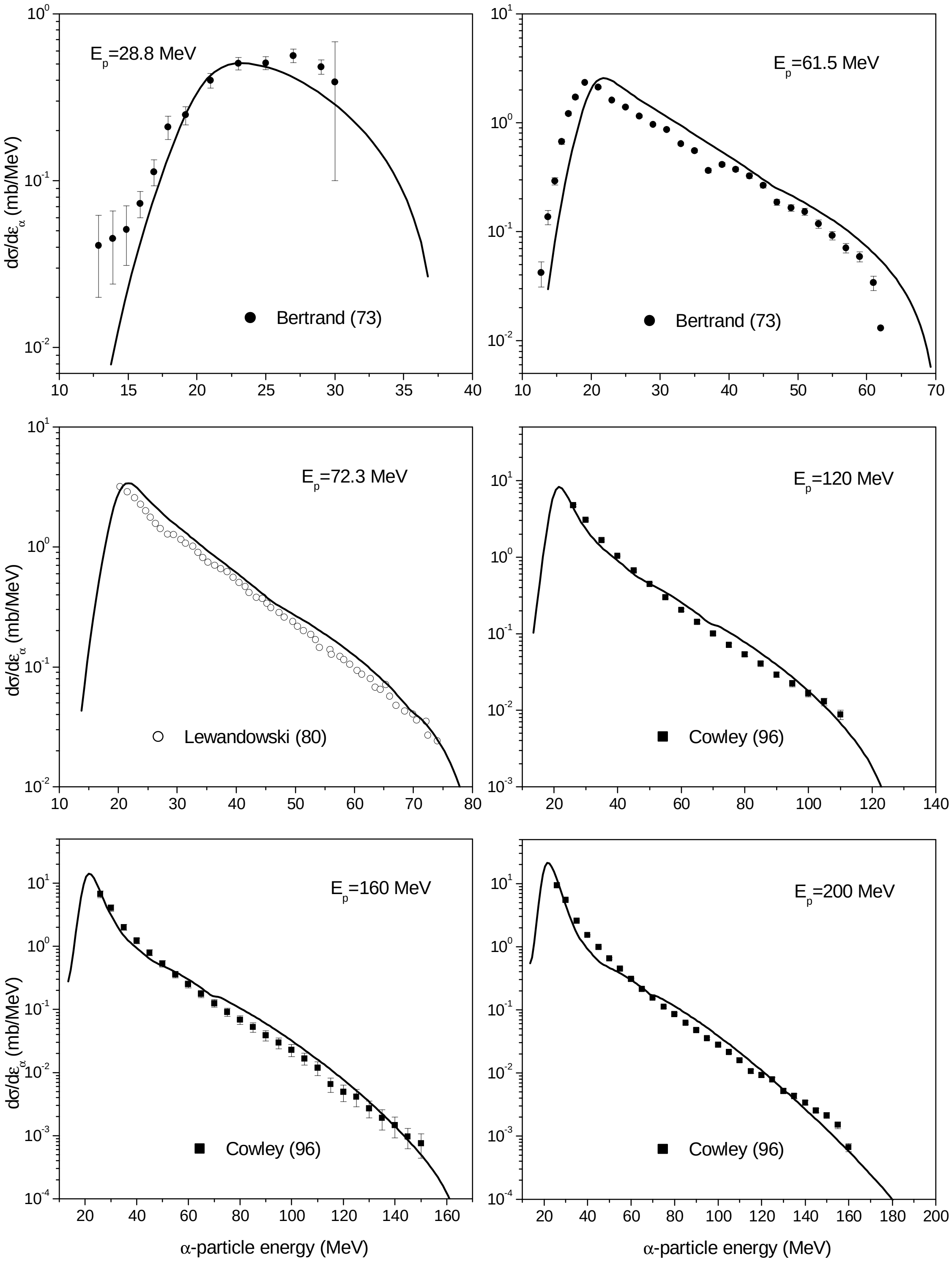

Fig.38 The α-particle emission spectra calculated with the help of the ALICE/ASH code for p+^{197}Au reaction at the primary proton energies from 28.8 to 200 MeV. The nuclear level density parameter "a" is equal to A/13. The experimental data are from Refs. [247,260,261].

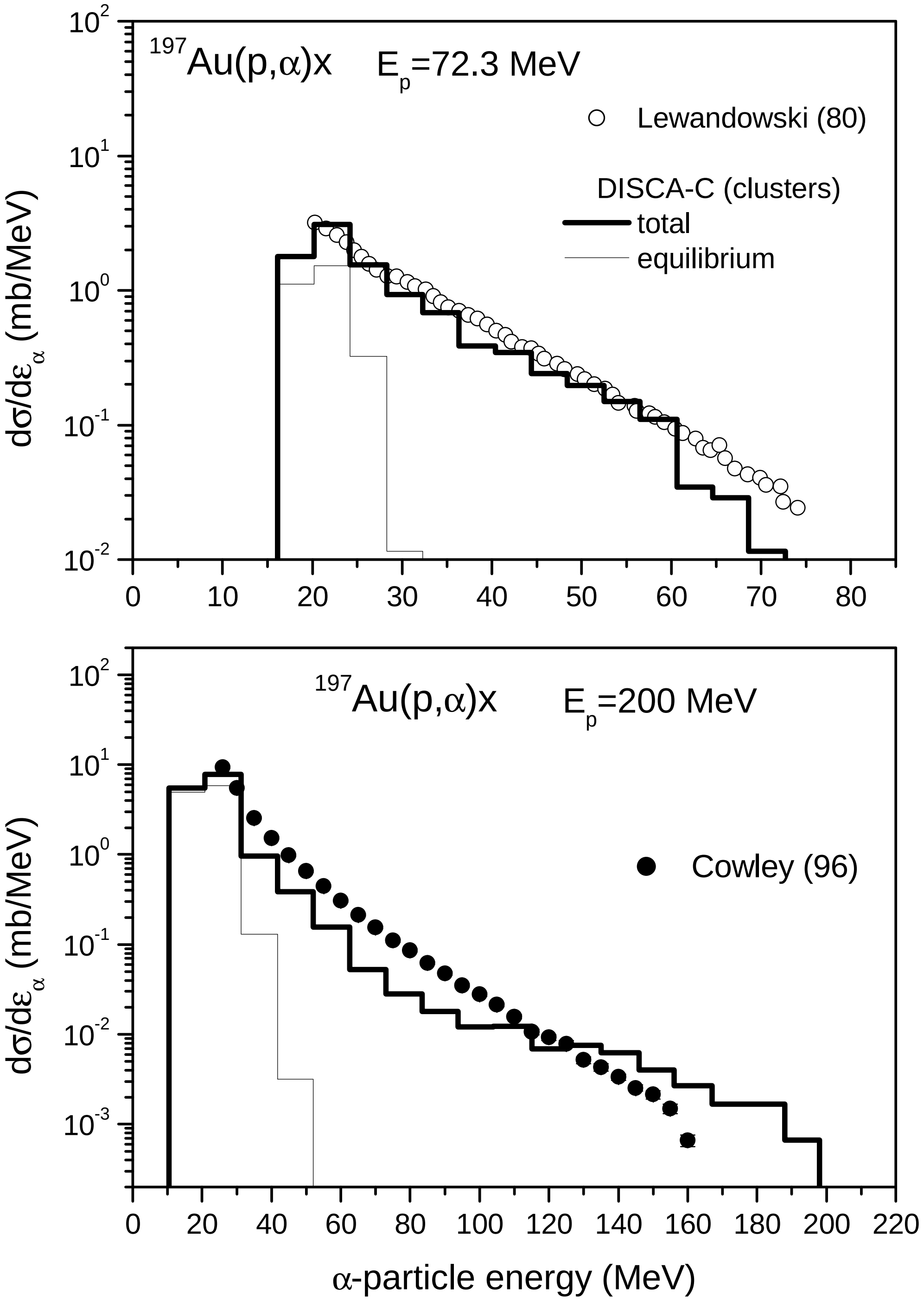

Fig.39 The α-particle emission spectra for p+^{197}Au reaction induced by protons with the energy 72.3 and 200 MeV calculated with the help of the DISCA-C code. The measured data are from Refs.[260,261].

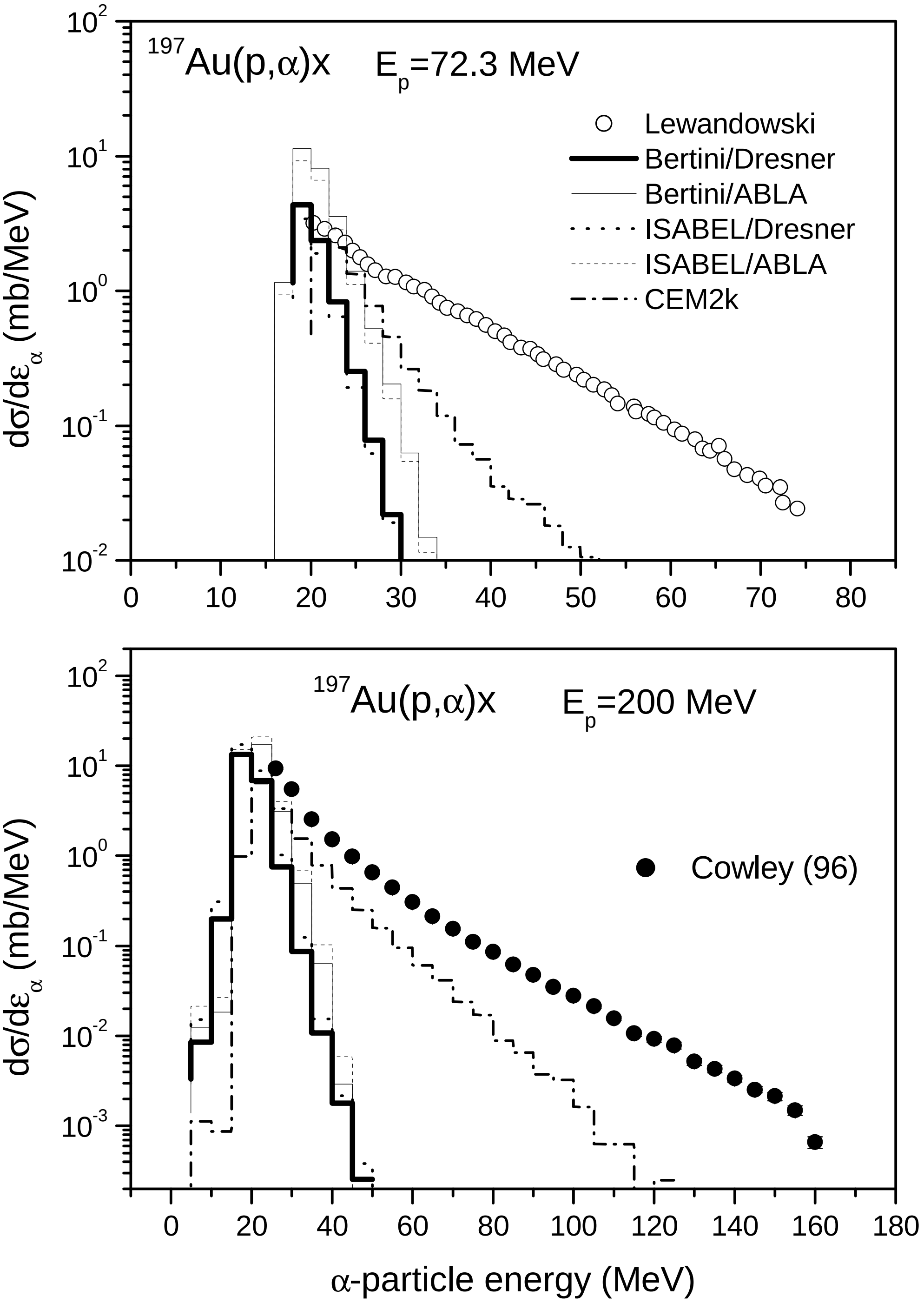

Fig.40 The α-particle emission spectra for p+^{197}Au reaction induced by protons with the energy 72.3 and 200 MeV calculated by MCNPX with the help of different models: Bertini/Dresner, Bertini/ABLA, ISABEL/Dresner, ISABEL/ABLA and CEM2k. The measured data are from Refs.[260,261].

coupling with Bertini and ISABEL does not substantially improve the agreement with experimental data comparing with the pre-equilibrium model [152] implemented in CEM2k. One should note that the use of the ABLA model comparing with the Dresner model overestimates the α-particle equilibrium spectrum (upper Fig.40). This fact is important for the further analyses of the difference between calculated and experimental yields of α-particles in nuclear reactions discussed in Section 3.2.3.

3.2.2 Non-equilibrium a-particle yield

The contribution of the non-equilibrium emission in the total α-particle yield have been obtained from the analyses of experimental data for ^{197}Au irradiated with protons in Refs.[252,254,262-264]. According to Ref.[264] the contribution of the non-equilibrium α-particle emission in the total α-particle production decreases from 100 % at the primary proton energy 20 MeV to 73 % at 40 MeV and to 60 % at 80 MeV. At the proton energy 156 MeV the contribution of the non-equilibrium α-particle yield is about 33 % [252].

Fig.41 shows the non-equilibrium component of the α-particle production cross-section (σ_α^{pre}) calculated with the help of the GNASH code and the ALICE/ASH code. The contribution of the first pre-compound α-particle obtained by ALICE/ASH is also shown. The reasonable agreement is observed between the data and the ALICE/ASH code calculations. The calculated σ_α^{pre} cross-section passes through a maximum at 130 MeV and slowly decreases with the primary proton energy growing. Probably, the decrease of the σ_α^{pre} value results because the escape of the third and subsequent pre-compound α-particles is not taken into account (Section 3.1.1.2).

Results obtained with the help of different intranuclear cascade models are shown in Fig.42. The pre-compound α-particle emission is described by exciton models in all cases except the use of the DISCA-C and DISCA-S codes. The cross-sections σ_α^{pre} calculated using the Bertini and ISABEL models are too low comparing with data [252,263,264]. The DISCA-C code gives the reasonable description of experimental data. DISCA-S better reproduces experimental σ_α^{pre} values [263,264] below 80 MeV. The agreement with the data [252] at 156 MeV can be improved by the appropriate choice of model parameters, Eq.(53).

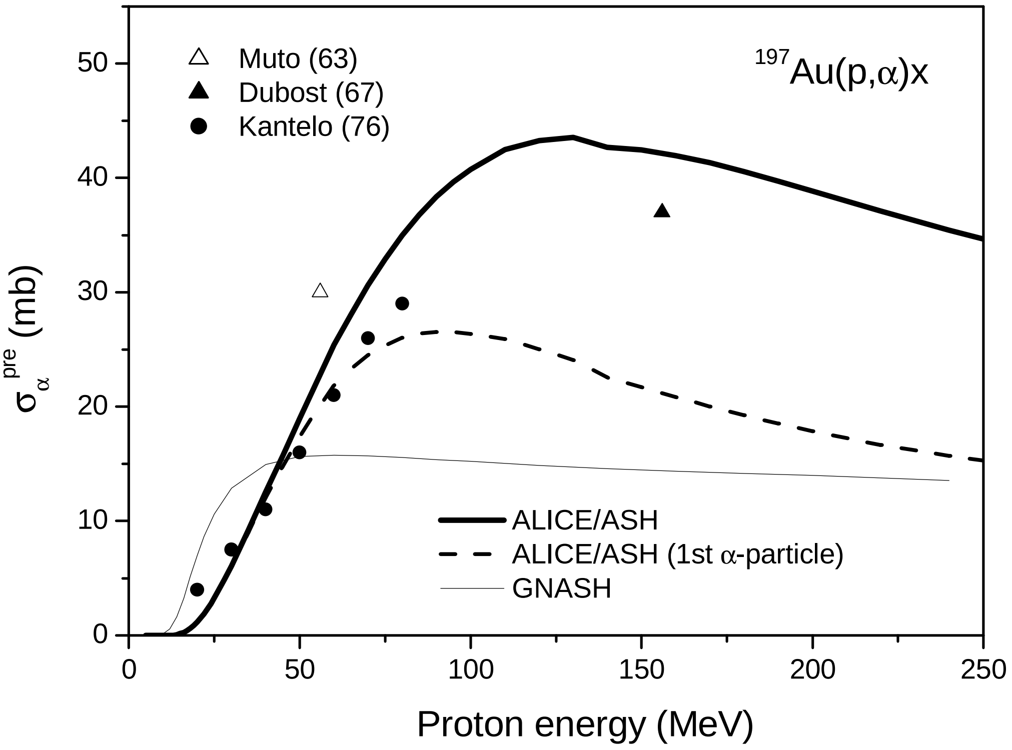

Fig.41 The non-equilibrium component of the α-particle production cross-section for p+^{197}Au reaction calculated with the help of the GNASH code and the ALICE/ASH code. The measured data are from Refs.[252,263,264].

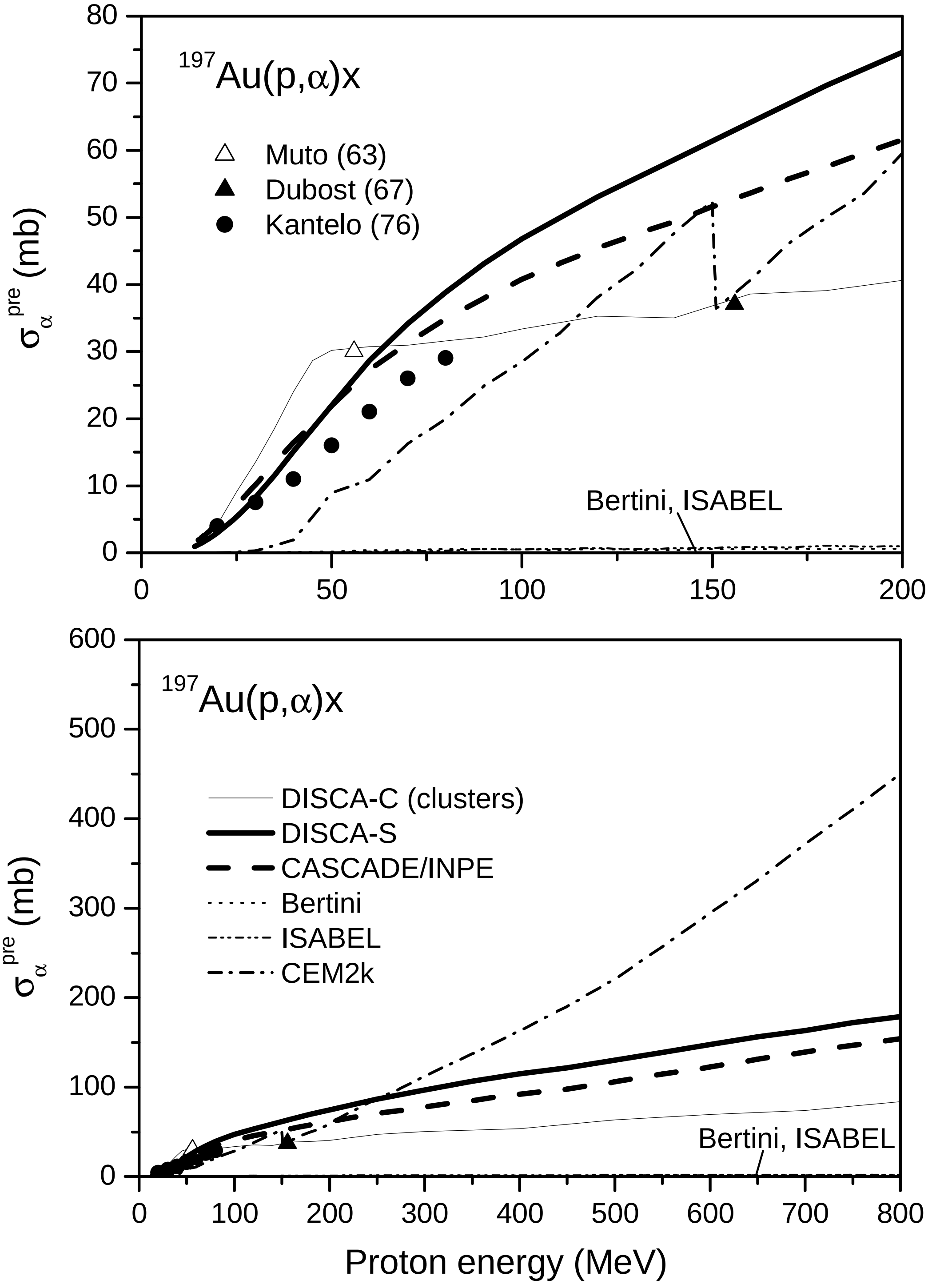

Fig.42 The non-equilibrium component of the α-particle production cross-section for p+^{197}Au reaction calculated with the help of the DISCA-C and DISCS-S codes and calculated by MCNPX using the Bertini, ISABEL and CEM2k models. The measured data are from Refs. [252,263,264].

The CEM2k model reproduces the general trend of the $\sigma_{\alpha}^{\mathrm{pre}}$ cross-section below 80 MeV. The calculated cross-section has a jump near 150 MeV, whose origin is not clear. The same jump is observed in the displacement cross-section calculated by CEM2k. The inconsistency of the calculation at 150 MeV should be removed in future versions of the MCNPX code.

At the energies above 400 MeV the difference between different calculations is rather big (lower Fig.42). The new measurements, which would make it possible to extract and to analyze the pre-equilibrium component of the α-particle production cross-section, are necessary in order to answer a question about the advantages of different methods of the α-particle cross-section calculation at these energies.

3.2.3 Total a-particle production

The α-particle production cross-section (σ_{α}) for proton induced reactions on ^{197}Au calculated by different codes is compared with experimental data in Figs.43-46.

Fig.43 shows measured α-production cross-sections [246,247,252,254,263-265], results of calculations performed with the help of the GNASH and ALICE/ASH codes and the systematics values, Eqs.(56)-(59). The calculations were carried out using different approaches for the description of the nuclear level density [190,191,193,201, 208]. The difference between the σ_{α} cross-section calculated by the same code and with the help of various models describing the level density is observed above 40 MeV. It is in a general agreement with a fact that the pre-equilibrium emission is the main origin of α-particles produced in the proton irradiation of ^{197}Au at the energies below 40 MeV. The good agreement is observed between the experimental data, systematics and the σ_{α} values calculated by the ALICE/ASH code using the superfluid nuclear model [193] and the Fermi gas model [190] at the primary proton energies below 90 MeV. At the energy around 150 MeV the α-particle production cross-section calculated using the Fermi gas model [190] is in a better agreement with the available experimental data than the σ_α values obtained with the help of the superfluid model. The acceptable agreement is observed between the experimental data and the σ_α values calculated by the ALICE/ASH code using the Fermi gas model with the nuclear level density parameter equal to A/13. The α-particle production cross-section calculated by the GNASH code is rather higher than the experimental points.

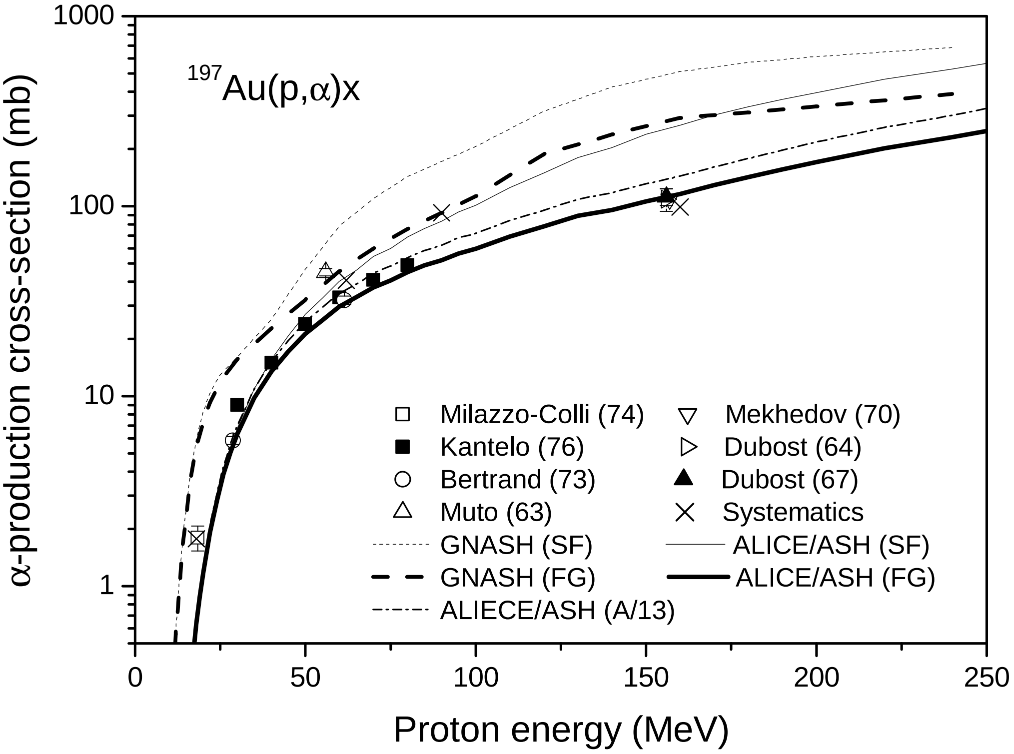

Fig.43 The α-particle production cross-section for the proton irradiation of ^{197}Au at the energy up to 200 MeV calculated with the help of the GNASH and ALICE/ASH codes, estimated by systematics and measured in Refs. [246,247,252,254,263-265].

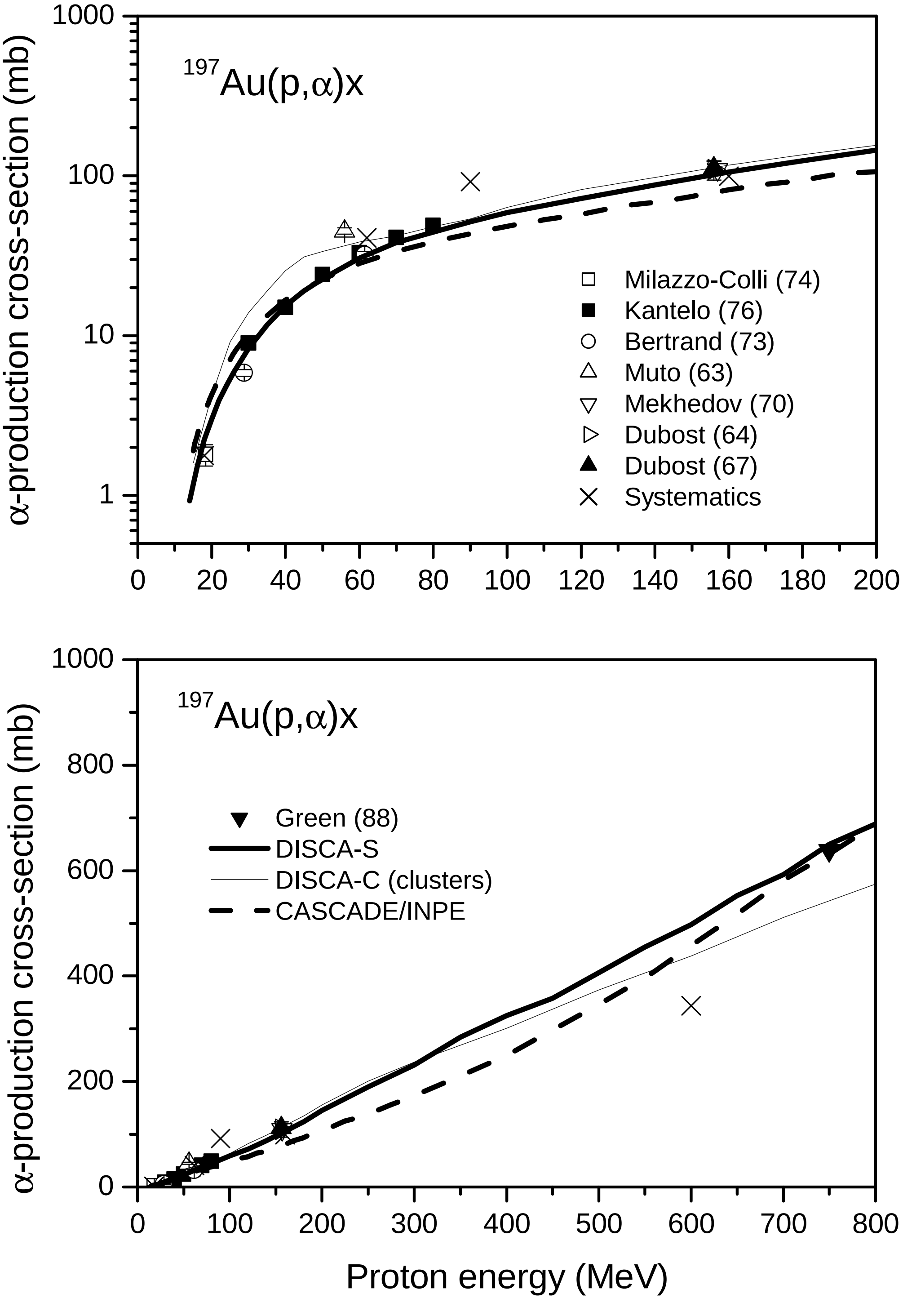

Fig.44 The α-particle production cross-section for the proton irradiation of ^{197}Au calculated using the DISCA-C, DISCA-S and CASCADE/INPE codes, estimated by systematics and measured in Refs. [246,247,252,254,263-266].

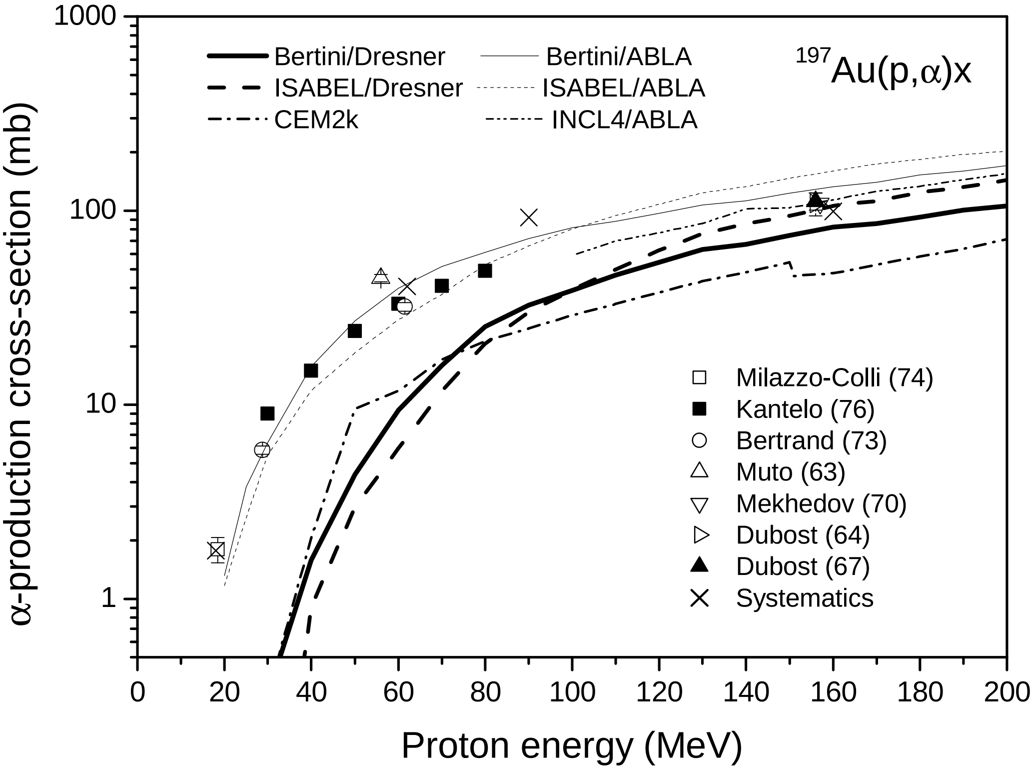

Fig.45 The α-particle production cross-section for the proton irradiation of ^{197}Au at the energy below 200 MeV calculated with the help of the Bertini/Dresner, Bertini/ABLA, ISABEL/Dresner, ISABEL/ABLA, INCL4/ABLA and CEM2k models, estimated by systematics and measured in Refs.[246,247,252,254,263-265].

All models implemented in GNASH and ALICE/ASH overestimate the σ_α cross-sections at the energies above 200 MeV comparing with calculations carried out by the DISCA-C and DISCA-S codes and the codes from the MCNPX package. In particular the calculated contribution of the equilibrium α-particle emission in the total production cross-section is too big. The main reason is that the energy of 200 MeV is likely out of the range of the applicability of pre-equilibrium models implemented in GNASH and ALICE/ASH. The limitation results from the approximate description of the nuclear geometry, the calculation of the R-factors, Eqs.(23),(37) the description of multiple pre-compound nucleon emission and others having impact on the calculated distribution of the excitation energy available for the particle evaporation.

Fig.44 shows the total α-particle production cross-section calculated with the help of the DISCA-C code and the DISCA-S code. The σ_α values calculated with the help of the DISCA-C code are in the general agreement with experimental data. At the same time the calculated α-production cross-section is higher than experimental points at the energies below 60 MeV and lower than the measured σ_α value [266] at 750 MeV. There is an excellent agreement between the α-production cross-section calculated by the DISCA-S code and measured cross-sections in a whole energy range from 18 to 750 MeV, where experimental data are available.

The α-particle production cross-section obtained with the help of codes from the MCNPX package is shown in Figs.45,46. The detail view for the proton energies below 200 MeV is given in Fig.45. The σ_α values calculated using the Bertini/ABLA and ISABEL/ABLA models are in the agreement with experimental data below the proton energy 150 MeV. At the same time, there is a discrepancy between the σ_α values calculated by the Bertini/Dresner and ISABEL/Dresner models and experimental cross-sections at these energies. At first sight the use of the ABLA model improves the agreement of calculations with measured data. On the other hand this improvement is obtained by the increased evaporation component of the σ_α cross-section, because the contribution of the non-equilibrium α-particle emission in σ_α predicted by the Bertini and ISABEL models is negligible (Fig.42). As a consequence the use of the ABLA model results in a poor agreement with experimental data at high proton energies (Fig.46). The best result for the combination of ABLA with intranuclear cascade model is observed for the INCL4/ABLA calculations. One should note that this result is observed for INCL4, where the simulation of the non-equilibrium α-particle emission is not performed.

The best agreement is observed between the experimental cross-section at 750 MeV [266] and calculations performed with the help of the ISABEL/Dresner model (Fig.46). The cross-section calculated by the CEM2k model is in the agreement with the systematics value at 600 MeV.

The comparison of the results of calculations with experimental data discussed in this Section shows that the reasonable evaluation of the α-particle production cross-section can be performed using the ALICE/ASH code, the DISCA-C or DISCA-S codes. The calculation by the ISABEL/Dresner model is also of interest at the energies above 150 MeV.

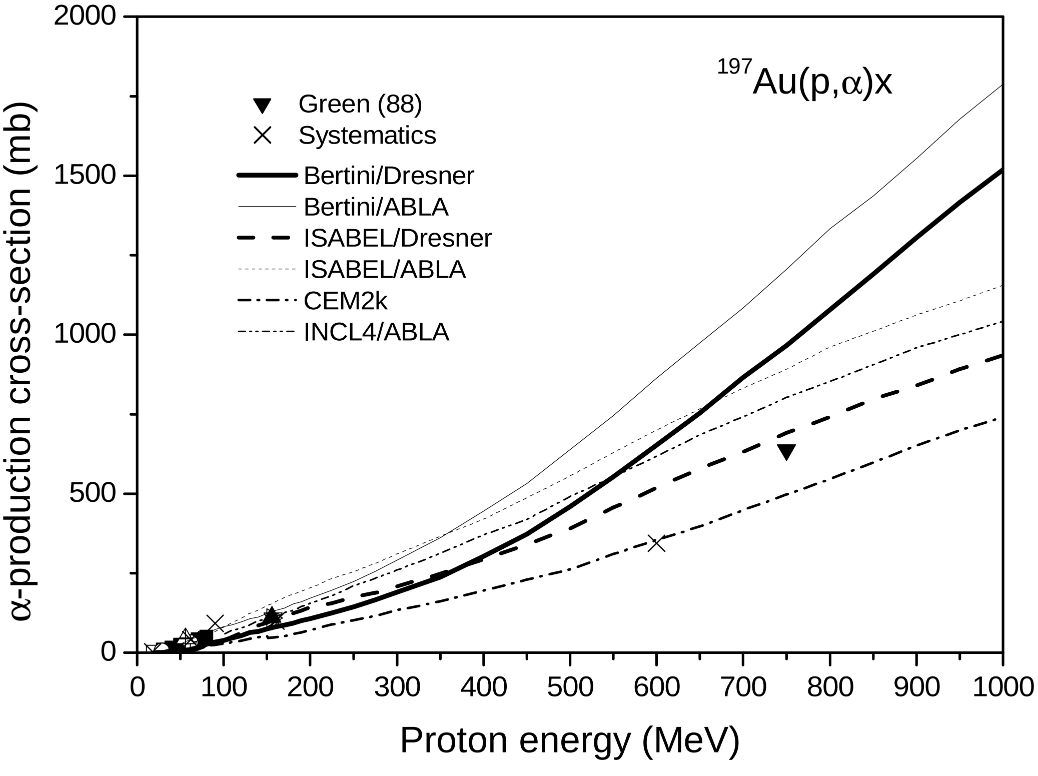

Fig.46 The α-particle production cross-section for the proton irradiation of ^{197}Au at the energy up to 1 GeV calculated with the help of the Bertini/Dresner, Bertini/ABLA, ISABEL/Dresner, ISABEL/ABLA, INCL4/ABLA and CEM2k models, estimated by systematics and measured in Refs.[246,247,252,254,263-266].

3.3 Evaluation of α-particle production cross-section

The evaluation of the α-particle production cross-section was done using the results of model calculations, systematics predictions and available experimental data. Calculations were performed by the ALICE/ASH code, the DISCA-S code and the ISABEL and Dresner modules of the MCNPX package.

3.3.1 ^{181}Ta

3.3.1.1 Proton induced reactions

Fig.47 shows the α-particle particle production cross-section for ^{181}Ta irradiated with protons calculated by the ALICE/ASH code, the DISCA-S code and the ISABEL/Dresner (MCNPX) code. The detail view of the energy range below 200 MeV, which corresponds to the rapid change in the cross-section value, is given in upper Fig.47. The σ_α values obtained by systematics Eqs.(56)-(60), the α-production cross-section measured [263] at the proton energy 56 MeV and the cross-section obtained from the analyses of the experimental data [252,267] at 156 and 800 MeV are also shown in Fig.47. To get the total α-particle production cross-section at 156 MeV the measured yield [252] of α-particles having isotropic angular distribution (100 mb) was added by the value obtained in Ref.[252] for heavy nuclei relating to anisotropic α-particle emission (37 mb). The helium production cross-section measured [267] at 800 MeV was corrected to exclude the contribution of ^{3}He. The yield of ^{3}He was estimated using the ^{3}He- and ^{4}He- production cross-section measured for seven elements from Al to Au in Ref.[266] at the proton energy 750 MeV and using experimental yields of ^{3}He and ^{4}He obtained in Ref.[268] for Au at 1.8 GeV.

Fig.47 shows a reasonable agreement between the σ_α cross-sections calculated by the ALICE/ASH and DISCA-S codes and experimental data and systematics values.

The results of calculations, systematics values and available measured data were assumed as the basis for the evaluation of the α-particle production cross-section for ^{181}Ta. The evaluated data are shown in Fig.48 and in Table 12.

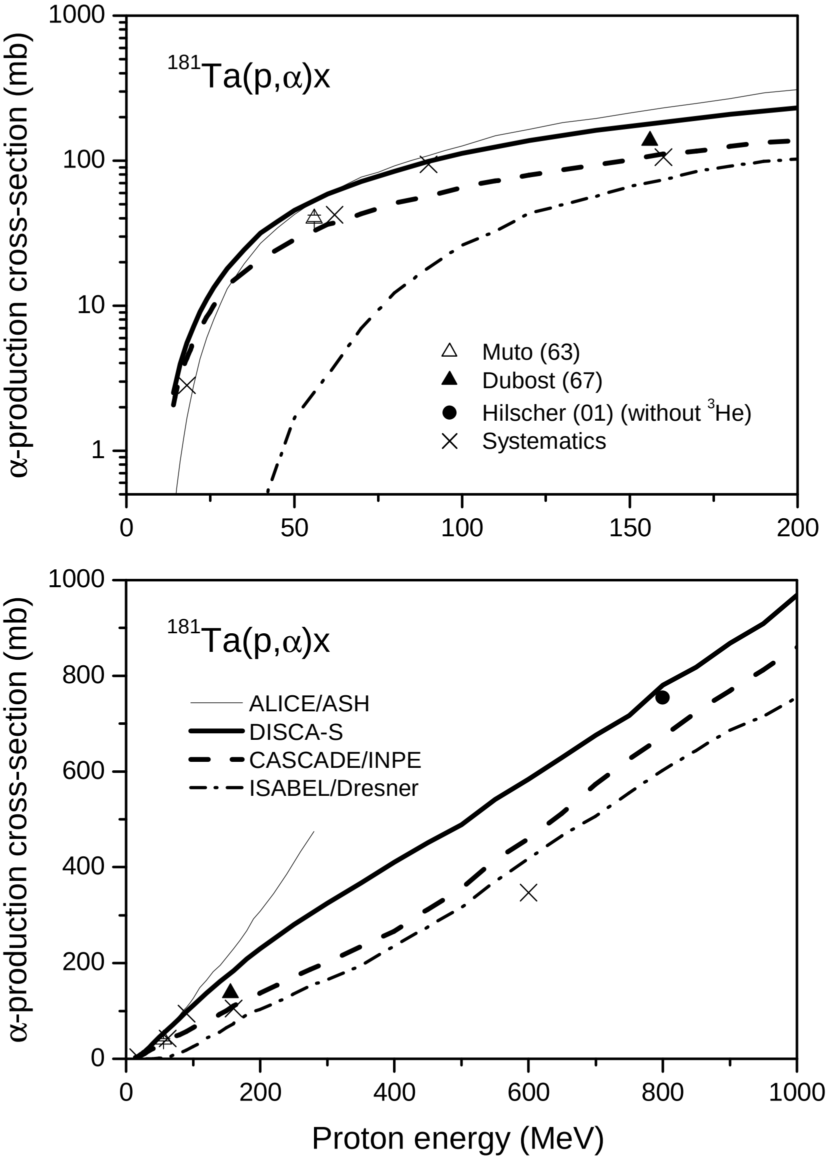

Fig.47 The α-particle production cross-section for proton irradiation of ^{181}Ta calculated by the ALICE/ASH code, the DISCA-S code, the CASCADE/INPE code and the ISABEL/Dresner (MCNPX) code, estimated by systematics, measured in Ref.[263] and extracted from experimental data [252,267].

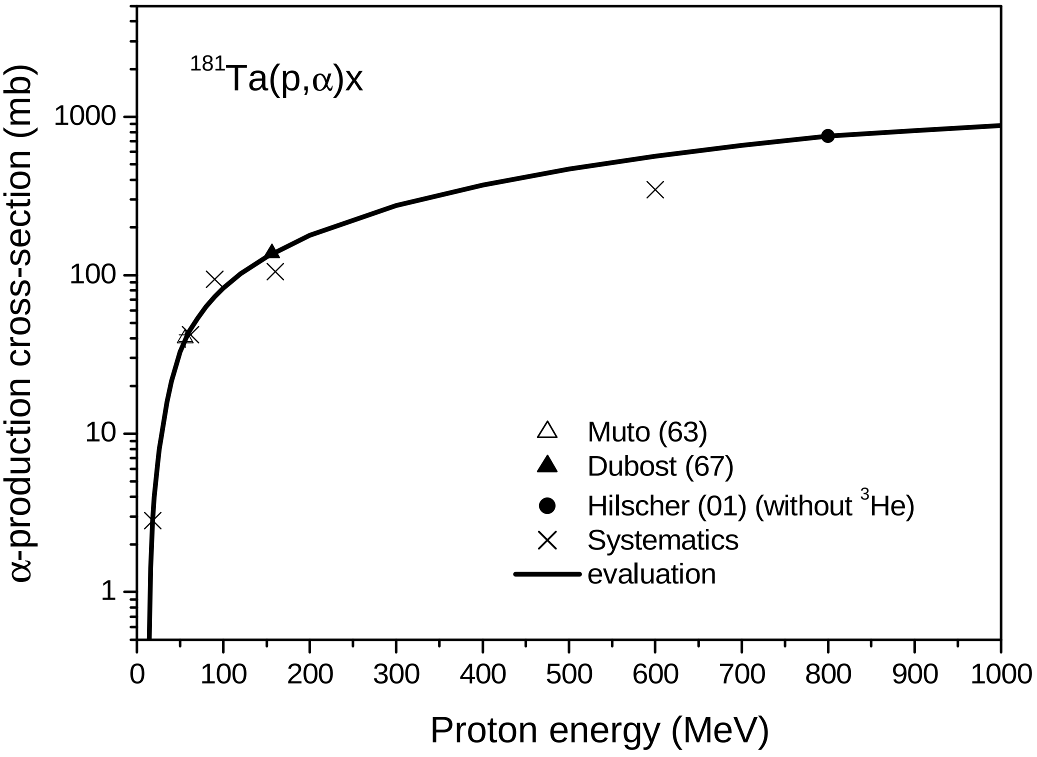

Fig.48 The evaluated α-particle production cross-section for ^{181}Ta irradiated with protons.

3.3.1.2 Neutron induced reactions

Experimental data for neutron induced reactions on ^{181}Ta are available at the energies below 20 MeV. Except the measurement of the α-production cross-section in Ref.[269] other data [270-277] were obtained for (n,α) reaction. The data measured recently [274-277] were not taken into account in the most of the evaluation for national and international data files.

A new evaluation of the α-particle production cross-section was performed for ^{181}Ta in the present work. The cross-sections were obtained separately for the reactions ^{181}Ta(n,α)^{178g}Lu and ^{181}Ta(n,α)^{178m}Lu ($T_{1/2}$=23.1 min) using measured data from Refs.[272,274-277].

Table 12

The evaluated ^{4}He production cross-section from ^{181}Ta, ^{nat}W and ^{197}Au irradiated with protons at the energies up to 1GeV.

Proton energy[1)] (MeV)	^{4}He production cross-section (mb)		
	^{181}Ta	^{nat}W	^{197}Au
6	4.15×10^{-06}	2.26×10^{-04}	1.21×10^{-03}
8	6.84×10^{-04}	1.86×10^{-03}	7.95×10^{-03}
10	1.70×10^{-02}	1.43×10^{-02}	4.47×10^{-02}
12	0.135	$8.848E^{-02}$	0.201
14	0.548	0.391	0.599
16	1.42	1.20	1.22
18	2.82	2.57	1.87
20	3.98	4.18	2.62
22	5.22	5.92	3.47
24	6.50	7.22	4.39
26	8.00	8.63	5.39
28	9.46	10.2	6.46
30	11.3	11.9	7.67
35	15.8	16.0	11.3
40	21.4	20.7	15.0
50	32.9	29.8	24.0
60	43.9	39.6	31.0
70	53.6	49.0	41.0
80	63.3	59.0	49.0
90	73.0	69.3	57.3
100	82.7	79.2	65.6

Table 12 continued

120	102.	99.6	82.2
150	131.	131.	107.
200	179.	186.	151.
300	275.	286.	240.
400	371.	376.	328.
500	467.	465.	417.
600	563.	559.	505.
700	659.	658.	594.
800	755.	762.	697.
900	817.	853.	814.
1000	880.	920.	932.

1) The cross-sections between the energy points shown should be found by the log-log interpolation of the data at the energies below 20 MeV, and by the linear-linear interpolation at the energies above 20 MeV

The sum of cross-sections obtained for reactions producing ^{178g}Lu and ^{178m}Lu, available experimental data, systematics values and the data from FENDL/A-2, JENDL-3.3, CENDL-2 and JEFF-3/A [278] are shown in Fig.49.

The total α-particle production cross-section at the energies below 20 MeV was obtained using the cross-section evaluated for the (n,α) reaction and the data for the (n,nα) reaction taken from JEFF-3/A (data are from the ADL-3 library [279]).

At the energies above 20 MeV the α-particle production cross-section has been calculated with the help of theoretical models. The evaluated α-particle production cross-section for ^{181}Ta irradiated with neutrons at the energies up to 1 GeV is shown in Fig.50 and Table 13.

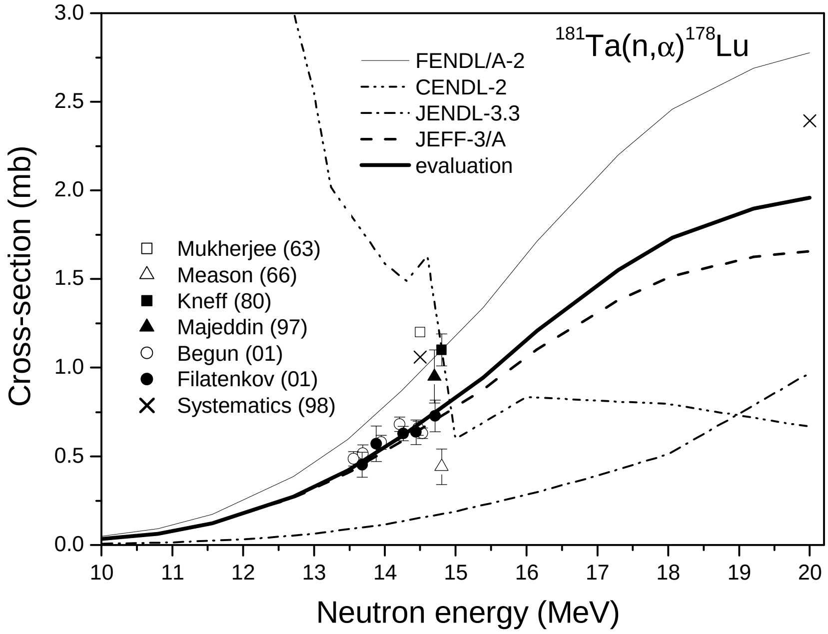

Fig.49 The (n,α) reaction cross-section for ^{181}Ta taken from FENDL/A-2, JENDL-3.3, CENDL-2 and JEFF-3/A, measured in Refs.[269-277], estimated by systematics and evaluated in the present work.

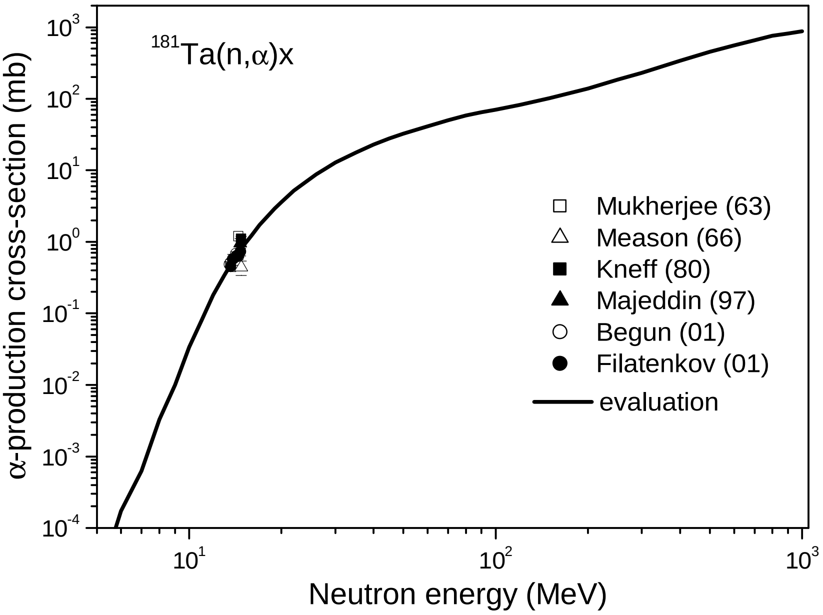

Fig.50 The evaluated α-particle production cross-section for ^{181}Ta irradiated with neutrons.

Table 13

The evaluated ^{4}He production cross-section from ^{181}Ta, ^{nat}W and ^{197}Au irradiated with neutrons at the energies from 5 MeV$^{1)}$ up to 1GeV. See comments in the text.

Neutron energy (MeV)	^{4}He production cross-section (mb)		
	^{181}Ta	^{nat}W	^{197}Au
5	1.49×10^{-05}	2.88×10^{-03}	4.00×10^{-07}
6	1.73×10^{-04}	5.31×10^{-03}	4.00×10^{-07}
7	6.27×10^{-04}	1.11×10^{-02}	4.00×10^{-07}
8$^{2)}$	3.26×10^{-03}	2.44×10^{-02}	2.40×10^{-02}
9	1.00×10^{-02}	5.62×10^{-02}	4.81×10^{-02}
10	3.36×10^{-02}	0.126	7.21×10^{-02}
11	8.00×10^{-02}	0.287	9.62×10^{-02}
12	0.182	0.572	0.120
13	0.335	0.922	0.156
14	0.570	1.32	0.301
14.5	0.719	1.53	0.439
15	0.868	1.74	0.577
16	1.23	2.23	1.00
17	1.71	2.74	1.47
18	2.28	3.20	1.86
19	2.91	3.72	2.21
20	3.61	4.37	2.52
22	5.17	5.47	3.65
24	6.91	7.24	4.96
26	8.78	9.14	6.40
28	10.7	11.1	7.92

Table 13 continued

30	12.7	13.3	9.48
35	17.7	18.5	13.6
40	22.8	23.0	17.9
45	27.9	27.5	21.3
50	32.4	30.9	25.0
60	41.3	37.3	29.0
70	49.9	44.2	35.0
80	57.9	51.5	41.1
90	64.5	57.9	46.2
100	70.3	64.8	50.9
120	82.2	77.8	63.2
150	102.	99.3	78.7
200	139.	139.	111.
250	185.	181.	151.
300	231.	229.	191.
400	340.	344.	300.
500	452.	449.	403.
600	556.	552.	499.
700	656.	655.	591.
800	753.	760.	696.
900	817.	852.	814.
1000	879.	920.	931.

---

1) Data below 5 MeV can be found in JEFF-3/A [278]

2) For ^{197}Au the cross-section is equal to 4.0×10^{-07} mb [278] at the energy from 7 to 8 MeV

3.3.2 ^{nat}W

To obtain the cross-sections for natural tungsten the calculations were performed for tungsten isotopes ^{180}W, ^{182}W, ^{183}W, ^{184}W and ^{186}W.

3.3.2.1 Proton induced reactions

Fig.51 shows the α-particle production cross-section calculated by the ALICE/ASH code, the DISCA-S code and the ISABEL/Dresner (MCNPX) code, systematics values obtained at 18, 62, 90, 160 and 600 MeV and experimental data [266]. The data taken from ENDF/B-VI Proton Sublibrary (Release 7) and from JENDL-HE [280] are also shown. There is the good agreement between the σ_α cross-sections calculated with the help of the DISCA-S code and the experimental data [266] at 750 MeV. Data from JENDL-HE are in the agreement with systematics values at 62 and 90 MeV and with the cross-section calculated by ALICE/ASH at the energies from 100 to 150 MeV. As whole, the data from JENDL-HE and ENDF/B-VI differ substantially.

The evaluation of the α-particle production cross-section was based on the results of the ALICE/ASH and DISCA codes calculations and the systematics value at 18 MeV. The evaluated cross-section is shown in Table 12 and Fig.52.

3.3.2.2 Neutron induced reactions

To get the α-particle production cross-section for natural tungsten the data for isotopes ^{180}W, ^{182}W and ^{183}W were taken from JEFF-3/A at the energies below 20 MeV. The new evaluation was performed for the (n,α) reaction cross-section for ^{184}W and ^{186}W. For both isotopes the JENDL-3.3 data were fitted to the cross-section measured in Refs.[272,281,282] for ^{184}W and in Refs.[272,281-284] for ^{186}W. The (n,nα) reaction cross-section was taken from JEFF-3/A. The data obtained for natural tungsten were adjusted to the results of calculations at the energies above 20 MeV.

Evaluated σ_α values are shown in Fig.53 and Table 13. For the comparison data from ENDF/B-VI and JENDL-HE are also plotted in Fig.53.

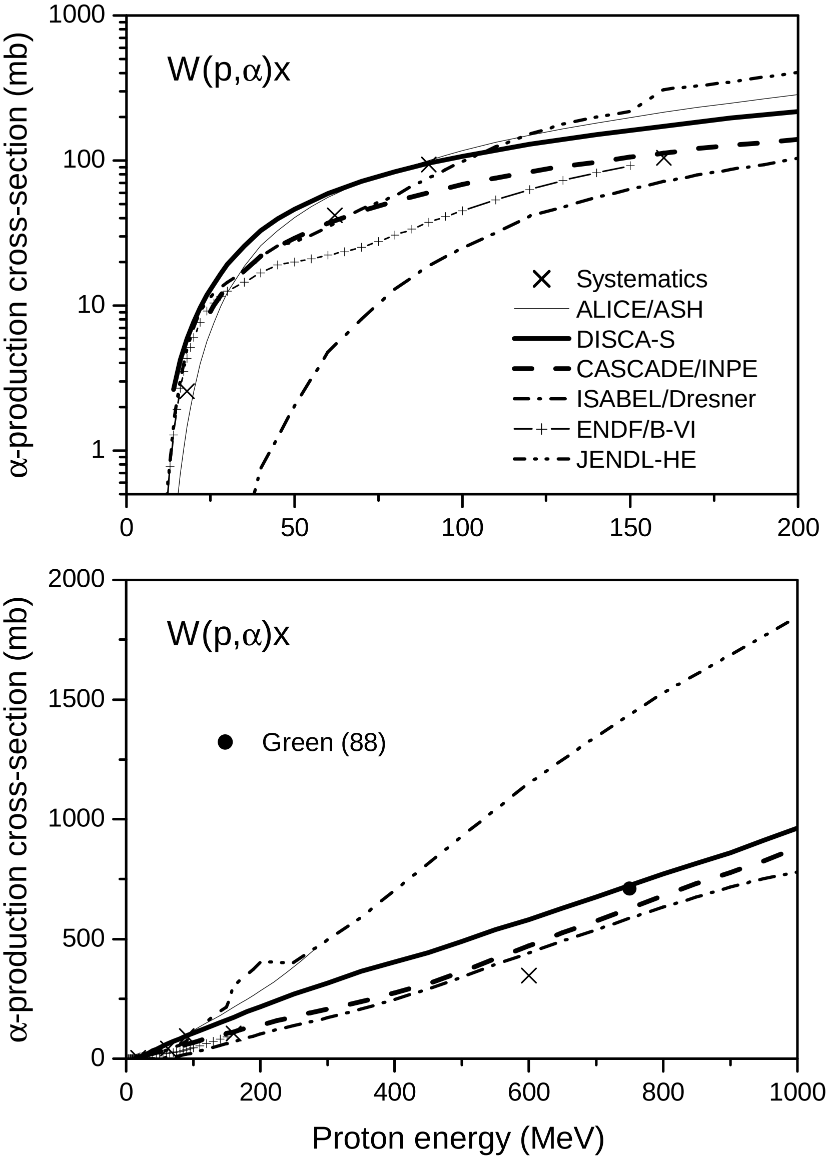

Fig.51 The α-particle production cross-section for proton irradiation of natural tungsten calculated by the ALICE/ASH code, the DISCA-S code, the CASCADE/INPE code and the ISABEL/Dresner (MCNPX) code, estimated by systematics, taken from ENDF/B-VI and JENDL-HE and measured in Ref. [266].

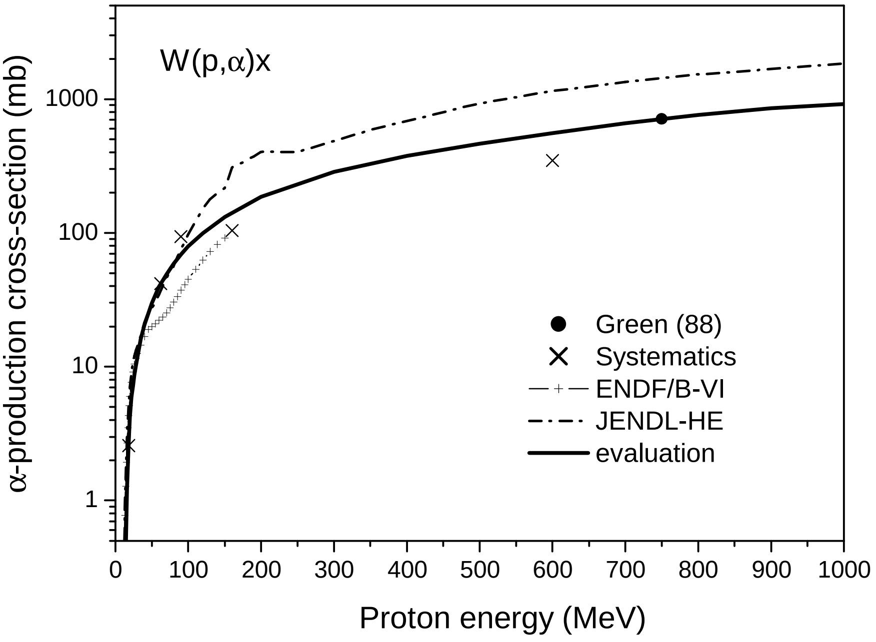

Fig.52 The α-particle production cross-section for tungsten irradiated with protons evaluated in the present work and taken from ENDF/B-VI and JENDL-HE.

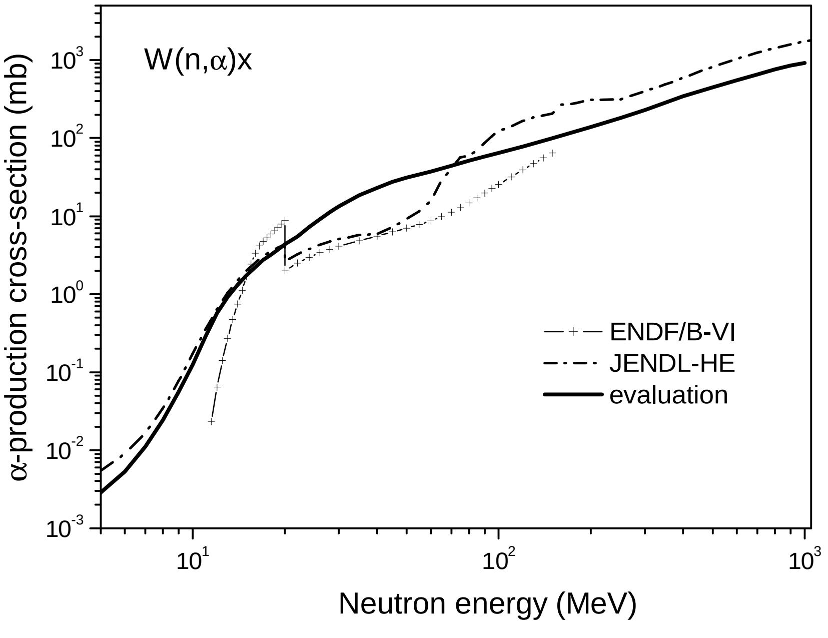

Fig.53 The α-particle production cross-section for tungsten irradiated with neutrons evaluated in the present work and taken from ENDF/B-VI and JENDL-HE.

3.3.3 ^{197}Au

3.3.3.1 Proton induced reactions

The comparison of the α-particle production cross-section calculated using different nuclear models with experimental data for ^{197}Au was discussed in detail in Section 3.2. The data evaluated in the present work are shown in Fig.54 and Table 12.

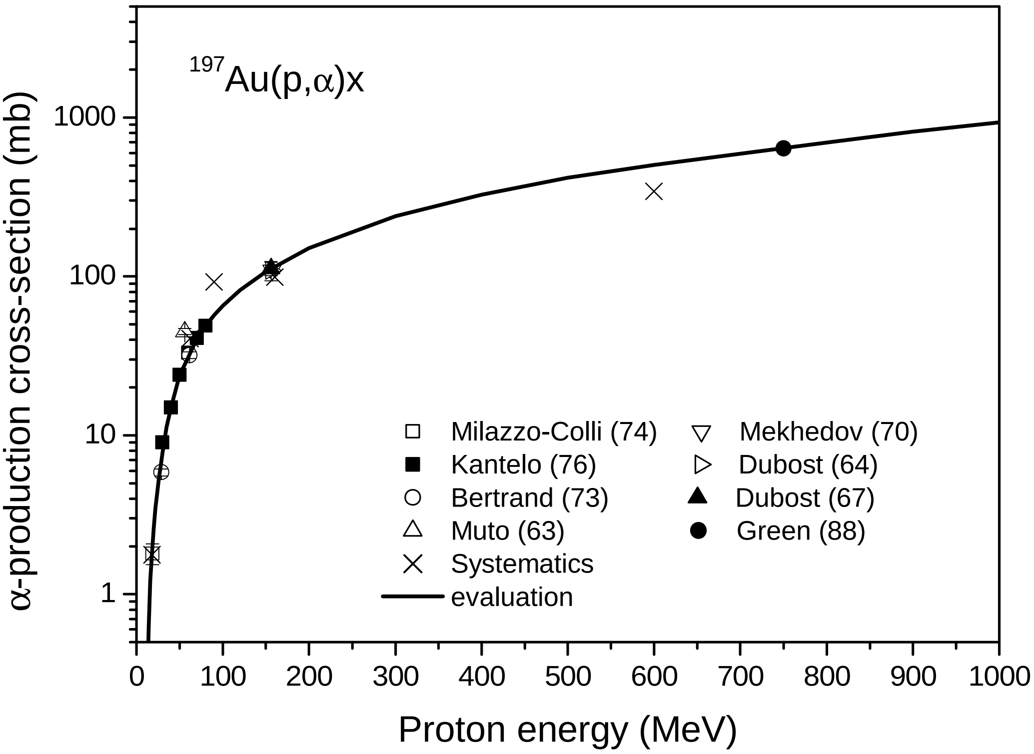

Fig.54 The evaluated α-particle production cross-section for ^{197}Au irradiated with protons.

3.3.3.2 Neutron induced reactions

Data from JEFF-3/A for (n,α) reaction were adopted after the comparison with experimental data [269,282,285] at the energy below 15 MeV. At the energies from 15 to 20 MeV the (n,α) cross-section is taken from ENDF/B-VI. The data for (n,nα) reaction were taken from JEFF-3/A. The calculation of the α-particle production cross-section was performed with the help of the ALICE/ASH code and the DISCA-S code at the energy above 20 MeV. The evaluated cross-section is shown in Fig.19 and Table 13.

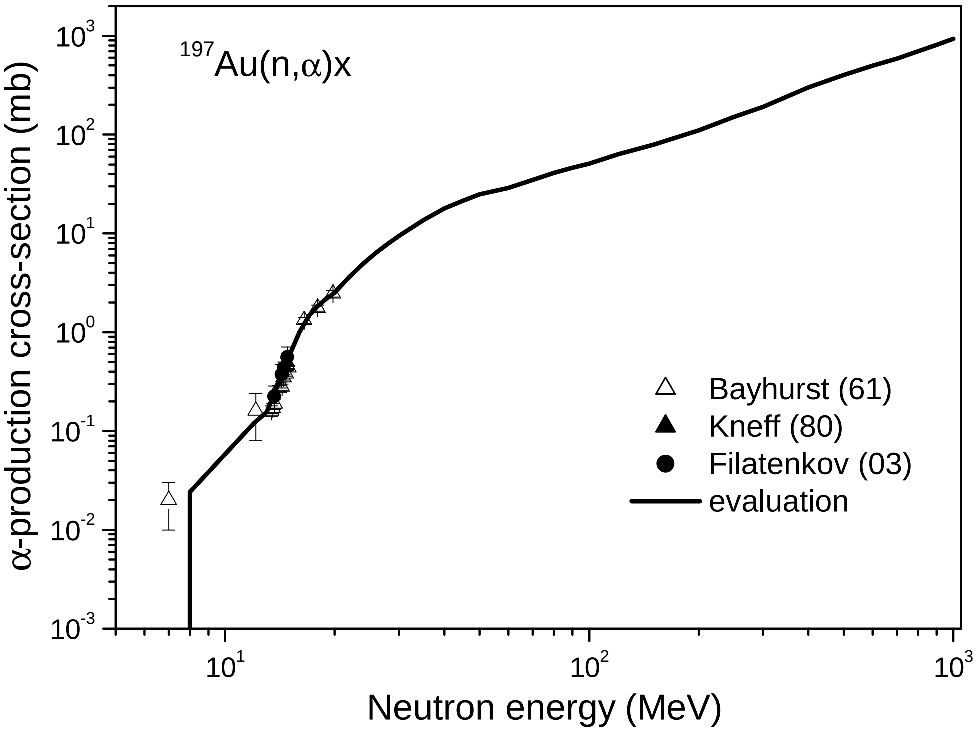

Fig.55 The evaluated α-particle production cross-section for ^{197}Au irradiated with neutrons.

3.4 Summary about the evaluation of the ^{4}He production cross-section for heavy nuclei

Different approaches and models used for the description of the α-particle emission in the reactions induced by intermediate energy nucleons on ^{181}Ta, tungsten isotopes and ^{197}Au were discussed. The comparison of the results of calculations with experimental data shows

i) The pre-equilibrium exciton model implemented in the GNASH code describes experimental α-particle spectra incorrectly (Fig.37). Calculations underestimate the α-spectrum at the energies after the evaporation peak and give too high spectrum values at high emission energies. The calculated pre-equilibrium yield of α-particles σ_{α}^{pre} is too low comparing with the data obtained from the analyses of experiments. Partly, it results that the multiple pre-compound α-particle emission is not taken into account.

ii) The Bertini model and the ISABEL model combined with the MPM exciton model [159] considerably underestimate the yield of non-equilibrium α-particles (Fig.42). The CEM2k model describes the general energy dependence of the σ_{α}^{pre} cross-section at the energies below 80 MeV. There is a strong difference between the σ_{α}^{pre} values calculated by CEM2k and by other codes at the energy above 400 MeV. There is a discrepancy between α-particle emission spectra calculated by the codes from the MCNPX package and experimental data (Fig.40).

iii) The use of the ABLA evaporation model coupled with the Bertini, ISABEL and INCL4 models overestimates the contribution of the equilibrium α-particle emission in the α-spectra and the total α-particle production cross-section (Figs.40,46).

iv) The α-particle emission spectra, the non-equilibrium and the total α-particle yields calculated by the ALICE/ASH code and the DISCA-C and DISCA-S codes are in a reasonable agreement with experimental data (Figs.37-39,41-44,47,51).

The discrepancy between the results of calculations performed with the help of the codes from MCNPX and experimental data results from the use in the MPM and MEM exciton models [245] the early versions of the coalescence model describing the pre-compound α-particle emission [243,244]. It seems reasonable to implement in the GNASH code and the codes from MCNPX the models used for the description of the pre-equilibrium α-particle emission in the ALICE/ASH and DISCA-C codes.

The ^{4}He particle production cross-section has been evaluated for ^{181}Ta, natural tungsten and ^{197}Au at the energies of incident neutrons and protons from several MeV to 1 GeV. The evaluated cross-sections are shown in Table 12 and Figs.48,52,54 for proton induced reactions and in Table 13 and Figs.50,53,55 for neutron induced reactions.

4. Helium (^{4}He+^{3}He) production cross-section for iron, tantalum, tungsten irradiated with neutrons and protons of intermediate and high energy

Evaluation of the helium production rate in irradiated materials is hindered by the significant spread of experimental helium formation cross-sections and deficiencies in the model calculations. For example the modern measurements of helium yield for iron [256,268] give the values, which are different in 1.8 times. Despite of progress in development of theoretical methods of calculation, their use encounters the problem of the correct description of the non-equilibrium helium isotope emission using the pre-compound exciton model and the intranuclear cascade model (Section 3.) Other problem is the simulation of the equilibrium emission of helium isotopes at high energies by the intranuclear cascade evaporation model, which assumes the use of simplified approaches for describing the particle emission rates.

The goal of the work is analysis and the evaluation of the helium production cross-section in iron, tungsten and tantalum irradiated with protons at energies from the reaction threshold up to several GeV. This energy range covers all possible proton irradiation conditions in the ADS systems [127,288-290] and neutron generators [291,292]. The calculations have been performed up to the maximal energy 25 GeV, where the experimental data for helium production are available.

4.1 Brief description of the method of helium production cross-section evaluation

Helium production cross-section has been calculated as a sum of cross-sections of ^{4}He (σ_α) and ^{3}He ($\sigma_{^3\mathrm{He}}$) formation

$$\sigma_{\mathrm{He}} = \sigma_\alpha + \sigma_{^3\mathrm{He}} \tag{63}$$

The analysis of the methods of calculation used in popular computer codes has shown$^{3)}$, that the helium production cross-section can be obtained with a good accuracy using the models describing the composite particle emission implemented in the ALICE/ASH code$^{10,11)}$ and in the DISCA code$^{3,12\text{-}14)}$. The application of the ALICE/ASH code is limited by the energy of projectiles up to 150-200 MeV and the DISCA code to ~ 800 MeV. These energies are insufficient for the analysis of the helium yield in materials irradiated with high energy protons in different emerging nuclear energy systems. Furthermore the codes indicated can not be used for the analysis of entire bulk of the experimental helium production cross-sections, which are available at low, intermediate and high energies. Such analysis is necessary for the definition of consistent sets of experimental data and elimination of uncertainty in values of helium production cross-section arising from the spread of data obtained in different experiments.

The ^{4}He- and ^{3}He- production cross-sections are calculated using the CASCADE/INPE code [162,209,286,287,293] implementing the intranuclear cascade evaporation model. The model is applicable for the calculation in the energy region of primary particles up to several tens of GeV [287]. The specific features of the model include the approximation of the nuclear density by the continuous Woods-Saxon distribution, the use of the “time-like” Monte Carlo technique and the consideration of the effect of nuclear density depletion due to the fast nucleon emission. The model is described in details in Refs.[151,286,295].

The contribution of the non-equilibrium emission in the ^{4}He- and ^{3}He- production cross-sections is calculated using the approximate approach close to the model of “nuclear bond breakdown” [237]. Considering the ^{3}He- and α-clusters as a stable nucleon association located on a periphery of the nucleus [151] it is easy to show, that at high projectile energies the number of clusters knocked-out from the nucleus is proportional to the number of nucleons emitted on the cascade stage of the reaction and the square of the nucleus radius. This implies, that the non-equilibrium component of the ^{4}He- and ^{3}He- production cross-sections at the high energies of projectiles can be evaluated as follows

$$\sigma_x^{non}(E) = \sigma_{non}(E)\ \gamma_x\ N_{casc}(E)\,, \qquad (64)$$

where $\sigma_{non}(E)$ is the cross-section for nonelastic interactions of the primary particle with the kinetic energy E and the nucleus, N_{casc} is the average number of nucleons emitted from the nucleus during the cascade (fast) stage of the reaction, γ_x is the energy independent parameter, which value should be defined from the analysis of experimental data or from independent theoretical calculations, “x” refers to the type of the cluster knocked out.

The number of cascade nucleons N_{casc} was calculated by the CASCADE/INPE code. The γ_x value has been defined using the result of the ALICE/ASH code calculation at the primary proton energy around 100 MeV. The models describing the complex particle emission [204-206,221,222] implemented in the ALICE/ASH code have been tested and approved at this energy in many works [202-206,208].

Fig.42 shows the non-equilibrium component of the ^{4}He- production cross-section σ_α^{pre} calculated using Eq.(64) for ^{197}Au. There is a reasonable agreement between the σ_{α}^{pre} values calculated by the CASCADE/INPE and DISCA-S codes and available experimental data.

Eq.(64) has been used to obtain the contribution of the non-equilibrium emission in the total ^{4}He- and ^{3}He- production cross-sections at intermediate and high energies of incident protons. At proton energies below 100 MeV the values of σ_{α}^{pre} and $\sigma_{^3He}^{pre}$ have been calculated by the ALICE/ASH code. The contribution of the equilibrium emission in the ^{4}He- and ^{3}He- production cross-sections has been obtained using the CASCADE/INPE code. The obtained value of the γ parameter, Eq.(64) for ^{4}He-emission is equal to 4.75×10^{-2} for ^{56}Fe, 2.3×10^{-2} for ^{181}Ta, from 2.58×10^{-2} to 2.31×10^{-2} for various tungsten isotopes and 1.85×10^{-2} for ^{197}Au. The value of γ for ^{3}He is equal to 8.57×10^{-3} for ^{56}Fe, 4.49×10^{-3} for ^{181}Ta, from 5.3×10^{-3} to 4.34×10^{-3} for tungsten isotopes and 3.81×10^{-3} for ^{197}Au.

The total reaction cross-section for protons σ_{non} at high energies has been obtained using the evaluated data from Ref.[296]. At low and intermediate energies the σ_{non} value was calculated by the optical model with the potential from Ref.[131] and using the MCNPX code built-in routine [142].

The example of the ^{4}He- and ^{3}He- production cross-sections calculated for the p+^{197}Au reaction is shown in Fig.56 and Figs.44. There is a rather good agreement between the calculated cross-sections and experimental data [151,246,247,252,254, 263-266,268,297] in the whole energy region, where the measured data are available. The agreement is also observed with the values of cross-section predicted by the empirical systematics, Eqs.(56)-(60), Ref.[42], except the calculated ^{4}He- production cross-section at 18 and 90 MeV and ^{3}He- production cross-section at 62 MeV.

The ^{4}He- production cross-section calculated using the CASCADE/INPE code are shown also in Figs.44,47,51.

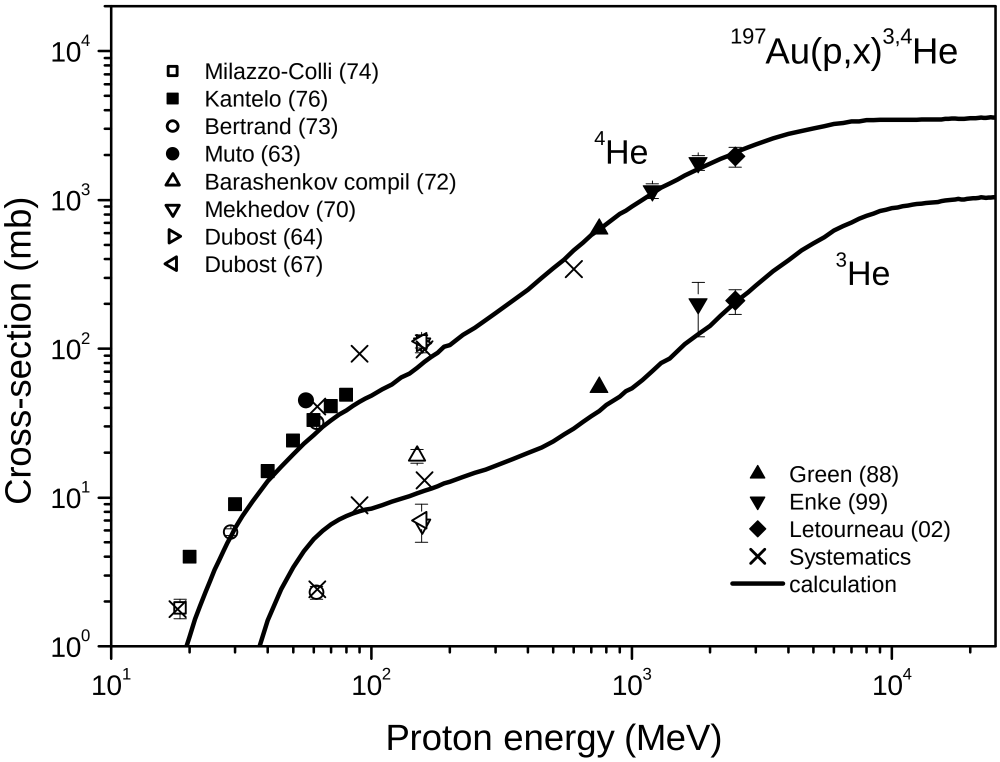

Fig.56 The α-particle and ^{3}He production cross-section for ^{197}Au calculated by the ALICE/ASH code and the CASCADE/INPE code, evaluated by the systematics, (^{4}He: Eqs.(56)-(60), ^{3}He: Ref.[194]) and measured in Refs.[151,246,247,252,254,263-266,268,297]. The data from Ref.[268] shown at 1.2 GeV were corrected for the ^{3}He contribution.

The results of calculations and available experimental data have been used for the evaluation of the helium production cross-section for iron, tantalum and tungsten. A rather small correction of theoretical curves was carried out to avoid the systematic difference between calculations and experiments.

4.2 Evaluation of helium production cross-section

The helium production cross-section has been calculated for ^{56}Fe, ^{181}Ta and tungsten isotopes ^{180}W, ^{182}W, ^{183}W, ^{184}W and ^{186}W.

4.2.1 Proton induced reactions

Fig.57 shows the ^{4}He- and ^{3}He- production cross-sections for ^{56}Fe calculated by the ALICE/ASH and CASCADE/INPE codes, the cross-sections evaluated by systematics, Eqs.(56)-(60), Ref.[194] and measured data [151,250,251,256,257,266, 298,299,300]. All measurements refer to natural iron, except the data [300] for ^{56}Fe. Data from Refs.[247,301] are not shown because the measurement has been performed with a high value of the cutoff energy for ^{4}He (14.26 MeV). The calculations were carried out using the ALICE/ASH code up to 200 MeV and by the CASCADE/INPE code in a whole energy region where experimental data exist. For the comparison the available data from ENDF/B-VI (Proton Sublibrary) and from JENDL-HE are shown. There is reasonable agreement between the calculated ^{4}He-production cross-section, systematics and experimental data. The agreement for ^{3}He is worse, and calculations as a whole overestimate the measured cross-sections. One should note, that the non-equilibrium component of helium isotope production cross-section has been calculated using the global systematics of parameters of the pre-compound model used in the ALICE/ASH code. The systematics has been obtained in Refs.[202,203] from the analysis of experimental data on the complex particle emission in nuclear reactions. The agreement between the results of calculations for ^{3}He can be improved by the appropriate choice of the pre-compound model parameters. From other side the observed difference does not essentially effect on the value of the total helium production cross-section because the contribution of ^{3}He is relatively small. The systematic deviation of the calculated and measured cross-section for the ^{3}He formation has been eliminated in the present work with the evaluation of the helium production cross-section.

Figs.58-60 show the ^{4}He- and total helium production cross-sections for ^{181}Ta calculated using the ALICE/ASH and CASCADE/INPE codes, measured in Refs.[252,263,267,268] and predicted by systematics. Experimental data for ^{3}He-production are not available. The detail view of the high energy region is given in Fig.60. There is the good agreement between calculations and experimental data.

The results obtained for natural tungsten are shown in Figs.61-63. The good agreement is observed between the σ_α and σ_{He} values calculated by the ALICE/ASH and CASCADE/INPE codes and the experimental data [266-268].

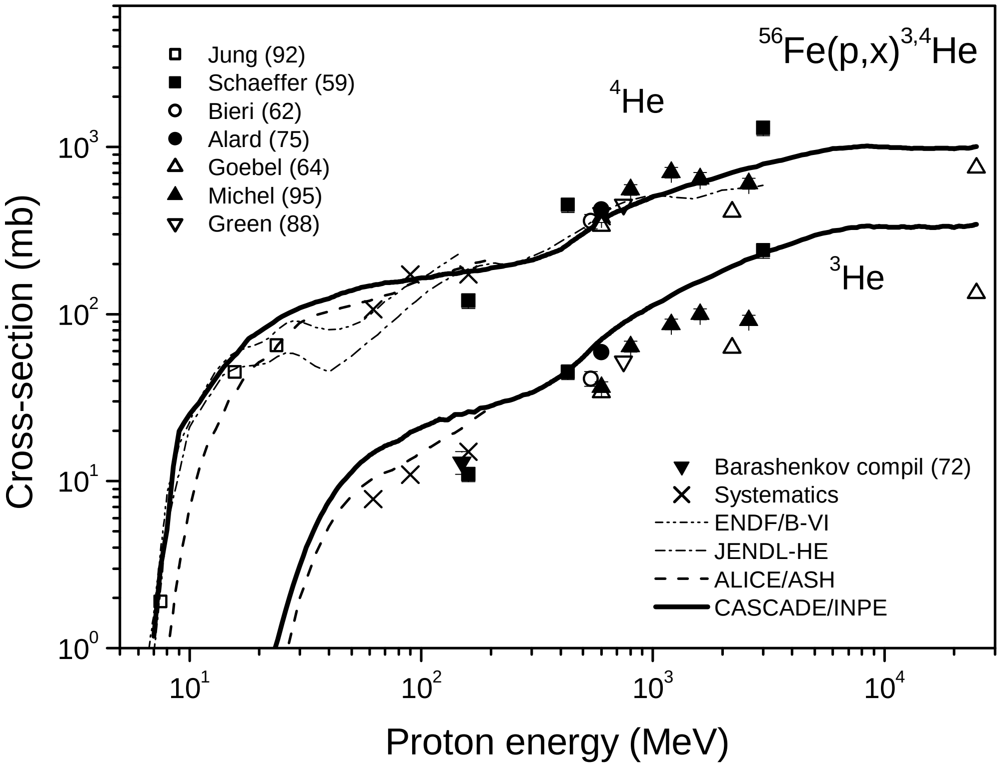

Fig.57 The α-particle and ^{3}He production cross-section for ^{56}Fe calculated by the ALICE/ASH code and the CASCADE/INPE code, evaluated by the systematics (^{4}He: Eqs.(56)-(60), ^{3}He: Ref.[194]) and measured in Refs.[151,250,251,256,257,266,298,299,300]. The α-particle production cross-sections from ENDF/B-VI and JENDL-HE are shown.

The evaluated helium production cross-sections are shown in Table 14. The data obtained can be used for the evaluation of the helium production rates in iron, tantalum and tungsten irradiated with protons with energies from several MeV up to 25 GeV.

Returning to the question about the difference in the helium production cross-sections measured for iron irradiated with 1.2 GeV- proton in Ref.[256] (792 mb) and in Ref.[268] (440 mb), one should note, that the evaluated value of the σ_{He} cross-section (634 mb, Table 14) is approximately on the middle. The data obtained in Ref.[268] seem underestimated because of the high value of minimal ^{4}He energy (10.8 MeV) adopted for the measurements. Calculations show that the energy 10.8 MeV lies in the region of the evaporation peak in the ^{4}He- emission spectrum, and the fraction of the ^{4}He nuclei emitted with energies below 10.8 MeV appears significant.

4.2.2 Neutron induced reactions

Experimental data for helium isotope production are absent at energies above 15 MeV for ^{181}Ta and for tungsten isotopes. The evaluation was based mainly on the results of calculations. Corrections were made at the energy below 15 MeV using the EXFOR data.

The (n,α) reaction cross-section for tungsten isotopes with A=180, 182 and 183 was taken from JEFF-3/A at the energies below 20 MeV. New evaluation was performed for the (n,α) reaction cross-section for ^{184}W and ^{186}W using the data from EXFOR (Section 3.3.2.2). The cross-sections for (n,nα) and (n,^{3}He) reactions were taken from JEFF-3/A. Evaluated helium production cross-sections are shown in Table 15.

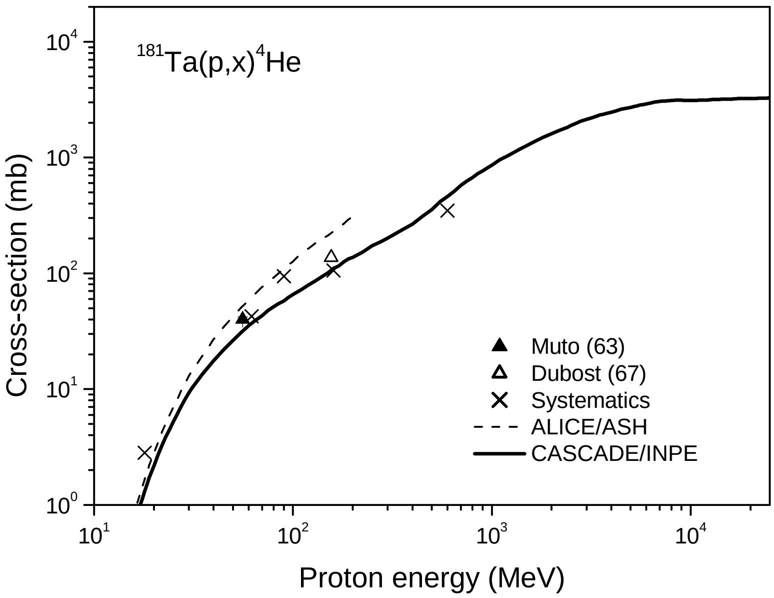

Fig.58 The α-particle production cross-section for ^{181}Ta calculated by the ALICE/ASH code and the CASCADE/INPE code, evaluated by the systematics (^{4}He: Eqs.(56)-(60), ^{3}He: Ref.[194]) and measured in Refs.[252,263]. The measured yield of α-particles having isotropic angular distribution [252] was added by the value obtained in Ref.[252] for heavy nuclei (Au, Bi) relating to anisotropic α-particle emission.

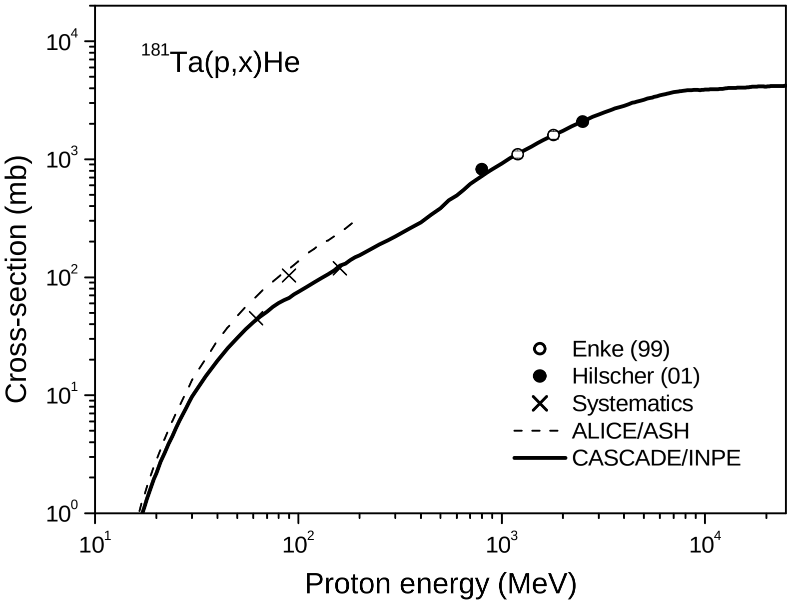

Fig.59 The helium production cross-section ($\sigma_{^3\mathrm{He}}$ + σ_α) for ^{181}Ta calculated by the ALICE/ASH code and the CASCADE/INPE code, evaluated by the systematics (^{4}He: Eqs.(56)-(60), ^{3}He: Ref.[194]) and measured in Refs.[267,268].

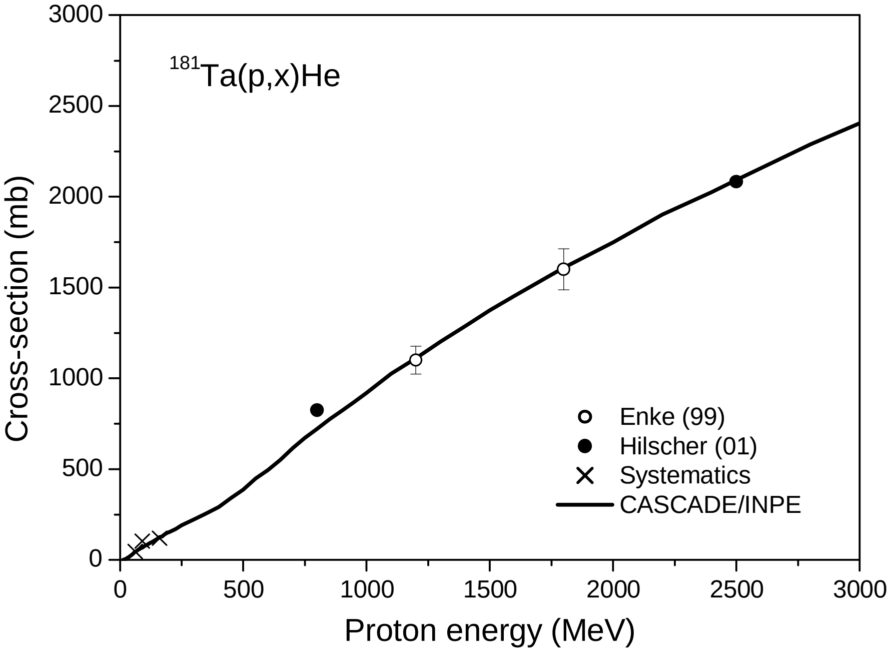

Fig.60 Detail view of the helium production cross-section for ^{181}Ta calculated at energies up to 3 GeV.

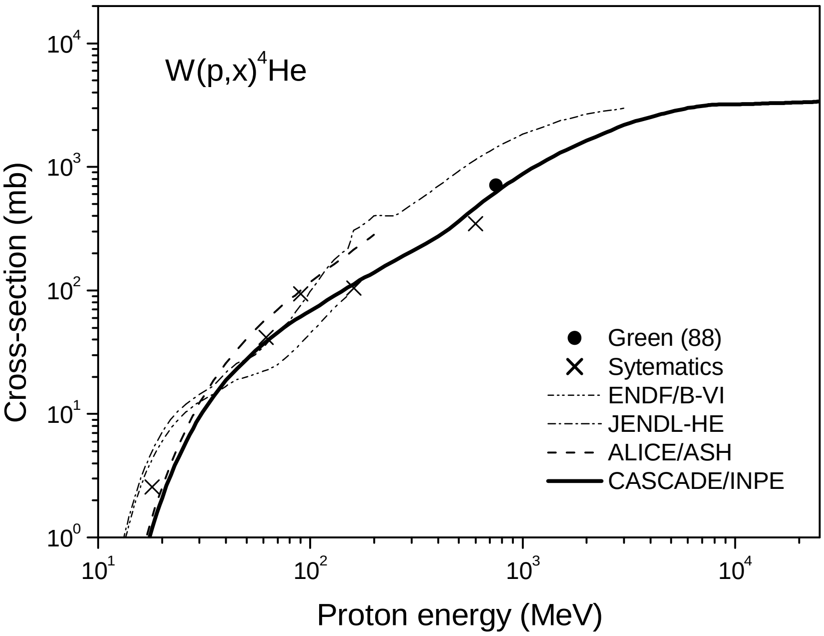

Fig.61 The α-particle production cross-section for natural tungsten calculated by the ALICE/ASH code and the CASCADE/INPE code, evaluated by the systematics (^{4}He: Eqs.(56)-(60), ^{3}He: Ref.[194]), measured in Ref.[266] and taken from ENDF/B-VI and JENDL-HE.

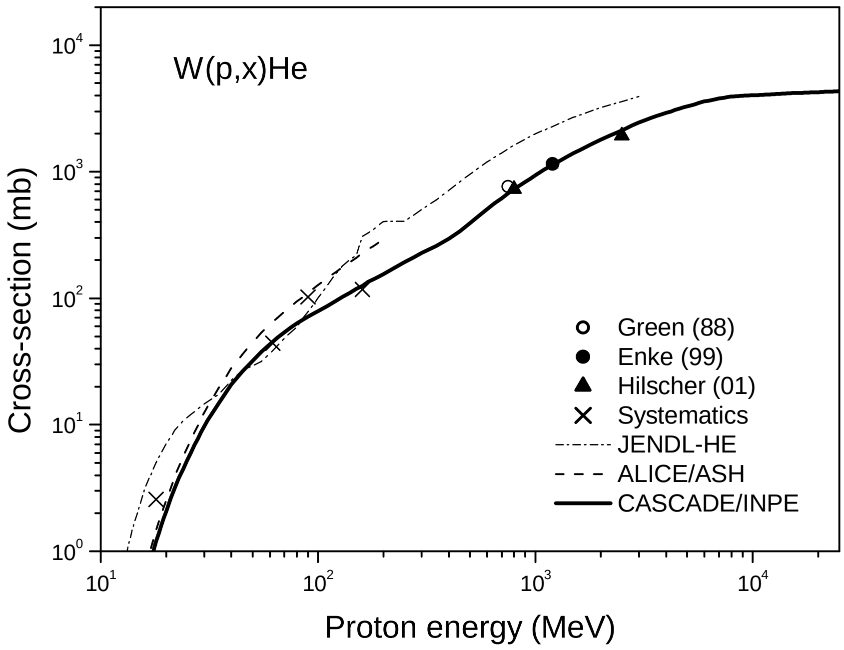

Fig.62 The helium production cross-section for natural tungsten calculated by the ALICE/ASH code and the CASCADE/INPE code, evaluated by the systematics (^{4}He: Eqs.(56)-(60), ^{3}He: Ref.[194]), measured in Refs.[266-268] and taken from JENDL-HE.

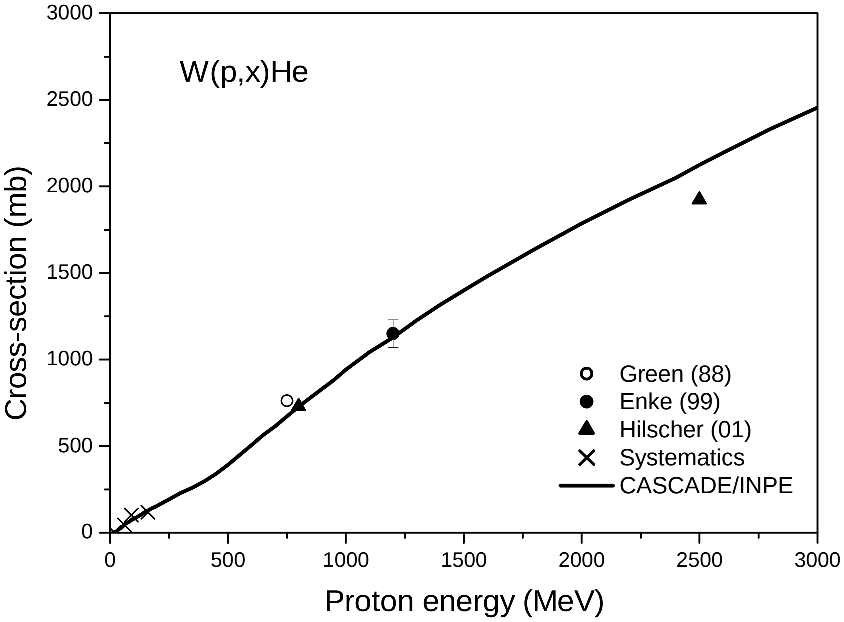

Fig.63 Detail view of the helium production cross-section for tungsten calculated at energies up to 3 GeV.

Table 14

The evaluated helium production cross-section ($\sigma_\alpha + \sigma_{^3He}$) for iron, ^{181}Ta and natural tungsten irradiated with protons at energies up to 25 GeV. The cross-sections between the energy points shown should be found by the linear(x)-log(y) interpolation at energies below 14 MeV, and by the linear-linear interpolation at energies above 14 MeV

Proton energy, MeV	Helium production cross-section (mb)		
	^{nat}Fe	^{181}Ta	^{nat}W
4	4.24×10^{-06}	1.03×10^{-09}	2.86×10^{-05}
5	6.90×10^{-04}	9.94×10^{-08}	5.88×10^{-05}
6	0.112	4.15×10^{-06}	2.26×10^{-04}
8	4.88	6.84×10^{-04}	1.86×10^{-03}
10	21.2	1.70×10^{-02}	1.43×10^{-02}
12	31.4	0.135	8.85×10^{-02}
14	43.4	0.548	0.391
16	45.3	1.42	1.20
18	50.4	2.82	2.57
20	55.4	3.98	4.18
22	60.6	5.22	5.92
24	65.9	6.52	7.24
26	75.1	8.09	8.69
28	82.4	9.66	10.3
30	91.2	11.7	12.2
35	102.	16.9	17.1
40	109.	23.4	22.8
50	121.	37.2	34.3
60	131.	50.2	46.2
70	141.	61.3	57.1
80	149.	72.0	68.2
90	165.	82.4	79.3
100	172.	92.4	89.5
120	181.	113.	111.
150	188.	144.	144.

Table 14 continued

200	201.	195.	202.
250	213.	246.	254.
300	226.	296.	306.
350	246.	346.	353.
400	266.	396.	399.
450	300.	446.	446.
500	335.	496.	493.
550	370.	548.	543.
600	406.	598.	593.
650	435.	649.	646.
700	464.	700.	698.
750	481.	751.	762.
800	507.	824.	805.
850	525.	836.	848.
900	544.	870.	891.
950	561.	906.	934.
1000	580.	940.	978.
1200	634.	1100.	1150.
1500	712.	1370.	1350.
2000	807.	1750.	1680.
2500	895.	2080.	1920.
3000	966.	2400.	2310.
4000	1060.	2840.	2860.
5000	1150.	3200.	3260.
6000	1210.	3480.	3580.
7000	1240.	3710.	3790.
8000	1250.	3830.	3920.
10000	1250.	3910.	4010.
15000	1230.	4040.	4170.
20000	1230.	4130.	4240.
25000	1250.	4210.	4330.

Table 14

The evaluated helium production cross-section ($\sigma_\alpha + \sigma_{^3He}$) for ^{181}Ta and natural tungsten irradiated irradiated with neutrons at energies from 5 MeV up to 1 GeV. (Data below 5 MeV can be found in JEFF-3/A.)

Neutron energy (MeV)	Helium production cross-section (mb)	
	^{181}Ta	^{nat}W
5	1.49×10^{-05}	2.88×10^{-03}
6	1.73×10^{-04}	5.41×10^{-03}
7	6.27×10^{-04}	1.15×10^{-02}
8	3.26×10^{-03}	2.54×10^{-02}
9	1.00×10^{-02}	5.88×10^{-02}
10	3.36×10^{-02}	0.132
11	8.00×10^{-02}	0.304
12	0.182	0.609
13	0.335	0.987
14	0.570	1.42
14.5	0.719	1.65
15	0.868	1.88
16	1.23	2.42
17	1.71	2.98
18	2.28	3.49
19	2.91	4.06
20	3.61	4.79
22	5.18	6.03
24	6.94	8.02
26	8.87	10.2
28	11.0	12.5

Table 14 continued

30	13.1	14.9
35	18.9	21.0
40	25.0	26.3
45	31.1	31.6
50	36.7	35.7
60	47.2	43.5
70	57.2	51.5
80	65.9	60.0
90	72.8	66.2
100	78.5	73.2
120	91.2	86.7
150	112.	109.
200	152.	151.
250	200.	194.
300	248.	245.
400	362.	365.
500	480.	477.
600	590.	586.
700	697.	695.
800	801.	807.
900	870.	905.
1000	939.	977.

4.3 Basic features of the helium production cross-section

The calculations performed make it possible to describe basic properties of the helium production cross-section. For the heavy nuclei (Ta, W, Au) the non-equilibrium emission of ^{4}He and ^{3}He nuclei gives the main contribution in the helium yield at energies below 80-100 MeV. With an increase of the primary proton energy the contribution of the non-equilibrium emission in the σ_{He} cross section decreases to 50 % at the energy 300 MeV and to ~ 20 % at energy 3 GeV. At the energy above 3 GeV the non-equilibrium fraction of the helium production cross-section barely changes. The total helium production cross section is almost linear function of the primary particle energy in the range from 200 MeV to 1.5 GeV. At the energy above 1.5 GeV the growth of the cross-section is slowed down and the σ_{He} value reaches “saturation” at the energy 8-10 GeV. In the energy region above 10 GeV, the cross-section does not change noticeably. For iron the energy dependence of the σ_{He} cross-section is more complex function. As for heavy nuclei, the σ_{He} value reaches the saturation at energies 5-6 GeV.

4.4 Summary about the evaluation of the helium production cross-section at intermediate and high energies

The helium production cross-section has been evaluated for iron, ^{181}Ta and natural tungsten at proton energies from several MeV to 25 GeV and for ^{181}Ta and tungsten at neutron energies up to 1 GeV.

The results of model calculations and available experimental data have been used for the cross-section evaluation. Main calculations have been carried out using the CASCADE/INPE code. The non-equilibrium component of the ^{4}He- and ^{3}He-production cross-sections has been obtained by Eq.(64). The value of the γ parameter was defined using the results of the ALICE/ASH code calculations.

The evaluated data are shown in Table 14 and 15. Data can be used for the calculation of the helium production rate in iron, tantalum and tungsten irradiated in various high energy units.

5. Modified intranuclear cascade evaporation model with detailed description of equilibrium particle emission

The modified intranuclear cascade evaporation model combining the Monte Carlo method for the simulation of non-equilibrium particle emission and deterministic algorithm for the description of equilibrium de-excitation is discussed in this Section. The model has been used for the analysis of radionuclide yields in proton induced reactions at energies from 0.8 to 2.6 GeV. The results of calculations show the advantage of the model proposed in accuracy of predictions comparing with other popular intranuclear cascade evaporation models.

During last decades intranuclear cascade evaporation model was successfully used for the prediction of nuclear reactions characteristics: energy and angular distributions of emitted particles, excitation functions, yields of fission fragments, residual recoil spectra and others.

The model consists of two parts, whose development historically occurred independently of each other: the intranuclear cascade model, which describes non-equilibrium processes in the nucleus, and statistical evaporation model. Progress in the description of intranuclear interactions is connected, mostly, to creation of the “time-dependent” models [149,286], the approaches modeling in details the density distribution of nucleons in the nucleus [158,286], the combination of the intranuclear cascade and precompound exciton models [152] and with the development of the model considering the interactions with “preformed” clusters (Section 3.1.2.1).

Traditionally, a number of approximations was used in the simulation of equilibrium process, whose need was caused by limited power of computers. The use of the simplest models for calculating the nuclear level density [138,162], the “sharp-cut off” approach to the inverse reaction cross-section calculation [138,184,238], other simplifications, which make it possible to obtain analytical expressions for calculating particle emission widths [151,302], can be attributed to these approximations. The simplified models are used in all popular codes implementing the intranuclear cascade evaporation model [142,302]. At the same time, the modern computer technology makes it possible to use more rigorous and advanced models for the simulation of the equilibrium particle emission using intranuclear cascade evaporation model.

This paper describes the intranuclear cascade evaporation model avoiding lacks of usual simplifications [138,142,151,162,184,238,302] in the modelling of equilibrium particle emission. The nuclear level density is calculated using the generalized superfluid model with parameters fitted to cumulative number of low-lying levels and observed neutron resonance densities [191,193]. Inverse reaction cross-sections are obtained by the optical model without “sharp-cut off” approximation. No simplification is made to get particle emission widths at low and high energy of excitation.

The proposed intranuclear cascade evaporation model is used for the calculation of the radionuclide yields in nuclear reactions induced by protons with energy of 0.8 – 2.6 GeV. The results are compared with experimental data and calculations performed using different intranuclear cascade evaporation model [142]: the Dresner [163] and ABLA [164] evaporation models combined with the Bertini [144], ISABEL [148,149] and INCL4 [158] intranuclear cascade models, as with help of the CEM2k [142,154] and CASCADE [286,287] models.

5.1 *Model description*

5.1.1 *Equilibrium model*

The modeling of equilibrium emission is performed without the consideration of angular momentum, what is the simple consequence of the limited power of computers. The particle emission rate is calculated as follows [200]

$$W_x(\varepsilon_x) = \frac{(2S_x+1)\mu_x\,\varepsilon_x}{\pi^2\,\mathbf{h}^3}\sigma_x^{inv}(\varepsilon_x)\,\frac{\rho(Z',A',U)}{\rho(Z,A,E)}, \tag{65}$$

where S_x, μ_x and ε_x are respectively spin, reduced mass and energy of the emitted particle, σ_x^{inv} is the inverse reaction cross-section, ρ(Z’,A’,U) is the nuclear level density for residual nucleus with the excitation energy U, ρ(Z,A,E) is the level density for the nucleus emitting the x-particle, E is the excitation energy.

The nuclear level density is calculated according to the generalized superfluid model [193]

$$\rho(U) = \rho_{qp}(U')K_{vib}(U')K_{rot}(U'), \tag{66}$$

where $\rho_{qp}(U')$ is the density of quasi-particle nuclear excitation [193], $K_{vib}(U')$ and $K_{rot}(U')$ are the vibrational and rotational enhancement factors at the effective energy of excitation U’ calculated according to Refs.[191,192].

The nuclear level density parameters are calculated according to Eq.(35). The shell correction to the mass formula, δW is using the liquid drop model [303], $\varphi(U)= 1-\exp(-\gamma U)$, $\gamma=0.4/A^{1/3}$ MeV^{-1}. The asymptotic value of nuclear level parameter is equal to

$$\tilde{a} = A(0.073 + 0.115A^{-1/3}) \tag{67}$$

The effective energy of excitation U’, the critical energy of the phase transition U_{cr} and the condensation energy E_{cond} are calculated as follows

$$U' = U - n\Delta_0, \quad (68)$$

$$U_{cr} = 0{,}472\, a(U_{cr})\Delta_0^2 - n\Delta_0, \quad (69)$$

$$E_{cond} = 0{,}152\, a(U_{cr})\Delta_0^2 - n\Delta_0, \quad (70)$$

The correlation function Δ_0 is equal to

$$\Delta_0 = 12A^{-1/2} \quad (71)$$

where n=0 for even-even nuclei, n=1 for nuclei with odd A value, n=2 for odd-odd nuclei.

The inverse reaction cross-section σ_x^{inv} is calculated by the optical model. The parameters of the optical potentials for nucleons and light charged fragments are discussed in Refs.[199,208]. The calculated σ_x^{inv} cross-section values are used in the integration of particle emission rates, Eq.(65).

The probability of the photon emission is calculated according to Weisskopf-Ewing model [200] with the photon absorption cross-section parameterized in Ref.[304]. The fission probability is calculated using the Bohr-Wheeler approach [305]. The distribution of fission fragments is calculated according to Ref.[209].

The discussed model is implemented in the computer code following Refs.[306,307]. The non-equilibrium particle emission is modelled by the Monte Carlo method using the intranuclear cascade model. The emission of fast particles for each Monte Carlo history results to the creation of residual nucleus with a certain atomic and mass numbers Z, A, with the excitation energy U. For the residual nucleus (Z,A,U) the calculation of reaction products is performed using the “deterministic” algorithm by the common integration of particle emission rates, without resorting to Monte Carlo. This method is more time consuming than usual intranuclear cascade evaporation algorithm, but that less consuming than the deterministic integration of all non-equilibrium and equilibrium particle emission rates. The advantage of the method consists of the relative simplicity and fast implementation in the computer code, since the routines describing the equilibrium emission in the widely used and verified computer codes, as STAPRE [308], GNASH [177], ALICE [201], etc. can be used for this purpose.

In the present work the calculations are performed using the equilibrium algorithm from the modified ALICE code [201].

5.1.2 Non-equilibrium model

The non-equilibrium particle emission is described using the intranuclear cascade model implemented in the CASCADE (Dubna) code [287]. Below, this model combined with the equilibrium model described in Section 5.1.1 is denoted by CASCADE/ASF.

5.2 Comparison of calculations with experimental data

The detail and adequate information, which can be used for the demonstration of predictive power of the equilibrium model combined with intranuclear cascade model, are the measured yields of radionuclides. By a principle of “random selection” we take the results of recent measurements of the radionuclide yield in the irradiation of ^{59}Co and ^{184}W by protons with the energy from 0.8 to 2.6 GeV [309].

The calculations were performed using the model discussed in Section 5.1 and by various intranuclear cascade evaporation models: the CASCADE [286,287] and CEM2k [142,154] models, the Bertini [144], ISABEL [148] and INCL4 [158] models combined with the Dresner [163] and ABLA [164] evaporation models. All four evaporation models considered (Dresner, ABLA, CASCADE and CEM2k) use a certain approximations in modelling of equilibrium particle emission: the Fermi gas model for the level density calculation [138,142,151,162], the “sharp cut-off” formulas for inverse cross-sections [238], other simplifications justified only at high excitation energies [151].

The calculated radionuclide yields were normalized on the values of the nonelastic cross-sections for proton interactions with nuclei, calculated by MCNPX [142] (Tables 15,16). The equal number of Monte Carlo histories was used in the simulations by different models. The cumulative cross-sections were obtained using the decay data from FENDL/D-2. The unknown isomeric cross-section ratios were taken equal to 0.5.

The quantification of the agreement between calculations and measured data has been done using the F-deviation factor [162,309,311]

$$F = 10^{\left(\frac{1}{N}\sum_{i=1}^{N}\left[\log(\sigma_i^{exp})-\log(\sigma_i^{calc})\right]^2\right)^{1/2}}, \tag{72}$$

For illustration purposes one can use also other deviation factors [310]

$$H = \left(\frac{1}{N}\sum_{i=1}^{N}\left(\frac{\sigma_i^{exp}-\sigma_i^{calc}}{\Delta\sigma_i^{exp}}\right)^2\right)^{1/2}, \tag{73}$$

$$D = \frac{1}{N}\sum_{i=1}^{N}\left|\frac{\sigma_i^{exp}-\sigma_i^{calc}}{\sigma_i^{exp}}\right|, \tag{74}$$

$$R = \frac{1}{N}\sum_{i=1}^{N}\frac{\sigma_i^{calc}}{\sigma_i^{exp}}, \tag{75}$$

where σ_i^{exp} and $\Delta\sigma_i^{exp}$ are the measured cross-section and its uncertainty, σ_i^{calc} is the calculated cross-section, N is the number of the experimental points.

The F - criterion [162,309,311], Eq.(72) is the most adequate for the comparative analyses of different calculations, taking into account that the measured yields are known only for the limited number of residual nuclei. In this case, the F - factor reproduces the systematic underestimation as the overestimation of the results of calculations compared with experimental data. In other criteria, Eqs.(73)-(75) the underestimation of the σ_i^{calc} values has an “advantage” compared with overestimation of the results. For this reason, in spite of the clarity of Eqs.(73)-(75), these criteria are of secondary importance and used in the present work for an illustrative purpose only.

Tables 15,16 show the values of different deviation factors obtained from the comparison of calculations with the experimental data [309]. Taking into account, that the use of the systematics Eq.(67) is justified for medium and heavy nuclei, the consideration is limited by the yields of residual nuclei with Z > 20. For an illustration, Fig.64 shows the absolute values of radionuclide yields calculated by the proposed CASCADE/ASF model and the Bertini/Dresner model and measured in Ref. [309] for ^{184}W irradiated with 1.6 GeV protons.

The comparison shows that the substitution of the original evaporation algorithm in the CASCADE code [286,287] by the model described in Section 5.1.1 results in a noticeable gain in accuracy of predictions. In most cases the model discussed is also the best comparing with other models (Tables 15,16, Fig.64).

5.3 Summary about modified intranuclear cascade evaporation model with detailed description of equilibrium particle emission

The modified intranuclear cascade evaporation model combining the Monte Carlo method for the simulation of non-equilibrium particle emission and deterministic algorithm for the description of equilibrium de-excitation was discussed. The nuclear level density for equilibrium states was calculated using the generalized superfluid model taking into account collective enhancement of the nuclear level density in addition to shell and superfluid effects [191,193]. The inverse reaction cross-sections were calculated by the nuclear optical model. Calculations were performed without additional simplifications [151,302], usually applied in the simulation of evaporation particle cascade at high energies.

The model proposed has been used for the analysis of radionuclide yields in the proton induced reaction at energies 0.8-2.6 GeV. The results of calculations show the definite advantage of the model in accuracy of predictions in comparison with other intranuclear cascade evaporation models [142,287].

Table 15

The results of the comparison of experimental data [309] with calculations for ^{59}Co irradiated with 1.2 – 2.6 GeV protons. The cross-section of nonelastic proton interaction σ_{non} is shown. The best results are underlined.

Factor	Bertini/ Dresner	Bertini/ ABLA	ISABEL/ Dresner	ISABEL/ ABLA	INCL4/ Dresner	INCL4/ ABLA	CEM2k	CASCADE (original)	CASCADE/ ASF (this work)
Proton energy 1.2 GeV, number of points 20, σ_{non} = 772 mb									
H	4.87	15.85	4.58	21.17	4.16	20.35	6.52	12.79	6.02
D	0.32	0.81	0.28	1.10	0.25	1.02	0.41	0.60	0.36
R	0.70	1.50	0.89	1.83	0.91	1.78	0.93	1.12	1.10
F	1.74	2.07	1.58	2.31	1.56	2.21	1.78	2.52	1.50
Proton energy 1.6 GeV, number of points 20, σ_{non} = 773 mb									
H	4.51	13.79	5.66	23.16	4.30	20.05	5.82	11.80	5.51
D	0.33	0.81	0.33	1.27	0.25	1.13	0.37	0.59	0.37
R	0.71	1.43	1.01	2.04	0.95	1.87	0.84	1.11	1.09
F	1.96	2.11	1.65	2.45	1.51	2.30	1.78	2.38	1.48
Proton energy 2.6 GeV, number of points 20, σ_{non} = 770 mb									
H	4.29	13.71	5.78	28.15	4.42	26.00	5.23	10.26	5.51
D	0.32	0.80	0.34	1.63	0.27	1.45	0.36	0.58	0.37
R	0.71	1.42	1.15	2.38	1.03	2.23	0.80	1.08	1.08
F	1.76	2.11	1.55	2.75	1.47	2.55	1.86	2.31	1.49
All energies, number of points 60									
H	4.56	14.48	5.37	24.34	4.29	22.30	5.88	11.66	5.69
D	0.32	0.81	0.32	1.33	0.26	1.20	0.38	0.59	0.37
R	0.71	1.45	1.02	2.08	0.96	1.96	0.86	1.10	1.09
F	1.82	2.10	1.59	2.50	1.51	2.35	1.81	2.40	1.49

Table 16

The results of the comparison of experimental data [309] with calculations for ^{184}W irradiated with 0.8 and 1.6 GeV protons. The cross-section of nonelastic proton interaction σ_{non} is shown. The best results are underlined.

Factor	Bertini/ Dresner	Bertini/ ABLA	ISABEL/ Dresner	ISABEL/ ABLA	INCL4/ Dresner	INCL4/ ABLA	CEM2k	CASCADE (original)	CASCADE/ ASF (this work)
Proton energy 0.8 GeV, number of points 67, σ_{non} = 1636 mb									
H	5.08	5.04	5.05	5.35	5.56	6.18	4.85	4.72	4.34
D	0.38	0.39	0.37	0.38	0.41	0.43	0.38	0.39	0.33
R	0.83	0.83	0.78	0.78	0.75	0.75	0.80	0.78	0.86
F	1.76	2.28	2.13	2.24	2.20	2.54	2.89	1.65(1)	<u>1.57</u>
Proton energy 1.6 GeV, number of points 91, σ_{non} = 1687 mb									
H	6.89	5.67	5.45	5.91	5.25	6.08	5.88	4.90	4.51
D	0.48	0.44	0.44	0.44	0.38	0.40	0.45	0.35	0.33
R	0.87	0.89	0.80	0.83	0.79	0.85	0.89	0.83	0.87
F	1.87	2.63	2.60	2.83	2.73	2.57	3.60	2.85(2)	<u>1.69</u>
All energies, number of points 158									
H	6.19	5.41	5.28	5.68	5.38	6.12	5.47	4.82	4.44
D	0.44	0.42	0.41	0.41	0.39	0.41	0.42	0.37	0.33
R	0.85	0.86	0.79	0.81	0.77	0.81	0.85	0.81	0.87
F	1.82	2.48	2.40	2.58	2.51	2.56	3.30	2.39(3)	<u>1.64</u>

(1) number of points (N) is equal to 58

(2) N is equal to 86

(3) N is equal to 144

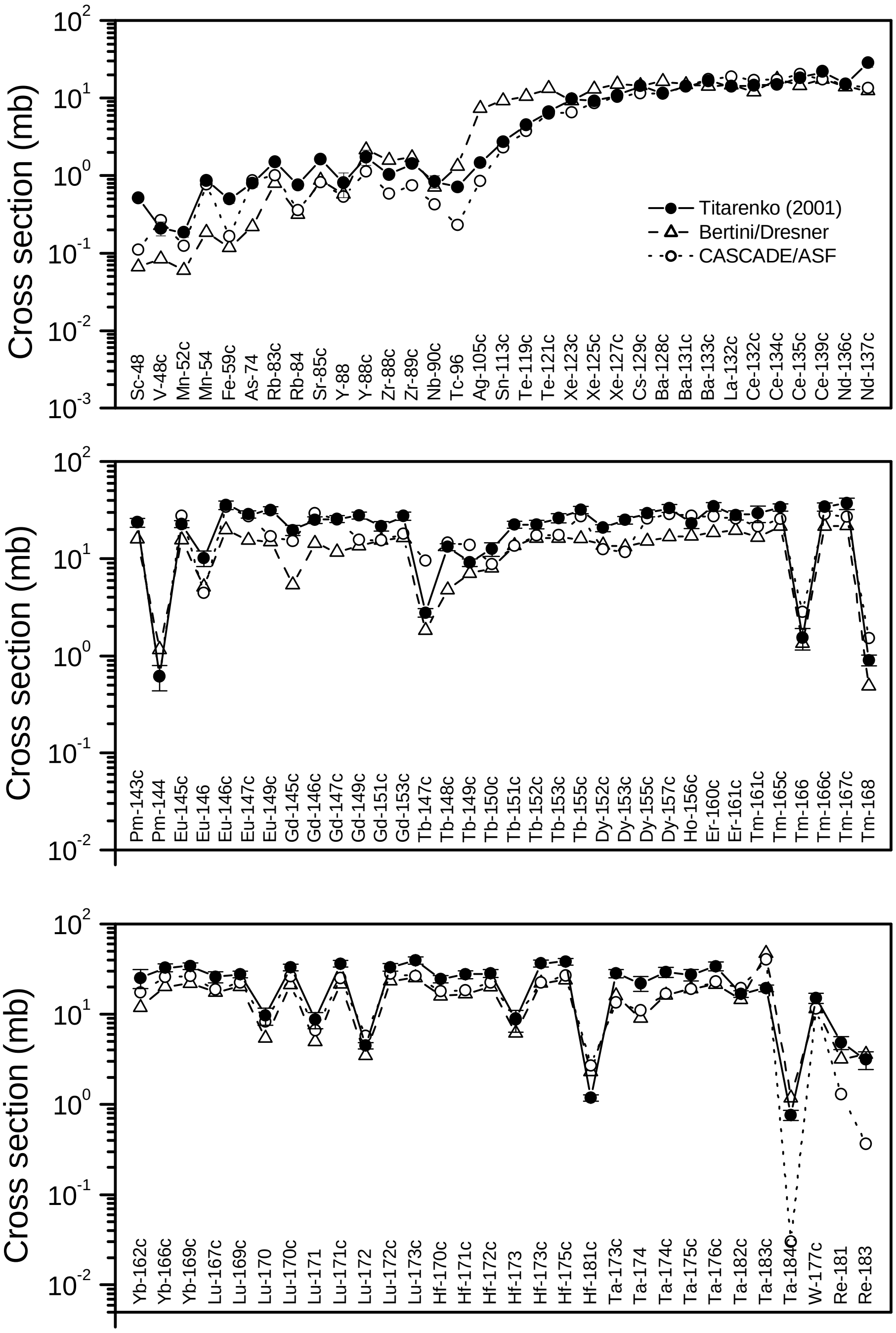

Fig.64 The radionuclide production cross-sections calculated by the proposed CASCADE/ASF model and the Bertini/Dresner model for ^{184}W irradiated with 1.6 GeV protons and measured in Ref.[309]. Cumulative yields are indicated. If the calculated value is absent, it coincides with the experimental point. The difference between two calculations for residual nuclei with atomic mass number close to 184 is rather due to the difference in intranuclear cascade models and not in evaporation ones.

6. Phenomenological model for non-equilibrium deuteron emission in nucleon induced reaction

Deuteron emission gives a noticeable contribution in the total hydrogen production cross-section for heavy and light nuclei (Fig.65). At the same time the theoretical description of the emission of deuterons is the most complicated comparing with other hydrogen isotopes [222]. The biggest problem is the description of the non-equilibrium deuteron emission.

A new approach is proposed for the calculation of non-equilibrium deuteron energy distributions in nuclear reactions induced by nucleons of intermediate energies. It combines the model of the nucleon pick-up, the coalescence and the deuteron knock-out. The calculated deuteron energy distributions are compared with experimental data from ^{12}C to ^{209}Bi.

Nine years ago a paper [206] was published concerning the precompound deuteron emission in nuclear reactions induced by nucleons of intermediate energies. The model proposed has been one of the first applications of the coalescence pick-up model [221,222] and the first application of the hybrid model [199] to the description of the non-equilibrium deuteron emission in nuclear reactions.

The model [206] was in a peculiar competition with the model of the complex particle emission [189] formulated basing on the theory of the pre-equilibrium particle emission. During long time both models [189,206] were used for the qualitative description of deuteron spectra in nucleon induced reactions. The need in reliable nuclear data at primary nucleon energies up to 150 MeV [218,312,313] in a new way raised a question about the accuracy of model calculations. The requirement of quantitative description of nuclear reaction characteristics has acquired a special importance. The pre-equilibrium exciton model [189] has been renewed in

Refs.[314,335] and the success of the improved model in the calculation of complex particle emission spectra has been demonstrated in Refs.[315-317].

The present work concerns the further development of the approach [206] formulated basing on the exciton coalescence pick-up model [222] and the hybrid model [199].

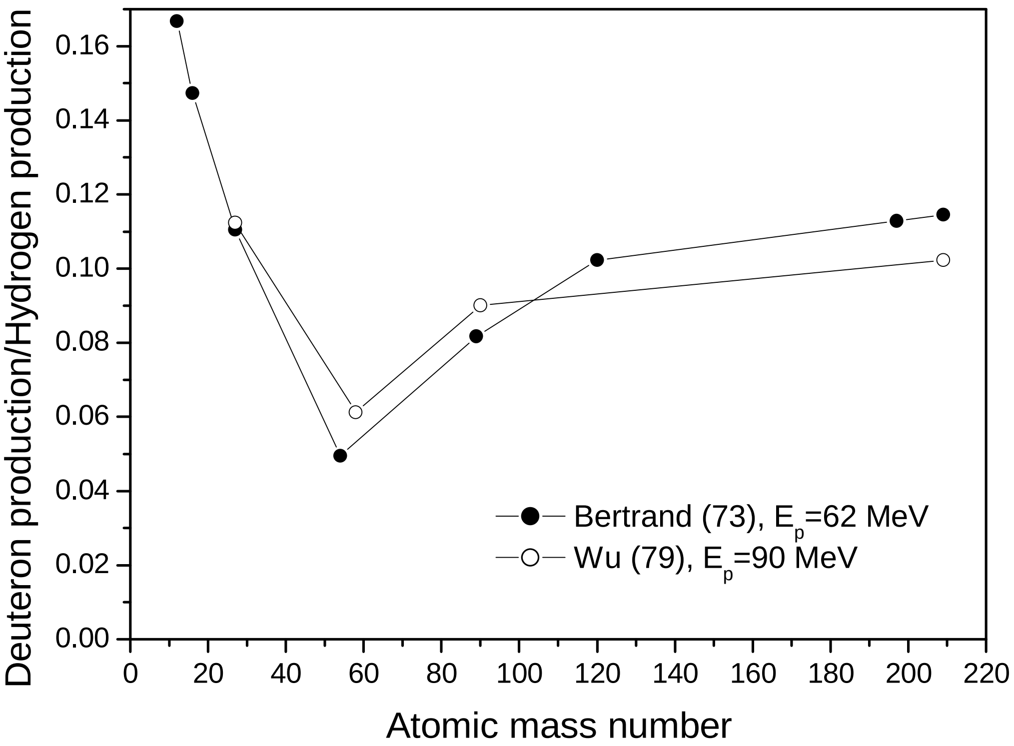

Fig.65 Contribution of deuterons in the total hydrogen production cross-section (sum of the proton, deuteron and triton contribution) obtained from the experimental data for different nuclei irradiated with 62 MeV [247] and 90 MeV [248] protons.

6.1 Model description

Both approaches [189,206] describing the non-equilibrium deuteron emission neglect of the final size of the nuclear potential well. Taking it into account, one obtains that the level density of the final state corresponding to the direct nucleon pick-up, $\omega(0p,1h,U)$ [189,206] is different from zero only at the energy of the residual excitation below the Fermi energy. It immediately results to a noticeable discrepancy of measured data and deuteron emission spectra calculated by both approaches [189, 206]. Formally, the pick-up component with the (0p,1h) final state can be referred to the high energy tail of the deuteron emission spectrum, which usually has a peak in the measured energy distribution [247,248]. The DWBA calculation [318] confirms this qualitative consideration.

This fact makes it necessary to search for other principles for the formulation of the pre-equilibrium model of the deuteron emission. Return to the coalescence model of Ribanský, Obložinský [244], which is used up to now for the analysis of complex particle emission [319], cannot be fully justified for reasons discussed and investigated in details in Refs.[221,222]. Most likely, it is necessary to search for the solution in a combination of the models describing different nuclear processes resulting to the deuteron emission, which physical validity meets no serious objections.

In the present work, it is supposed that the non-equilibrium deuteron emission in nucleon induced reactions results from: i) the pick-up of nucleon with the energy below the Fermi energy (E_F) after the formation of the (2p,1h) initial exciton state, ii) the coalescence of two excited nucleons with energies above E_F, iii) the knock-out of the “preformed” deuteron, iv) the direct process resulting in the deuteron formation and escape. The non-equilibrium deuteron spectrum is calculated as a sum of different components

$$\frac{d\sigma}{d\varepsilon_d} = \frac{d\sigma^{P-U,C}}{d\varepsilon_d} + \frac{d\sigma^{K-O}}{d\varepsilon_d} + \frac{d\sigma^{D}}{d\varepsilon_d} \quad , \tag{76}$$

where the first term relates to the pick-up and the coalescence after the formation of the (2p,1h) exciton state, the second component describes the contribution of the deuteron knock-out and the last term relates to the direct process.

The analytical expressions for each component of the deuteron emission spectrum were obtained using basic statements of the hybrid model [199].

The exciton level density is calculated following Bĕták and Dobeš [220] taking into account the finite depth of the nuclear potential well

$$\omega(p,h,E) = g^p \tilde{g}^h \sum_{k=0}^{h} {}_hC_k \, (-1)^k \;\; \Theta(E - k\,E_F) \frac{(E - k\,E_F)^{n-1}}{p!h!(n-1)!} \tag{77}$$

where “p” is the number of particles; “h” is the number of holes; “n” is equal to the sum of “p” and “h”; E is the energy of the excitation; E_F is the Fermi energy; g and $\tilde{g}$ are the single level density for particles and holes, respectively; Θ(x) is the Heaviside function, Θ = 0 for x < 0 and Θ = 1 for x > 0.

The single level density for particles and holes are calculated according to Ref.[220]

$$g = A/14, \tag{78}$$

$$\tilde{g} = A / E_F \tag{79}$$

The surface nucleus effects [320,321] make an influence on the effective value of the Fermi energy E_F used for the calculation of precompound particle spectra. It is discussed below.

6.1.1 Pick-up and coalescence

The exciton coalescence pick-up model proposed in Refs.[221,222] is used for the calculation of the $d\sigma^{P\text{-}U,C}/d\varepsilon_d$ spectrum component [206]

$$\frac{d\sigma^{P-U,C}}{d\varepsilon_d} = \sigma_{non}(E_0)$$

$$\times \sum_{n=n_0} \sum_{k+m=2} F_{k,m}(\varepsilon_d + Q_d)\, \frac{\omega(p-k,h,U)}{\omega(p,h,E)}\, \frac{\lambda_d^e(\varepsilon_d)}{\lambda_d^e(\varepsilon_d)+\lambda_d^+(\varepsilon_d)}\, g_d\, D(n), \tag{80}$$

where σ_{non} is the cross-section of nonelastic interaction of the nucleus and the primary nucleon with the kinetic energy E_0; $F_{k,m}$ is the deuteron formation factor equal to the probability that the deuteron is composed of “k” particles above the Fermi level and “m” particles below; the residual excitation energy U is equal to $E - Q_d - \varepsilon_d$, and E is the excitation energy of the composite nucleus, Q_d is the separation energy for the deuteron; ε_d is the channel emission energy corresponding to the deuteron emission; λ_d^e is the deuteron emission rate; λ_d^+ is the intranuclear transition rate for the absorption of the formed deuteron in the nucleus; g_d is the density of single states for the deuteron; D(n) is the factor describing the “depletion” of the n-exciton state due to the particle emission; n_0 is the initial exciton number, ($n_0 = 3$).

The deuteron emission rate is calculated with the following formula

$$\lambda_d^e = \frac{(2S_d+1)\mu_d\, \varepsilon_d\, \sigma_d^{inv}(\varepsilon_d)}{\pi^2 \mathbf{h}^3 g_d}, \tag{81}$$

where S_d and μ_d are spin and reduced mass of the outgoing deuteron; σ_d^{inv} is the inverse reaction cross-section for deuteron. The deuteron absorption rate is equal to

$$\lambda_d^+ = 2W_d^{opt}/\mathbf{h}, \tag{82}$$

where W_d^{opt} is the imaginary part of the optical potential for deuteron.

The form factors of the deuteron formation $F_{k,m}$ were calculated in Ref.[222] for the effective nuclear radius with the dR parameter value equal to 1 fm. The original values [222] are approximated and presented as follows

$$
F_{1,1}(\varepsilon) = \begin{cases} -1.409\cdot 10^{-2}\varepsilon + 0.6 & \text{for } \varepsilon \le 30\,\text{MeV} \\ 1.377\cdot 10^{-4}\varepsilon^2 - 1.807\cdot 10^{-2}\varepsilon + 0.5946 & \text{for } 30 < \varepsilon \le 65\,\text{MeV} \\ 0 & \text{for } \varepsilon > 65\,\text{MeV} \end{cases}, \qquad (83)
$$

$$
F_{2,0}(\varepsilon) = 0.6 - F_{1,1}(\varepsilon) \qquad (84)
$$

As an illustration, Fig.66 shows the pick-up and coalescence contribution in the deuteron emission spectrum for ^{54}Fe and ^{197}Au irradiated with 61.5 MeV protons.

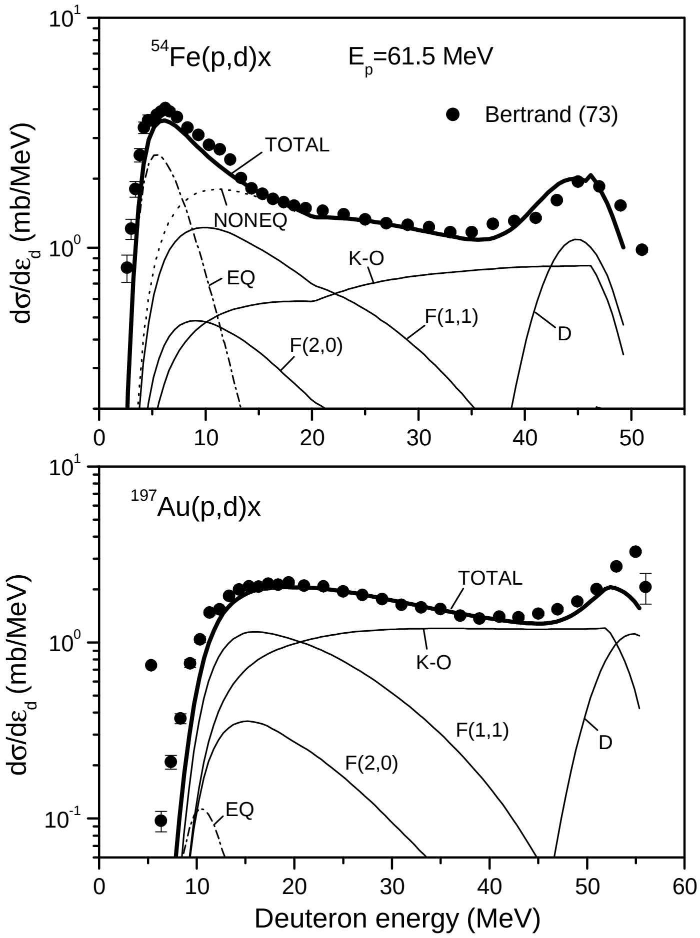

Fig.66 The contribution of different nuclear processes in the deuteron emission in reactions p+^{54}Fe and p+^{197}Au induced by 61.5 MeV protons: the equilibrium emission (EQ), the pick-up of nucleon from the exciton states starting from (2p,1h) (F(1,1)), the coalescence of two excited nucleons (F(2,0)), the direct pick-up (D). Also the sum of all non-equilibrium components (NONEQ) and the total spectrum (TOTAL) are shown. The nonequilibrium deuteron spectrum for p+^{197}Au reaction almost coincides with the total spectrum. Experimental data (black circles) are taken from Ref.[247]. The deuteron energy is shown in laboratory coordinate system as in other Figures below.

6.1.2 *Knock-out*

The deuteron knock-out process has been studied in Ref.[322] relating to (n,d) reaction cross-section. The present work concerns the possible contribution of the knock-out in deuteron emission spectra. By the analogy with the α-particle emission [205] the knock-out component of the precompound deuteron emission spectrum is written as follows

$$\frac{d\sigma^{K-O}}{d\varepsilon_d} = \sigma_{non}(E_0) \sum_{n=n_0} \Phi_d(E_0) \frac{g}{g_d\, p} \frac{\omega(p-1,h,U)}{\omega(p,h,E)} \frac{\lambda_d^e(\varepsilon_d)}{\lambda_d^e(\varepsilon_d)+\lambda_d^+(\varepsilon_d)} g_d\, D(n), \quad (85)$$

where the factor $g/(g_d p)$ justifies the substitution of the level density $\omega(\pi,\tilde{\pi},\nu,\tilde{\nu},d,\tilde{d},E)$ for the three-component system (neutron, proton, deuteron) [223,205] by the one-component state density $\omega(p,h,E)$ in Eq.(85). The factor Φ_d describes the initial number of excited deuteron clusters in the nucleus

$$\Phi_d = 2\, F_d(E_0), \quad (86)$$

where F_d is the probability of interaction of the incident particle with the “preformed” deuteron resulting in its excitation in the nucleus; factor of two reflects the normalization on the number of particles in the initial exciton state n_0.

The general expression for F_d is

$$F_d = \frac{\varphi\sigma_{xd}(E_0)}{\frac{Z'}{A'}\sigma_{xp}(E_0) + \frac{(A'-Z')}{A'}\sigma_{xn}(E_0) + \varphi\sigma_{xd}(E_0)}, \quad (87)$$

where “x” refers to the initial proton or neutron; σ_{xd}, σ_{xp} and σ_{xn} are the cross-sections of the elastic interaction of projectile with deuteron, proton and neutron, respectively corrected for a Pauli principle; φ is the number of “preformed” deuterons in the nucleus; Z’ and A’ are number of protons and nucleons in the nucleus corrected for a number of deuterons clustered.

Assuming that the number of preformed deuterons φ has a rather small value and Z'≈A'/2 one can obtain, approximately

$$F_d \cong \frac{2\,\varphi\sigma_{xd}}{\sigma_{xp} + \sigma_{xn}}. \qquad (88)$$

For the evaluation of the cross-section ratio in Eq.(88) the cross-section of the free elastic nucleon-deuteron scattering was taken from ENDF/B-VI at the energy up to 150 MeV and evaluated above 150 MeV using the data from EXFOR. The free nucleon-nucleon interaction cross-sections were obtained from Ref.[149]. The σ_{xd}, σ_{xp} and σ_{xn} cross-sections were calculated taking into account the limitation superimposed by the Pauli principle on the number of intranuclear interactions. It was assumed, that the angular distribution of interacting particles is approximately isotropic in the center-of-mass system. The Fermi energy for deuterons was taken equal to $2E_F$.

Fig.67 shows the ratio of the cross-sections $\sigma_{xd}/(\sigma_{xp} + \sigma_{xn})$ at the different kinetic energy of the incident nucleon calculated for the nuclear potential well with the Fermi energy equal to 32 MeV. The ratio for the free nucleon-deuteron and free nucleon-nucleon scattering cross-sections is also shown.

The obtained value of $\sigma_{xd}/(\sigma_{xp} + \sigma_{xn})$ for the nuclear potential well (Fig.67) was approximated as follows

$$\frac{\sigma_{xd}}{\sigma_{xp} + \sigma_{xn}} = 0.512 \exp(-9.81\cdot 10^{-3} E_p), \qquad (89)$$

where E_p is the kinetic energy of projectile outside of the nucleus in MeV units.

Eqs.(85),(86),(88),(89) were used in the present work for the calculation of the knock-out component of deuteron precompound spectra.

Fig.66 shows the calculated contribution of the deuteron knock-out in the deuteron emission spectrum for ^{54}Fe and ^{197}Au irradiated with 61.5 MeV protons. Parameters used for the calculation are discussed in Section 6.1.5.

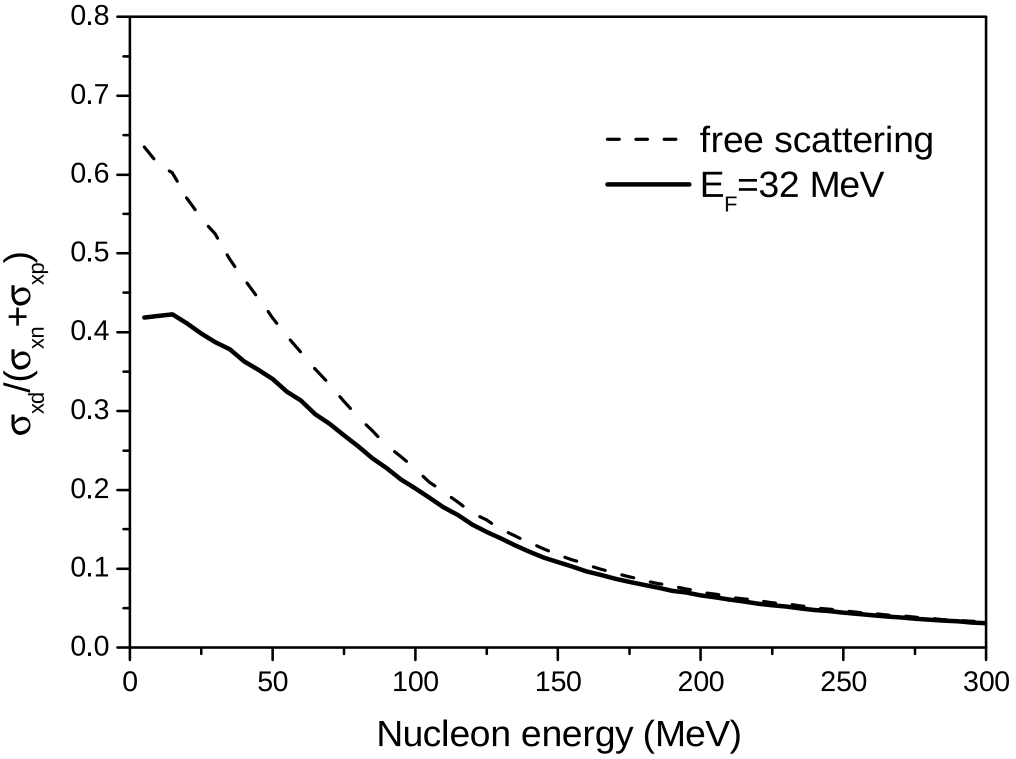

Fig.67 The ratio of the elastic nucleon-deuteron scattering cross-section to the sum of the elastic nucleon-nucleon cross-sections $\sigma_{xd}/(\sigma_{xp} + \sigma_{xn})$ calculated for the nuclear potential well with the Fermi energy equal to 32 MeV (solid line) and for the free scattering (dashed line). Incident nucleon kinetic energy is outside the nucleus (x-axis)

6.1.3 Multiple pre-equilibrium emission

The multiple particle emission gives a noticeable contribution in precompound emission spectra of composite particles forming in nuclear reactions induced by nucleons with energies above 50 MeV [205].

The multiple pre-equilibrium effect is taken into account for the deuteron emission as described below. The pick-up and coalescence contributions for the spectrum of deuterons escaping after the pre-equilibrium emission of nucleons are calculated by the following expression

$$\frac{d\sigma_2^{F-U,C}}{d\varepsilon_d} = \pi \mathbf{D}^2 \sum_{l=0}^{\infty} (2l+1) T_l \sum_{x=\pi,\nu}^{2} \int_{E_x^{min}}^{E_x^{max}} \sum_{n=n_0} {}_n X_x \frac{\omega(p-1,h,E-Q_x-\varepsilon_x)}{\omega(p,h,E)} \frac{\lambda_x^e(\varepsilon_x)}{\lambda_x^e(\varepsilon_x)+\lambda_x^+(\varepsilon_x)} g\, D(n)$$

$$\times \sum_{n'=p+h-1} \sum_{k+m=2} F_{k,m}(\varepsilon_d + Q_d') \frac{\omega(p'-k,h',E-Q_x-\varepsilon_x-Q'_d-\varepsilon_d)}{\omega(p',h',E-Q_x-\varepsilon_x)} \frac{\lambda_d^e(\varepsilon_d)}{\lambda_d^e(\varepsilon_d)+\lambda_d^+(\varepsilon_d)}\, g_d\, D_2(n')\, d\varepsilon_x \tag{90}$$

where $\mathbf{D}$ is the reduced de Broglie wavelength of the incident particle; T_l is the transmission coefficient for l-th partial wave; ${}_nX_x$ is the number of nucleons of x-type in the n-exciton state; “x” refers to proton and neutron emitted; Q_x is the separation energy for nucleon in the composite nucleus; ε_x is the channel energy for x-particle; Q'_d is the separation energy for deuteron in the nucleus formed after the emission of nucleon of x-type; E_x^{min} and E_x^{max} define the energy range, where the emission of the x-particle occurs; D_2 is the depletion factor concerning the escape of particles from n’-exciton state.

The analogous formula is written for the deuteron knock-out following the fast nucleon emission. The successive emission of three and more pre-equilibrium particles is not considered here.

Fig.68 shows the influence of the multiple pre-equilibrium emission on the calculated energy distribution of deuterons emitted.

6.1.4 Direct pick-up process

The process corresponds to the pick-up of nucleon without formation of the (2p,1h) exciton configuration. The final state is (0p,1h). The rigorous description of this process can be done only outside the pre-equilibrium theory. However, the mathematical expressions obtained formally with the help of the precompound exciton model [189,206] are used for the phenomenological and qualitative description of the direct nucleon pick-up.

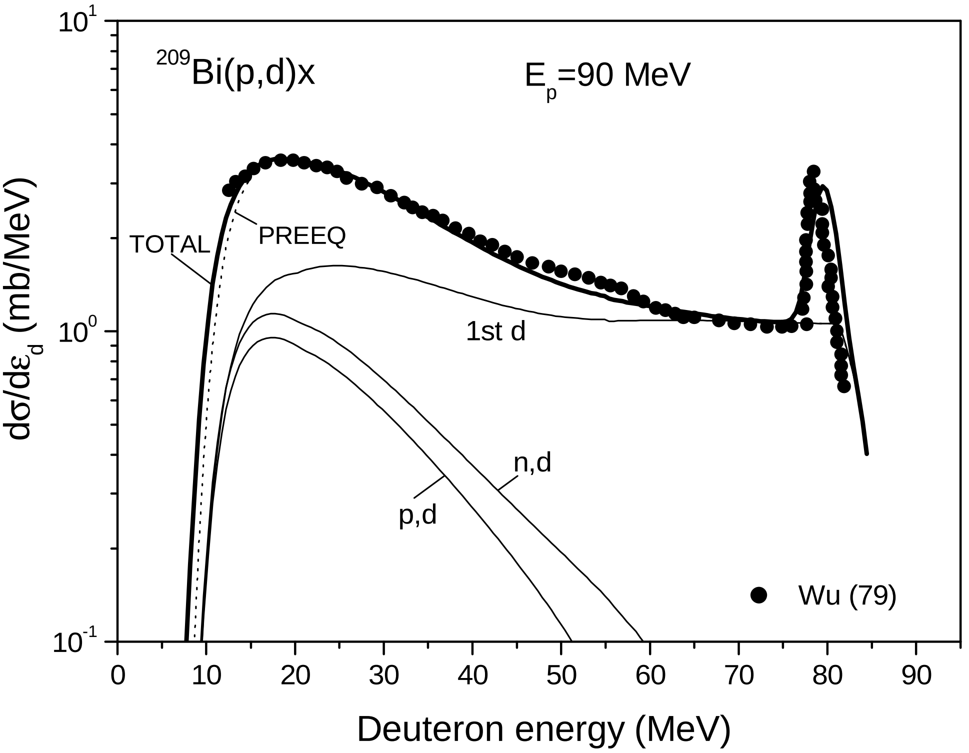

Fig.68 The contribution of deuterons formed on different pre-equilibrium stages of the nuclear reaction p+^{209}Bi induced by 90 MeV protons in the total deuteron emission spectrum: the emission of the first precompound deuteron (“1st d”), the pre-compound deuteron emission after the pre-equilibrium proton escape (“p,d”), the pre-compound deuteron emission following the pre-equilibrium neutron emission (“n,d”). The sum of all pre-equilibrium components (“1st d”+”p,d”+”n,d”) (PREEQ) and the total spectrum (TOTAL) are shown. Experimental data (black circles) are taken from Ref.[248].

According to Ref.[206] the direct component of the deuteron spectrum is

$$\frac{d\sigma^D}{d\varepsilon_d}=\sigma_{non}\,\frac{\omega^*(U)}{\omega(1p,0h,E)}\,\frac{\lambda_d^e(\varepsilon_d)}{\lambda_d^e(\varepsilon_d)+\lambda_d^+(\varepsilon_d)}\,g_d\;, \tag{91}$$

where the final level density $\omega^*(U)$ is approximated in Ref.[206] by $\omega(0p,1h,U)\cdot\gamma/g_d$ with the γ value equal to $2\cdot10^{-3}$ MeV^{-1} for all nuclei and excitation energies.

The formal consideration of the finite depth of the nuclear potential well shows that Eq.(91) can contribute only in the most high energy part of the deuteron emission spectrum, as it has been mentioned above. In this case the calculated part of the spectrum is a rectangular step with the width equal to E_F. To improve the agreement of calculations and the measured deuteron spectra it is useful to write the direct component of the spectrum in the following form

$$\frac{d\sigma^D}{d\varepsilon_d} = \sigma_{non}\ \alpha_1 \exp\left(-\frac{(E-\alpha_2 E_F)^2}{2(\alpha_3 E_F)^2} \right) \frac{\lambda_d^e(\varepsilon_d)}{\lambda_d^e(\varepsilon_d) + \lambda_d^+(\varepsilon_d)}\ g_d\ , \qquad (92)$$

where α_1, α_2 and α_3 are parameters, E_F is the effective value of the Fermi energy.

The values of α_i can be obtained from the analysis of experimental deuteron spectra (Section 6.1.5). The global parameterization of α_i parameters is hardly possible.

Fig.66 shows the $d\sigma^D/d\varepsilon_d$ component of the calculated deuteron spectrum for ^{54}Fe(p,d)x and ^{197}Au(p,d)x reactions induced by 61.5 MeV protons.

6.1.5 Parameters of the model

Model parameters were obtained from the comparison of calculations with the experimental data [247,248,319,323-328]. The deuteron spectra were calculated using Eqs.(76)-(86),(88)-(90),(92).

The change in values of different parameters results to the different energetic dependence of calculated deuteron spectrum. In most cases such change cannot be represented by simple redefinition of other model parameters.

The global normalization of the sum for the $F_{1,1}$ pick-up and the $F_{2,0}$ coalescence components adopted in Ref.[206] was kept unchanged

$$\sum_{k+m=2} F_{k,m} = 0.3 \qquad (93)$$

The single particle state density for deuteron g_d was taken equal to g/2.

The φ parameter of the knock-out model obtained from the comparison of the experimental data and calculations for different nuclei is equal to 0.18 ± 0.03.

The effective value of the Fermi energy E_F was found equal to 5 MeV. This rather small value reflects the influence of surface nuclear effects on the deuteron emission. The similar reduction of the effective Fermi energy was obtained from the analysis of nucleon pre-equilibrium spectra in Refs.[320,321]. Fig.69 shows the influence of the effective E_F value on the calculated deuteron energy distribution.

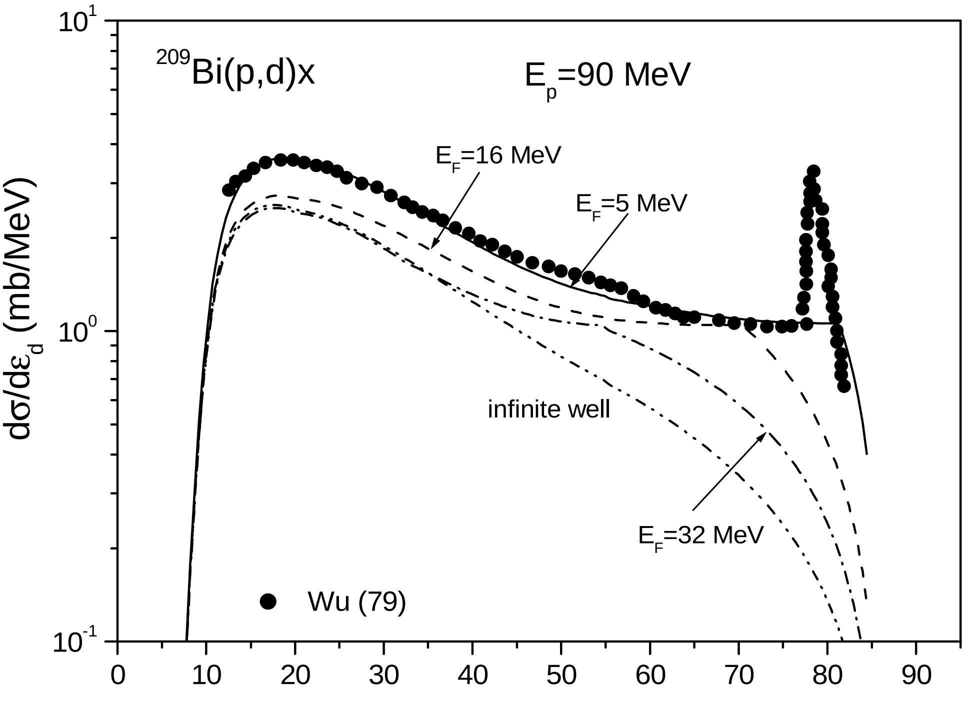

Fig.69 The deuteron emission spectrum for ^{209}Bi(p,d)x reaction induced by 90 MeV protons calculated using different value of the effective Fermi energy E_F. Experimental data (black circles) are taken from Ref.[248].

The imaginary part of the optical potential W_d^{opt} was parameterized as follows $W_d^{opt} = W_0$ at $\varepsilon_d < \varepsilon_1$ and $W_d^{opt} = W_0 \cdot \exp(\beta \cdot (\varepsilon_d - \varepsilon_1))$ at $\varepsilon_d \geq \varepsilon_1$; $W_0 = \gamma_1 \cdot (E_1 - E_p) + W_1$ at $E_p \leq E_1$, $W_0 = \gamma_2 \cdot (E_p - E_1) + W_1$ at $E_p > E_1$ and $W_0 = \gamma \cdot (E_2 - E_1) + W_1$ at $E_p > E_2$, where $\varepsilon_1 = 20$ MeV, $\beta = -0.1027 \cdot \exp(-11.45 \cdot (A - 2\ Z)/A)$, $E_1 = 62$ MeV, $E_2 = 90$ MeV, $\gamma_1 = -1.37 \cdot 10^{-3} A - 0.213$, $\gamma_2 = -0.45$, $W_1 = 32$ MeV. This rather complex energy and A- dependence of W_d^{opt} results from the fitting of calculations to experimental deuteron spectra. Partly, it accumulates an uncertainty of different measurements and reflects general approximate character of the model discussed.

The parameters of Eq.(92) have been obtained from the analysis of the experimental data. For the most nuclei the value of α_1 is equal to $1.5 \cdot 10^{-3}$. The α_2 parameter value is equal to 0.77 ± 0.54 and α_3 is equal to 0.52 ± 0.18. It is supposed that E_F is equal to 5 MeV in Eq.(92).

The inverse reaction cross-sections have been calculated as described in Refs.[201,208]. The optical potential of Koning and Delaroche [131] has been used for the calculation of the cross-section of nonelastic interactions, σ_{non} for primary neutrons and protons.

The numerical calculations were performed with the help of the modified version of the ALICE/ASH code [202,203].

The model parameters used for the computation of nucleon precompound spectra make an influence on the calculated energy distribution of deuterons. The nucleon spectra were calculated using the geometry dependent hybrid model [199]. The results of calculations were compared with the experimental data [247,248,319,325,326,329, 330] for several nuclei from ^{27}Al to ^{209}Bi. The comparison shows that in most cases the measured nucleon spectra are described by model calculations with the multiplication factor for the free nucleon path in the nucleus [199,201-203] equal to one. For the incident nucleon energy above 90 MeV the factor of two has been adopted.

6.2 Comparison of calculations with experimental data

The calculation of deuteron energy distributions has been carried out using Eqs.(76)-(86),(88)-(90),(92) with the help of the ALICE/ASH code.

Figs.70-78 shows the deuteron emission spectra calculated for nuclei from ^{12}C to ^{209}Bi irradiated with 61.5-62.9 MeV protons. The deuteron energy distributions calculated for reactions induced by 90 MeV protons and 96 MeV neutrons are shown in Figs.78-84. The experimental data presented in Figs.70-84 are taken from Refs.[247,248,319]. There is an agreement between calculated and measured spectra.

Examples of deuteron emission spectra calculated for nuclear reactions induced by nucleons of lower energies are shown in Figs.85,86. The reasonable agreement is observed for calculations and experimental data [247,326-328].

Recently a large number of measurements [330-334] has been made for charge particle emission spectra in neutron induced reactions. A special comment is required concerning deuteron distributions obtained in Refs.[330-334]. The comparison of model calculations with the experimental data shows a large discrepancy at the high energy tail of measured deuteron spectra [315]. Partly experimental points are in kinematically forbidden energy region. The authors [315] mentioned that it results from the measurement technique concerning i) the energy resolution of the incident neutron spectrum, ii) the flat neutron energy distribution at lower incident neutron energy used in measurements.

The comparison of present calculations with the experimental data [315,334] also shows a noticeable difference. It is more obvious at lower projectile energy, where the experimental points are above the kinematic limit of the reaction. Fig.87 shows the calculated deuteron spectrum for n+^{nat}Fe reaction at the projectile energy 28.5 and 53.5 MeV. The small step in the high energy part of calculated spectra is due to the ^{54}Fe(n,d) reaction contribution. The isotope ^{54}Fe has the highest value of the (n,d) reaction energy ($Q_{n,d}$ = –6.63 MeV) comparing with other stable iron isotopes ($Q_{n,d}$: ^{56}Fe: –7.96, ^{57}Fe: –8.335, ^{58}Fe: –9.73 MeV). The maximal energy of deuterons corresponding to ^{54}Fe(n,d) and ^{56}Fe(n,d) reactions are shown by touches on the energy axis (Fig.87). Fig.87 shows that the measured deuteron spectra are partly above the kinematic limit of the (n,d) reaction. At the lower incident neutron energy (28.5 MeV) the discrepancy between the calculated high energy part of the spectrum and the measured data is more evident. The lacks of measurements mentioned above make a rather questionable to test theoretical models of deuteron emission using the data discussed at least at lower incident neutron energies.

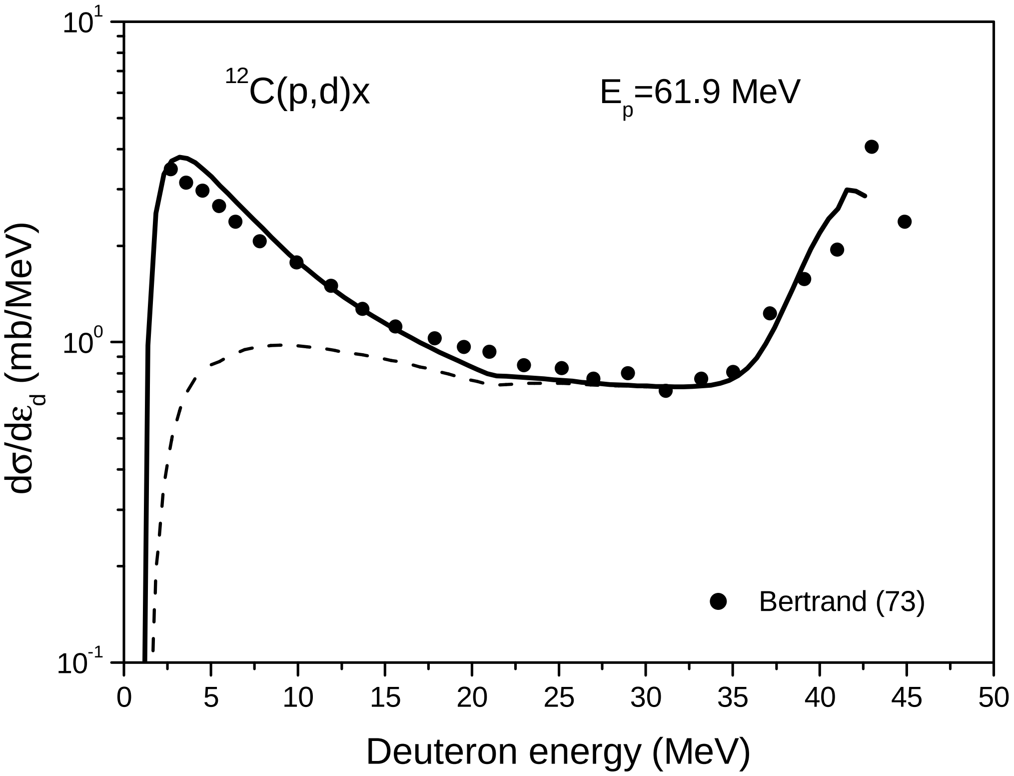

Fig.70 Calculated total deuteron emission spectrum (solid line) and nonequilibrium deuteron emission spectrum (dashed line) for the ^{12}C(p,d)x reaction induced by 61.9 MeV protons. Experimental data are from Ref.[247].

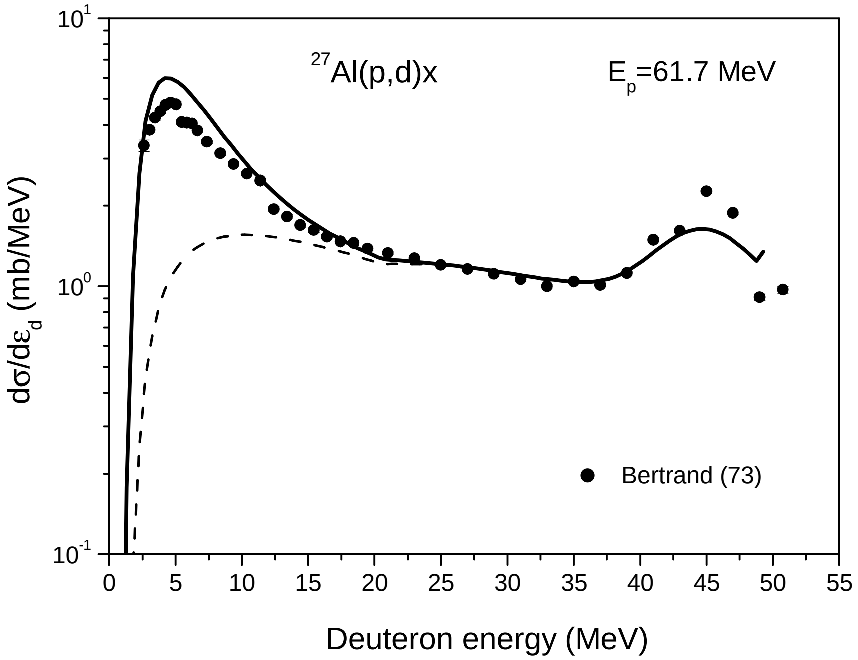

Fig.71 Calculated deuteron emission spectrum for the ^{27}Al(p,d)x reaction induced by 61.7 MeV protons. Symbols as in Fig.70

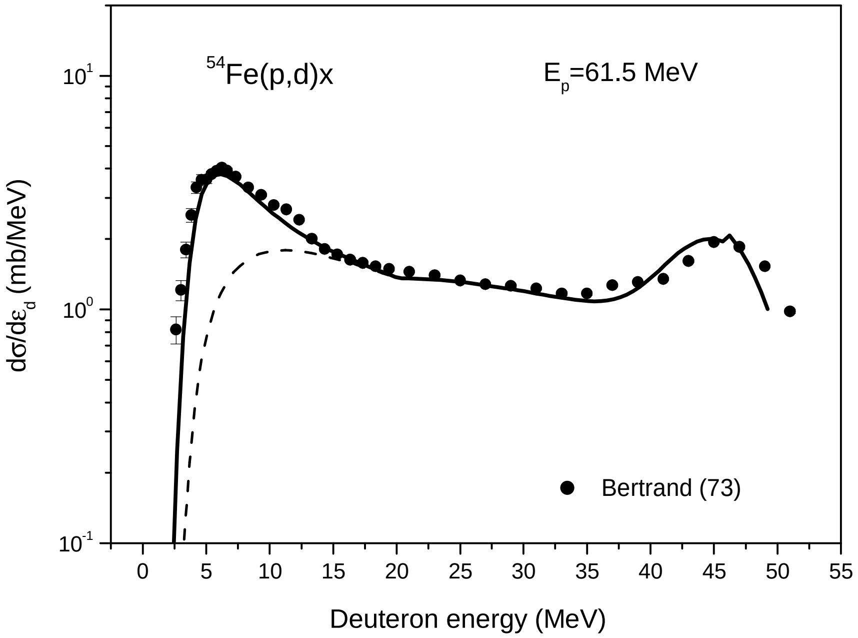

Fig.72 Calculated deuteron emission spectrum for the ^{54}Fe(p,d)x reaction induced by 61.5 MeV protons. Symbols as in Fig.70

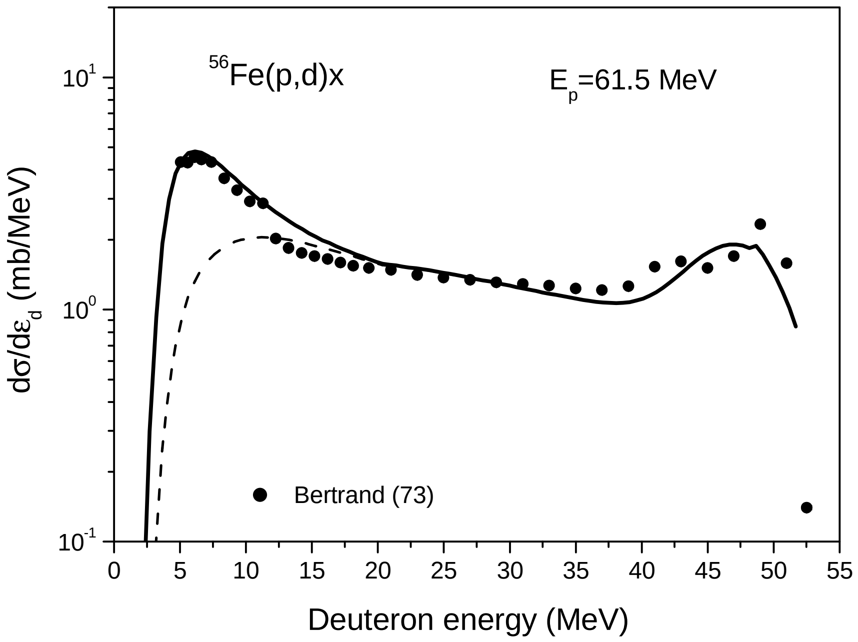

Fig.73 Calculated deuteron emission spectrum for the ^{56}Fe(p,d)x reaction induced by 61.5 MeV protons. Symbols as in Fig.70.

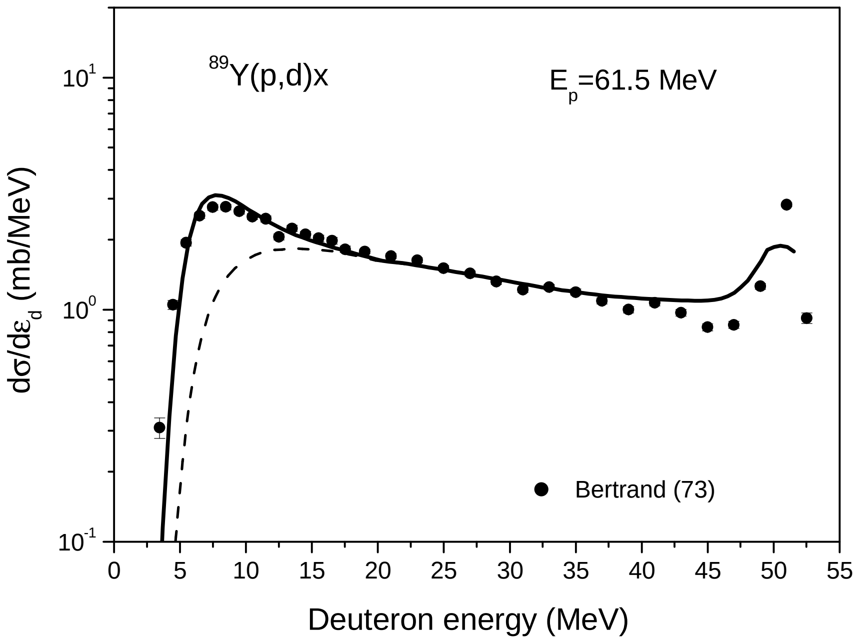

Fig.74 Calculated deuteron emission spectrum for the ^{89}Y(p,d)x reaction induced by 61.5 MeV protons. Symbols as in Fig.70.

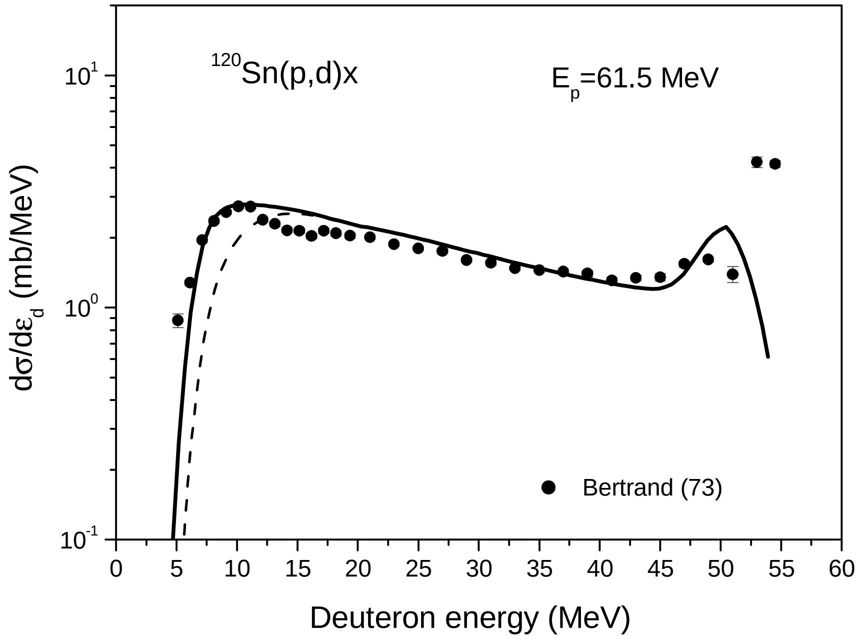

Fig.75 Calculated deuteron emission spectrum for the ^{120}Sn(p,d)x reaction induced by 61.5 MeV protons. Symbols as in Fig.70.

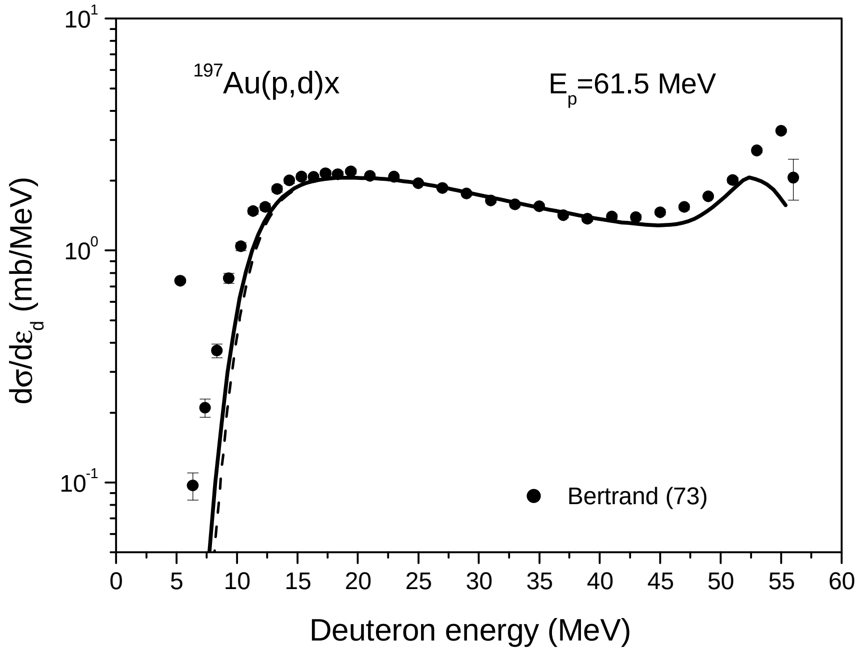

Fig.76 Calculated deuteron emission spectrum for the ^{197}Au(p,d)x reaction induced by 61.5 MeV protons. Symbols as in Fig.70.

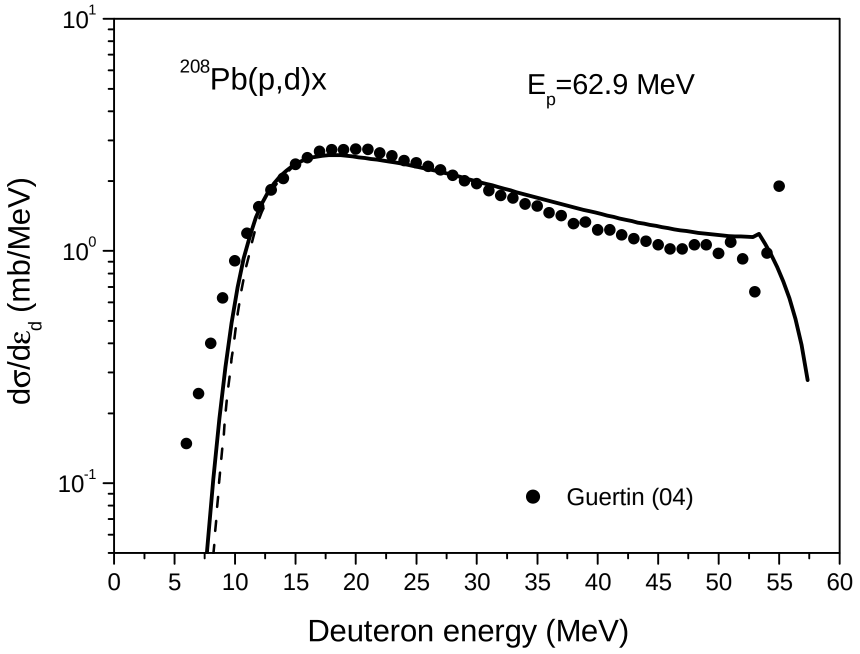

Fig.77 Calculated deuteron emission spectrum for the ^{208}Pb(p,d)x reaction induced by 62.9 MeV protons. Experimental data are taken from Ref.[325]. Other symbols as in Fig.70.

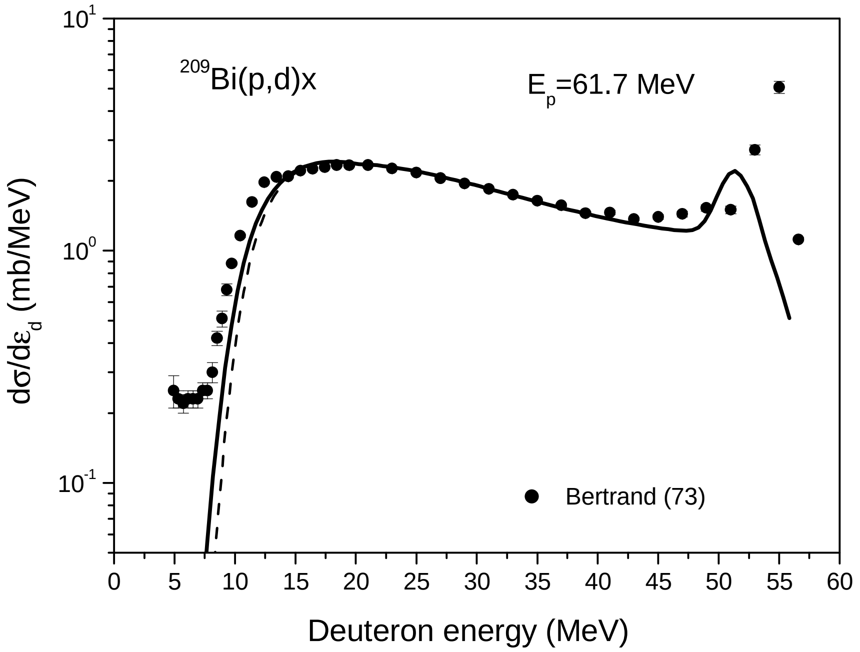

Fig.78 Calculated deuteron emission spectrum for the ^{209}Bi(p,d)x reaction induced by 61.7 MeV protons. Experimental data are taken from Ref.[247]. Other symbols as in Fig.70.

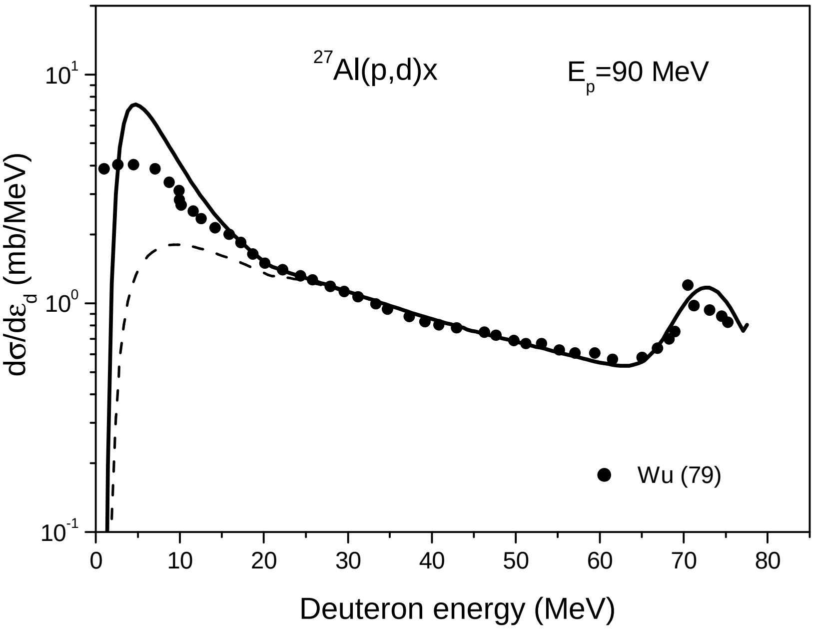

Fig.79 Calculated deuteron emission spectrum for the ^{27}Al(p,d)x reaction induced by 90 MeV protons. Experimental data are taken from Ref.[248]. Other symbols as in Fig.70.

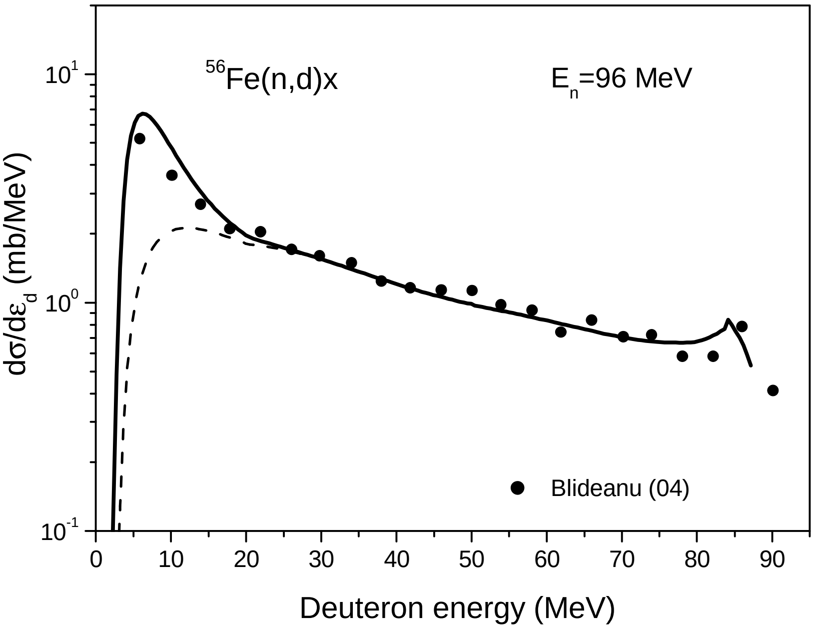

Fig.80 Calculated deuteron emission spectrum for the ^{56}Fe(p,d)x reaction induced by 96 MeV neutrons. Experimental data are taken from Ref.[319]. Other symbols as in Fig.70.

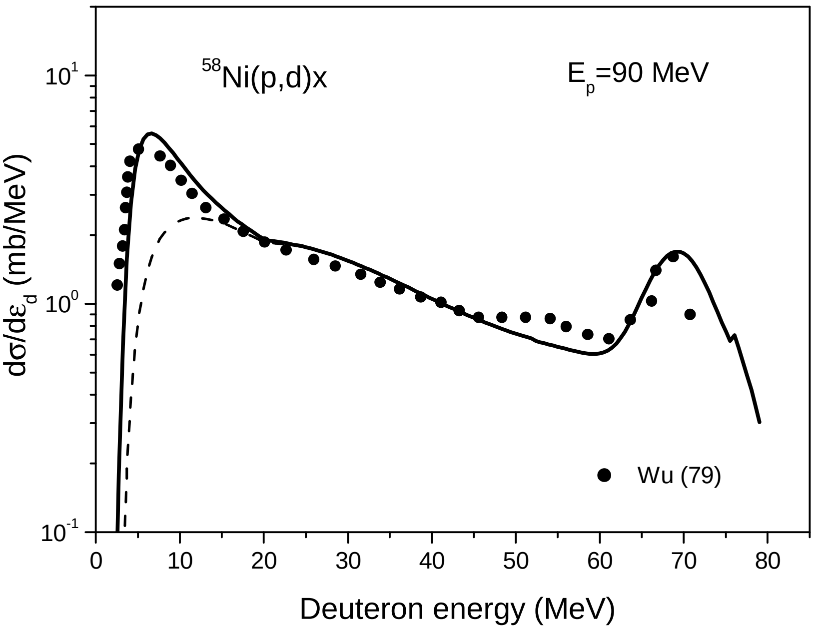

Fig.81 Calculated deuteron emission spectrum for the ^{58}Ni(p,d)x reaction induced by 90 MeV protons. Experimental data are taken from Ref.[248]. Other symbols as in Fig.70.

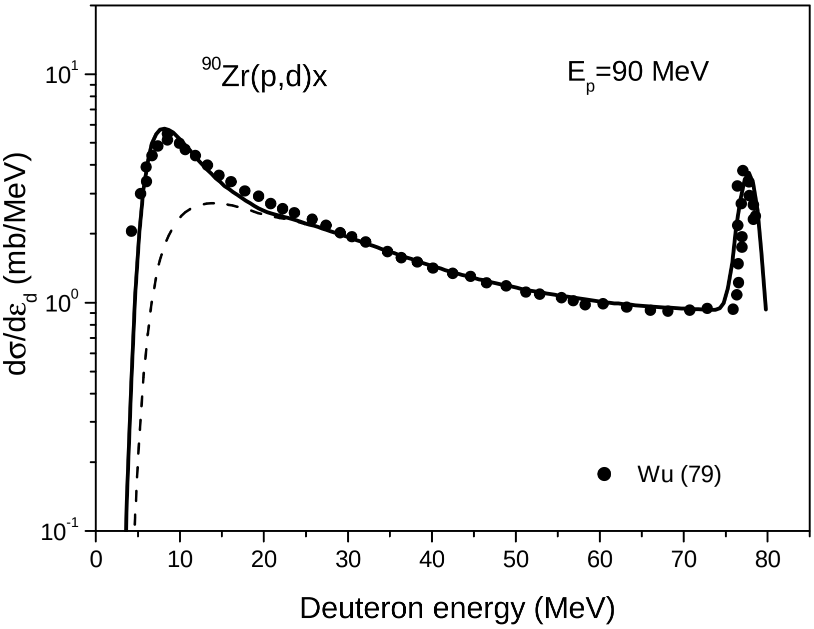

Fig.82 Calculated deuteron emission spectrum for the ^{90}Zr(p,d)x reaction induced by 90 MeV protons. Experimental data are taken from Ref.[248]. Other symbols as in Fig.70.

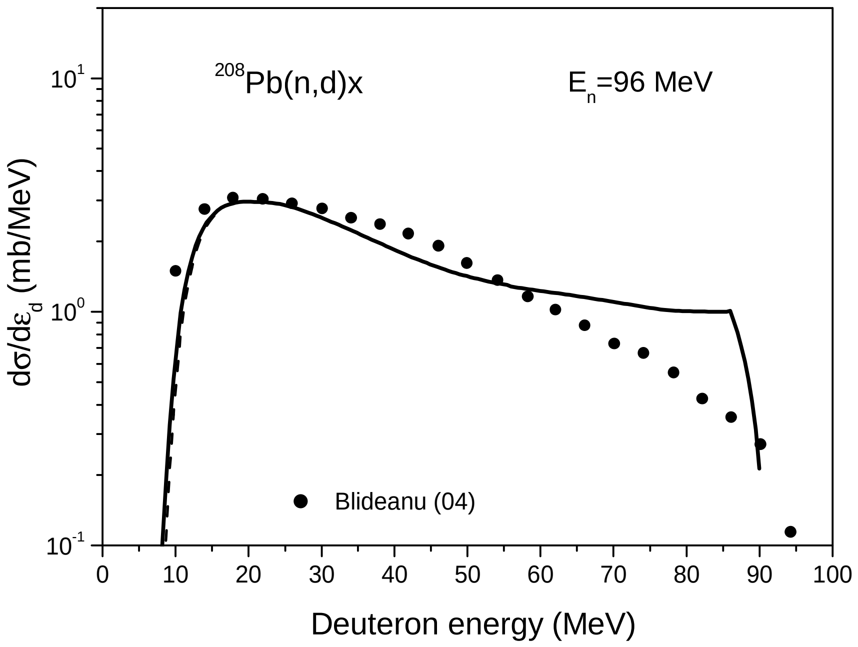

Fig.83 Calculated deuteron emission spectrum for the ^{208}Pb(p,d)x reaction induced by 96 MeV neutrons. Experimental data are taken from Ref.[319]. Other symbols as in Fig.70.

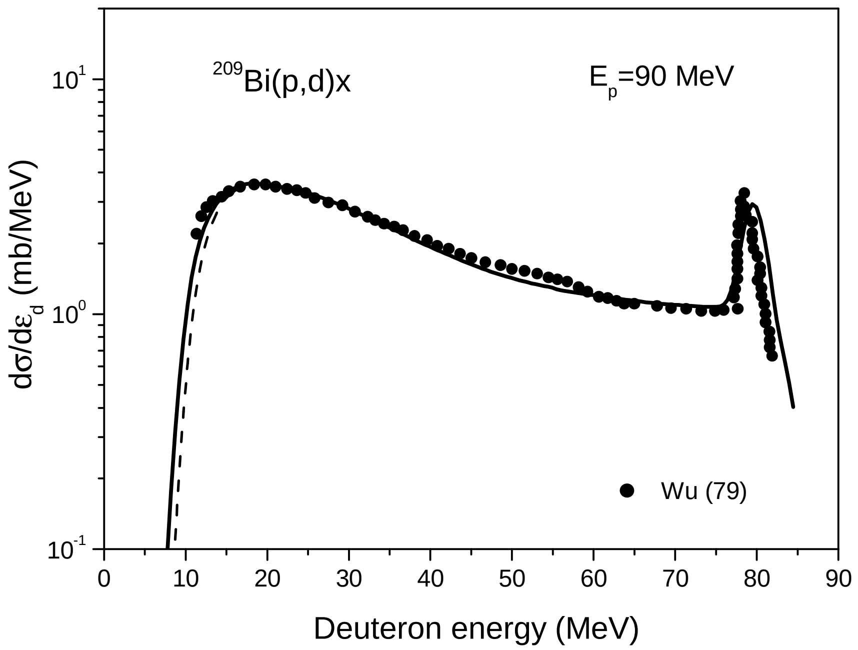

Fig.84 Calculated deuteron emission spectrum for the ^{209}Bi(p,d)x reaction induced by 90 MeV protons. Experimental data are taken from Ref.[248]. Other symbols as in Fig.70.

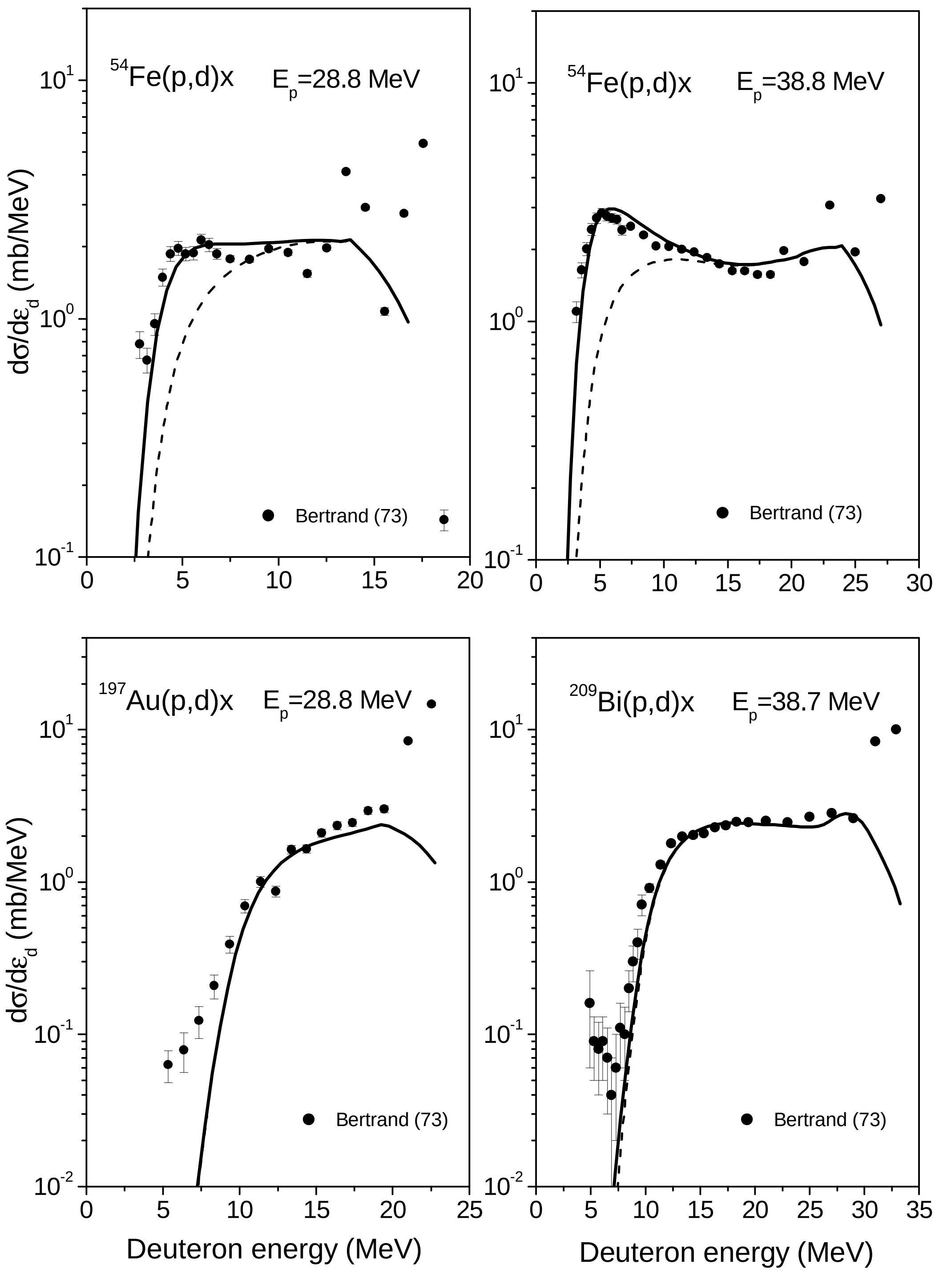

Fig.85 Calculated deuteron emission spectra for p+^{54}Fe, p+^{197}Au and p+^{209}Bi reactions induced by protons with the energy from 28.8 to 38.8 MeV. Experimental data are taken from Ref.[247. Other symbols as in Fig.70.

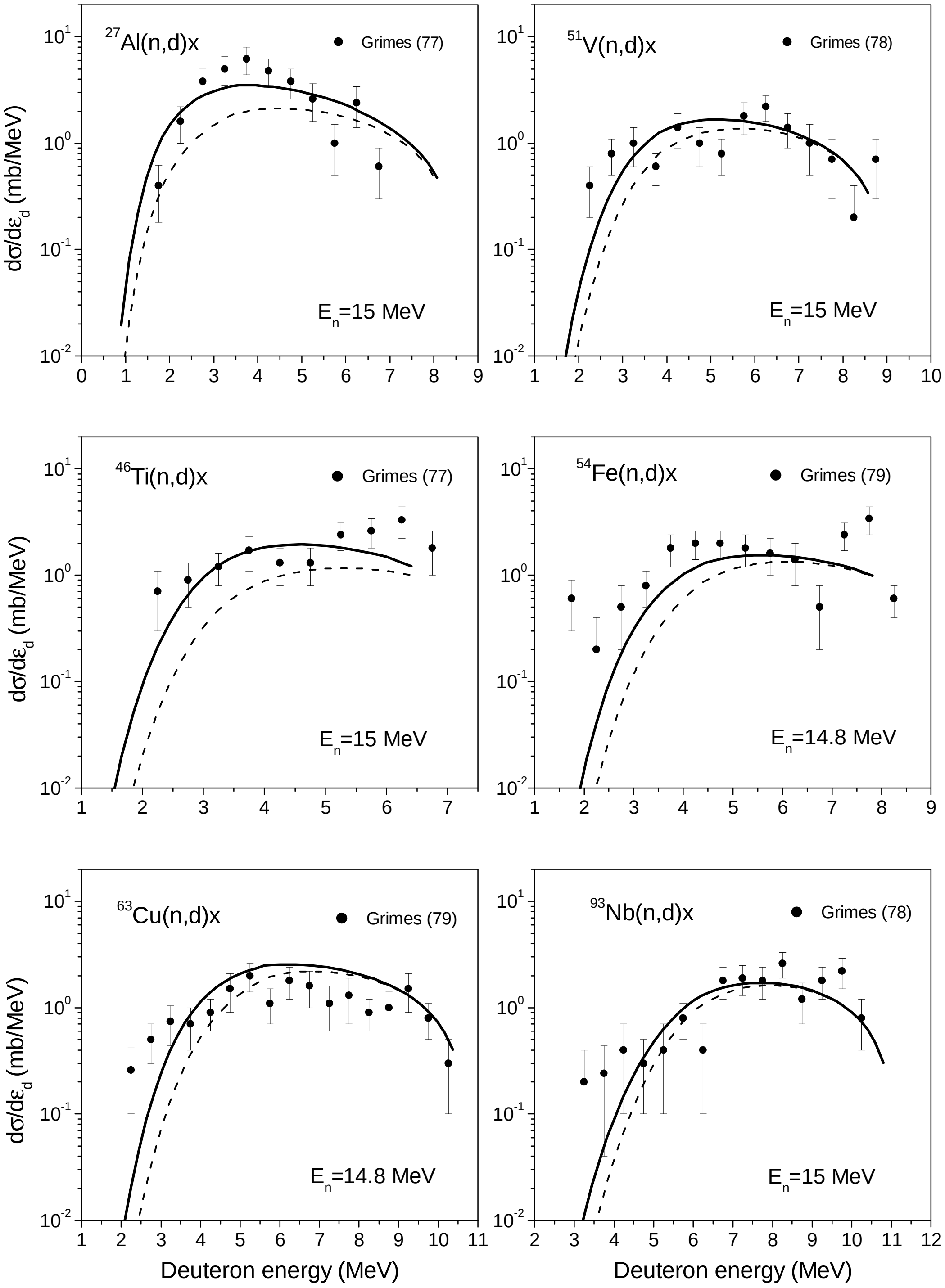

Fig.86 Calculated deuteron emission spectra for a number of neutron induced reactions at the incident neutron energy 14.8 and 15 MeV Experimental data are taken from Refs.[326-328]. Other symbols as in Fig.70.

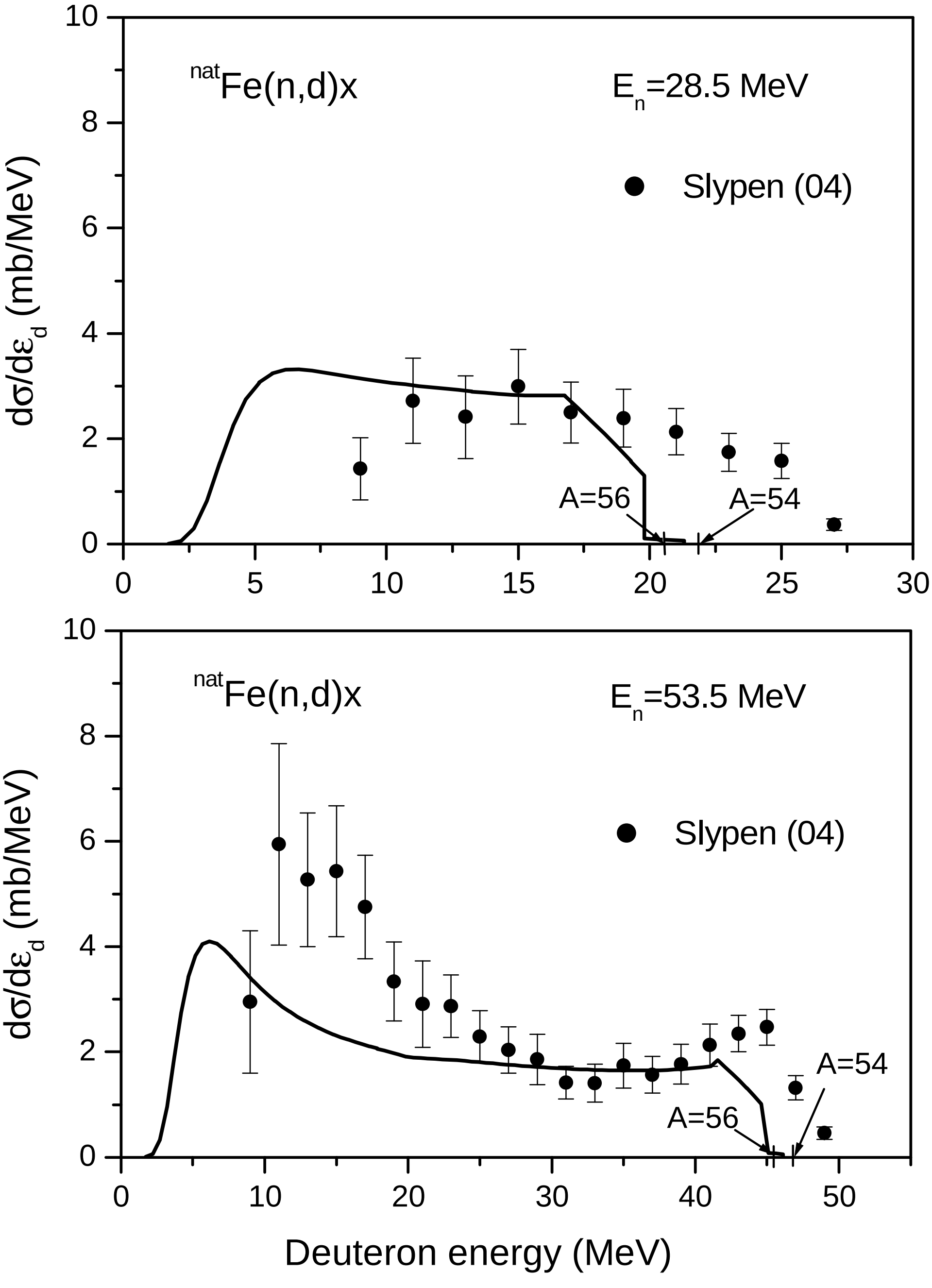

Fig.87 Calculated deuteron emission spectra for Fe(n,d)x reaction induced by 28.5 and 53.5 MeV neutrons (solid line). The maximal energy of deuterons for ^{54}Fe(n,d) and ^{56}Fe(n,d) reactions is shown by touches on the x-axis. Experimental data are taken from Refs.[315,334].

6.3 Summary about phenomenological model for non-equilibrium deuteron emission in nucleon induced reaction

A new approach is proposed for the non-equilibrium deuteron emission in nuclear reactions induced by nucleons of intermediate energies. The model combines the model of the nucleon pick-up, the coalescence and the deuteron knock-out.

The model of Sato, Iwamoto, Harada [221,222] is used to describe the nucleon pick-up and the nucleon coalescence from exciton states starting from the (2p,1h) configuration. The probability of the nucleon interaction with “preformed” deuterons in the knock-out model is calculated taking into account the Pauli principle. The contribution of the direct pick-up is described phenomenologically. The multiple pre-equilibrium emission of deuterons (the precompound deuteron escape after the fast nucleon emission) is considered. The emission and absorption rates of excited particles are calculated by the hybrid model [199]. The exciton level density is calculated taking into account the finite depth of the nuclear potential depth.

The calculated deuteron energy distributions are in a good agreement with measured data.

7. **Calculation of the energy deposition in the targets from C to U irradiated with intermediate energy protons**

The energy deposition was calculated for the targets from lithium to uranium irradiated with intermediate energy protons with the help of different models incorporated in the MCNPX code package and with the help of the CASCADE/INPE code. The values obtained using different models and codes are in a good agreement for all targets except uranium. The comparison with available experimental data for the heat deposition for 0.8, 1.0 and 1.2 GeV protons has been performed. The good agreement is observed for copper, lead and bismuth target. The best result is obtained with the help of the ISABEL model. The systematic dependence of the heat deposition from atomic number of the target was investigated. The contribution of different particles and energy ranges in the heat deposition has been studied at the primary proton energies from 0.3 to 2.5 GeV.

7.1 Brief description of the models and codes used for the energy deposition calculation

The calculation of the energy deposition has been performed using the MCNPX code package and using the CASCADE/INPE code [294] which includes the original high energy particle transport code and the MCNP/4C code [341].

7.1.1 The MCNPX code

Three intranuclear cascade models (Bertini, CEM and ISABEL) combined with pre-equilibrium model and evaporation model (Dresner) implemented in the MCNPX code package were used for calculations.

The stopping power for protons and other charged nuclear reaction products was calculated using the module from the LAHET Code System modified as described in Ref.[138].

7.1.2 The CASCADE/INPE code

The CASCADE/INPE code has being developed and improved during the last decades [150,151,286,293,294]. The model for the simulation of the intranuclear cascade nucleon and meson interactions is quite different from the models incorporated in the MCNPX package. The detail description is given in Ref.[286]. The main features of the model are the consideration of the time coordinate, the use of the realistic nuclear density with the diffuse boundary and the description of the change in the nuclear density during the fast particle emission. The pre-equilibrium stage of the reaction describing by the exciton model is not considered in present calcualtions. After the finish of the fast particle emission the evaporation stage occurs.

To describe the non-equilibrium α-particle emission from an excited nucleus the coalescence model from Refs.[342,343] is used.

The Fermi gas model with level density parameter equal to A/10 is used to calculate the nuclear level density for the excited nuclei. The general expressions describing the particle evaporation widths in the CASCADE/INPE model and in the CEM model are the same. The fission channel is described according to Ref.[209].

The creation and the emission of the following particles have been simulated in the present work with the help the MCNPX code and the CASCADE/INPE code: neutrons, protons, deuterons, tritons, ^{3}He, α-particles, charged pions π^+, π^-, neutral pions and photons.

7.1.3 Use of evaluated nuclear data files for low energy particle transport calculation

Data from ENDF/B-VI (Release 8) library were used for the particle transport calculations with the MCNPX code at low energies. The evaluated data up to 150 MeV from ENDF/B-VI (8) were applied for the energy deposition calculations for carbon, aluminum, iron, copper, lead and bismuth. For uranium the available data up to 20 MeV were used.

For the systematic calculation of the energy deposition the neutron data for the nuclides with Z=3-92, which are absent in ENDF/B-VI (8), were taken from other nuclear data libraries at the energies below 20 MeV. For ^{nat}Zn data were taken from JEFF-3.0 (original BROND-2.2 data), for ^{70}Ge, ^{162}Er, ^{164}Er, ^{168}Er, and ^{170}Er the

JENDL-3.3 data were adopted, for ^{nat}Pt data were taken from JEFF-3.0 (original ENDL-78 data).

The low energy neutron transport calculations with the help of the CASCADE/INPE code were also based on the ENDF/B-VI (8) data. The photon transport was treated with the help of the MCNP/4C code. The protons and other particles were tracked with the help of the theoretical models.

7.2 Experimental data for the heat deposition

The heat deposition has been measured in Refs.[336-339] for two cylindrical targets with radius equal to 5 and 10 cm and height equal to 60 cm irradiated with 0.8, 1.0 and 1.2 GeV protons. The data were obtained for protons impinging on the butt-end of the cylinder with the Gaussian radial distribution with a full width at half-maximum equal to 2.4 cm.

The most detailed data were obtained for the target with the radius R=10 cm [336-339]. The data for this target is used for the comparison of the experimental data and the code calculations in the present work.

The experimental values of the total heat deposition for the carbon, aluminum, iron and copper targets were obtained by the integration of the linear density of the energy deposition (dQ/dz) along the beam axis measured in Refs.[338,339]. Data for lead and bismuth were taken from Ref.[336] and for uranium from Ref.[340].

7.3 Results

7.3.1 The total values of the heat deposition

The calculated and measured values of the total heat deposition (Q) are presented in Figs.88-94 for carbon, aluminum, iron, copper, lead, bismuth and uranium. Data correspond to the cylindrical target with the radius equal to 10 cm. Figs.92-94 show also the values of the heat deposition obtained with the help of the LAHET code in Ref.[340].

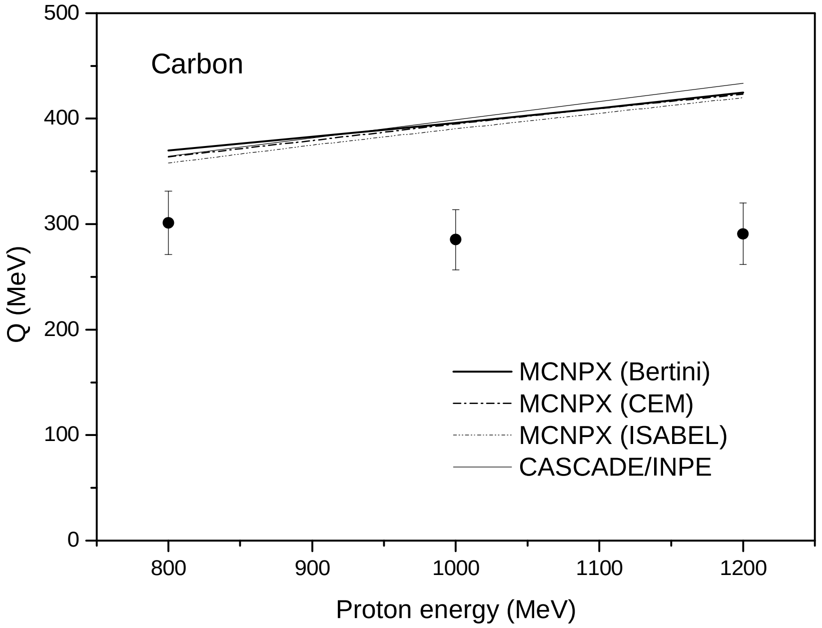

Fig.88 Total heat deposition in the carbon target calculated using the MCNPX code package and the CASCADE/INPE code. The experimental data (black circle) are from Ref.[338].

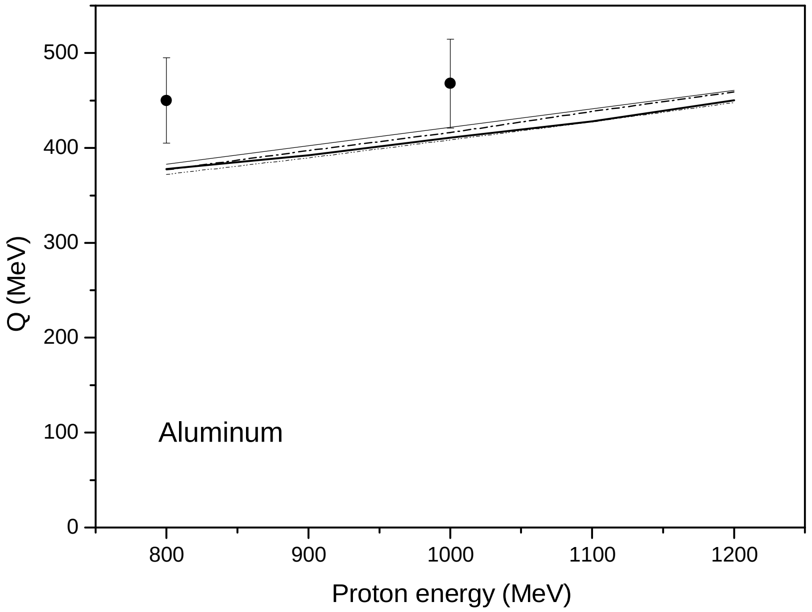

Fig.89 Total heat deposition in the aluminum target. The experimental data are from Ref.[338]. The symbols are as in Fig.88.

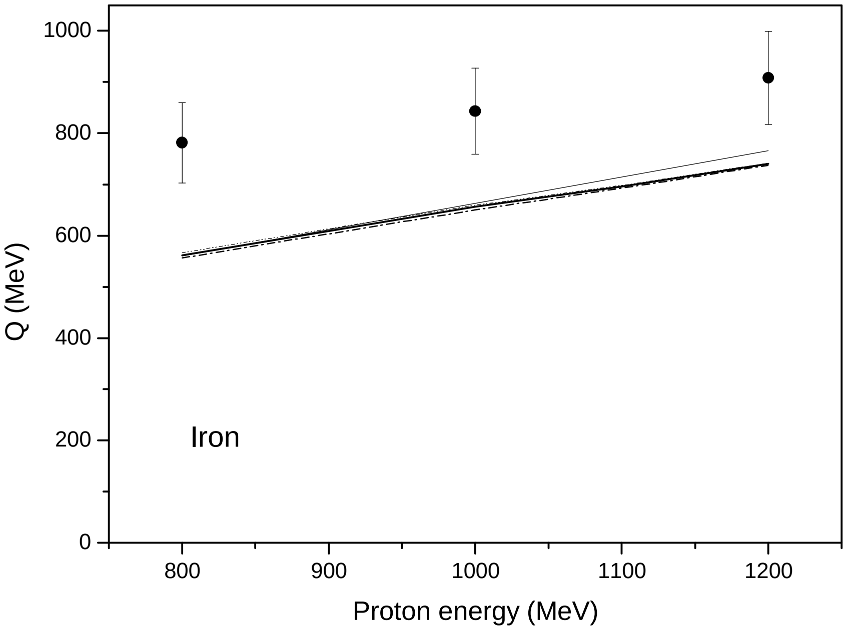

Fig.90 Total heat deposition in the iron target. The experimental data are from Ref.[339]. The symbols are as in Fig.88.

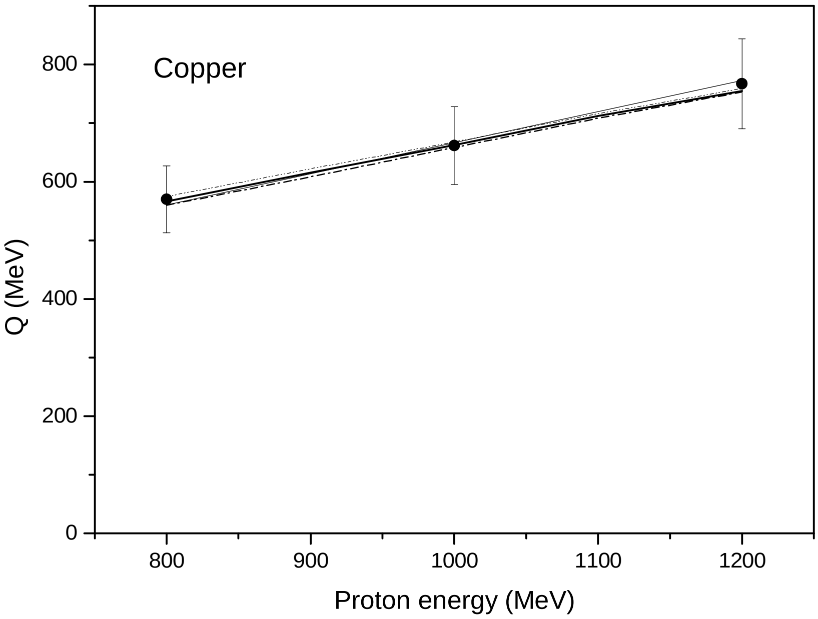

Fig.91 Total heat deposition in the copper target. The experimental data are from Ref.[339]. The symbols are as in Fig.88.

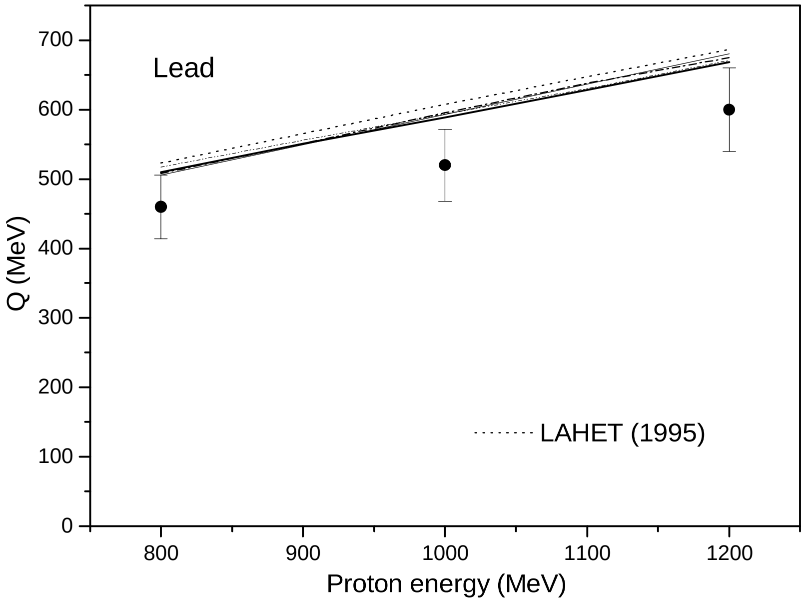

Fig.92 Total heat deposition in the lead target calculated with the help of the MCNPX code, the CASCADE/INPE code and the LAHET code (dashed line). The experimental data are from Ref.[336]. The symbols are as in Fig.88.

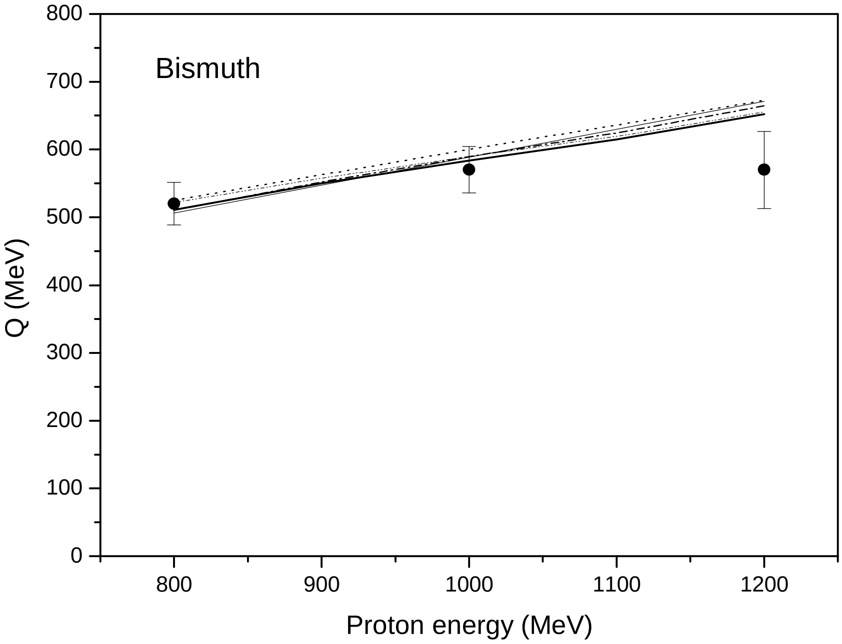

Fig.93 Total heat deposition in the bismuth target. The experimental data are from Ref.[336]. The symbols are as in Figs.88,92.

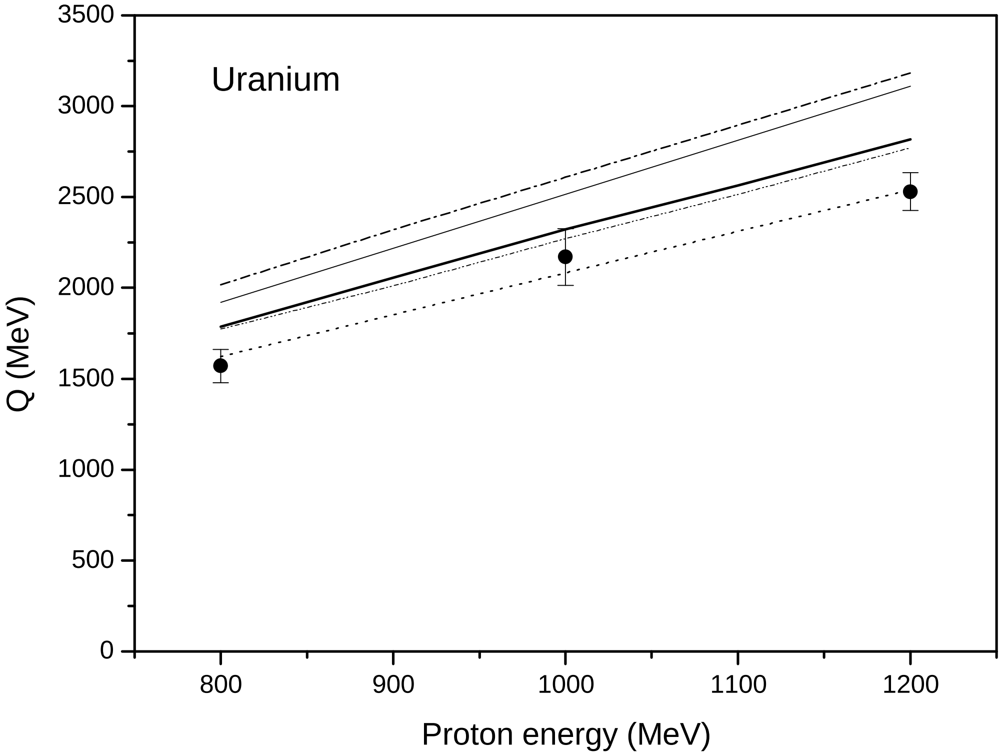

Fig.94 Total heat deposition in the uranium target. The experimental data are from Refs.[4,7]. The symbols are as in Figs.88,92.

There is a rather good agreement between predictions of different models and codes except the calculations for uranium (Fig.94). For uranium the values of Q calculated with the help of the CEM model and the CASCADE/INPE model are close. The ISABEL model predictions are in the agreement with the Bertini model, but not with the CEM model and the CASCADE/INPE model. The origin of the difference is the use of the different approaches to describe the fission-evaporation competition in the models.

As compared with the experimental data, the calculation overestimates the heat deposition for carbon (Fig.88) and underestimates for aluminum and iron (Figs.89,90). There is a good agreement between the experimental and calculated values of the heat deposition for copper (Fig.91). For lead, bismuth and uranium the results of the calculations are rather higher than the measured values of Q. The deviation of the experimental data and calculated values increases for carbon and bismuth with the proton energy growth, For aluminum, iron and lead one may say about “energy independent” discrepancy. The LAHET code calculation has the maximal deviation from the experimental values for lead and bismuth (Figs.92,93) and shows the best result for uranium (Fig.94).

The values describing the deviation of the experimental data and the MCNPX code and the CASCADE/INPE code calculations are given in Table 17.

According to the data from Table 17, the Bertini model gives the best description of the experimental data for copper, lead and bismuth. The ISABEL model provides the best result for carbon and uranium. The CASCADE/INPE calculations have the minimal error for aluminum and iron. Formally, for all seven elements the ISABEL model gives the best description of the measured data (last row in Table 17). At the same time the error values shown in Table 17 for different codes are rather close (14.2 to 17) and the use of any code does not give the substantial gain in the experimental data description comparing with other codes.

To understand better the general character of the difference between the calculated values and the experimental data the calculations have been performed for a wide number of the elements irradiated with intermediate energy protons. The energy deposition has been calculated for seventy natural mixtures of isotopes with atomic number from Z = 3 to 92 except gases. The target was the cylinder with radius equal to 10 cm and the height equal to 60 cm, for which the measurement of the heat deposition was performed in Refs.[336-339]. Fig.95 shows the results of the calculation performed with the help of the Bertini model and the measured values of the energy deposition for the proton energy equal to 0.8 GeV and 1.2 GeV. The statistical error of the Monte Carlo calculations does not exceed 1 % for all elements considered.

Table 17

The error between the calculated and measured values of the heat deposition (%), calculated as follows $(1/N)\sum |Q_i^{exp}-Q_i^{calc}|/Q_i^{exp}$. The minimal value for each target is marked out.

Target	Proton energy (MeV)	MCNPX			CASCADE/INPE
		Bertini model	CEM model	ISABEL model	
Carbon	800	22.8	20.7	18.8	20.9
	1000	38.8	38.5	36.8	39.8
	1200	46.0	45.5	44.4	49.0
	all energies	35.9	34.9	33.3	36.6
Aluminum	800	16.0	16.2	17.3	15.0
	1000	12.2	11.1	12.7	9.9
	all energies	14.1	13.6	15.0	12.4
Iron	800	28.1	28.8	27.5	28.2
	1000	22.1	22.9	21.8	21.3
	1200	18.5	18.8	18.4	15.7
	all energies	22.9	23.5	22.5	21.8
Copper	800	0.7	1.7	0.9	1.6
	1000	0.2	0.5	0.9	0.8
	1200	1.6	1.8	1.1	0.8
	all energies	0.8	1.3	1.0	1.1

Table 17 continued

Target	Proton energy (MeV)	MCNPX			CASCADE/INPE
		Bertini model	CEM model	ISABEL model	
Lead	800	10.8	10.4	12.5	9.9
	1000	13.3	14.5	14.2	14.0
	1200	11.4	12.5	11.8	13.4
	all energies	11.8	12.5	12.8	12.4
Bismuth	800	1.7	1.8	0.3	2.7
	1000	2.4	3.4	3.5	3.2
	1200	14.4	16.5	15.0	17.7
	all energies	6.1	7.2	6.3	7.9
Uranium	800	13.7	28.5	12.9	22.3
	1000	7.0	20.3	4.6	15.9
	1200	11.4	25.8	9.5	23.0
	all energies	10.7	24.9	9.0	20.4
All targets		14.7	17.0	14.2	16.3

Fig.95 shows that the general dependence of Q is not monotonous function of the atomic number Z. The holes correspond to the alkali elements Li, Na, K, Rb and Cs which have the maximal values of the proton ranges and also to lead and bismuth. The calculated values of Q are in a general agreement with the experimental values of the heat deposition for all cases except iron. The measured heat deposition is noticeably higher then the values of Q calculated for iron and neighboring elements. It should be noted that for 800 MeV protons the measured value of the heat deposition for iron (Q=780 MeV) is peculiarly close to the primary proton energy.

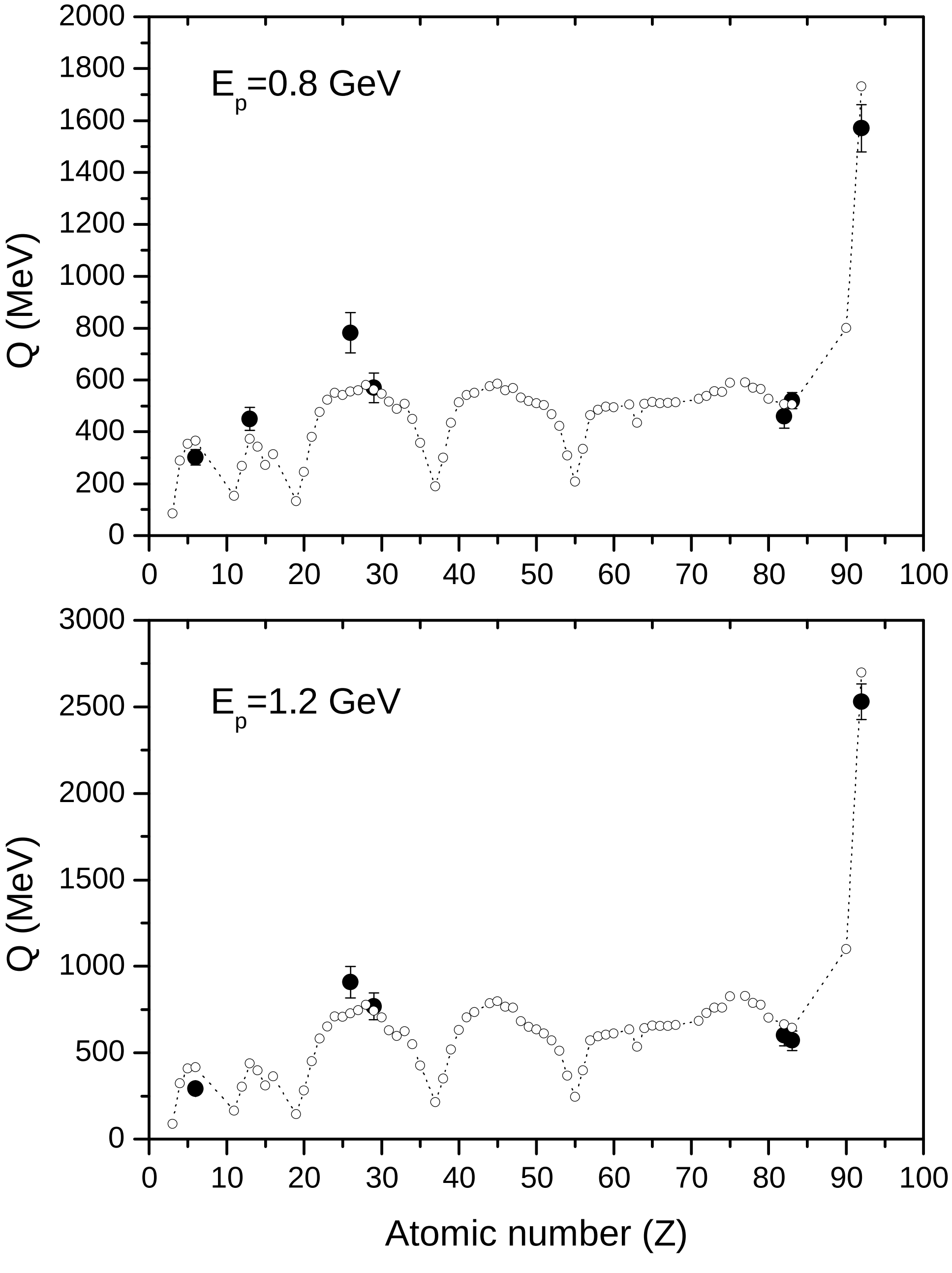

Fig.95 Total heat deposition in the cylindrical target (R=10 cm, H=60 cm) calculated using the Bertini/Dresner model by the MCNPX code (open circle) for natural mixtures of isotopes from Li to U at the energy of primary protons equal to 0.8 and 1.2 GeV. The experimental data (black circle) are from Refs.[336-339].

7.3.2 The linear density of the heat deposition

The linear density of the energy deposition along the target axis calculated and measured for the target with R=10 cm and H=60 cm is shown in Figs.96-107. The calculations were performed with the help of the MCNPX code using the Bertini model, the CEM model and the ISABEL model and with the help of the CASCADE/INPE code. Figs.96-107 show the results obtained for 0.8 GeV, 1.0 GeV (for Al) and 1.2 GeV protons and the values of the heat deposition measured in Refs.[336,338,339].

The noticeable deviation of the calculated and measured values of the heat deposition is for carbon (Figs.96,97) at the distance up to 30 - 40 cm from the point of the beam penetration along the target axis. For aluminum the calculated values of Q are lower than the measured ones for a whole target length (Figs.98,99). The substantial difference between the measured and calculated energy deposition is for iron at the distance z > 5 cm (Figs.100,101). The most relative deviation is for 0.8 GeV protons at the distance z exceeding the proton range (R_p) in iron equal to 42.3 cm (Fig.100). There is a quite good agreement between measurements and calculations for the copper target for a whole target length (Figs.102,103) except the distance z =40 – 45 cm for 0.8 GeV protons (Fig.102) which is close to the proton range in copper, R_p = 38.8 cm. There is a good agreement between different code calculations and the experimental data for the lead and bismuth target (Fig.104-107). The Q(z) dependence for 0.8 GeV protons shows the weak growth at the distance close to proton ranges in the targets (Figs.100,102,104,106). It is due to the sharp rise of the proton stopping power in this region and the presence of the relatively small part of the primary protons not undergoing the nuclear interactions. For the carbon and aluminum targets and for all targets at 1.2 GeV proton energy the range of protons exceeds the target length.

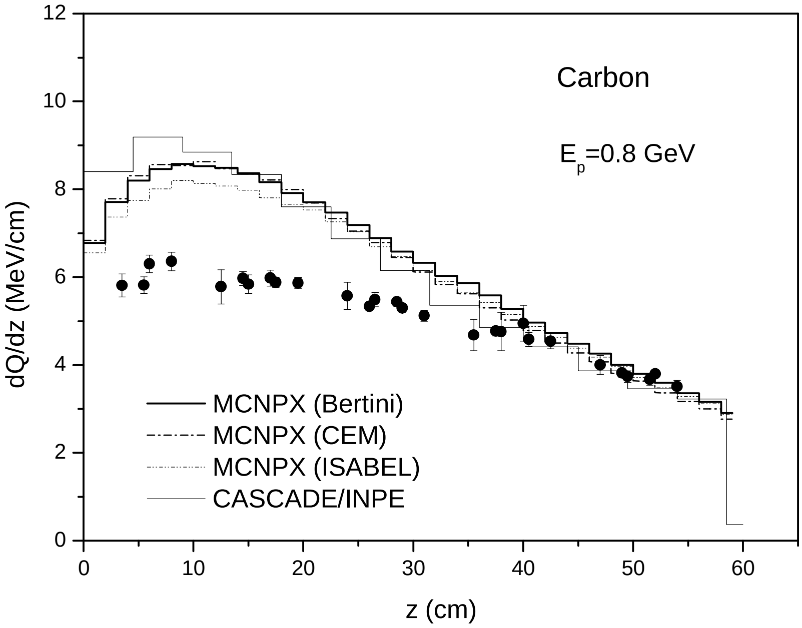

Fig.96 Energy deposition in the carbon target irradiated with 0.8 GeV protons calculated using the MCNPX code package and the CASCADE/INPE code. The experimental data (black circle) are from Ref.[338].

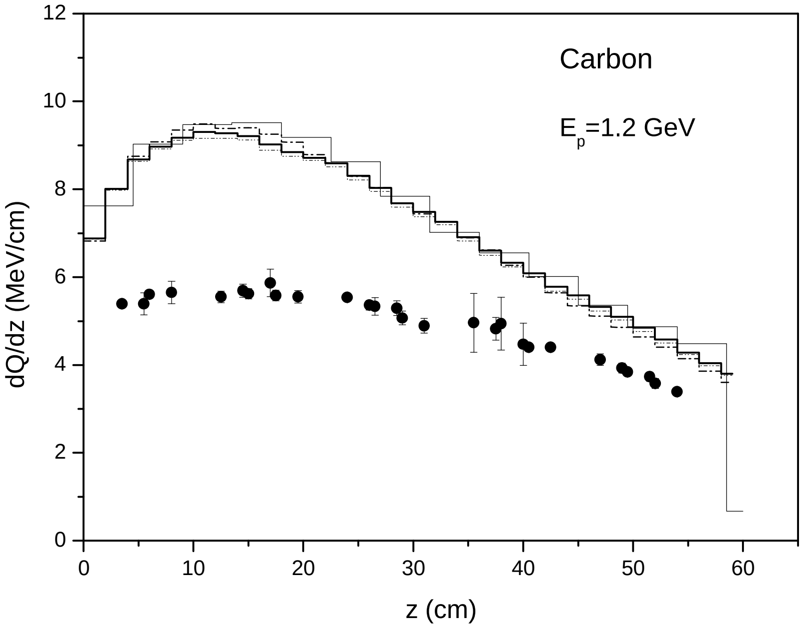

Fig.97 Energy deposition in the carbon target irradiated with 1.2 GeV protons. The experimental data are from Ref.[338]. The symbols are as in Fig.96.

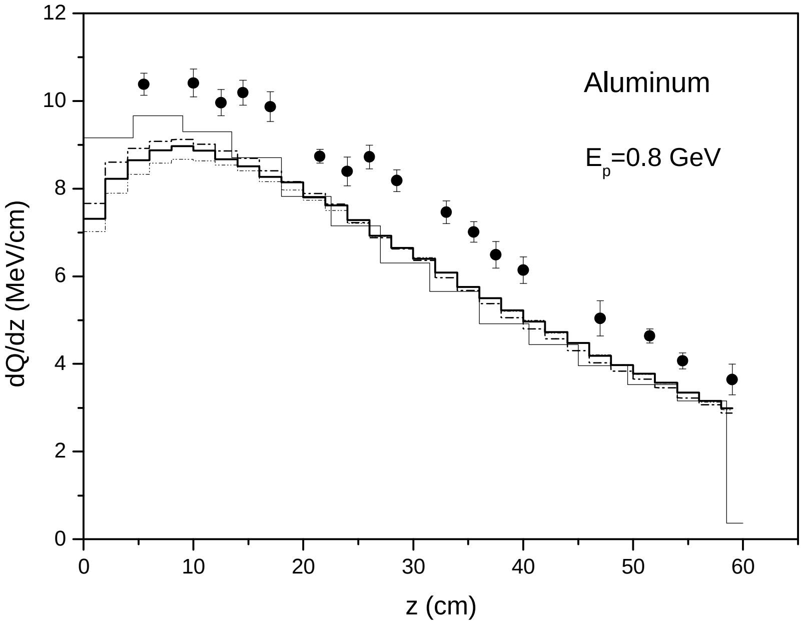

Fig.98 Energy deposition in the aluminum target irradiated with 0.8 GeV protons. The experimental data are from Ref.[338]. The symbols are as in Fig.96.

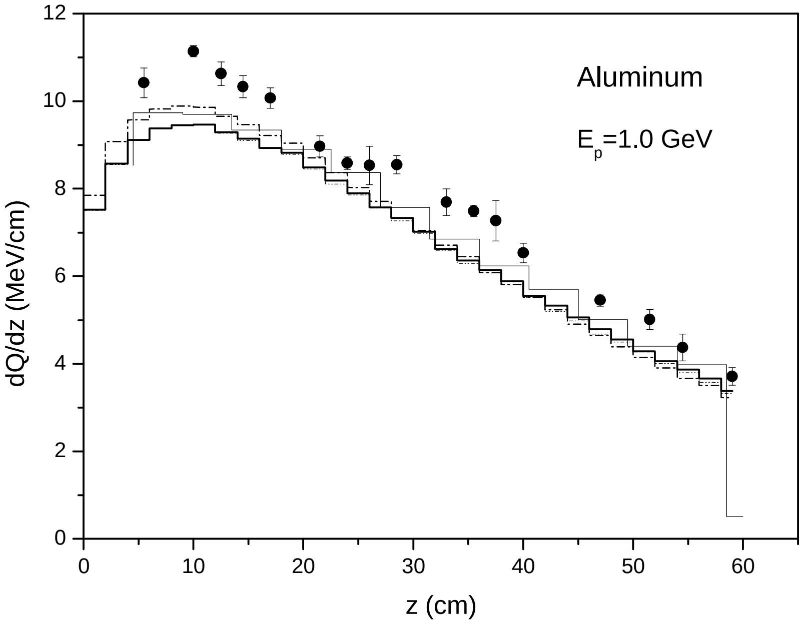

Fig.99 Energy deposition in the aluminum target irradiated with 1.0 GeV protons. The experimental data are from Ref.[338]. The symbols are as in Fig.96.

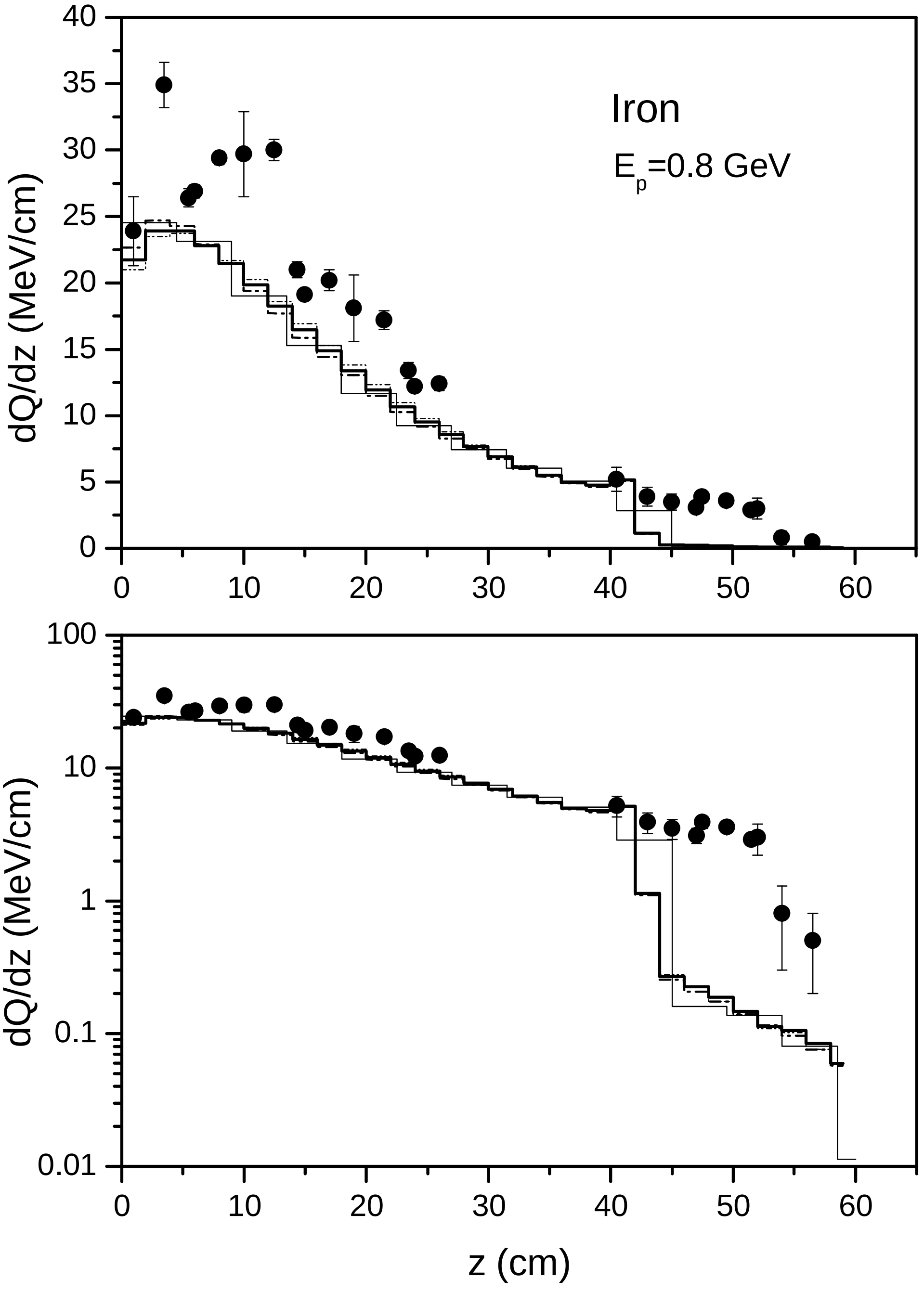

Fig.100 Energy deposition in the iron target irradiated with 0.8 GeV protons. The experimental data are from Ref.[339]. The symbols are as in Fig.96.

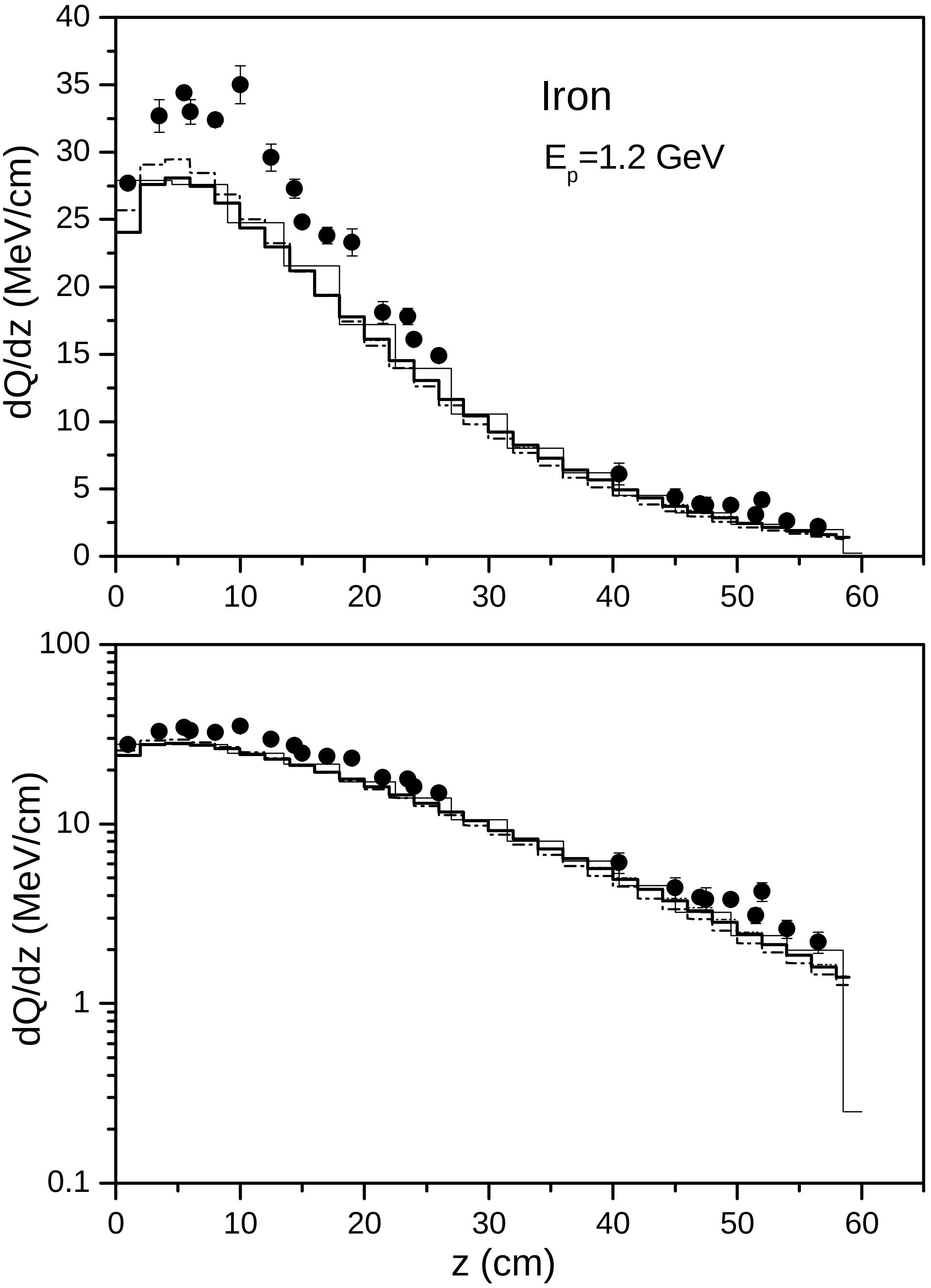

Fig.101 Energy deposition in the iron target irradiated with 1.2 GeV protons. The experimental data are from Ref.[339]. The symbols are as in Fig.96.

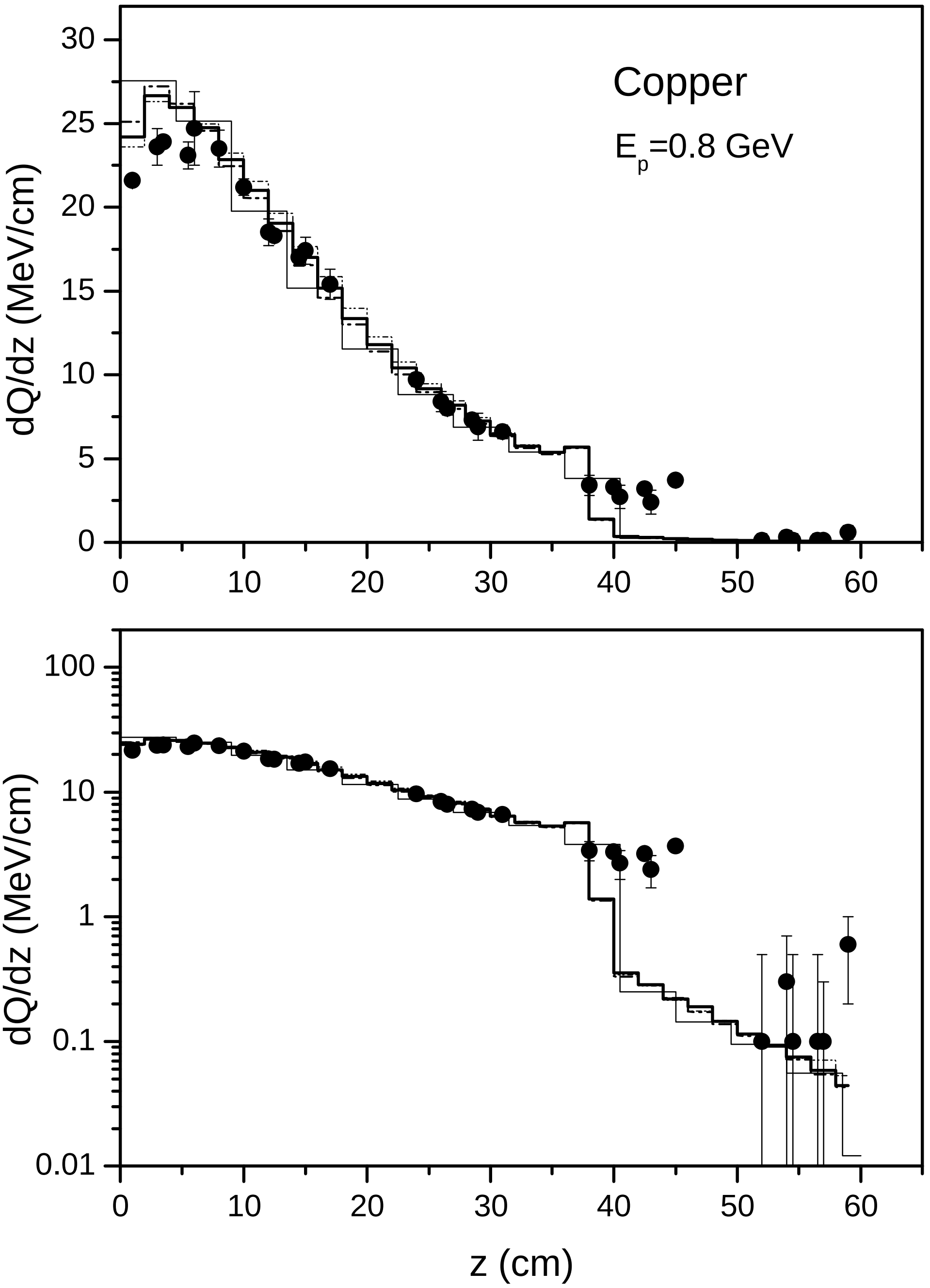

Fig.102 Energy deposition in the copper target irradiated with 0.8 GeV protons. The experimental data are from Ref.[339]. The symbols are as in Fig.96.

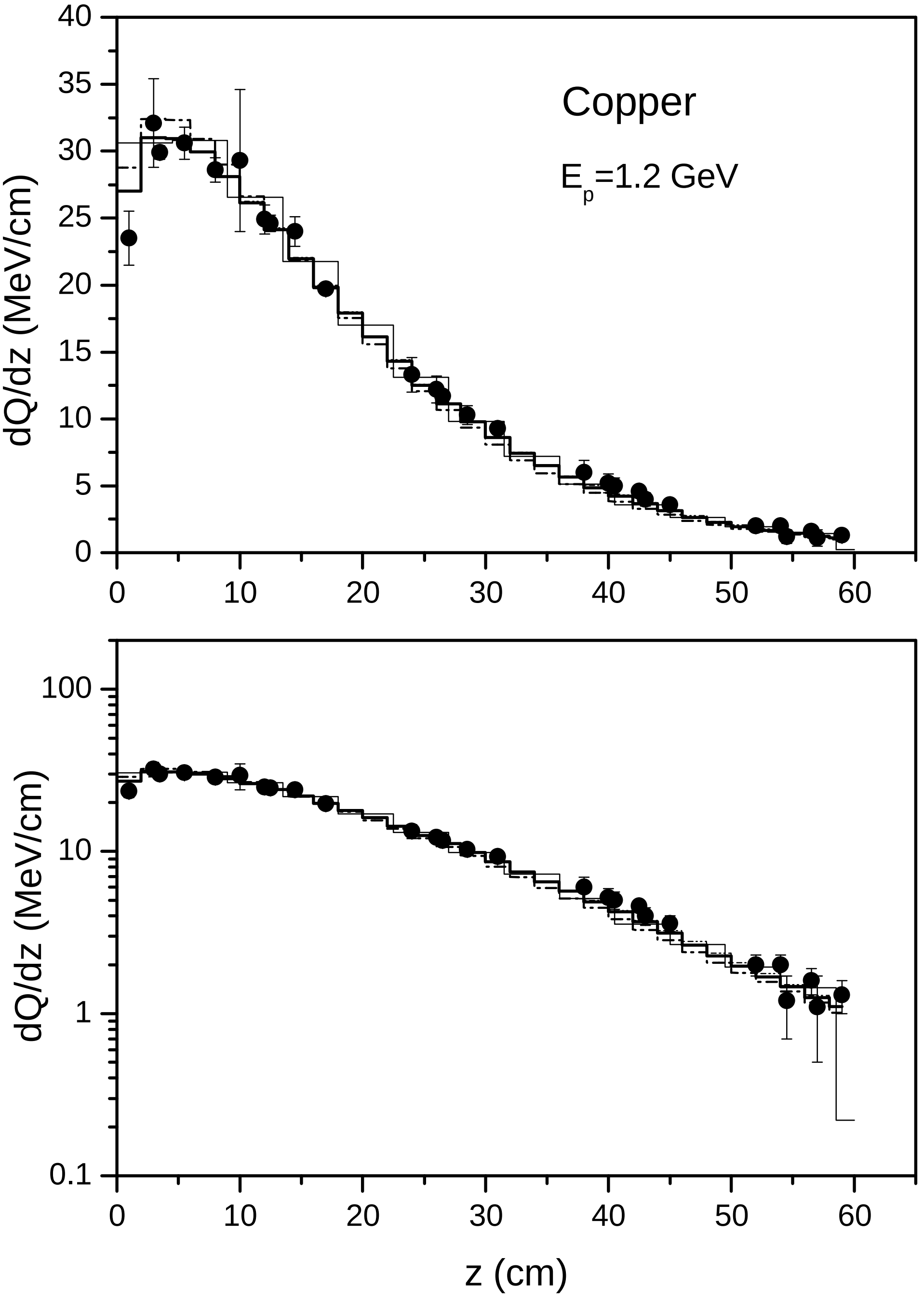

Fig.103 Energy deposition in the copper target irradiated with 1.2 GeV protons. The experimental data are from Ref.[339]. The symbols are as in Fig.96.

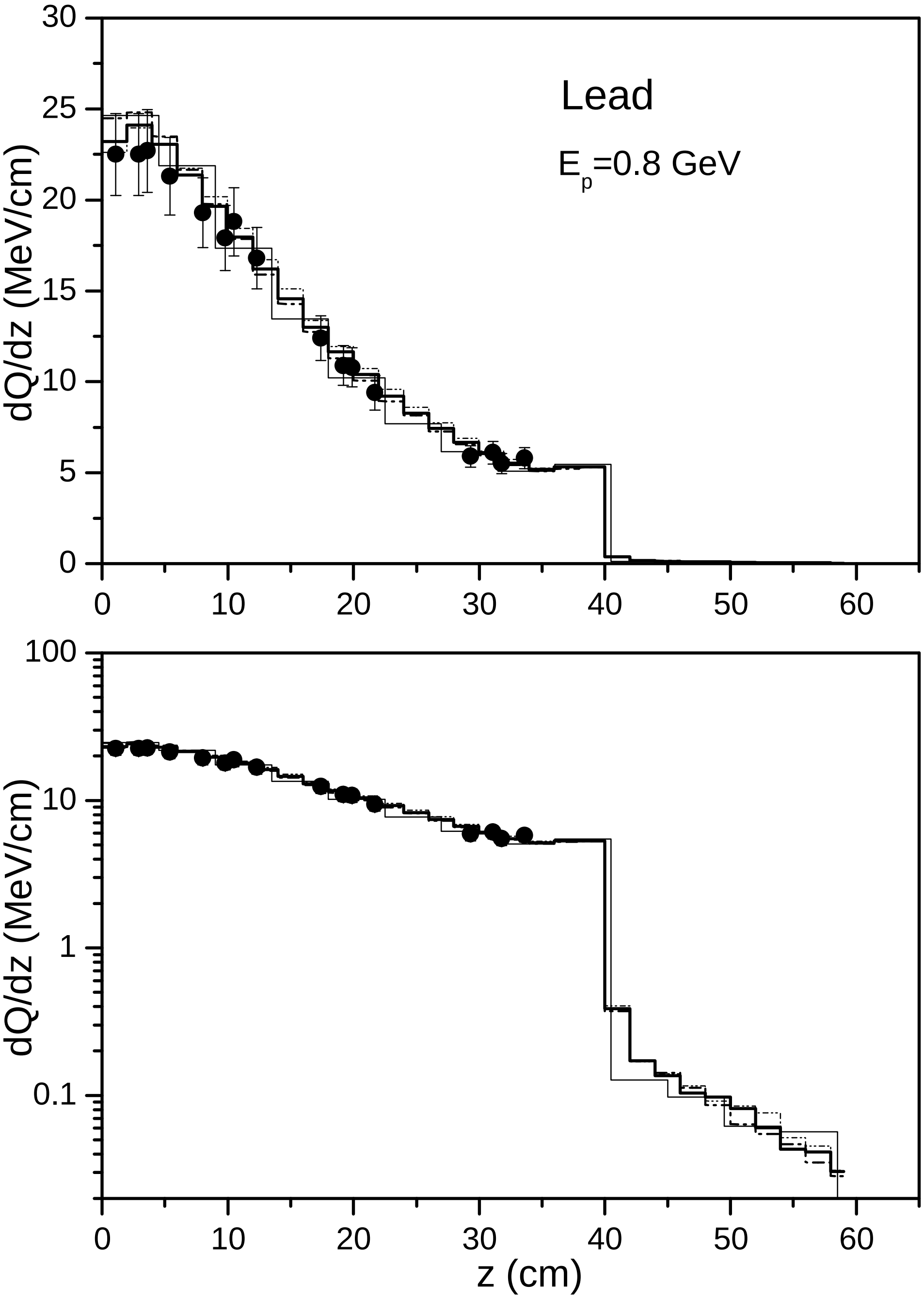

Fig.104 Energy deposition in the lead target irradiated with 0.8 GeV protons. The experimental data are from Ref.[336]. The symbols are as in Fig.96.

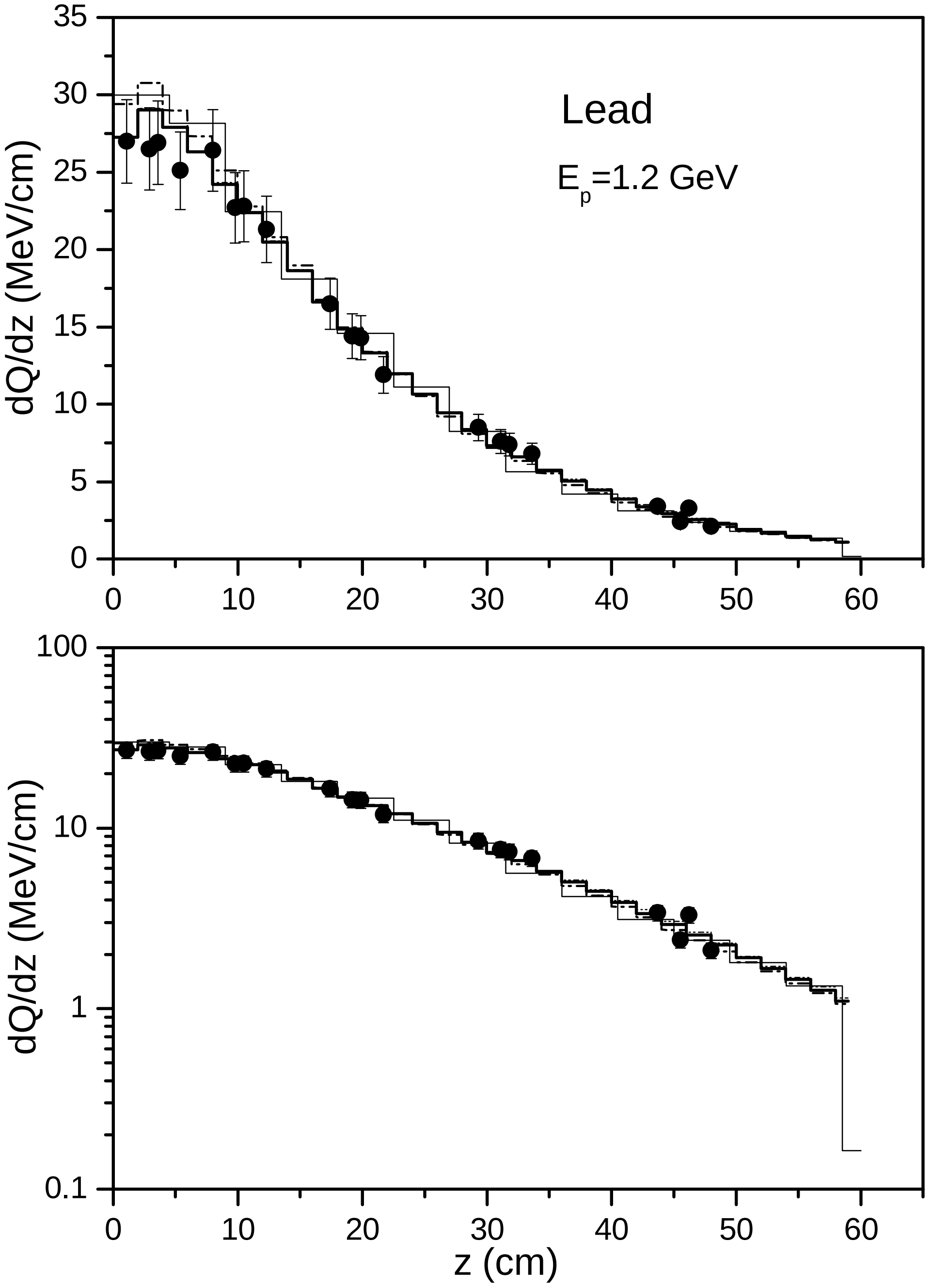

Fig.105 Energy deposition in the lead target irradiated with 1.2 GeV protons. The experimental data are from Ref.[336]. The symbols are as in Fig.96.

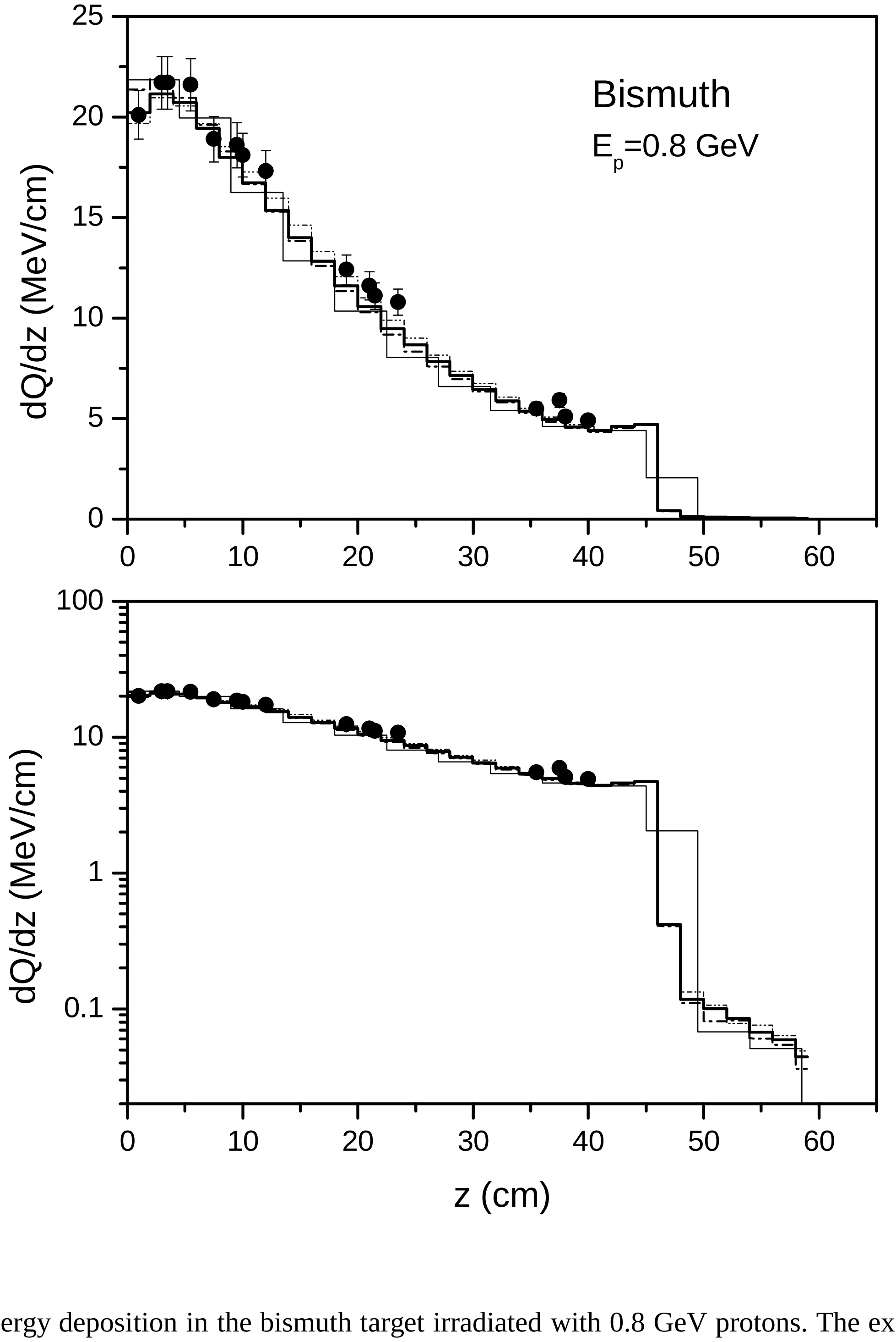

Fig.106 Energy deposition in the bismuth target irradiated with 0.8 GeV protons. The experimental data are from Ref.[336]. The symbols are as in Fig.96.

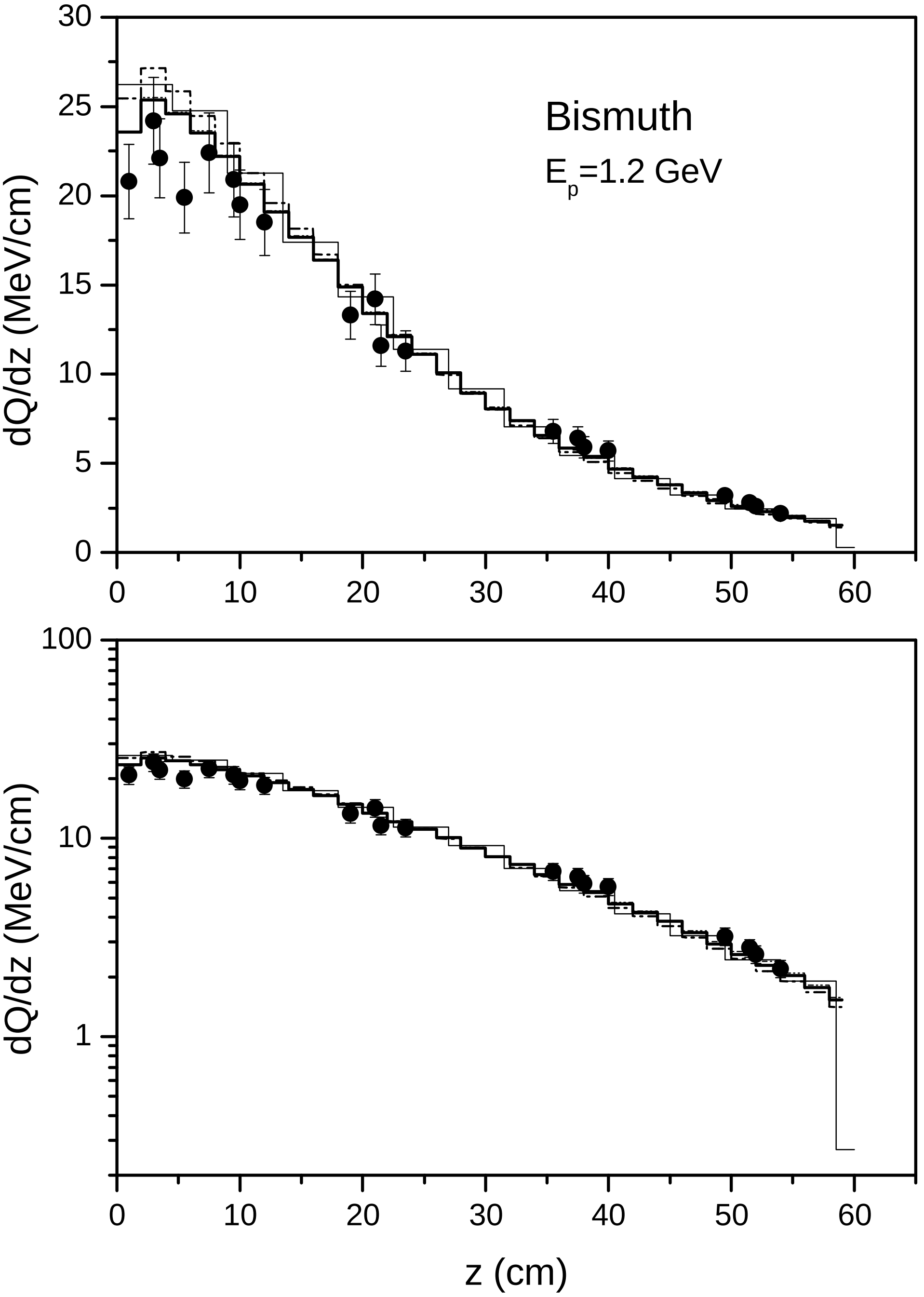

Fig.107 Energy deposition in the bismuth target irradiated with 1.2 GeV protons. The experimental data are from Ref.[336]. The symbols are as in Fig.96.

7.3.3 The contribution of different particles and energy ranges in the heat deposition

The contribution of the different particles and energy regions in the total value of the energy deposition has been studied for the different targets with the help of the MCNPX code and the CASCADE/INPE code.

Tables 18,19 show the calculated contributions of the different physical processes in the heat deposition in the iron target irradiated with 0.8 and 1.2 GeV protons. It is seen that the principal contribution to the total heat deposition is due to the ionization from the primary and secondary protons and photon interactions with the matter. With the growth of the initial proton energy the contribution of the primary protons decreases. The part of other particles is growing.

The good agreement is observed for different code calculations for the contribution of the ionization from primary and secondary protons and photon interactions including the photons produced from the π^0 decay. The contribution of the ionization from the light clusters (d, t, ^{3}He, α) are close for both the Bertini model and the ISABEL model and for the CEM model and the CASCADE/INPE model. At the same time the separate contribution of deuterons, tritons, ^{3}He and α-particles are different for the CEM model and the CASCADE/INPE model calculations. The calculated contribution of charged pions is in a good agreement for the Bertini, CEM and ISABEL models. The result of the CASCADE/INPE code is twice more than the other code calculations. The energy released by the heavy recoils calculated with the help of the different codes is similar.

The contribution of different physical processes to the heat deposition in the lead target is shown in Tables 20,21. The principal contributors are the proton and photon interactions, the same as for the iron target. The different codes predict the close values of Q for the ionization of primary protons, for the photon and neutron interactions. As for the iron target the CASCADE/INPE code predicts more charged pions than the models included in the MCNPX code. The energy deposited by the ionization from the light clusters is close for the Bertini model and the ISABEL model and for the CEM model and the CASCADE/INPE model.

Table 18

Energy deposition (MeV) in the cylindrical iron target (R=10 cm, H=60 cm) irradiated with 0.8 GeV protons calculated with the help of the different models. (Empty cell means that the contribution is not identified).

Value	MCNPX			CASCADE/INPE
	Bertini	CEM	ISABEL	
Total	561.29 (100.0 %)	555.85 (100.0 %)	566.21 (100.0 %)	561.81 (100.0 %)
Ionization from primary proton	238.69 (42.53)	238.69 (42.94)	238.69 (42.16)	252.70 (44.98)
Ionization from secondary protons	250.29 (44.59)	233.91 (42.08)	258.02 (45.57)	220.30 (39.21)
Photon interactions	41.00 (7.31)	40.18 (7.23)	40.98 (7.24)	34.64 (6.17)
photons formed from π^0 decay	21.75 (3.87)	21.45 (3.86)	23.51 (4.15)	17.28 (3.08)
Charged pions (π^+,π^-)	10.52 (1.87)	10.24 (1.84)	11.16 (1.97)	25.23 (4.49)
negative pions, (π^-)				2.51 (0.45)
Ionization from light clusters (d, t, ^{3}He, α)	11.26 (2.01)	22.16 (3.99)	9.24 (1.63)	17.37 (3.09)
deuterons	5.35 (0.95)	11.02 (1.98)	4.40 (0.78)	2.51 (0.45)
tritons	0.57 (0.10)	2.96 (0.53)	0.41 (0.07)	0.56 (0.10)
^{3}He	0.36 (0.06)	2.39 (0.43)	0.20 (0.03)	0.50 (0.09)
α-particles	4.98 (0.89)	5.78 (1.04)	4.23 (0.75)	13.80 (2.46)
non-equilibrium α-particles				7.58 (1.35)
Total recoils	9.52 (1.70)	10.67 (1.92)	8.12 (1.43)	11.57 (2.06)
recoils from neutron induced reactions	3.01 (0.54)	3.09 (0.56)	2.75 (0.48)	2.89 (0.51)

Table 19

Energy deposition (MeV) in the cylindrical iron target (R=10 cm, H=60 cm) irradiated with 1.2 GeV protons calculated with the help of the different models. (Empty cell means that the contribution is not identified).

Value	MCNPX			CASCADE/INPE
	Bertini	CEM	ISABEL	
Total	739.15 (100.0 %)	737.57 (100.0 %)	740.43 (100.0 %)	765.31 (100.0 %)
Ionization from primary proton	198.94 (26.91)	198.94 (26.97)	198.94 (26.87)	208.90 (27.30)
Ionization from secondary protons	379.10 (51.29)	352.68 (47.82)	382.06 (51.60)	358.72 (46.87)
Photon interactions	91.29 (12.35)	94.39 (12.80)	91.65 (12.38)	85.91 (11.23)
photons formed from π^0 decay	60.11 (8.13)	64.71 (8.77)	61.87 (8.36)	56.99 (7.45)
Charged pions (π^+,π^-)	30.88 (4.18)	31.06 (4.21)	31.27 (4.22)	63.96 (8.36)
negative pions, (π^-)				8.92 (1.17)
Ionization from light clusters (d, t, ^{3}He, α)	21.08 (2.85)	40.97 (5.55)	19.61 (2.65)	34.02 (4.45)
deuterons	10.18 (1.38)	19.33 (2.62)	9.64 (1.30)	5.16 (0.67)
Tritons	1.31 (0.18)	6.02 (0.82)	1.19 (0.16)	1.26 (0.16)
^{3}He	0.97 (0.13)	5.05 (0.68)	0.87 (0.12)	1.13 (0.15)
α-particles	8.63 (1.17)	10.57 (1.43)	7.91 (1.07)	26.47 (3.46)
non-equilibrium α-particles				14.18 (1.85)
Total recoils	17.85 (2.42)	19.53 (2.65)	16.89 (2.28)	13.79 (1.80)
recoils from neutron induced reactions	5.17 (0.70)	5.20 (0.70)	4.96 (0.67)	5.46 (0.71)

Fig.108-110 show the contribution of the interactions of different particles in the total heat deposition for the iron and lead targets at the energies of primary protons from 0.3 to 2.5 GeV. The calculations are performed with the help of the Bertini model and the MCNPX code for the cylindrical target (R=10 cm, H=60 cm). The absolute values of the different contributions are shown in Fig.108,109 and the relative values are presented in Fig.110. One can see the decrease of the relative contribution of the proton interactions in the energy deposition and the increase of other contributions with the primary particle energy growing.

Table 20

Energy deposition (MeV) in the cylindrical lead target (R=10 cm, H=60 cm) irradiated with 0.8 GeV protons calculated with the help of the different models. (Empty cell means that the contribution is not identified).

Value	MCNPX			CASCADE/INPE
	Bertini model	CEM model	ISABEL model	
Total	510.49 (100.0 %)	510.52 (100.0 %)	519.44 (100.0 %)	507.19 (100.0 %)
Proton interactions$^{(*)}$	441.48 (86.48)	432.75 (84.77)	454.48 (87.49)	429.56 (84.69)
ionization from primary protons	260.46 (51.02)	260.46 (51.02)	260.46 (50.14)	260.35 (51.33)
fission induced by protons				8.51 (1.68)
Photon interactions	45.13 (8.84)	43.89 (8.60)	43.74 (8.42)	40.23 (7.93)
photons produced in neutron in-duced reactions below 20 MeV				16.93 (3.34)
photons formed from π^0 decay	18.28 (3.58)	17.78 (3.48)	18.29 (3.52)	13.22 (2.61)
Charged pions (π^+,π^-)	7.80 (1.53)	7.52 (1.47)	6.97 (1.34)	16.97 (3.35)
negative pions, (π^-)				2.15 (0.42)
fission induced by pions				0.10 (0.02)
Ionization from light clusters (d, t, ^{3}He, α)	14.36 (2.81)	24.69 (4.84)	12.53 (2.41)	18.67 (3.68)
deuterons	3.42 (0.67)	13.87 (2.72)	2.82 (0.54)	2.39 (0.47)
tritons	1.54 (0.30)	4.10 (0.80)	1.24 (0.24)	1.22 (0.24)
^{3}He	0.11 (0.02)	2.15 (0.42)	0.07 (0.01)	0.18 (0.04)
α-particles	9.28 (1.82)	4.58 (0.90)	8.40 (1.62)	14.88 (2.93)
non-equilibrium α-particles				7.75 (1.53)

Table 20 continued

Value	MCNPX			CASCADE/INPE
	Bertini model	CEM model	ISABEL model	
Neutron interactions (**)	1.71 (0.34)	1.67 (0.33)	1.73 (0.33)	1.76 (0.35)
fission induced by neutrons				0.46 (0.09)
Fission				9.08 (1.79)

(*) including ionization, fission and recoils induced by primary and secondary protons
(**) including fission and recoils

Table 21

Energy deposition (MeV) in the cylindrical lead target (R=10 cm, H=60 cm) irradiated with 1.2 GeV protons calculated with the help of the different models. (Empty cell means that the contribution is not identified).

Value	MCNPX			CASCADE/INPE
	Bertini model	CEM model	ISABEL model	
Total	665.93 (100.0 %)	676.53 (100.0 %)	668.71 (100.0 %)	685.66 (100.0 %)
Proton interactions(*)	511.76 (76.85)	502.56 (74.29)	516.24 (77.20)	499.50 (72.85)
ionization from primary protons	223.92 (33.62)	223.92 (33.10)	223.92 (33.49)	218.58 (31.88)
fission induced by protons				12.40 (1.81)
Photon interactions	93.66 (14.07)	94.22 (13.93)	93.53 (13.99)	89.79 (13.10)
photons produced in neutron in-duced reactions below 20 MeV				29.50 (4.30)
photons formed from π^0 decay	48.37 (7.26)	51.35 (7.59)	49.17 (7.35)	44.01 (6.42)
Charged pions (π^+,π^-)	22.93 (3.44)	22.76 (3.36)	22.41 (3.35)	44.59 (6.50)
negative pions, (π^-)				8.12 (1.18)
fission induced by pions				0.47 (0.07)

Table 21 continued

Value	MCNPX			CASCADE/INPE
	Bertini model	CEM model	ISABEL model	
Ionization from light clusters (d, t, ^{3}He, α)	34.45 (5.17)	54.02 (7.98)	33.41 (5.00)	48.30 (7.04)
deuterons	8.89 (1.33)	28.68 (4.24)	8.64 (1.29)	6.29 (0.92)
Tritons	4.59 (0.69)	9.97 (1.47)	4.41 (0.66)	3.49 (0.51)
^{3}He	0.62 (0.09)	5.75 (0.85)	0.60 (0.09)	0.61 (0.09)
α-particles	20.35 (3.06)	9.62 (1.42)	19.77 (2.96)	37.91 (5.53)
non-equilibrium α-particles				19.50 (2.84)
Neutron interactions (**)	3.12 (0.47)	2.96 (0.44)	3.11 (0.47)	3.48 (0.51)
fission induced by neutrons				1.13 (0.16)
Fission				14.00 (2.04)

(*) including ionization, fission and recoils induced by primary and secondary protons
(**) including fission and recoils

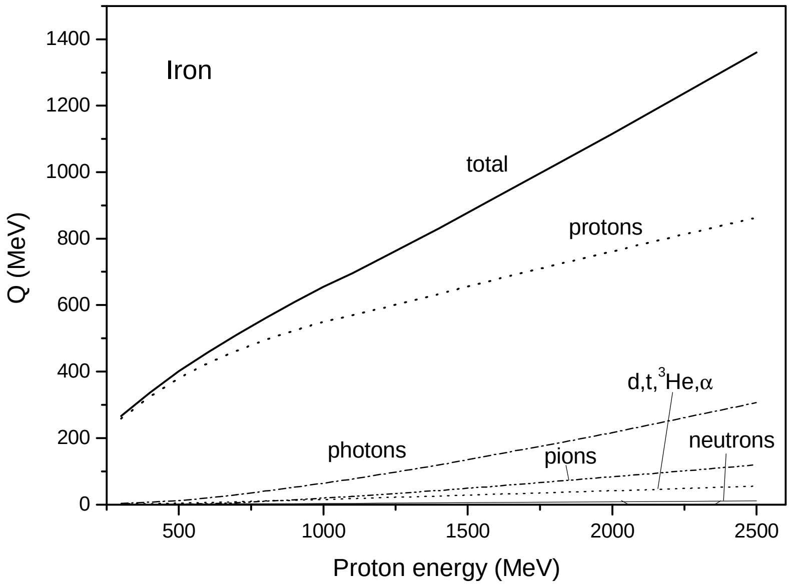

Fig.108 Absolute contribution of different particles in the heat deposition in the iron target irradiated with intermediate energy protons. “Neutrons” means the contribution of recoils produced in neutron induced reactions.

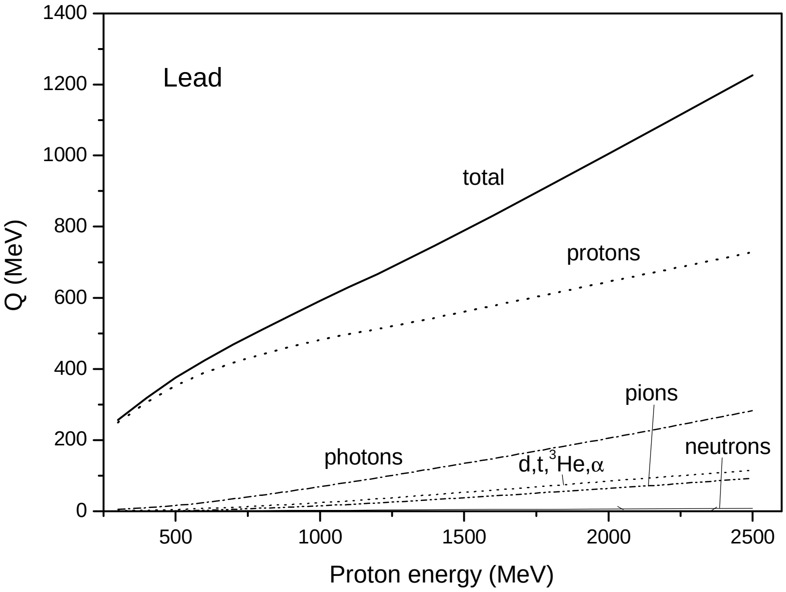

Fig.109 Absolute contribution of different particles in the heat deposition in the lead target irradiated with intermediate energy protons. “Neutrons” means the contribution of fission and recoils in neutron induced reactions.

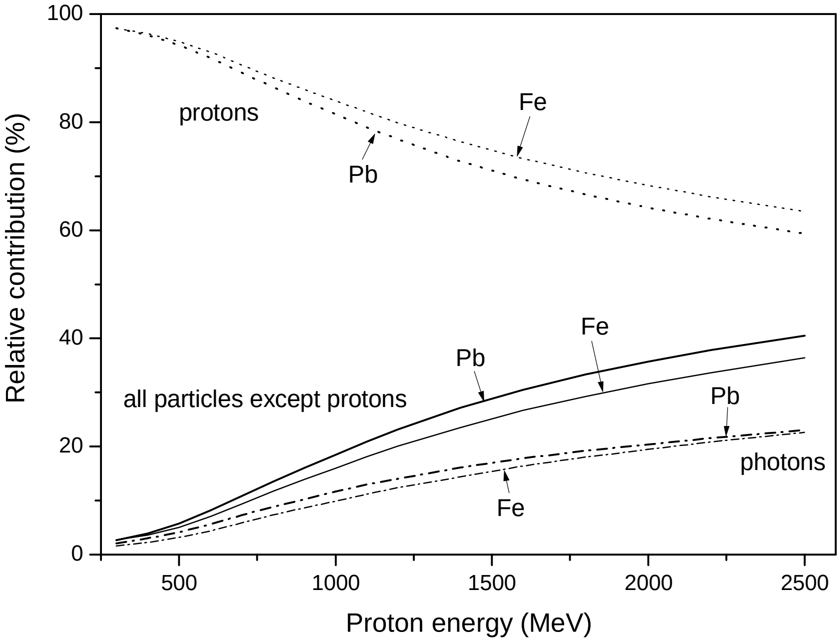

Fig.110 Comparison of the relative contributions of different particles in the total heat deposition in the iron and lead targets irradiated with intermediate energy protons.

Figs.111-117 show the relative contribution of different energy range of protons, photons and pions in the heat deposition calculated for the iron and lead targets. Here the relative values correspond to the ratio of the heat deposition from the fixed energy ranges of particles, below 1 MeV, from 1 to 20 MeV, from 20 to 150 MeV and above 150 MeV to the total energy deposition due to the interactions of the considered particles with the target. The contribution of protons with the energy below 20 MeV is growing with the increase of the primary proton energy (Figs.111,114). The contribution of the energy range from 20 to 150 MeV decreases up to ~ 700 MeV and slowly increases at higher energies. The contribution of protons with the energy above 150 MeV grows up to ~ 700 MeV and then decreases. For the photons and pions (Figs.112,113,115,116) the energy dependence of the contribution of different energy ranges differs from the protons. There is the constant decrease of the contribution of particles with the energy below 20 MeV. The region 20 to 150 MeV shows the maximum located at the different primary proton energy for iron and lead. The contribution of particles with the energy above 150 MeV rises steadily.

The relative contribution of the energy ranges for all particles is shown in Fig.117 for the iron and lead target. Fig.117 illustrates the increasing importance of the energy range below 150 MeV for the heat deposition calculations.

7.4 *Summary about the calculation of the energy deposition in targets from C to U irradiated with intermediate energy protons*

The energy deposition has been calculated for targets from carbon to uranium irradiated with intermediate energy protons using the MCNPX code package and the CASCADE/INPE code.

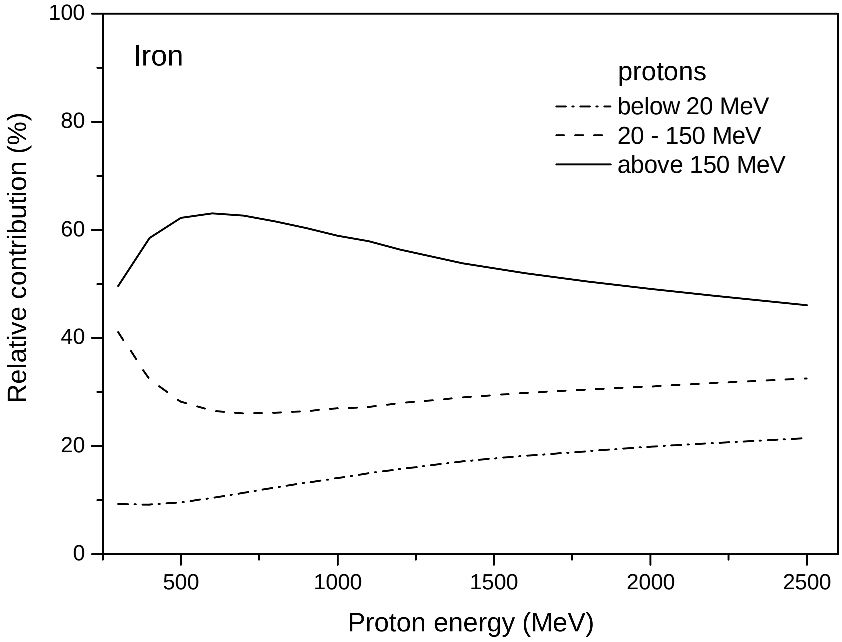

Fig.111 Relative contribution of protons with different energies in the proton induced heat deposition in the iron target (R=10 cm, H=60 cm) irradiated with intermediate energy protons calculated using the Bertini/Dresner model (MCNPX).

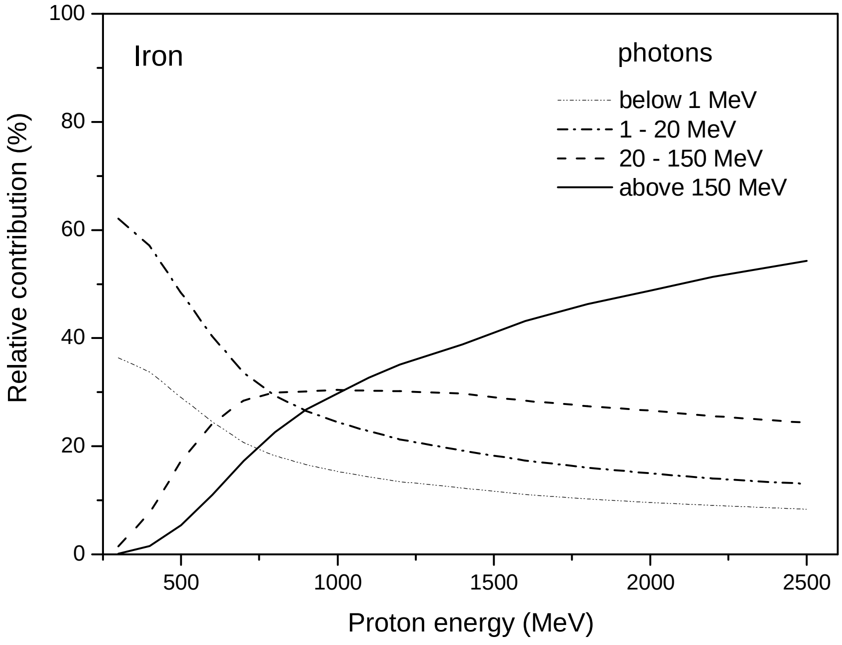

Fig.112 Relative contribution of photons of different energies in the photon induced heat deposition in the iron target (R=10 cm, H=60 cm) irradiated with intermediate energy protons calculated using the Bertini/Dresner model (MCNPX).

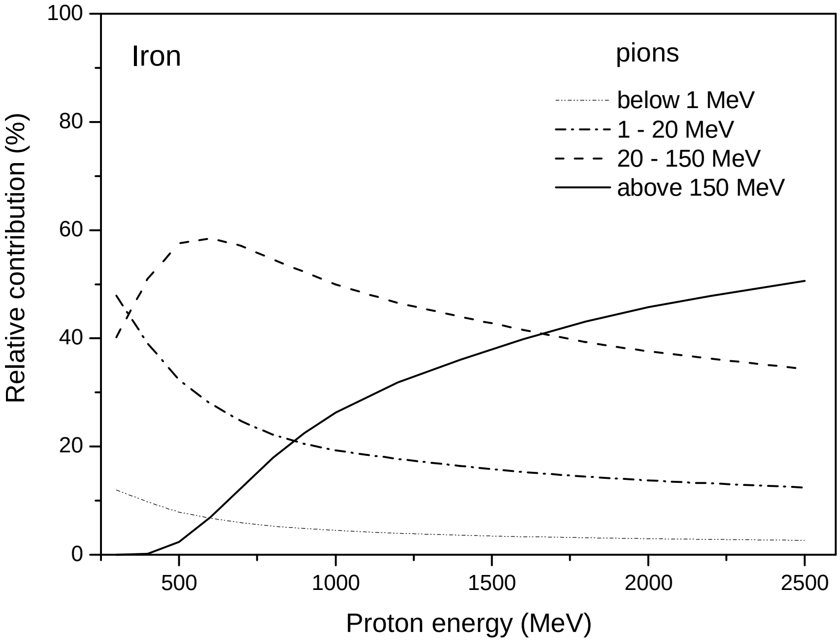

Fig.113 Relative contribution of π^+ and π^- of different energies in the charged pion induced heat deposition in the iron target (R=10 cm, H=60 cm) irradiated with intermediate energy protons calculated using the Bertini/Dresner model (MCNPX).

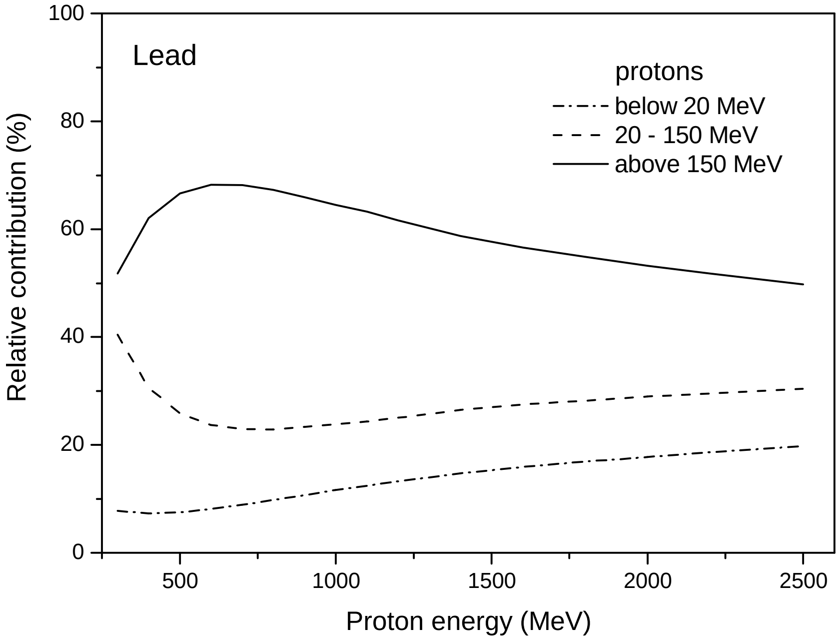

Fig.114 Relative contribution of protons of different energies in the proton induced heat deposition in the lead target (R=10 cm, H=60 cm) irradiated with intermediate energy protons calculated using the Bertini model (MCNPX).

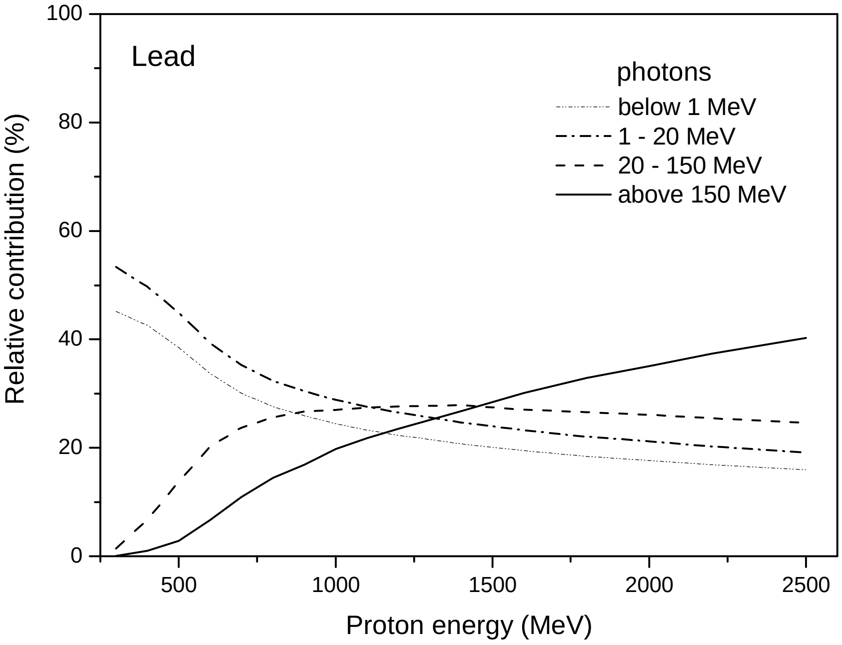

Fig.115 Relative contribution of photons of different energies in the photon induced heat deposition in the lead target irradiated with intermediate energy protons calculated using the Bertini/Dresner model (MCNPX).

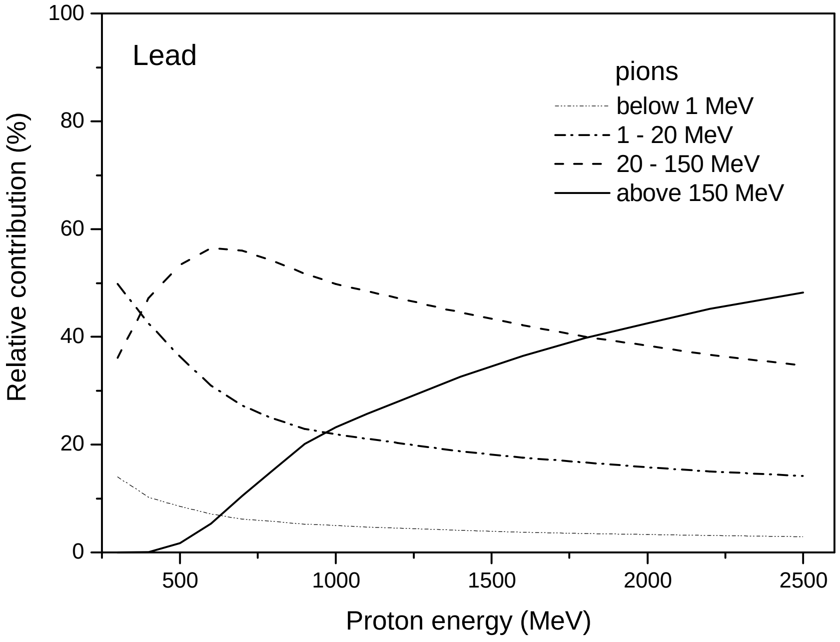

Fig.116 Relative contribution of π^+ and π^- of different energies in the charged pion induced heat deposition in the lead target irradiated with intermediate energy protons calculated using the Bertini/Dresner model (MCNPX).

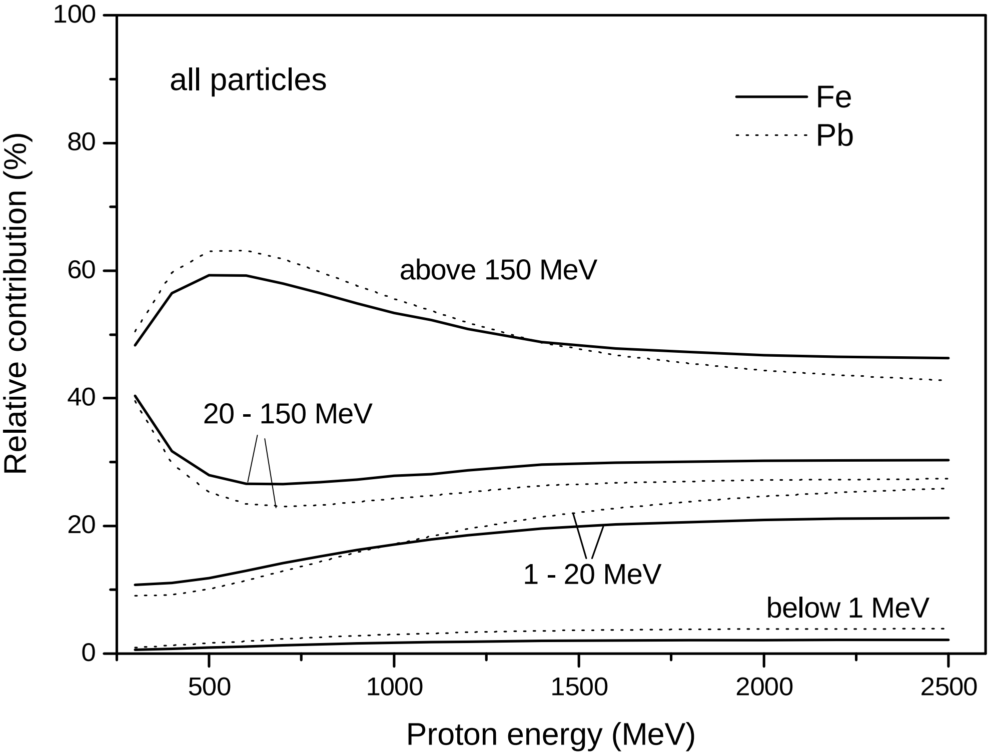

Fig.117 Comparison of the relative contributions of the particles of different energies in the total heat deposition in the iron and lead target irradiated with intermediate energy protons calculated using the Bertini/Dresner model (MCNPX).

The values obtained using different models and codes are in a good agreement for the carbon, aluminum, copper, lead and bismuth target. For uranium the prediction of the CEM model is close to the CASCADE/INPE model and values calculated by the Bertini model are close to result obtained using the ISABEL model.

The comparison with measured data for the heat deposition for 0.8, 1.0 and 1.2 GeV protons has been performed. The good agreement is observed for copper, lead and bismuth target (Figs.91-93,102-107). Calculated energy deposition is noticeably higher than experimental data for the carbon target (Figs.88,96,97) and lower for the iron target (Figs.90,100,101). At the proton energy equal to 0.8 GeV the calculations underestimate the heat deposition measured at the distance above the proton range in the targets (Figs.100, 102).

The ISABEL model describes the total heat deposition measured for different targets in the best way (Table 17). At the same time the prediction power of different models is rather similar (Table 17). The general trend of calculated total energy deposition with the change of atomic number of the target is in the agreement with experimental data, except the case of iron (Fig.95).

The contribution of different particles and energy ranges in the energy deposition has been studied. Different models predict similar values of the relative contribution of protons, photons and neutrons in the total heat deposition (Tables 18-21). Results show the significant importance of the energy range of the particles up to 150 MeV for energy deposition calculations (Fig.117).

It is expedient to perform a new set of heat deposition measurements to study the observed systematics in the dependency of atomic number Z and to clarify the difference with experimental data, especially for iron.

8. Conclusion

1. A method of the evaluation of the defect production rate in metals irradiated with neutrons in various power units was proposed. The method is based on the calculation of the radiation damage rate using nuclear models and the NRT model and the use of corrections (defect production efficiency values) obtained from the analysis of available experimental data and from the molecular dynamics simulation.

To obtain the defect production efficiencies the available data for Frenkel pair resistivity and the damage resistivity rate in metals were compiled and analyzed. The systematics of Frenkel pair resistivity was constrained. The average defect production efficiency in metals was calculated for various neutron irradiation spectra.

2. A method combining the method of the molecular dynamics and the binary collision approximation model was proposed for the calculation of the number of defects in irradiated materials. The method was used for the displacement cross-section calculation for tantalum and tungsten irradiated with protons at energies from several keV up to 1 GeV and with neutrons at energies from 10^{-5} eV to 1 GeV.

The recoil spectra for the proton and neutron elastic scattering has been calculated using the data from ENDF/B-VI and by the optical model using the ECIS96 code. The good agreement was found for the proton displacement cross-sections obtained using various modern optical potentials. For neutrons the agreement is worse. The final evaluation of the neutron displacement cross-section was done using the optical potential of Koning, Delaroche at energies from 20 to 200 MeV. Above 200 MeV the neutron elastic displacement cross-section was obtained with the help of the Madland potential and by the calculation with the MCNPX code.

The displacement cross-section for the nucleon nonelastic interactions has been calculated using the MCNPX code package.

3. Various approaches and models used for the description of the α-particle emission in nuclear reactions induced by intermediate energy nucleons were discussed and analyzed. The comparison of the results of calculations with experimental data shows

- the pre-equilibrium model implemented in the GNASH code and various models implemented in the MCNPX code package describes experimental α-particle yields and spectra incorrectly. The reason is the lacks of phenomenological models for complex particle emission implemented in the GNASH code and in the different modules of the MCNPX package

- α-particle emission spectra, the non-equilibrium and the total α-particle yields calculated by the ALICE/ASH code and the DISCA-C and DISCA-S codes are in an agreement with experimental data.

It seems reasonable to implement in the GNASH code and in the modules of MCNPX the models used for the description of the pre-equilibrium α-particle emission in the ALICE/ASH and DISCA-C codes.

The ^{4}He particle production cross-section has been evaluated for ^{181}Ta, natural tungsten and ^{197}Au at energies of incident neutrons and protons from several MeV to 1 GeV.

4. A new approach has been proposed for the calculation of the non-equilibrium fragment yields in nuclear reactions at intermediate and high energies. It was used for the evaluation of the non-equilibrium component of the ^{4}He and ^{3}He production cross-section. The main model calculations have been carried out using the CASCADE/INPE code.

The helium production cross-section has been obtained for iron, ^{181}Ta and tungsten at proton energies from several MeV to 25 GeV and for ^{181}Ta and tungsten at neutron energies up to 1 GeV.

5. A new model for the simulation of interactions of intermediate and high energy particles with nuclei was discussed. The non-equilibrium particle emission is simulated by the intranuclear cascade model using the Monte Carlo method. The deterministic evaporation model is used for the description of the equilibrium de-excitation. The idea of the method was expressed in Refs.[306,307].

The deterministic algorithm of the evaporation model allows to perform a detailed simulation of the equilibrium process. The nuclear level density for equilibrium states is calculated by the generalized superfluid model taking into account collective enhancement of the nuclear level density. The inverse reaction cross-sections are calculated by the optical model. Calculations are performed without simplifications, usually applied for the simulation of evaporation particle cascade using the intranuclear cascade evaporation model at high energies.

The model was used for the analysis of radionuclide yields in proton induced reactions at energies from 0.8 to 2.6 GeV. The results of calculations show the advantage of the model proposed in accuracy of predictions comparing with other popular intranuclear cascade evaporation models.

6. A new approach is proposed for the calculation of non-equilibrium deuteron energy distributions in nuclear reactions induced by nucleons of intermediate energies. It combines the model of the nucleon pick-up, the coalescence and the deuteron knock-out. The calculated deuteron energy distributions are in a good agreement with the measured data for nuclei from ^{12}C to ^{209}Bi.

7. The energy deposition has been calculated for targets from lithium to uranium irradiated with intermediate energy protons using the MCNPX code package and the CASCADE/INPE code. The values obtained using different models and codes are in a good agreement for the carbon, aluminum, copper, lead and bismuth target.

The comparison with measured data for the heat deposition was performed. The calculations are in a good agreement with the experimental data for copper, lead and bismuth targets irradiated with 0.8-1.2 GeV protons. Calculated energy deposition is noticeably higher than measuremed data for the carbon target and lower for the iron target.

The necessity of new measurements of the heat deposition was noted.

References

[1] M.J. Norgett, M.T. Robinson, I.M. Torrens, Nucl. Eng. Des. 33 (1975) 50.

[2] R.E. MacFarlane, NJOY99.0: Code System for Producing Pointwise and Multigroup Neutron and Photon Cross Sections from ENDF/B Data, RSICC Code Package PSR-480 (Report).

[3] J.S. Hendricks, G.W. McKinney, L.S. Waters, T.L. Roberts et al. MCNPX, Version 2.5.d, Report LA-UR-03-5916, 2003.

[4] R.E. Prael, H. Lichtenstein, User Guide to LCS: The LAHET Code System, Report LA-UR-89-3014, 1989.

[5] L.R. Greenwood, R.K. Smither, SPECTER: Neutron Damage Calculations for Materials Irradiations, Report ANL/FPP-TM-197, 1985.

[6] M.T. Robinson, MARLOWE: Computer Simulation of Atomic Collisions in Crystalline Solids (Version 15b), RSICC Code Package PSR-137 (Report).

[7] G. Wallner, M.S. Anand, L.R. Greenwood, M.A. Kirk, W. Mansel, W. Waschkowski, J. Nucl. Mater. 152 (1988) 146.

[8] D.J. Bacon, A.F. Calder, F. Gao, V.G. Kapinos, S.J. Wooding, Nucl. Instr. Meth. Phys. Res. B102 (1995) 37.

[9] P. Jung, Phys. Rev. B23 (1981) 664.

[10] P. Jung, J. Nucl. Mater. 117 (1983) 70.

[11] J.W. Martin, J. Phys. F2 (1972) 842.

[12] R.S. Averback, R. Benedek, K.L. Merkle, Phys. Rev. B18 (1978) 4156.

[13] K.L. Merkle, Wayne E. King, A.C. Baily, K. Haga, M. Meshii, J. Nucl. Mater. 117 (1983) 4.

[14] M.J. Caturla, T. Diaz de la Rubia, M. Victoria, R.K. Corzine, M.R. James, G.A. Greene, J. Nucl. Mater. 296 (2001) 90.

[15] P. Ehrhart, W. Schilling, Phys. Rev. B8 (1973) 2604.

[16] P. Ehrhart, H.G. Haubold, W. Schilling, Adv. Solid State Phys. 14 (1974) 87.

[17] J.B. Roberto, B. Schoenfeld, P. Ehrhart, Phys. Rev. B18 (1978) 2591.

[18] P. Jung, Rad. Eff. 51 (1980) 249.

[19] O. Dimitrov, C. Dimitrov, Rad. Eff. 84 (1985) 117.

[20] G. Burger, H. Meissner, W. Schilling, Phys. Stat. Sol. 4 (1964) 281.

[21] J.A. Horak, T.H. Blewitt, Phys. Stat. Sol. 9 (1972) 721.

[22] P. Lucasson, in: Fundamental Aspects of Radiation Damage in Metals, Eds. M.T. Robinson, F.W. Young, Jr., Vol.1 (1976), p.42 (CONF-75-1006-P1, US ERDA, Washington, DC, 1975)

[23] R.S. Averback, R. Benedek, K.L. Merkle, J. Sprinkle, L.J. Thompson, J. Nucl. Mater. 113 (1983) 211.

[24] O. Bender, P. Ehrhart, J. Phys. F: Metal Phys. 13 (1983) 911.

[25] R.S. Averback, T. Diaz de la Rubia, Solid State Physics 51 (1997) 281.

[26] P. Jung, R.L. Chaplin, H.J. Fenzl, K. Reichelt, P. Wombacher, Phys. Rev. B8 (1973) 553.

[27] P. Ehrhart, U. Schlagheck, J. Phys. F: Metal Phys. 4 (1974) 1575.

[28] W.E. King, R. Benedeck, K.L. Merkle, M. Meshii, in: Point Defects and Defect Interactions in Metals, Eds. J. Takamura, M. Doyama, M. Kiritani, University of Tokyo Press, 1982, p. 789.

[29] M.T. Robinson, I.M. Torrens, Phys. Rev. B9 (1974) 5008.

[30] R.E. MacFarlane, D.W. Muir, The NJOY Nuclear Data Processing System, Ver. 91, Report LA-12740 M, UC-413, 1994.

[31] M. Nakagawa, K. Böning, P. Rosner, G. Vogl, Phys. Rev. B16 (1977) 5285.

[32] C.M. Jimenez, L.F. Lowe, E.A. Burke, C.H. Sherman, Phys. Rev. 153 (1967) 735.

[33] P.G. Lucasson, R.M. Walker, Phys. Rev. 127 (1962) 485.

[34] A. Sosin, Phys. Rev. 126 (1962) 1698.

[35] E.A. Burke, C.M. Jimenez, L.F. Lowe, Phys. Rev. 141 (1966) 629.

[36] J.S.N. Hancock, J.N. Lomer, cited by P. Vajda, Rev. Mod. Phys. 49 (1977) 481.

[37] P. Ehrhart, E. Segura, in: Fundamental Aspects of Radiation Damage in Metals, Eds. M.T. Robinson, F.W. Young, Jr., Vol.1 (1976), p.295 (CONF-75-1006-P1, US ERDA, Washington, DC, 1975)

[38] R.R. Coltman, Jr., C.E. Klabunde, J.M. Williams, J. Nucl. Mater. 99 (1981) 284.

[39] W. Bauer, A. Sosin, Phys. Rev. 135 (1964) A521.

[40] W. Bauer, in Lattice Defects and Their Interactions, (Ed. R.R. Hasiguti, Gordon and Breach Science Publ., New York, London, Paris), 1967, p.567.

[41] R.O. Simmons, R.W. Baluffi, Phys. Rev. 129 (1963) 1533.

[42] B.S. Brown, T.H. Blewitt, T.L. Scott, A.C. Klank, J. Nucl. Mater. 52 (1974) 215.

[43] C.E. Klabunde, R.R. Coltman, J. Nucl. Mater. 108 & 109 (1982) 183.

[44] F. Maury, M. Biget, P. Vajda, A. Lucasson, P. Lucasson, Phys. Rev. B14 (1976) 5303.

[45] A. Iwase, S. Ishino, J. Nucl. Mater. 276 (2000) 178.

[46] P. Ehrhart, Mater. Res. Soc. Symp. 41 (1985) 13.

[47] M.A. Kirk, L.R. Greenwood, J. Nucl. Mater. 80 (1979) 159.

[48] P. Ehrhart, cited by O. Dimitrov, C. Dimitrov, Rad. Eff. 84 (1985) 117.

[49] M. Biget, R. Rizk, P. Vajda, A. Besis, Solid State Commun. 16 (1975) 949.

[50] P. Vajda, M. Biget, Phys. Stat Sol. A23 (1974) 251.

[51] F. Maury, P. Vajda, M. Biget, A. Lucasson, P. Lucasson, Rad. Eff. 25 (1975) 175.

[52] P. Ehrhart, J. Nucl. Mater. 69 & 70 (1978) 200.

[53] W. Schilling, J. Nucl. Mater. 69 & 70 (1978) 465.

[54] M. Hou, A. van Veen, L.M. Caspers, M.R. Yrma, Nucl. Instr. Meth. 209/210 (1983) 19.

[55] P. Jung, W. Schilling, Phys. Rev. B5 (1972) 2046.

[56] M. Biget, F. Maury, P. Vajda, A. Lucasson, P. Lucasson, Phys. Rev. B19 (1979) 820.

[57] M.W. Guinan, J.H. Kinney, J. Nucl. Mater. 103 & 104 (1981) 1319.

[58] T.N. O'Neal, R.L. Chaplin, Phys. Rev. B5 (1972) 3810.

[59] C.G. Shirley, R.L. Chaplin, Phys. Rev. B5 (1972) 2027.

[60] P. Vajda, Rev. Mod. Phys. 49 (1977) 481.

[61] F. Maury, P. Vajda, A. Lucasson, P. Lucasson, Phys. Rev. B8 (1973) 5496; Phys. Rev. B8 (1973) 5506.

[62] P. Ehrhart, B. Schönfeld, Phys. Rev. B19 (1979) 3896.

[63] S. Takamura, T. Aruga, K. Nakata, J. Nucl. Mater. 136 (1985) 159.

[64] S. Myhra, R.B. Gardiner, Rad. Eff. 27 (1975) 35.

[65] M.W. Guinan, J.H. Kinney, J. Nucl. Mater. 108 & 109 (1982) 95.

[66] P. Ehrhart, B. Schönfeld, in: Point Defects and Defect Interactions in Metals, Eds. J. Takamura, M. Doyama, M. Kiritani, University of Tokyo Press, 1982, p.47.

[67] M. Biget, F. Maury, P. Vajda, A. Lucasson, P. Lucasson, Rad. Eff. 7 (1971) 223.

[68] J. McIlwain, R. Gardiner, A. Sosin, S. Myhra, Rad. Eff. 24 (1975) 19.

[69] Smithels Metals Reference Book, Eds. E.A. Brandes, G.B. Brook, Butterworth Heinemann, 7th Ed., 1992, Chapter 19.

[70] Fizicheskie Velichini, Reference Book, Ed. I.S. Grigor’ev, E.Z. Meilikhov, Energoatomizdat, Moscow, 1991.

[71] C. Kittel, Introduction to Solid State Physics, John Wiley & Sons, New York, 1986.

[72] R.C. Birtcher, R.S. Averback, T.H. Blewitt, J. Nucl. Mater. 75 (1978) 167.

[73] F. Rullier-Albenque, H. Bielska-Lewandowska, Y. Quere, G. Wallner, P. Müller, J. Nucl. Mater. 151 (1988) 251.

[74] M. Nakagawa, W. Mansel, K. Böning, P. Rosner, G. Vogl, Phys. Rev. B19 (1979) 742.

[75] G. Wallner, K. Böning, U. Dedek, J. Phys. F16 (1986) 257.

[76] D.E. Cullen, PREPRO 2002, ENDF/B Pre-processing Codes, GROUPIE, Report IAEA-NDS-39, Feb. 5, 2003, http://www.llnl.gov/cullen1/

[77] L.R. Greenwood, private communication.

[78] Horngming Hsieh, T. Diaz de la Rubia, R.S. Averback, Phys. Rev. B40 (1989) 9986.

[79] T. Diaz de la Rubia, W.J. Phythian, J. Nucl. Mater. 191-194 (1992) 108.

[80] A.J.E. Foreman, W.J. Phythian, C.A. English, Phil. Mag. A66 (1992) 671.

[81] D.J. Bacon, T. Diaz de la Rubia, J. Nucl. Mater. 216 (1994) 275.

[82] W.J. Phythian, R.E. Stoller, A.J.E. Foreman, A.F. Calder, D.J. Bacon, J. Nucl. Mater. 223 (1995) 245.

[83] R.E. Stoller, J. Nucl. Mater. 233-237 (1996) 999.

[84] R.E. Stoller, G.R. Odette, B.D. Wirth, J. Nucl. Mater. 251 (1997) 49.

[85] N. Soneda, T. Diaz de la Rubia, Phil. Mag. A78 (1998) 995.

[86] R.E. Stoller, L.R. Greenwood, J. Nucl. Mater. 271&272 (1999) 57.

[87] M.J. Caturla, N. Soneda, E. Alonso, B.D. Wirth, T. Diaz de la Rubia, J.M. Perlado, J.Nucl.Mater. 276 (2000) 13.

[88] R.E. Stoller, Nucl. Eng. Des. 195 (2000) 129.

[89] R.E. Stoller, J. Nucl. Mater. 276 (2000) 22.

[90] E. Alonso, M.J. Caturla, T. Diaz de la Rubia, J.M. Perlado, J. Nucl. Mater. 276 (2000) 221.

[91] N.V. Doan, J. Nucl. Mater. 283-287 (2000) 763.

[92] R.E. Stoller, J. Nucl. Mater. 307-311 (2002) 935.

[93] Yu.N. Osetsky, D.J. Bacon, B.N. Singh, J. Nucl. Mater. 307-311 (2002) 866.

[94] F. Gao, D.J. Bacon, P.E.J. Flrwitt, T.A. Lewis, J. Nucl. Mater. 249 (1997) 77.

[95] M.T. Robinson, Phys. Rev. B40 (1989) 10717.

[96] M.T. Robinson, J. Nucl. Mater. 216 (1994) 1.

[97] M.T. Robinson, Rad. Eff. 141 (1997) 1.

[98] A.F. Calder, D.J. Bacon, J. Nucl. Mater. 207 (1993) 25.

[99] J.F. Ziegler, J.P. Biersack, U. Littmark, Stopping Powers and Ranges of Ions in Matter, Pergamon, New York, 1985.

[100] Y. Chen, U. Fischer, P. Pereslavtsev, F. Wasastjerna, The EU Power Plant Conceptual Study - Neutronic Design Analyses for Near Term and Advanced Reactor Models, Report FZKA 6763, 2003.

[101] S.J. Zinkle, B.N. Singh, J. Nucl. Mater. 199 (1993) 173.

[102] P. Jung, Production of Atomic Defects in Metals, in: Landolt-Börnstein, Croup III: Crystal and Solid State Physics, Ed. H. Ullmaier, Springer-Verlag, Berlin, 25 (1991) 1.

[103] G.W. Iseler, H.I. Dawson, A.S. Mehner, J.W. Kauffman, Phys. Rev. 146 (1966) 468.

[104] H.H. Neely, W. Bauer, Phys. Rev. 149 (1966) 535.

[105] H.M. Simpson, R.L. Chaplin, Phys. Rev. 185 (1969) 958.

[106] H.G. Haubold, D. Martinsen, J. Nucl. Mater. 69 & 70 (1978) 644.

[107] D.N. Borton, A.E. Mardiguian, H.B. Huntington, G.L. Salinger, Bull. Amer. Phys. Soc. 19 (II) (1974) 257 (CI9).

[108] R.L. Chaplin, K. Sonnenberg, R.R. Coltman Jr., Rad. Eff. 27 (1975) 119.

[109] M. Biget, F. Maury, P. Vajda, A. Lucasson, P. Lucasson, J. de Physique 40 (1979) 293.

[110] M. Biget, P. Vajda, F. Maury, A. Lucasson, P. Lucasson, in: Fundamental Aspects of Radiation Damage in Metals, Eds. M.T. Robinson, F.W. Young, Jr., (1976), p.66 (CONF-75-1006-P1, US ERDA, Washington, DC,. 1975)

[111] R. Rizk, P. Vajda, A. Lucasson, P. Lucasson, Phys. Stat. Sol. A18 (1973) 241.

[112] F. Maury, M. Biget, P. Vajda, A. Lucasson, P. Lucasson, Rad. Eff. 38 (1978) 53.

[113] H. Kugler, Ph. D. Thesis, University of Stuttgart, 1980, cited by P. Jung, Production of Atomic Defects in Metals, in: Landolt-Börnstein, Croup III: Crystal and Solid State Physics, Ed. H. Ullmaier, Springer-Verlag, Berlin, 25 (1991) 1.

[114] W.E. Faust, T.N. O'Neal, R.L. Chaplin, Phys. Rev. 183 (1969) 609.

[115] F. Maury, A. Lucasson, P. Lucasson, Crystal Lattice Defects 2 (1971) 47.

[116] S. Myhra, R.B. Gardiner, Rad. Eff. 18 (1973) 39.

[117] J.N. Daou, J.E. Bonnet, P. Vajda, M. Biget, A. Lucasson, P. Lucasson, Phys. Stat. Sol. A40 (1977) 101.

[118] J.N. Daou, E.B. Hannech, P. Vajda, M. Biget, A. Lucasson, P. Lucasson, Philos. Mag. A41 (1980) 225.

[119] H. Vandenborre, L. Stals, J. Cornelis, J. Nihoul, Rad. Eff. 21 (1974) 137.

[120] G. Quelard, J. Dural, J. Ardonceau, D. Lesueur, Rad. Eff. 39 (1978) 45.

[121] J.N. Daou, P. Vajda, A. Lucasson, P. Lucasson, Rad. Eff. 61 (1982) 93.

[122] A. Dunlop, M.H. Gely, Rad. Eff. 79 (1983) 159.

[123] J.N. Daou, P. Vajda, A. Lucasson, P. Lucasson, Rad. Eff. 84 (1985) 211.

[124] J.N. Daou, P. Vajda, A. Lucasson, P. Lucasson, J.P. Burger, Phys. Lett. 107A (1985) 142.

[125] J.N. Daou, P. Vajda, A. Lucasson, P. Lucasson, J. Phys. F: Metal Phys. 10 (1980) 583.

[126] C. Weinberg, Y. Quere, Material Science Forum 15-18 (1987) 943.

[127] TRADE Final Feasibility Report – March 2002 by the Working Group on TRADE: TRiga Accelerator Driven Experiment.

[128] C.H.M. Broeders, A.Yu. Konobeyev, J. Nucl. Mater. 328 (2004) 197.

[129] J. Lindhard, M. Scharff, H.E. Schiott, Range Concepts and Heavy Ion Ranges, K. Dan. Vidensk. Selsk. Mat. Fys. Medd., 33, N14 (1963) 1.

[130] K.B. Winterbon, P. Sigmund, J.B.K. Sanders, Spatial Distribution of Energy Deposited by Atomic Particles in Elastic Collisions, K. Dan. Vidensk. Selsk. Mat. Fys. Medd., 37, N14 (1970) 1.

[131] A.J. Koning, J.P. Delaroche, Nucl. Phys. A713 (2003) 231; data are taken from the Internet at <http://ndswebserver.iaea.org/RIPL-2/>

[132] P. Schwandt, H.O. Meyer, W.W. Jacobs, A.D. Bacher, S.E. Vigdor, M.D. Kaitchuck et al., Phys. Rev. C26 (1982) 55.

[133] R.L. Walter, P.P. Guss, Rad. Eff. 92 (1985) 1079; data are taken from http://www-nds.iaea.org/RIPL-2/

[134] D.G. Madland, in: Proc. Specialists' Meeting on the Nucleon-Nucleus Optical Model up to 200 MeV, Bruyeres-le-Chatel, France, November 13-15, 1996, p.129; Report LA-UR-97-0306 (1985); text is available at http://arxiv.org/abs/nucl-th/9702035; data are taken from http://www-nds.iaea.org/RIPL-2/

[135] H. Kamitsubo, H. Ohnuma, K. Ono, A. Uchida, M. Imaizumi, S. Kobayashi, M. Sekiguchi, J. Phys. Soc. Jap. 22 (1967) 19.

[136] D.J. Steinberg, J.N. Palmieri, A.M. Cormack, Nucl. Phys. 56 (1964) 46.

[137] R.E. Richardson, W.P. Ball, C.E. Leith, B.J. Moyer, Phys. Rev. 86 (1952) 29.

[138] L.S. Waters (editor): MCNPX^{TM} User’s manual, Version 2.3.0, LA-UR-02-2607, 2002.

[139] W.A. Richter, S.W. Steyn, A.A. Cowley, J.A. Stander, J.W. Koen, R. Lindsay, G.C. Hillhouse, R.E. Julies, J.J. Lawrie, J.V. Pilcher, P.E. Hodgson, Phys. Rev. C54 (1996) 1756.

[140] C.H.M. Broeders, A.Yu. Konobeyev, K. Voukelatou, IOTA - a Code to Study Ion Transport and Radiation Damage in Composite Materials, Report FZKA 6984, Karlsruhe, 2004.

[141] J. Raynal, ECIS96, in: Proc. Specialists' Meeting on the Nucleon Nucleus Optical Model up to 200 MeV, Bruyères-le-Chatel, France, November 13-15, 1996; http:// www.nea.fr/html/science/om200/raynal.pdf

[142] J.S. Hendricks, G.W. McKinney, L.S. Waters, T.L. Roberts et al., MCNPX Extensions. Version 2.5.0, Report LA-UR-04-0570 (Feb. 2004).

[143] H.W. Bertini, Phys. Rev. 131 (1963) 1801.

[144] H.W. Bertini, Phys. Rev. 188 (1969) 1711.

[145] W.A. Coleman, T.W. Armstrong, Nucleon-Meson Transport Code NMTC, Report ORNL-4606 (Jan. 1970).

[146] T.A. Gabriel, High Energy Transport Code HETC, Report ORNL/TM-9727;CONF-850140-2-Rev. (Sep. 1985).

[147] Y. Yariv, Z. Fraenkel, Phys. Rev. C 20 (1979) 2227.

[148] Y. Yariv, Z. Fraenkel, Phys. Rev. C 24 (1981) 488.

[149] K. Chen, Z. Fraenkel, G. Friedlander, J.R. Grover, J.M. Miller, Y. Shimamoto, Phys. Rev. 166 (1968) 949.

[150] A.S. Iljinov, A Code for Intranuclear Cascade Calculation in the Energy Range < 5 GeV, JINR Report B1-4-5478, Dubna (1970).

[151] V.S. Barashenkov, V.D. Toneev, Interaction of High Energy Particles and Nuclei with Atomic Nuclei, Atomizdat, Moscow, 1972.

[152] K.K. Gudima, S.G. Mashnik, V.D. Toneev, Nucl. Phys. A 401 (1983) 329.

[153] S.G. Mashnik, Nucl. Phys. A 568 (1994) 703.

[154] S.G. Mashnik, A.J. Sierk, O. Bersillon, T. Gabriel, Nucl. Instr. Meth. A 414 (1998) 68; Report LA-UR-97-2905 (1997); http://t2.lanl.gov/publications/publications.html

[155] S.G. Mashnik, R.J. Peterson, A.J. Sierk, M.R. Braunstein, Phys. Rev. C 61 (2000) 034601.

[156] S.G. Mashnik, K.K. Gudima, I.V. Moskalenko, R.E. Prael, A.J. Sierk, Advances in Space Research 34 (2004) 1288.

[157] J. Cugnon, C. Volant, S. Vuillier, Nucl. Phys. A 620 (1997) 475.

[158] A. Boudard, J. Cugnon, S. Leray, C. Volant, Phys. Rev. C 66 (2002) 044615.

[159] R.E. Prael, M.Bozoian, Adaptation of the Multistage Pre-equilibrium Model for the Monte Carlo Method (I), Report LA-UR-88-3238 (Sep. 1998); http://www-xdiv.lanl.gov/XCI/ PEOPLE/rep/plist.html

[160] R.E. Prael, A Review of Physics Models in the LAHETTM Code, LA-UR-94-1817, Los Alamos National Laboratory (1994).

[161] S.G. Mashnik, K.K. Gudima, I.V. Moskalenko, R.E. Prael, A.J. Sierk, Advances in Space Research 34 (2004) 1288.

[162] International Codes and Model Intercomparison for Intermediate Energy Activation Yields," NSC/DOC(97)-1 (Jan. 1997), http://www.nea.fr/html/science/docs/1997/nsc-doc97-1/

[163] L. Dresner, EVAP - A Fortran Program for Calculating the Evaporation of Various Particles from Excited Compound Nuclei, Report ORNL-TM-196 (1961).

[164] A.R. Junghans, M. De Jong, H.-G. Clerc, A.V. Ignatyuk, G.A. Kudyaev, K.-H. Schmidt, Nucl. Phys. A 629 (1998) 635.

[165] R.H. Hildebrand, C.E. Leith, Phys. Rev. 80 (1950) 842.

[166] B. Ragent, The Variation of High-Energy Total Neutron Cross Sections with Energy, Report UCRL-2337 (1953).

[167] J.M. Peterson, A. Bratenahl, J.P. Stoering, Phys. Rev. 120 (1960) 521.

[168] J. Franz, H.P. Grotz, L. Lehmann, E. Roessle, H. Schmitt, L. Schmitt, Nucl. Phys. A 490 (1988) 667.

[169] R.W. Finlay, W.P. Abfalterer, G. Fink, E. Montei, T. Adami, P.W. Lisowski, G.L. Morgan, R.C. Haight, Phys. Rev. C 47 (1993) 237.

[170] V.P. Dzhelepov, V.I. Satarov, B.M. Golovin, Zhurnal Eksperimental'noi i Teoret. Fiziki 29 (1955) 369; English translation: Soviet Physics – JETP 2 (1956) 349.

[171] W.P. Abfalterer, F.B. Bateman, F.S. Dietrich, R.W. Finlay, R.C. Haight, G.L. Morgan, Phys. Rev. C 63 (2001) 044608.

[172] A. Marcinkowski, J. Rapaport, R.W. Finlay, C. Brient, M.B. Chadwick, Nucl. Phys. A 561 (1993) 387.

[173] A. Marcinkowski, R.W. Finlay, J. Rapaport, P.E. Hodgson, M.B. Chadwick, Nucl. Phys. A 501 (1989) 1.

[174] D. Filges, S. Cierjacks, Y. Hino, T.W. Armstrong, P. Cloth, Validation of the Intra-Nuclear Cascade Evaporation Model for Particle Production, Report KFK-3779 (Nov. 1984).

[175] K.R. Cordell, S.T. Thornton, L.C. Dennis, R.R. Doering, R.L. Parks, T.C. Schweizer, Nucl. Phys. A 352 (1981) 485.

[176] E. Daum, U. Fischer, A.Yu. Konobeyev, Yu.A. Korovin, V.P. Lunev, U. von Möllendorff, P.E. Pereslavtsev, M. Sokcic-Kostic, A.Yu. Stankovsky, P.P.H. Wilson, D. Woll, Neutronics of the High Flux Test Region of the International Fusion Materials Irradiation Facility, Report FZKA 5868 (June 1997).

[177] P.G. Young, E.D. Arthur, M.B. Chadwick, Comprehensive Nuclear Model Calculations: Theory and Use of the GNASH Code, Proc. Int. Atomic Energy Agency Workshop on Nuclear Reaction Data and Nuclear Reactors, April 15-May 17, 1996, v.1, p.227; LA-12343-MS, Los Alamos National Laboratory (1992); GNASH-FKK: Pre-equilibrium, Statistical Nuclear-Model Code System for Calculation of Cross Sections and Emission Spectra, RSIC Code Package PSR-125.

[178] C. Kalbach, Phys. Rev. C 32 (1985) 1157.

[179] C. Kalbach, PRECO-D2: Program for Calculating Preequilibrium and Direct Reaction Double Differential Cross Sections, LA-10248-MS, Los Alamos National Laboratory (1985).

[180] M.B. Chadwick, P.G. Young, P. Oblozinsky, A. Marcinkowski, Phys. Rev. C 49 (1994) R2885.

[181] M.B. Chadwick P.G. Young, D.C. George, Y. Watanabe, Phys. Rev. C 50 (1994) 996.

[182] A.Yu. Konobeyev, T. Fukahori, O. Iwamoto, Nuclear Data Evaluation for ^{238}Pu, ^{239}Pu, ^{240}Pu, ^{241}Pu and ^{242}Pu Irradiated by Neutrons and Protons at the Energies up to 250 MeV, JAERI-Research 2002-029, Japan Atomic Energy Research Institute (Dec. 2002).

[183] M.B. Chadwick, P.G. Young, R.E. Macfarlane, A.J. Koning, High-Energy Nuclear Data Libraries for Accelerator-Driven Technologies: Calculational Method for Heavy Recoils, Proc. of 2nd Int. Conf. on Accelerator Driven Transmutation Technology and Applications, Kalmar, Sweden, June 3-7, 1996, p.483.

[184] A.Yu. Konobeyev, Yu.A. Korovin, Kerntechnik 63 (1998) 124.

[185] F.D.Becchetti, Jr., G.W.Greenlees, Phys. Rev. 182 (1969) 1190; data are taken from http://www-nds.iaea.org/RIPL-2/

[186] W. Hauser, H. Feshbach, Phys. Rev. 87 (1952) 366.

[187] F.C. Williams, Nucl. Phys. A 166 (1971) 231.

[188] C. Kalbach, Z. Phys. A 287 (1978) 319.

[189] C. Kalbach, Z. Phys. A 283 (1977) 401.

[190] A.V. Ignatyuk, G.N. Smirenkin, A.S. Tishin, Sov. J. Nucl. Phys. 21 (1975) 255.

[191] A.V. Ignatyuk, Level Densities, In: Handbook for Calculations of Nuclear Reaction Data, Report IAEA-TECDOC-1034 (1998) p.65, http://www-nds.iaea.or.at/ripl/ripl_handbook.htm

[192] G. Hansen, A. Jensen, Nucl. Phys. A 406 (1983) 236.

[193] A.V. Ignatyuk, K.K. Istekov, G.N. Smirenkin, Yadernaja Fizika 29 (1979) 875; English translation: Sov. J. Nucl. Phys. 29(4) (1979) 450.

[194] A.Yu. Konobeyev, T. Fukahori, O. Iwamoto, Neutron and Proton Nuclear Data Evaluation for ^{235}U and ^{238}U at Energies up to 250 MeV, Report JAERI-Research 2002-028 (Dec. 2002).

[195] Reference Input Parameter Library for Theoretical Calculations of Nuclear Reactions. Level Densities. File obninsk_bcs.dat, http://www-nds.iaea.or.at/ripl/densities.htm

[196] A.Yu. Konobeyev, T. Fukahori, O. Iwamoto, Nuclear Data Evaluation for ^{237}Np, ^{241}Am, ^{242g}Am and ^{242m}Am Irradiated by Neutrons and Protons at Energies up to 250 MeV, Report JAERI-Research 2002-032 (Dec. 2002).

[197] V. Avrigeanu, P.E. Hodgson, M. Avrigeanu, Phys. Rev. C 49 (1994) 2136.

[198] M. Blann, Phys. Rev. Lett. 28 (1972) 757.

[199] M. Blann, H.K. Vonach, Phys. Rev. C 28 (1983) 1475.

[200] V.F. Weisskopf, D.H. Ewing, Phys. Rev. 57 (1940) 472.

[201] M. Blann, ALICE-91: Statistical Model Code System with Fission Competition, RSIC Code Package PSR-146.

[202] A.Yu. Konobeyev, Yu.A. Korovin, P.E. Pereslavtsev, Code ALICE/ASH for Calculation of Excitation Functions, Energy and Angular Distributions of Emitted Particles in Nuclear Reactions, Obninsk Institute of Nuclear Power Engineering (1997).

[203] A.I. Dityuk, A.Yu. Konobeyev, V.P. Lunev, Yu.N. Shubin, New Advanced Version of Computer Code ALICE-IPPE, Report INDC(CCP)-410 (1998).

[204] A.Yu. Konobeyev, A.Yu. Korovin, Kerntechnik 59 (1994) 72.

[205] A.Yu. Konobeyev, V.P. Lunev, Yu.N. Shubin, Acta Physica Slovaca 45 (1995) 705.

[206] A.Yu. Konobeyev, Yu.A. Korovin, Kerntechnik 61 (1996) 45.

[207] A.Yu. Konobeyev, Yu.A. Korovin, P.E. Pereslavtsev, Izvestija Vuzov. Ser.: Yadernaja Energetika (Transactions of High School. Ser.: Nuclear Power Engineering) 1 (1997) 2.

[208] Yu.N. Shubin, V.P. Lunev, A.Yu. Konobeyev, A.I. Dityuk, Cross-Section Library MENDL-2 to Study Activation and Transmutation of Materials

Irradiated by Nucleons of Intermediate Energies, Report INDC(CCP)-385 (1995).

[209] A.Yu. Konobeyev, Yu.A. Korovin, M. Vecchi, Kerntechnik 64 (1999) 216.

[210] A.Yu. Konobeyev, Yu.A. Korovin, V.P. Lunev, V.S. Masterov, Yu.N. Shubin, Voprosy Atomnoi Nauki i Techniki (Problems of Nuclear Science and Technology), Series: Nuclear Data 3-4 (1992) 55.

[211] Yu.N. Shubin, V.P. Lunev, A.Yu. Konobeyev, A.I. Dityuk, MENDL-2P. Proton Reaction Data Library for Nuclear Activation, Report IAEA-NDS-204 (1998), http://www-nds.iaea.org/reports/nds-204.pdf

[212] U. Fischer, D. Leichtle, A. Konobeyev, Yu. Korovin, U. von Möllendorff, P.E. Pereslavtsev, I. Schmuck, Intermediate Energy Activation File 2001 (IEAF-2001), Report of Forschungszentrum Karlsruhe, Interner Bericht, IRS-Nr.10/01-Fusion-Nr.179 (Aug. 2001).

[213] Yu.A. Korovin, A.Yu. Konobeyev, P.E.Pereslavtsev, A.Yu. Stankovsky, C. Broeders, I. Broeders, U. Fischer, U von Möllendorf, Nucl. Instr. Meth. A 463 (2001) 544.

[214] U. Fischer, A. Konobeyev, Yu. Korovin, D. Leichtle, U. von Möllendorff, P.E. Pereslavtsev, I. Schmuck, S.P. Simakov, H. Tsige-Tamirat, P.P.H. Wilson, in: Proc. Workshop on Nuclear Data for the Transmutation of Nuclear Waste, GSI, Darmstadt, September 1-5, 2003, http://www-wnt.gsi.de/tramu/proceedings/Fischer.pdf

[215] A.Yu. Konobeyev, Yu.A. Korovin, V.I. Plyaskin, Kerntechnik 59 (1994) 87.

[216] A.Yu. Konobeyev, Yu.A. Korovin, P.E. Pereslavtsev, V.I. Plyaskin, A.Yu. Stankovsky, WIND. Nuclear Data Library for Transactinides at Energies up to 100 MeV, Report INDC(CCP)-384 (1995).

[217] Yu.A. Korovin, A.Yu. Konobeyev, P.E. Pereslavtsev, V.I. Plyaskin, A.Yu. Stankovsky, Progress in Nuclear Energy, 29 Supplement (1995) 297.

[218] Yu.A. Korovin, A.Yu. Konobeyev, P.E. Pereslavtsev, A.Yu. Stankovsky, C. Broeders, I. Broeders, U. Fischer, U. von Möllendorff, P. Wilson, D. Woll, in: Proc. Int. Conf. Nuclear Data for Science and Technology, Trieste, Italy, May 1997, p.851.

[219] A.Yu. Konobeyev, Yu.A. Korovin, Kerntechnik 60 (1995) 147.

[220] E. Bĕták, J. Dobeš, Z. Phys. A 279 (1976) 319.

[221] A. Iwamoto, K. Harada, Phys. Rev. C 26 (1982) 1821.

[222] K. Sato, A. Iwamoto, K. Harada, Phys. Rev. C 28 (1983) 1527.

[223] P. Obložinský, I. Ribanský, Phys. Lett. 74B (1978) 6.

[224] O.T. Grudzevich, A.V. Zelenetsky, A.B. Pashchenko, KOP Code for Calculation of Cross-Section for Interaction of Neutrons and Charged Particles with Atomic Nuclei Based on Optical Model, Report of Institute of Physics and Power Engineering, Obninsk, N1802 (1986).

[225] J.R. Huizenga, G. Igo, Nucl. Phys. 29 (1962) 462.

[226] A.Yu. Konobeyev, Yu.A. Korovin, P.E. Pereslavtsev, U. Fischer, U. von Möllendorff, Nucl. Sci. Eng. 139 (2001) 1.

[227] A. Ferrero, E. Gadioli, E. Gadioli Erba, I. Iori, N. Molho, L. Zetta, Z. Phys. A 293 (1979) 123.

[228] V.I. Ostroumov, R.A. Filov, Sov. Phys. JETP 37(10) (1959) 459.

[229] V.E. Bunakov, M.M. Nesterov, I.A. Tarasov, Bulletin of the Academy of Sciences of the USSR. Physical Series 41(10) (1977) 168; Izvestiya Akademii Nauk SSSR. Seriya Fizicheskaya 41 (1977) 2187.

[230] A. Chatterjee, K.H.N. Murthy, S.K. Gupta, Optical Reaction Cross Sections for Light Projectiles, Report INDC(IND)- 27/GJ (1980).

[231] Yu.N. Shubin, V.P. Lunev, A.Yu. Konobeyev Yu.A. Korovin, in: Proc. of a Specialists Meeting. Intermediate Energy Nuclear Data: Models and Codes, Issy-Les-Moulineaux, France, 30 May-1 June 1994, p.35, http://www.nea.fr/html/science/docs/pubs/iendsm94/

[232] V.V. Artisyuk, A.Yu. Konobeyev, Yu.A. Korovin, Kerntechnik 58 (1993) 174.

[233] Yu.A. Korovin, A.Yu. Konobeyev, P.E. Pereslavtsev, in: Proc. Int. Conf. on Emerging Nuclear Energy Systems, Makuhari, Japan, September 1993, p.444.

[234] A.Yu. Konobeyev, Yu.A. Korovin, V.N. Sosnin, J. Nucl. Mater. 186 (1992) 117.

[235] A.Yu. Konobeyev, Yu.A. Korovin, J. Nucl. Mater. 195 (1992) 286.

[236] A.Yu. Konobeyev, Yu.A. Korovin, Nucl. Instr. Meth. B 82 (1993) 103.

[237] F.P. Denisov, V.N. Mekhedov, Nuclear Reactions at High Energies, Atomizdat, Moscow 1972.

[238] I. Dostrovsky, Z. Fraenkel, G. Friedlander, Phys. Rev. 116 (1959) 683.

[239] S.G. Mashnik, in: Proc. of a Specialists Meeting. Intermediate Energy Nuclear Data: Models and Codes, Issy-Les-Moulineaux, France, 30 May-1 June 1994, p.107, http://www.nea.fr/html/science/docs/pubs/iendsm94/

[240] A. Boudard, J. Cugnon, S. Leray, C. Volant, Nucl. Phys. A 740 (2004) 195.

[241] K. Ackerstaff, et al, Nucl. Instr. Meth. A 491 (2002) 492.

[242] H.W. Bertini, G.D. Harp, F.E. Bertrand, Phys. Rev. C 10 (1974) 2472.

[243] C.K. Cline, Nucl. Phys. A 193 (1972) 417.

[244] I. Ribanský, P. Obložinský, Phys. Lett. 45B (1973) 318.

[245] MCNPX^{TM} User’s Manual. Version 2.4.0, Report LA-CP-02-408 (Sept. 2002).

[246] L. Milazzo-Colli, G.M. Braga-Marcazzan, M. Milazzo, C. Signorini, Nucl. Phys. A 218 (1974) 274.

[247] F.E. Bertrand, R.W. Peelle, Phys. Rev. C 8 (1973) 1045.

[248] J.R. Wu, C.C. Chang, H.D. Holmgren, Phys. Rev. C 19 (1979) 698.

[249] I. Leya, H. Busemann, H. Baur, R. Wieler, M. Gloris, S. Neumann, R. Michel, F. Sudbrock, U. Herpers, Nucl. Instr. Meth. B 145 (1998) 449.

[250] O.A. Schaeffer, J. Zähringer, Zeitschrift für Naturforschung A 13 (1958) 346.

[251] O.A. Schaeffer, J. Zähringer, Phys. Rev. 113 (1959) 674.

[252] H. Dubost, B. Gatty, M. Lefort, J. Peter, X. Tarrago, J. de Physique 28 (1967) 257.

[253] H. Gauvin, M. Lefort, X. Tarrago, Nucl. Phys. 39 (1962) 447.

[254] H. Dubost, M. Lefort, J. Peter, X. Tarrago, Phys. Rev. 136 (1964) B1618.

[255] R.E. Segel, T. Chen, L.L. Rutledge, Jr., J.V. Maher, J. Wiggins, P.P. Singh, P.T. Debevec, Phys. Rev. C 26 (1982) 2424.

[256] R. Michel, M. Gloris, H.-J. Lange, I. Leya, M. Luepke, U. Herpers, B. Dittrich-Hannen, R. Roesel, Th. Schiekel, D. Filges, P. Dragovitsch, M. Suter, H.-J. Hofmann, W. Woelfli, P.W. Kubik, H. Baur, R. Wieler, Nucl. Instr. Meth. B 103 (1995) 183.

[257] K. Goebel, H. Schultes, J. Zähringer, Production Cross Sections of Tritium and Rare Gases in Various Target Elements, Report CERN 64-12 (1964), cited by Ref.[151].

[258] A.Yu. Konobeyev, V.P. Lunev, Yu.N. Shubin, Nucl. Instr. Meth. B 108 (1996) 233.

[259] A.Yu. Konobeyev, Yu. A.Korovin, Atomic Energy 85 (1998) 556.

[260] Z. Lewandowski, E. Loeffler, R. Wagner, H.H. Mueller, W. Reichart, P. Schober, E. Gadioli, E.Gadioli Erba, Lett. Nuovo Cimento 28 (1980) 15.

[261] A.A. Cowley, G.J. Arendse, J.W. Koen, W.A. Richter, J.A. Stander, G.F. Steyn, P. Demetriou, P.E. Hodgson, Y. Watanabe, Phys. Rev. C 54 (1996) 778.

[262] M. Lefort, J. P. Cohen, H. Dubost, X. Tarrago, Phys. Rev. 139 (1965) B1500.

[263] J. Muto, H. Iton, K. Okano, N. Shiomi, K. Fukuda, Y. Omori, M.Kinara, Nucl. Phys. 47 (1963) 19.

[264] M.V. Kantelo, J.J. Hogan, Phys. Rev. C 13 (1976) 1095.

[265] B.N. Mekhedov, V.N. Mekhedov, (1970), cited by Ref.151.

[266] S.L. Green, W.V. Green, F.H. Hegedus, M. Victoria, W.F. Sommer, B.M.Oliver, J. Nucl. Mater. 155/157 (1988) 1350.

[267] D. Hilscher, C.-M. Herbach, U. Jahnke, V. Tishchenko, M. Enke, D. Filges, F. Goldenbaum, R.-D. Neef, K. Nünighoff, N. Paul, H. Schaal, G. Sterzenbach, A. Letourneau, A. Böhm, J. Galin, B. Lott, A. Péghaire, L. Pienkowski, J. Nucl. Mater. 296 (2001) 83.

[268] M. Enke, C.-M. Herbach, D. Hilscher, U. Jahnke, O. Schapiro, A. Letourneau, J. Galin, F. Goldenbaum, B. Lott, A. Péghaire, D. Filges, R.-D. Neef, K. Nünighoff, N. Paul, H. Schaal, G. Sterzenbach, A. Tietze, L. Pienkowski, Nucl. Phys. A 657 (1999) 317.

[269] D.W. Kneff, B.M. Oliver, H. Farrar, L.R. Greenwood, in: Proc. Symp. on Neutron Cross Sections from 10 - 50 MeV, Brookhaven Nat. Lab., May 12-14, 1980, p.289; Nucl. Sci. Eng. 92 (1986) 491.

[270] S.K. Mukherjee, H.Bakhru, in: Proc. Symp. on Nuclear Physics and Solid State Physics, Bombay, India, February 27 – March 2, 1963, p.244.

[271] J.L. Meason, R. Ganapathy, P.K. Kuroda, Radiochimica Acta 6 (1966) 26.

[272] Y. Kasugai, H. Yamamoto, A. Takahashi, T. Iida, K. Kawade, Report JAERI-M-93-046 (1992), p.277.

[273] A.D. Majeddin, V. Semkova, R. Doczi, Cs.M. Buczko, J.Csikai, Investigations on (n,alpha) cross sections in the 14 MeV region, EXFOR 31481, (1997).

[274] S.V. Begun, V.O. Zheltonozhskyj, I.M. Kadenko, V.K. Maidanyuk, V.M. Neplyuev, G.I. Primenko, L.V. Sadovnikov, V.K.Tarakanov, Zbirnik naukovyh prac Kyiv Inst. yadernyh doslidzhen 1(1) (1999) 74.

[275] S.V. Begun, I.M. Kadenko, V.K. Maidanyuk, V.M. Neplyuev, V.A. Plujko, G.I. Primenko, V.K.Tarakanov, in: Proc. Features of Nuclear Excitation States and Mechanisms of Nuclear Reactions, 51-th Meeting on Nuclear Spectroscopy and Nuclear Structure, Sarov, Russia, September 3-8, 2001, the Book of Abstracts, p.203, 2001.

[276] S.V. Begun, I.M. Kadenko, V.K. Maidanyuk, V.M. Neplyuev, G.I. Primenko, V.K. Tarakanov, in: Proc. Int. Conf. on Nuclear Data for Science and

Technology, Tsukuba, Ibaraki, Japan, October 7-12, 2001, Nuclear Science and Technology Supplement, 2 (1) (2002) 425.

[277] A.A. Filatenkov, S.V. Chuvaev, Measurement of a Set of Badly Known Neutron Induced Cross Sections, RI-258, Khlopin Radiev. Inst., St.Petersburg (2001).

[278] J.-Ch. Sublet, A.J. Koning, R.A. Forrest, J. Kopecky, The JEFF-3.0/A Neutron Activation File. EAF-2003 into ENDF-6 Format, JEFDOC-982 (Nov. 2003).

[279] O.T. Grudzevich, A.V. Zeleneckij, A.V. Ignatyuk, A.B. Pashchenko, Yadernye Konstanty 3-4 (1993) 1.

[280] JENDL High Energy Data File 2004, http://wwwndc.tokai.jaeri.go.jp/jendl/jendl.html#jendl-sp

[281] A. Grallert, J. Csikai, Cs.M. Buczko, I. Shaddad, Investigations on the Systematics in (n,alpha) Cross Sections at 14.6 MeV, Report INDC(NDS)-286, 131 (1993).

[282] A.A. Filatenkov, S.V. Chuvaev, Experimental Determination of Cross Sections of a Set of Badly known Neutron Induced Reactions for Heavy Elements (Z=74-79), Report RI-259, Khlopin Radiev. Inst., St.Petersburg (2003).

[283] Y. Ikeda, C. Konno, K. Oishi, T. Nakamura, H. Miyade, K. Kawade, H. Yamamoto, T. Katoh, Activation Cross Section Measurements for Fusion Reactor Structural Materials at Neutron Energy from 13.3 to 15.0 MeV Using FNS Facility, Report JAERI-1312 (1988).

[284] Kong Xiangzhong, Hu Shangbin, Yang Jingkang, Communication of Nuclear Data Progress 17 (1997) 9.

[285] B.P. Bayhurst, R.J. Prestwood, J. Inorg. Nucl. Chem. 23 (1961) 173.

[286] V.S. Barashenkov, B.F. Kostenko, A.M. Zadorogny, Nucl. Phys. A338 (1980) 413.

[287] V.S. Barashenkov, Comp. Phys. Com. 126 (2000) 28.

[288] A European Roadmap for Developing Accelerator Driven Systems (ADS) for Nuclear Waste Incineration. The European Technical Working Group on ADS, April 2001, Ente per le Nuove tecnologie, l’Energia e l’Ambiente (ENEA), April 2001, http://fachp1.ciemat.es/references/roadmap_eu_xads.pdf

[289] Multi-Purpose Hybrid Research Reactor for High-Tech Applications. A European XT-ADS at Mol, http://www.sckcen.be/myrrha/

[290] Accelerator-Driven Transmutation Experimental Facility. High Intensity Proton Accelerator Project. JAERI and KEK Joint Project, http://j-parc.jp/Transmutation/en/ads.html

[291] European Spallation Source (ESS) Project, Forschungszentrum Jülich, http://www.fz-juelich.de/ess/

[292] Spallation Neutron Source. A US Department of Energy Multilaboratory Project, http://www.sns.gov/

[293] V.S. Barashenkov, Le Van Ngok, L.G. Levchuk, Zh.Zh. Musulmanbekov et al: CASCADE – the Code Package for the Simulation of Nuclear Processes Induced by High Energy Particles and Nuclei in Gaseous and Condensed Matter. Report JINR R2-85-173, Dubna (1985).

[294] V.S. Barashenkov, A.Yu. Konobeyev, Yu.A. Korovin, V.N.Sosnin, Atomic Energy 87 (1999) 742.

[295] V.S. Barashenkov et al., Uspekhi Fiz. Nauk 109 (1973) 91.

[296] V.S. Barashenkov, A. Polanski, Electronic Guide for Nuclear Cross Sections, Report JINR E2-94-417, Dubna, 1994, http://doc.cern.ch/tmp/convert_SCAN-9503228.pdf

[297] A. Letourneau, A. Böhm, J. Galin, B. Lott, A. Péghaire, M. Enke, C. -M. Herbach, D. Hilscher, U. Jahnke, V. Tishchenko, D. Filges, F. Goldenbaum, R. D. Neef, K. Nünighoff, N. Paul, G. Sterzenbach, L. Pienkowski, J. Tõke, U. Schröder, Nucl. Phys. A 712 (2002) 133.

[298] P. Jung, in Proc. Int. Conf. on Nuclear Data for Science and Technology, Jülich, Germany, Springer-Verlag, 13 - 17 May 1991, p.352.

[299] von R.H. Bieri, W. Rutsch, Helvetica Physica Acta 35 (1962) 553.

[300] J.P. Alard, A. Baldit, R. Brun, J.P. Costilhes, J. Dhermain, J. Fargeix, L. Fraysse, J. Pellet, G. Roche, J.C. Tamain, Nuovo Cimento A 30 (1975) 320.

[301] F.E. Bertrand, R.W. Peelle, EXFOR O0294001.

[302] S. Furihata, Nucl. Instr. Meth. B171 (2000) 251.

[303] W.D. Myers, W.J. Swiatecki, Ark. Fysik 36 (1967) 343.

[304] M. Blann, G. Reffo, F. Fabbri, Nucl. Instr. Meth. A265 (1988) 490.

[305] N. Bohr, J. A. Wheeler, Phys. Rev. 56 (1939) 426.

[306] S. Yavshits, G. Boykov, V. Ippolitov, S. Pakhomov, A. Roschin, O. Grudzevich, Report INDC(CCP)-430, 2001, p.83; translated from Journal Yadernye Konstanty (Nuclear Constants), Iss. No 1, 2000.

[307] A.Yu. Konobeyev, T. Fukahori, Neutron Data Evaluation for ^{238}U and ^{235}U Irradiated by Neutrons at Energies up to 250 MeV, Periodical Report on Progress from March 1 to May 31, 2001, NDC, JAERI.

[308] M. Uhl, B. Strohmaier, STAPRE - A Computer Code for Particle Induced Activation Cross Sections and Related Quantities, Report IRK-76/01, Vienna, 1976; Addenda 1978.

[309] Yu.E. Titarenko (Project manager), Experimental and Theoretical Study of the Yields of Residual Product Nuclei Produced in Thin Targets Irradiated by 100-2600 MeV Protons, ISTC 839B-99, February 2001.

[310] N.V. Kurenkov, V.P. Lunev, Yu.N. Shubin, Appl. Rad. Isot. 50 (1999) 541.

[311] R. Michel, R. Bodemann, H. Busemann, R. Daunke, M. Gloris, H.-J. Lange, B. Klug, A. Krins, I. Leya, M. Lüpke, S. Neumann, H. Reinhardt, M. Schnatz-Büttgen, U. Herpers, Th. Schiekel, F. Sudbrock, B. Holmqvist, H. Condé, P. Malmborg, M. Suter, B. Dittrich-Hannen, P.-W. Kubik, H.-A. Synal, D. Filges, Nucl. Instr. Meth. B129 (1997) 153.

[312] Yu.A. Korovin, A.Yu. Konobeyev, P.E. Pereslavtsev, Progress in Nuclear Energy 40 (2002) 673.

[313] M.B.Chadwick, P.G.Young, S.Chiba, S.C.Frankle, G.M.Hale, H.G.Hughes, A.J.Koning, R.C.Little, R.E.MacFarlane, R.E.Prael, L.S.Waters, Nucl. Sci. Eng. 131 (1999) 293.

[314] C. Kalbach Walker, PRECO-2000: Exciton Model Preequilibrium Code with Direct Reactions, Triangle Universities Nuclear Laboratory, Duke University, Durham, March 2001; http://www.nndc.bnl.gov/nndcscr/model-codes/preco-2000/index.html

[315] I. Slypen, N. Nica, A. Koning, E. Raeymackers, S. Benck, J.P. Meulders, V. Corcalciuc, J. Phys. G: Nucl. Part. Phys. 30 (2004) 45.

[316] E. Raeymackers, S. Benck, N. Nica, I. Slypen, J.P. Meulders, V. Corcalciuc, A. Koning, A., Nucl. Phys. A726 (2003) 210.

[317] E. Raeymackers, S. Benck, I. Slypen, J.P. Meulders, N. Nica, V. Corcalciuc, A. Koning, Phys. Rev. C68 (2003) 024604.

[318] S.A. Sultana, Syafarudin, F. Aramaki, D. Maki, G. Wakabayashi, Y. Uozumi, N. Ikeda, M. Matoba, Y. Watanabe, H.M. Sen Gupta, Proc. of the 2003 Symposium on Nuclear Data, JAERI, Tokai, Japan, November 27-28, 2003; http://wwwndc.tokai.jaeri.go.jp/nds/proceedings/2003/contents.html

[319] V. Blideanu, F.R. Lecolley, J.F. Lecolley, T. Lefort, N. Marie, A. Ataç, G. Ban, B. Bergenwall, J. Blomgren, S. Dangtip, K. Elmgren, Ph. Eudes, Y. Foucher, A. Guertin, F. Haddad, A. Hildebrand, C. Johansson, O. Jonsson, M. Kerveno, T. Kirchner, J. Klug, Ch. Le Brun, C. Lebrun, M. Louvel, P. Nadel-Turonski, L. Nilsson, N. Olsson, S. Pomp, A.V. Prokofiev, P.-U. Renberg, G. Rivière, I. Slypen, L. Stuttgé, U. Tippawan, M. Österlund, Phys. Rev. C 70 (2004) 014607.

[320] C. Kalbach, Phys. Rev. C 62 (2000) 044608; Phys. Rev. C 64 (2001) 039901(E).

[321] C. Kalbach, Phys. Rev. C 69 (2004) 014605.

[322] S.S. Dimitrova, G.Z. Krumova, P.E. Hodgson, V. Avrigeanu, A.N. Antonov, J. Phys. G: Nucl. Part. Phys. 23 (1997) 961.

[323] F.B. Bateman, R.C. Haight, M.B. Chadwick, S.M. Sterbenz, S.M. Grimes, H. Vonach, Phys. Rev. C 60 (1999) 064609.

[324] A. Duisebayev, K.M. Ismailov, I. Boztosun, Phys. Rev. C 67 (2003) 044608.

[325] A. Guertin, N. Marie, S. Auduc, V. Blideanu, Th. Delbar, P. Eudes, Y. Foucher, F. Haddaa, T. Kirchner, A.J. Koning, Ch. Lebrun, C. Lebrun, F.R. Lecolley, J.F. Lecolley, X. Ledoux, F. Lefebvres, M. Louvel, A. Ninane, Y. Patin, Ph. Pras, G. Riviere, C. Varignon, EXFOR O1146015.

[326] S.M. Grimes, R.C. Haight, J.D. Anderson, Nucl. Sci. Eng. 62 (1977) 187.

[327] S.M. Grimes, R.C. Haight, J.D. Anderson, Phys. Rev. C 17 (1978) 508.

[328] S.M. Grimes, R.C. Haight, K.R. Alvar, H.H. Barschall, R.R. Borchers, Phys. Rev. C 19 (1979) 2127.

[329] A.M. Kalend, B.D. Anderson, A.R. Baldwin, A.R. Madey, J.W. Watson, C.C. Chang, H.D. Holmgren, R.W. Koontz, J.R. Wu, H. Machner, Phys. Rev. C 28 (1983) 105.

[330] I. Slypen, S. Benck, J.P. Meulders, V. Corcalciuc, Atomic Data and Nuclear Data Tables 76 (2000) 26.

[331] S. Benck, I. Slypen, J.P. Meulders, V. Corcalciuc, Atomic Data and Nuclear Data Tables 72 (1999) 1.

[332] S. Benck, I. Slypen, J.P. Meulders, V. Corcalciuc, Atomic Data and Nuclear Data Tables 78 (2001) 161.

[333] S. Benck, I. Slypen, J.-P. Meulders, V. Corcalciuc, Nucl. Sci. Eng. 141 (2002) 55.

[334] E. Raeymackers, I. Slypen, S. Benck, J.P. Meulders, N. Nica, V. Corcalciuc, Atomic Data and Nuclear Data Tables 87 (2004) 231.

[335] C. Kalbach, Phys. Rev. C 71 (2005) 034606.

[336] V.I. Belyakov-Bodin, V.D. Kazaritsky, A.L. Povarov, I.V. Chuvilo, V.A. Sherstnev, J.M. Ado, I.L. Azhgirey, N.V. Mokhov, Nucl. Instr. Meth. Phys. Res. A295 (1990) 140.

[337] V.I. Belyakov-Bodin et al: Calorimetric measurements and Monte Carlo analyses of medium-energy protons bombarding uranium targets. Atomic Energy 70 (1991) 339.

[338] V.I. Belyakov-Bodin, A.M. Andreev, V.D. Dubinsky, V.D. Kazaritsky, A.L. Povarov, I.V. Chuvilo, V.A. Sherstnev, Nucl. Instr. Meth. Phys. Res. A314 (1992) 508.

[339] V.I. Belyakov-Bodin, A.M. Andreev, V.D. Dubinsky, I.V. Chuvilo, V.A. Sherstnev, Nucl. Instr. Meth. Phys. Res. A335 (1993) 30.

[340] C.A. Beard, V.I. Belyakov-Bodin, Nucl. Sci. Eng. 119 (1995) 87.

[341] J.F. Briesmeister (Ed.): MCNP^{TM} – A general Monte Carlo N-particle transport code, UC abc and UC 700, LA-13709-M, March 2000.

[342] M. Kozłowski, H.H. Müller, R. Wagner, Nucl. Phys. A420 (1984) 1.

[343] T.C. Awes, G. Poggi, C.K. Gelbke, B.B. Back, B.G. Glagola, H. Breuer, V.E. Viola, Phys. Rev. C 24 (1981) 89.